Protic-*N*-Heterocyclic Carbene Ruthenium Pincer Complexes: Design, Mechanistic Insights, and Applications in Sustainable Catalysis

Ph.D. Thesis

By

EKTA YADAV

DEPARTMENT OF CHEMISTRY

INDIAN INSTITUTE OF TECHNOLOGY INDORE

JANUARY, 2026

Protic-*N*-Heterocyclic Carbene Ruthenium Pincer Complexes: Design, Mechanistic Insights, and Applications in Sustainable Catalysis

A THESIS

Submitted in partial fulfillment of the
requirements for the award of the degree
of
DOCTOR OF PHILOSOPHY

by

EKTA YADAV



DEPARTMENT OF CHEMISTRY
INDIAN INSTITUTE OF TECHNOLOGY INDORE
JANUARY, 2026

INDIAN INSTITUTE OF TECHNOLOGY INDORE

I hereby certify that the work which is being presented in the thesis entitled **Protic-*N*-Heterocyclic Carbene Ruthenium Pincer Complexes: Design, Mechanistic Insights, and Applications in Sustainable Catalysis** in the partial fulfillment of the requirements for the award of the degree of **DOCTOR OF PHILOSOPHY** and submitted in the **DEPARTMENT OF CHEMISTRY, Indian Institute of Technology Indore**, is an authentic record of my own work carried out during the time period from July 2019 to January 2026 under the supervision of Dr. Amrendra K. Singh, Associate Professor, Department of Chemistry, Indian Institute of Technology Indore, and Dr. Abhinav Raghuvanshi, Assistant Professor, Department of Chemistry, Indian Institute of Technology Indore.

The matter presented in this thesis has not been submitted by me for the award of any other degree of this or any other institute.

Ekta Yadav 12/01/26

Signature of the student with date
(EKTA YADAV)

This is to certify that the above statement made by the candidate is correct to the best of my/our knowledge.

A Singh 12/1/26

Signature of Thesis Supervisor with date
(Dr. AMRENDRA K. SINGH)

13/1/2026

Signature of Thesis Supervisor with date
(Dr. ABHINAV RAGHUVANSHI)

EKTA YADAV has successfully given her Ph.D. Oral Examination held on……...

A Singh 16/11/2026

Signature of Thesis Supervisor with date
(Dr. AMRENDRA K. SINGH)

16/11/2026

Signature of Thesis Supervisor with date
(Dr. ABHINAV RAGHUVANSHI)

ACKNOWLEDGEMENTS

This thesis would not have been possible without the guidance and encouragement of several individuals.

I would like to express my gratitude to my supervisor, ***Dr. Amrendra K. Singh****, for his invaluable guidance, unwavering support, and encouragement throughout my Ph.D. journey. I could not have completed this journey without his thorough knowledge, superior command over the subject, and precious advice. I am deeply grateful for his mentorship, which has significantly influenced my academic growth and the successful completion of this thesis. Especially, I am thankful that my supervisor has been easily approachable and has always taken the time to answer my queries. I also extend my sincere thanks to my co-supervisor,* ***Dr. Abhinav Raghuvanshi****, for his guidance, support, and positive encouragement throughout this work.*

I would like to thank my research PSPC members, ***Prof. Chelvam Venkatesh*** *and* ***Dr. Selvakumar Sermadurai****, for their insightful comments and encouragement, which have greatly contributed to the improvement of my work. I also extend my sincere gratitude to* ***Prof. Tushar Kanti Mukherjee*** *(HoD, Department of Chemistry),* ***Prof. Suhas Joshi*** *(Director, IIT Indore), and all the faculty members of the Department of Chemistry for their consistent support and guidance throughout my PhD journey. I am deeply grateful for the excellent infrastructure provided by the Department of Chemistry, IIT Indore. I am grateful to the entire staff of the Department of Chemistry, particularly* ***Mr. Manish Kushwaha****,* ***Mr. Parthiban P. K****.,* ***Mr. Rameshwar Dauhare****,* ***Vinita Kothari****, and* ***Shouvik Debnath****, for their invaluable assistance. My sincere gratitude goes to the SIC staff at IIT Indore,* ***Mr. Kinny Pandey****,* ***Mr. Ghanshyam Bhavasar,*** ***Mr. Ravindra****, and* ***Mr. Atul Singh*** *for their support with the characterization facilities. I am also equally appreciative of the assistance provided by both the technical*

and non-technical staff of IIT Indore, whose direct and indirect contributions have been immensely helpful.

I would like to extend my sincere thanks to ***Dr. Shilpi Misra*** *for her warm support over the years. A special thanks to my ray of light,* ***Arya****, whose visits always filled our surroundings with warmth, joy, and love. I would also like to express my gratitude to past and present lab members,* ***Dr. Dibya Yadav, Dr. Rahul Singh, Naveen****,* ***Ashu****,* ***Vishal****,* ***Dheeraj****,* ***Gaurav****,* ***Ankita****,* ***Saurabh****, and* ***Subhobrato****, for their support and cooperation during my thesis work. I would like to extend my special gratitude to my seniors,* ***Dr. Navdeep Srivastava*** *and* ***Dr. Nida Shahid****, for their support, guidance, and positive outlook towards life, which has been truly inspiring.*

The journey towards my Ph.D. at IIT Indore would not have been as smooth and fulfilling without the constant scientific and mental support of ***Dr. Shambhu Nath*** *and* ***Dr. Achena****. I would like to express my heartfelt gratitude to my senior and mentor,* ***Dr. Shambhu Nath****, for always being by my side and patiently guiding me through my research. A special thanks to my friend* ***Achena*** *for her companionship and unwavering support. We began this journey together, and now conclude it together. Despite our differing opinions, we have always stood by each other. Additionally, I am grateful to have roommates like* ***Achena*** *and* ***Dr. Amrita****, who cared for me and made me feel at home away from home. I am deeply grateful to* ***Amrita*** *for always being there for me, listening attentively, and being available for late-night talks and morning songs. I would like to express my sincere gratitude to my seniors, friends, and juniors from the department, including* ***Dr. Neha Choudhary****,* ***Dr. Debanjan****,* ***Dr. Sayantan****,* ***Dr. Arghya****,* ***Dr. Shivendu****,* ***Dr. Shivendra****,* ***Dr.Vaishnavi****,* ***Dr. Dilip****,* ***Dr. Rahul****,* ***Dr. Ashvani****,* ***Dr. Shikha****,* ***Ritika****,* ***Poonam****,* ***Neha****,* ***Vidhi****,* ***Supritam*** *for their cooperation throughout the journey. I am also deeply thankful to my dear friends,* ***Shubhi Srivastava****,* ***Pratoli Khare****,* ***Priya Srivastava****,* ***Akansha***

***Patel**, and **Archna Kumari**, who have always been there through the ups and downs of this journey, standing by me unfailingly.*

*My most heartfelt thanks go to my family. I am deeply grateful to my father, **Dr. Siya Ram Yadav**, and my mother, **Smt. Meena Yadav**, for always believing in me and supporting every decision I have made. As a proud daughter, it gives me immense joy to acknowledge their constant encouragement to be independent and to pursue higher studies. Their unconditional love and faith have given me the strength to overcome every obstacle along this journey. My sweetest gratitude also goes to my siblings, **Ms. Namrata Yadav**, **Ms. Sameeksha Yadav**, and **Mr. Abhinav Krishna**, my eternal sources of hope and motivation. Words are truly insufficient to express their contribution to my Ph.D. journey and my life.*

*I would like to express my heartfelt gratitude to the love of my life, **Dr. Pradeep K. Yadav**, my husband, who has always been just a call away whenever I faced challenges. He has been my constant source of strength and encouragement throughout these years. Though moments of failure sometimes made me hesitant, his unwavering support and presence strengthened me each day to keep moving forward. I am also deeply thankful to my supportive in-laws, **Mr. Dinesh K. Yadav** and **Smt. Gyanwati Yadav**, for their understanding and patience throughout this journey. My sincere thanks to my brother-in-law, **Mr. Ashish Kumar**, for his brotherly affection and motivation.*

Finally, I would like to extend my heartfelt thanks to all those who have supported me, directly or indirectly, throughout this journey. Your contributions have been invaluable, and I deeply appreciate each one of you. Although I wish I could mention everyone by name, limitations of time and space compel me to conclude here with my sincere gratitude to all.

with gratitude,

Ekta Yadav

Dedicated

to

My Family

SYNOPSIS

1. Introduction

The growing global demand for sustainable energy has intensified the focus on catalytic systems that enable eco-friendly chemical transformations. Transition metal catalysts, especially those crafted through meticulous ligand engineering, play a crucial role in activating small molecules such as H_2O, HCOOH, and CO_2, which are essential to renewable energy processes. By adjusting the electronic, steric, and cooperative characteristics of ligands, particularly in pincer and N-heterocyclic carbene (NHC) structures, chemists can influence the reactivity and stability of metal centers, thereby enhancing the efficiency of processes such as water oxidation, hydrogen storage, and environmentally friendly synthesis.

Pincer ligands provide a modular and robust scaffold for implementing these design principles, offering a rigid tridentate binding motif whose donor set and substituents can be systematically varied. Palindromic vs non-palindromic frameworks, along with the incorporation of different carbene types such as classical, protic, and anionic, create tunable electronic and steric environments that control hemilability, trans influence, and metal-ligand cooperativity. Embedding N-heterocyclic carbene (NHC) fragments, especially protic NHCs (pNHCs), combines a strong σ-donation with proton-responsive functionality and substrate recognition capability, expanding the catalytic range of pincer complexes.

Within the pincer frameworks, ligand-centered design has emerged as a powerful strategy, positioning ligands not as passive supporters but as active participants in catalytic cycles. Protic NHCs exemplify this advancement by enabling metal-ligand cooperativity (MLC) through proton transfer, hydrogen bonding, and bifunctional activation of substrates. Their integration into pincer architectures provides both geometric rigidity and dynamic reactivity, allowing efficient transformations under mild

conditions and addressing challenges of overpotential, catalyst degradation, and selectivity. These features make pNHC complexes highly effective for key applications, including electrochemical water oxidation, formic acid dehydrogenation, and N-methylation of anilines using sustainable C1 sources.

This thesis explores the design, synthesis, and catalytic evaluation of Ru-based pincer complexes featuring systematically varied β-N, γ-N, and carbene functionalities to establish structure-activity relationships relevant to energy-focused catalysis. Through mechanistic investigations and comparative studies of protic versus classical NHC ligands, the work aims to develop robust catalysts for hydrogen generation, green methylation, and water oxidation. By demonstrating how ligand architecture governs reactivity, selectivity, and stability, the study highlights the broader significance of pNHC-based systems in enabling circular carbon processes, sustainable hydrogen technologies, and environmentally responsible synthetic methodologies.

2. Objectives: The main goals of this thesis are as follows:

- Systematic modification of our unsymmetrical CPAP ligand platform for investigation on the effect of substituent and azole moieties.
- To synthesize a series of Ru-complexes with new CPAP ligands.
- Explore the reactivity of these complexes and catalytic applications, and analyze the effect of various structural modifications.
- To establish the structure-property relationship of the complexes with CPAP ligands.

3. Summary of the Thesis

Based on our previously synthesized ligands, we have introduced a common ligand scaffold that can be tuned from various positions to obtain different

ligands, which further results in the formation of complexes. These complexes are used for analysing different catalytic applications capable of investigating the effect of structural modifications in ligands.

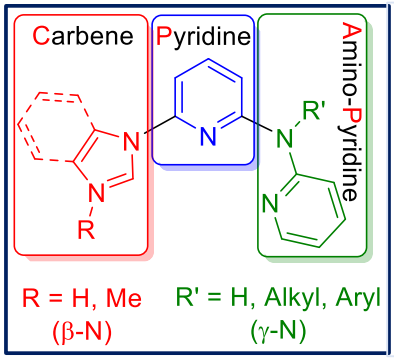

Chapter 2- Based on β-N substitution

Chapter 3- Based on azole moiety

Chapter 4- Based on γ-N substitution

Chapter 5- Fluorescence as a probe for hemilability

Figure 1. Demonstration of CPAP ligands.

Based on the different substitutions, positions, and the moiety, we have divided the thesis into six parts, including four experimental chapters:

Chapter 1. Introduction

This chapter introduces the transition-metal catalysis, guided by deliberate ligand design, which offers a practical route to activate small molecules (H_2O, HCOOH, CO_2) for clean energy and green synthesis in response to the growing global challenges. It explains how ligand-centered strategies, particularly tunable pincer frameworks and tunable N-heterocyclic carbene (NHC) variants, modulate electronic, steric, and cooperative properties at the metal center to improve activity, selectivity, and stability. The chapter highlights protic NHCs (pNHCs) as an advanced ligand class whose N-H functionality enables proton shuttling, hydrogen bonding, and heterolytic H_2 activation. It outlines key catalytic applications targeted here (electrochemical water oxidation, formic-acid dehydrogenation for H_2 storage, and green N-methylation of anilines) and discusses the remaining challenges of catalyst degradation, selectivity, and operational overpotential. Finally, the chapter frames the thesis scope and objectives: to

design and synthesize a family of Ru-pincer complexes with systematic β-N/γ-N and carbene variations, evaluate their comparative performance, and elucidate mechanistic structure-activity relationships that advance robust, energy-relevant catalytic systems.

Chapter 2. Ru(II)-Bis(pincer) Complexes for Electrochemical Water Oxidation

This chapter describes the synthesis of complexes based on the β-N substitution in the CPAP ligand. A series of homoleptic ruthenium(II)-bis(pincer) complexes (**Ru1-4**) featuring unsymmetrical CNN pincer ligands is synthesized and characterized using spectroscopic and single-crystal X-ray diffraction techniques. Additionally, this chapter investigates the catalytic electrochemical water oxidation of these complexes, revealing that **Ru1** and **Ru3**, with proton-responsive protic-NHC ligands featuring β-NH functionalities, demonstrate better water oxidation performance compared to their classical-NHC counterparts, **Ru2** and **Ru4**, respectively. Cyclic voltammetry was conducted at low temperatures (-30 °C) to gain insight into the potentially active intermediates. The foot of the wave analysis (FOWA) was used to elucidate the operating reaction mechanism, revealing a water nucleophilic attack (WNA) mechanism. Catalytic Tafel plots are used to evaluate the performance and benchmark the catalyst. The **Ru1** complex is found to be the most efficient catalyst, among all four complexes in this study, at a modest overpotential (~330 mV vs NHE) with an impressive TON value of 1.6 x 10^5 over a period of 8 h, giving TOF of 5.53 s^{-1}. Even at a lower overpotential of 140 mV vs. NHE the TON (62560) for **Ru1** outperforms most of the homogeneous Ru-systems, other than the Ru(bda) family of complexes, reported so far for the electrochemical water oxidation.

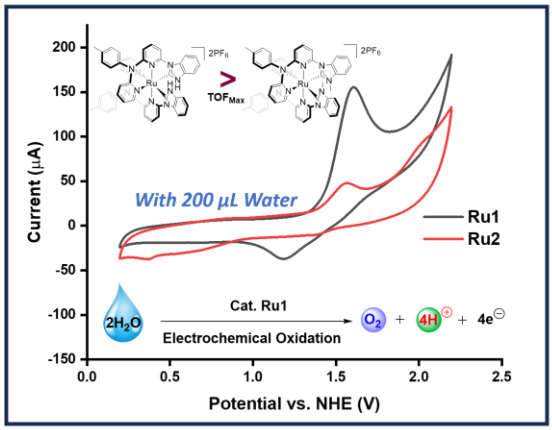

Figure 2. Graphical representation of Ru(II)-bis(pincer) complexes catalysed electrochemical water oxidation.

Chapter 3. Microwave-Accelerated Catalysis with Ru(II)-pNHC Complexes for Selective N-Methylation of Anilines Using Methanol as a Sustainable C1 Source

This chapter describes the synthesis of complexes based on different azole rings in the CPAP ligand scaffold. In this chapter, we discuss a sustainable and atom-economic strategy for the selective N-methylation of anilines using methanol as a benign C1 source with Ru(II)-protic-NHC complexes, resulting in excellent performance under microwave irradiation. A series of Ru(II)-protic-N-heterocyclic carbene complexes bearing unsymmetrical CNN pincer ligands with benzimidazolylidene-based (**[Ru-A]-[Ru-b]**), triazolylidene-based (**[Ru-C]-[Ru-d]**), and newly synthesized imidazolylidene-based complexes (**Ru5** & **Ru6**) have been evaluated, among which the benzimidazolylidene complex **[Ru-A]** exhibited outstanding catalytic performance. Under optimized conditions, **[Ru-A]** achieved >99% conversion and excellent mono-*N*-methylation selectivity using methanol as both the methyl donor and hydrogen source. Remarkably, microwave irradiation accelerated the reaction, reducing the time from 12 h (thermal) to just 35 min at 40 °C with comparable efficiency. The method

displays broad substrate scope, tolerating electron-donating, electron-withdrawing, heteroaromatic, and sterically hindered substrates to afford quantitative *N*-methylated products. Gram-scale synthesis confirmed the robustness and scalability of the process. Mechanistic studies, supported by NMR, mass spectrometry, and GC-MS analyses, along with control experiments, identified *N*-phenylmethanimine and *N*-phenylformamide as key intermediates in a borrowing-hydrogen pathway. The synergistic Ru-protic-NHC framework, combined with microwave-acceleration, provides a green, rapid, and scalable approach for the efficient *N*-methylation of anilines.

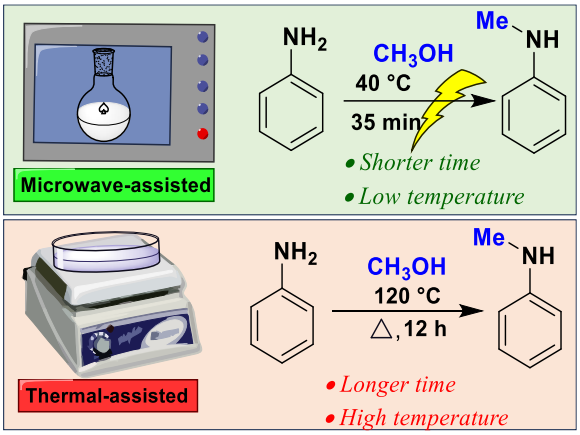

Figure 3. Graphical representation of Ru(II) complexes catalysed *N*-methylation of anilines

Chapter 4. Structure-Activity Relationships and β- vs γ-Substituent Effects on Formic Acid Dehydrogenation

This chapter describes the synthesis of complexes based on different substitutions on the γ-N of the ligand scaffold. In this chapter, we report the synthesis and catalytic evaluation of new Ru(II)-protic-NHC complexes featuring β-NH backbones with either γ-NH (**Ru7**) or γ-NMe (**Ru8**) substituents. These, along with previously reported Ru(II)-protic-NHC and classical NHC analogues (**[Ru-A]-[Ru-d]**), provide a platform for

systematically probing the influence of β- and γ-substituents on formic acid dehydrogenation (FADH). All complexes exhibited notable catalytic activity under both base-assisted, solvent-free conditions and in the ionic liquid 1-butyl-3-methylimidazolium acetate (BMIMOAc) without an external base. Among them, **Ru1** excelled in the ionic liquid medium, achieving a remarkable turnover number (TON) of 65,000 and turnover frequency (TOF) of 4,300 h^{-1} over 15 consecutive formic acid addition cycles. Mechanistic investigations, supported by NMR and control experiments, reveal that under base-assisted conditions, catalysis proceeds via a protic-NHC pathway, whereas in ionic-liquid mediated FADH, anionic-NHC intermediates dominate. Furthermore, the evolved H_2/CO_2 mixture was successfully applied for the hydrogenation of alkenes, and CO_2 capture experiments confirmed the selective utilization of the generated gases. The presence of a β-NH moiety enhances the catalytic activity relative to its *N*-methylated analogue, suggesting a favorable role in facilitating the reaction pathway, whereas the γ-NH functionality exerts a detrimental effect compared to its corresponding γ-N-alkyl and γ-N-aryl substituted derivatives.

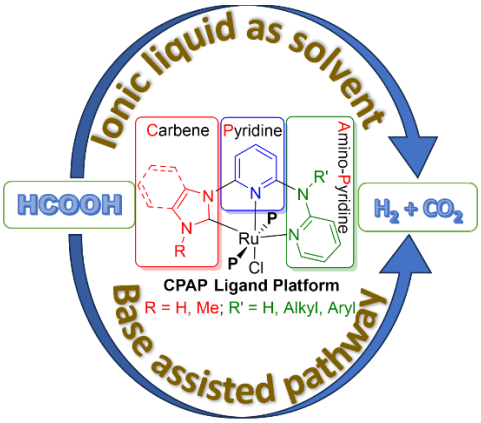

Figure 4. Graphical representation of Ru(II) complexes catalysed formic acid dehydrogenation.

Chapter 5. Structural and Photophysical Correlation in γ-Substituted Metal Complexes: Fluorescence as a Probe for Ligand Hemilability

This chapter discusses a new Ru(II)-pNHC complex synthesized from a previously reported precursor, exhibiting dual-emission fluorescence. To determine the source of each emission band, a comparative analysis was conducted using a series of related ligands that are fluorescent in their own. The fluorescence characteristics of both the free ligands and their respective complexes are influenced by the hemilabile nature of substituents and the type of N-linker within the ligand structure. Minor changes in donor flexibility and coordination reversibility affect the photophysical properties, suggesting that hemilability plays a key role in controlling the excited-state dynamics. These findings demonstrate that strategic ligand design and metal-ligand cooperation can be utilized to tailor the emission properties of coordination complexes.

Chapter 6. Conclusion and Future Scope

In conclusion, this thesis demonstrates that a rational, multi-site tunable pincer ligand scaffold (CPAP) enables systematic control over electronic, steric, and cooperative features of Ru-pincer complexes, and that these structural modifications profoundly influence catalytic performance across energy-relevant transformations. We demonstrate that proton-responsive protic-NHC motifs, featuring β-NH, enhance catalytic activity. **Ru1** emerges as a top performer, delivering low overpotential electrochemical water oxidation (TON ≈1.6×10^5, TOF 5.53 s^{-1}), while **[Ru-A]** performed well in microwave-accelerated, scalable N-methylation of anilines with >99% conversion, and highly efficient towards formic-acid dehydrogenation in ionic liquid media (TON 65,000; TOF 4,300 h^{-1}). Comparative studies reveal clear β- vs. γ-substituent effects (β-NH beneficial; certain γ-substituents deleterious), mechanistic divergence between protic and anionic-NHC pathways depending on the medium/base,

and a tunable balance between hemilability and structural modifications that also controls photophysical behavior. Collectively, these findings establish robust structure-activity relationships that link ligand design to catalytic outcome, validate practical, green protocols (microwave acceleration, ionic-liquid operation, direct gas reuse), and identify remaining challenges, such as catalyst durability, overpotential minimization, and broadened substrate/metal scope, that motivate future work on ligand stabilization strategies and deeper mechanistic exploration.

LIST OF PUBLICATIONS

Publications included in the thesis

1) **Yadav, E**.; Nath, S.; Shahid, N.; Saha, A.; Das, B.; Singh, A. K. (2025), Enhanced activity of proton-responsive protic-NHC-Ru(II) bis(pincer) complexes for electrochemical water oxidation. *ChemCatChem* 17, e01003. (https://doi.org/10.1002/cctc.202501003). (IF: 4.1)

2) **Yadav, E.**; Nath, S.; Saha, A.; Singh, A. K. Structure-Activity Relationships in Ru(II)-Protic-NHC Complexes: β- vs γ-Substituent Effects on Formic Acid Dehydrogenation Performance. *Chem. Asian J*., 2026, 21, e70621(https://doi.org/10.1002/asia.70621). (IF: 3.2)

3) **Yadav, E.**; Saha, A.; Nath, S.; Singh, A. K. Microwave-Accelerated Catalysis with Ru(II)-pNHC Complexes for Selective N-Methylation of Anilines Using Methanol as a Sustainable C1 Source. *Molecular Catalysis*, 593, 2026, 115764. (https://doi.org/10.1016/j.mcat.2026.115764). (IF: 4.3)

Publications other than those included in the thesis

1) Nath, S.; **Yadav, E.**; Raghuvanshi, A.; Singh, A. K. (2023), Ru(II) Complexes with Protic- and Anionic-Naked-NHC Ligands for Cooperative Activation of Small Molecules. *Chem. Eur. J. 29* (52). (DOI: 10.1002/chem.202301971). (IF: 3.6)

2) Nath, S.; **Yadav, E.**; Raghuvanshi, A.; Singh, A. K. (2023), Mechanistic Insights and Comparative Analysis of Ru(ii)–NNC Pincer Complexes with Anionic-, Protic-, and Classical-NHCs for Transfer Hydrogenation of Ketones. *Catal. Sci. Technol.*, *13* (24), 7085-7099. (DOI:10.1039/D3CY01383A). (IF: 4.0)

3) Saha, A.; Nath, S.; **Yadav, E.**; Singh, A. K. (2025), Ru(II)-protic-NHC complex Catalyzed Selective N-alkylation of Anilines with Primary

Alcohols: Mechanistic Insights and Role of Salt Additives. *ChemCatChem*, e202500184. (DOI: 10.1002/cctc.202500184). (IF: 4.1)

4) Saha, A.; **Yadav, E.**; Nath, S.; Singh, A.; Singh, A. K. (2025), Ru(II)-CNC pincer complexes with bis(protic-NHC): Comparative analysis with bis(classical-NHC) and mixed protic- & classical-NHC analogues. New J. Chem. 49, 18191-18201.(https://doi.org/10.1039/D5NJ03111G). (IF: 2.6)

5) Saha, A.; Nath, S.; **Yadav, E.**; Singh, A. K. Highly Efficient Microwave-Accelerated Transfer Hydrogenation for CO_2-Derived Carbonate Valorization by Ru(II)-Protic NHC Pincer Catalysts. Green Chem. 2026, 28 (30): 12647-12661. (https://doi.org/10.1039/d6gc00476h) (IF: 10.6)

Conferences/Oral/Poster presentation

Poster presentation

1) Presented a poster at the **"Royal Society of Chemistry and IIT Indore Symposium on Materials Science Towards New Horizons-2023"** on January 19-20, 2023, organized by the Department of Chemistry, Indian Institute of Technology Indore.

2) Presented a poster at **"Frontiers in Chemistry, CRSI Bhopal/Indore local chapter one-day conference,"** Organized by IISER Bhopal and IIT Indore on May 4, 2024.

3) Presented a poster at the conference **"Frontiers in Sustainable Catalysis and Organometallics (FISCO-2024)"** on July 11-12, 2024, organized by the Department of Chemistry, Malaviya National Institute of Technology, Jaipur.

4) Presented a poster at the **"CHEM 2024, In-house symposium"** on March 2022, organized by the Department of Chemistry, Indian Institute of Technology Indore.

Oral presentation

1) Oral presentation at the **"CHEM-2024 In-House Symposium"** organized by the Department of Chemistry, IIT-Indore, India, on March 21, 2024.

TABLE OF CONTENTS

LIST OF FIGURES		XXIII-XXIX
LIST OF SCHEMES & TABLES		XXX-XXXI
NOMENCLATURE		XXXII
ACRONYMS		XXXIII-XXXIV

Chapter 1

Introduction

1.1	Background and motivation	**3-6**
1.2	Ligand Design and Its Impact on Catalytic Applications	**6-7**
1.3	Pincer Ligand Frameworks as Modular Scaffolds for Catalyst Design	**8-10**
1.4	*N*-Heterocyclic Carbenes (NHCs) in Catalysis	**10-14**
1.5	Metal ligand cooperativity	**14-19**
1.6	Key Catalytic Applications Explored	**19-25**
1.7	Research gap	**26**
1.8	Scope of the thesis	**26-27**
1.9	Objectives of the thesis	**27**
1.10	Organization of the Thesis	**27-28**
1.11	References	**28-50**

Chapter 2

Ru(II)-Bis(pincer) Complexes for Electrochemical Water Oxidation

2.1	Introduction	**53-54**
2.2	Results and discussion	**54-76**
	2.2.1 Synthesis of ligands (L1, L2·HI, L3 and L4·HI)	**54-56**
	2.2.2 Preparation of Ru(II)-bis(pincer) complexes	**56-59**

2.2.3 Molecular structures of **Ru1**-**Ru4** complexes **59-62**
2.2.4 Electrochemical analysis **62-65**
2.2.5 Electrochemical experiments at low temperature **66-67**
2.2.6 Water oxidation reaction (WOR) **67-71**
2.2.7 FOWA analysis of **Ru1-Ru4** for WNA mechanism **71-72**
2.2.8 Chronoamperometry **72-75**
2.2.9 pH-dependent electrochemical analysis **75-76**
2.3 Conclusion **76-77**
2.4 Experimental section **77-95**
2.5 References **96-109**

Chapter 3

Microwave-Accelerated Catalysis with Ru(II)-pNHC Complexes for Selective N-Methylation of Anilines Using Methanol as a Sustainable C1 Source

3.1 Introduction **113-116**
3.2 Results and discussion **116-137**
3.2.1 Reaction optimization and comparative evaluation **121**
3.2.1.1 Thermal *N*-methylation of anilines **121-125**
3.2.1.2 Microwave-assisted *N*-methylation of anilines **125-127**
3.2.2 Evaluation of substrate scopes under thermal and microwave conditions **127-130**
3.2.3 Gram-scale synthesis of *N*-methyl aniline **130-131**
3.2.4 Control Studies **131-132**
3.2.5 Mechanistic Studies **132-134**
3.2.6 Proposed reaction mechanism **134-137**
3.3 Conclusion **137**
3.4 Experimental section **138-150**

3.5 References **150-160**

Chapter 4

Structure-Activity Relationships and β- vs γ-Substituent Effects on Formic Acid Dehydrogenation

4.1 Introduction **163-166**

4.2 Results and discussion **166-194**

4.2.1 CPAP series of ligands **166**

4.2.2 Synthesis and Characterization of ligands **167-170**

4.2.3 Synthesis and Characterization of Complexes **170-175**

4.2.4 Comparative study of Ru(II) complexes in formic acid dehydrogenation (FADH) **175-180**

4.2.4.1 Base-assisted FADH **175-178**

4.2.4.2 Ionic liquid-mediated FADH **178-180**

4.2.5 Kinetics of formic acid dehydrogenation: temperature, TON evolution, and reaction order **180**

4.2.6 Time-resolved kinetic analysis of formic acid dehydrogenation **180-182**

4.2.7 Effect of sequential base addition on catalytic performance and gas evolution **182-184**

4.2.8 TON/TOF Calculation details **184-185**

4.2.9 Controlled Experiments **185-187**

4.2.10 Formic acid dehydrogenation (FADH) reaction setup **187-188**

4.2.11 Systematic utilization and characterization of H_2/CO_2 evolved from FADH. **188-190**

4.2.12 Comparative mechanistic insights into base- and ionic liquid-mediated FADH by [Ru-A] **190-192**

4.2.13 Proposed mechanistic pathways for FADH under basic and ionic liquid conditions **192-194**

4.3 Conclusion **195**
4.4 Experimental section **196-208**
4.5 References **208-220**

Chapter 5

Structural and Photophysical Correlation in γ-Substituted Metal Complexes: Evidence for Ligand Hemilability

5.1 Introduction **223-225**
5.2 Results and discussion **225-238**
5.2.1 Synthesis and characterization of complex **Ru9** **225-227**
5.2.2 Molecular structure of complex **Ru9** **228**
5.2.3 Photophysical properties **229**
5.2.4 UV-visible and fluorescence study of complex **Ru9** **229-230**
5.2.5 Photophysical properties of **[Ru-A]** and ligand **L1** **230-232**
5.2.6 UV-Vis absorption and fluorescence for the ligands and metal complexes, illustrating structural effects **232-235**
5.2.7 Effect of the addition of 4-aminopyridine on fluorescence **235-238**
5.3 Conclusion **238**
5.4 Experimental section **238-245**
5.5 References **245-250**

Chapter 6

Summary and Future Scope

6.1 Summary **253-256**
6.2 Future Scope **256-257**

LIST OF FIGURES

Figure 1.1	Energy production from renewable energy sources and chemical transformations as an alternative	**4**
Figure 1.2	Utilization of transition metal catalysts in various applications	**5**
Figure 1.3	**(a)** Schematic representation of a pincer framework **(b)** Diversification of pincer ligands and incorporation of NHCs in a non-palindromic ligand	**9**
Figure 1.4	A general structure for N-heterocyclic carbene in azole rings (a) Classical NHCs (b) Protic-NHCs bearing NH, NR- and NH, NH substituents	**10**
Figure 1.5	Representative examples of bidentate and tridentate pNHC precursors	**13**
Figure 1.6	Schematic representation of metal-ligand cooperation (MLC) in protic-NHC pincer complexes	**15**
Figure 1.7	Selected examples of MLC catalysts with protic functionalization.	**18**
Figure 1.8	Selected examples of catalysts for electrochemical water oxidation.	**21**
Figure 1.9	Schematic representation of the formic acid dehydrogenation process	**22**
Figure 1.10	Selected examples of catalysts for formic acid dehydrogenation	**23**
Figure 1.11	Demonstration of previously synthesized complexes based on a series of ligands called CPAP	**27**

Figure 2.1	^{1}H NMR spectrum of **Ru1** in DMSO-d_6.	**58**
Figure 2.2	^{13}C NMR spectrum of **Ru1**in DMSO-d_6.	**58**
Figure 2.3	Molecular structures of **Ru1-Ru4.**	**60**
Figure 2.4	Cyclic Voltammograms of all the complexes (**Ru1**-**Ru4**).	**63**
Figure 2.5	Differential Pulse voltammograms for all complexes (**Ru1**-**Ru4**).	**63**
Figure 2.6	Cyclic Voltammogram of Complexes at different scan rates.	**65**
Figure 2.7	Cyclic Voltammogram of **Ru1** complex at low temperature (-30 °C)	**66**
Figure 2.8	Cyclic Voltammogram of **Ru3** complex at low temperature (-30 °C)	**67**
Figure 2.9	Cyclic Voltammograms of all the complexes (**Ru1**-**Ru4**) showing the electrochemical behavior before and after the addition of 200 µL of water	**68**
Figure 2.10	Cyclic Voltammogram of **Ru1** complex in dry ACN using 0.1 M $TBAPF_6$ as electrolyte at room temperature	**69**
Figure 2.11	A plot of i/i_p vs. $1/\{1 + e [(f(E-E°)]\}$ where f = nF/RT, assuming WNA mechanism for the electrochemical water oxidation using all the complexes **Ru1**-**Ru4**.	**71**
Figure 2.12	(**a**) A chronoamperometry experiment was conducted for 2 hours at 1.56 V vs. NHE using **Ru1** (**b**) Cyclic voltammograms (CVs) were recorded up to 200 cycles at a scan rate of 50 mV/s	**72**

Figure 2.13	Chronoamperometry measurements of complexes **Ru1-Ru4** for an 8 h period for potential 1.56 V vs. NHE	**73**
Figure 2.14	Chronoamperometry measurements of complex **Ru1** for a 20 h period	**74**
Figure 2.15	Cyclic Voltammograms showcasing the catalyst behaviour before and after the 20 hr chronoamperometry	**75**
Figure 2.16	Cyclic voltammograms of **Ru1**and **Ru2** in H_2O/CH_3CN with added aqueous acid (1M HCl), basic (1M NaOH), and buffer solutions (Citric acid + NaH_2PO_4), showing pH-dependent OER activity	**76**
Figure 2.17-2.43	Additional characterization and catalytic experimental data	**82-95**
Figure 3.1	A general hydrogen borrowing reaction mechanism of *N*-methylation of amines with methanol	**114**
Figure 3.2	Selected examples of reported catalysts for *N*-methylation of anilines	**115**
Figure 3.3	^{1}H NMR of **Ru5** in DMSO-d_6	**118**
Figure 3.4	^{13}C NMR of **Ru5** in DMSO-d_6	**119**
Figure 3.5	^{31}P NMR of **Ru5** in DMSO-d_6	**119**
Figure 3.6	^{1}H NMR of **Ru6** in DMSO-d_6	**120**
Figure 3.7	^{13}C NMR of **Ru6** in DMSO-d_6	**120**
Figure 3.8	^{31}P NMR of **Ru6** in DMSO-d_6	**121**
Figure 3.9	Reaction profile for the *N*-methylation of aniline using methanol as the methylating agent, monitored by GC.	**127**

Figure 3.10	Control experiments elucidating the reaction pathway for [Ru-A]-catalyzed *N*-methylation of anilines	**132**
Figure 3.11	Mechanistic investigation using NMR experiments	**133**
Figure 3.12	Proposed mechanism for N-methylation of anilines catalysed by [**Ru-A]** and **Ru5** using methanol	**135**
Figure 3.13	Proposed mechanism for Ru(II)-classical-NHC complexes, [**Ru-B]** and **Ru6**	**136**
Figure 3.14	GC-MS for the identification of N-phenylmethanimine at room temperature	**148**
Figure 3.15	GC-MS for the reaction mixture by using deuterated methanol (CD_3OD)	**149**
Figure 3.16	LC-MS of **[Ru-A]** under standard conditions after two minutes	**150**
Figure 4.1	Some representative homogeneous Ru-catalysts for formic acid dehydrogenation (FADH)	**165**
Figure 4.2	Complexes [**Ru-A]-[Ru-d**] and **Ru7-Ru8** were used in this study for formic acid dehydrogenation (FADH)	**166**
Figure 4.3	Demonstration of the CPAP series of ligands	**167**
Figure 4.4	^{1}H NMR of **L5** in $CDCl_3$	**168**
Figure 4.5	^{13}C NMR of **L5** in $CDCl_3$	**168**
Figure 4.6	^{1}H NMR of **L6** in $CDCl_3$	**169**
Figure 4.7	^{13}C NMR of **L6** in $CDCl_3$	**169**
Figure 4.8	^{1}H NMR of **Ru7** in DMSO-d_6	**171**

Figure 4.9	^{13}C NMR of **Ru7** in DMSO-d_6	**171**
Figure 4.10	^{31}P NMR of **Ru7** in DMSO-d_6	**172**
Figure 4.11	^{1}H NMR of **Ru8** in DMSO-d_6	**173**
Figure 4.12	^{13}C NMR of **Ru8** in DMSO-d_6	**173**
Figure 4.13	^{31}P NMR of **Ru8** in DMSO-d_6	**174**
Figure 4.14	^{1}H NMR of **Ru8** in CD_3CN	**174**
Figure 4.15	^{31}P NMR of **Ru8** in CD_3CN	**175**
Figure 4.16	**(a)** Temperature-dependent gas evolution for **[Ru-A] (b)** Time-resolved TON profile of **[Ru-A]** under optimized reaction conditions	**181**
Figure 4.17	**(a)** Reaction time versus substrate concentration plots **(b)** Dependence of the initial dehydrogenation rate on **[Ru-A]** catalyst concentration	**181**
Figure 4.18	Plot of gas volume versus number of cycles for formic acid dehydrogenation at standard conditions	**182**
Figure 4.19	The graph between the number of cycles and the volume of gas collected using a single addition of catalyst **[Ru-A]** with BMIMOAc under standard conditions	**183**
Figure 4.20	Controlled experiments were conducted in both conditions: base-assisted solvent-free and ionic liquid as solvent	**186**
Figure 4.21	Experimental setup employed for formic acid dehydrogenation studies	**188**

Figure 4.22	Schematic representation of the controlled experiments designed to evaluate the utilization of evolved gases	**189**
Figure 4.23	Stepwise ^{1}H NMR spectra illustrating the sequential transformations of [**Ru-A]** upon successive additions of the ionic liquid (as solvent) and formic acid	**191**
Figure 4.24-4.38	Additional experimental data	**201-208**
Figure 5.1	Complexes **[Ru-A], Ru7**, and **Ru8** used for the fluorescence study	**225**
Figure 5.2	^{1}H NMR of Ru-bpy complex, **Ru9**	**226**
Figure 5.3	^{13}C NMR of Ru-bpy complex, **Ru9**	**227**
Figure 5.4	^{31}P NMR of Ru-bpy complex, **Ru9**	**227**
Figure 5.5	Molecular structure of complex **Ru9** obtained from a single-crystal X-ray diffraction study	**228**
Figure 5.6	Absorbance spectrum of complex **Ru9**	**229**
Figure 5.7	Emission spectra for complex **1**; **(a)** Emission at different wavelength ranges, **(b)** Emission at fixed wavelength range on different concentrations	**230**
Figure 5.8	**(a)** Absorption spectrum for complex **[Ru-A]**; **(b)** Emission spectrum of **[Ru-A]** at fixed wavelength range on different concentrations	**231**
Figure 5.9	**(a)** Absorption spectrum for ligand, **L1**; **(b)** Emission spectrum of **L1** at fixed wavelength range on different concentrations	**232**
Figure 5.10	Absorption spectra for **(a)** γN-H ligand (**L5**);**(b)** γN-Me ligand (**L6**); **(c)** γN-H complex (**Ru7**); **(d)** γN-Me complex (**Ru8**)	**233**

		234
Figure 5.11	Emission spectra for Ligands **L5** and **L6** in methanol at room temperature; **(a)** Emission spectrum of **L5** on different concentrations, **(c)** Emission spectrum of **L6** on different concentrations	
Figure 5.12	Emission spectra for Complexes **Ru7** and **Ru8** in methanol at room temperature; **(a)** Emission spectrum of **Ru7** on different concentrations, **(b)** Emission spectrum of **Ru8** on different concentrations	**235**
Figure 5.13	Emission spectra for Complexes **[Ru-A]**, **Ru7,** and **Ru8** in methanol at room temperature after the addition of 4-aminopyridine sequentially	**236**
Figure 5.14	LCMS of **Ru9** for $[M-2Cl]^{2+}$	**241**
Figure 5.15	LCMS of **Ru9** for $[M-2Cl-H]^{+}$	**242**
Figure 5.16	HRMS of **Ru9** for $[M-2Cl-H]^{+}$	**243**
Figure 5.17	HRMS of **Ru9** for $[M-2Cl]^{2+}$	**244**
Figure 5.18	Correlation of fluorescence intensity and the concentrations of (a-b) ligands; (c-e) complexes; (f-h) after addition of 4-aminopyridine	**245**

LIST OF SCHEMES

Scheme 1.1	Metal complexes showing the effect of tuning ligand design on the catalytic reactivity	**7**
Scheme 1.2	Grubbs catalysts demonstrate the effect of NHCs insertion in the ligand platform	**11**
Scheme 1.3	Reactivity of a protic-NHC Ruthenium complex	**12**
Scheme 1.4	Illustration of metal-ligand cooperation in protic-NHC complexes	**17**
Scheme 1.5	General reaction for Water splitting	**20**
Scheme 1.6	Selected examples of catalysts for N-methylation of anilines	**25**
Scheme 2.1	Synthesis of ligands (**L1, L2·HI, L3** and **L4·HI**)	**55**
Scheme 2.2	Synthetic procedure for ligand **L3**	**56**
Scheme 2.3	Synthetic procedure for ligand **L4·HI**	**56**
Scheme 2.4	Synthesis of complexes **Ru1-Ru4**	**57**
Scheme 3.1	Synthesis of Ru(II) pNHC complex, **Ru5** and Ru(II) classical-NHC complex, **Ru6**.	**117**
Scheme 3.2	Gram-scale reaction for *N*-methylation of anilines	**131**
Scheme 4.1	Synthetic route for the preparation of ligands **L5** and **L6**	**167**
Scheme 4.2	Synthetic route for the preparation of **Ru7** and **Ru8** complexes	**170**
Scheme 4.3	Proposed catalytic cycle for base-assisted dehydrogenation of formic acid by [**Ru-A]**	**193**

Scheme 4.4 Proposed catalytic cycle for formic acid dehydrogenation by **[Ru-A]** in an ionic liquid medium **194**
Scheme 5.1 Synthetic representation for the formation of complex **Ru9** **225**

LIST OF TABLES

Table 2.1 Crystal data and structural refinement parameters for complexes **Ru1** and **Ru2** **61**
Table 2.2 Crystal data and structural refinement parameters for complexes **Ru3** and **Ru4** **61-62**
Table 3.1 Optimization of thermal *N*-methylation of anilines catalyzed by ruthenium complexes **122-123**
Table 3.2 Optimization for reaction conditions for microwave-assisted N-methylation of anilines catalysed by **[Ru-A]** **126**
Table 3.3 Substrate scope for the *N*-methylation of anilines catalyzed by **[Ru-A]** **130**
Table 4.1 Dehydrogenation of formic acid with ruthenium complexes **177-178**
Table 4.2 Optimization for reaction conditions using **[Ru-A]** in the presence of ionic liquid as solvent **179-180**

NOMENCLATURE

α	Alpha
β	Beta
γ	Gamma
°C	Degree centigrade
Å	Angstrom
%	Percentage
σ	Sigma
π	Pi
δ	Chemical shift
J	Coupling constant
V	Volts
Hz	Hertz
μM	Micromolar
μL	Microliter
μA	Microampere
mL	Milliliter
mV	Millivolt
λ	Wavelength
θ	Angle
W	Watt

ACRONYMS

pNHC	Protic N-Heterocyclic carbene complex
NHC	N-heterocyclic carbene complex
FADH	Formic acid dehydrogenation
$CDCl_3$	Deuterated chloroform
DMSO-d_6	Deuterated dimethyl sulfoxide
CCDC	The Cambridge Crystallographic Data Centre
DMSO	Dimethyl sulfoxide
EDG	Electron-donating group
EWG	Electron-withdrawing group
Et_2O	Diethyl ether
EtOAc	Ethyl acetate
MeOH	Methanol
ACN	Acetonitrile
^{t}BuOH	*tert*-Butanol
equiv.	Equivalent
ESI-MS	Electrospray ionization mass spectrometry
m/z	Mass/Charge
HRMS	High-resolution mass spectrometry
NMR	Nuclear Magnetic Resonance
CV	Cyclic Voltammetry
DPV	Differential Pulse Voltammetry
FOWA	Foot of the Wave
WNA	Water Nucleophilic Attack
I2M	Intermolecular mechanism
OER	Oxygen evolution reaction
UV-Vis	Ultraviolet Visible spectroscopy
GC-MS	Gas Chromatography-Mass Spectrometry

KO^tBu	Potassium tert-butoxide
$TBAPF_6$	Tetrabutylammonium hexafluorophosphate
BMIMOAc	1-butyl-3-methylimidazolium acetate
PPh_3	Triphenyl phosphine
SCXRD	Single Crystal X-ray Diffraction
TEMPO	(2,2,6,6-Tetramethylpiperidin-1-yl)oxyl
CO_2	Carbon dioxide
N_2	Nitrogen
4-AP	4-aminopyridine
bpy	2,2′-bipyridine
MW	Microwave
GC	Glassy Carbon
WOR	Water oxidation reaction



CHAPTER 1

Introduction



1. Introduction

1.1 Background and Motivation

The modern world today faces significant global challenges, including the energy crisis and climate change.[1,2] The rapid depletion of fossil fuels, combined with the rising energy demands driven by population growth and industrialization, has intensified the need for alternative energy solutions.[3,4] Simultaneously, the continued dependence on carbon-intensive fuels has led to significant environmental consequences, including global warming, extreme weather events, and widespread biodiversity loss.[5,6] These challenges underscore the urgent need for sustainable and renewable energy sources that can ensure long-term energy security while minimizing ecological impacts.[7] In this context, organic transformations via chemical reactions play a crucial role in facilitating energy-efficient processes, such as the synthesis of energy carriers, fuel additives, and high-value chemicals from biomass or carbon-neutral feedstocks (Figure 1.1).[8] The utilization of transition metal catalysts has become essential for facilitating these transformations by improving their reaction efficiency, selectivity, and sustainability. The ability of transition metal complexes to activate small molecules, such as H_2, CO_2, and formic acid, as catalysts has opened up novel strategies for green energy storage and utilization. [9,10] Therefore, implementing advanced catalytic systems based on transition metals in the chemical and energy sectors is vital for addressing these global challenges through innovative and environmentally sustainable technologies.

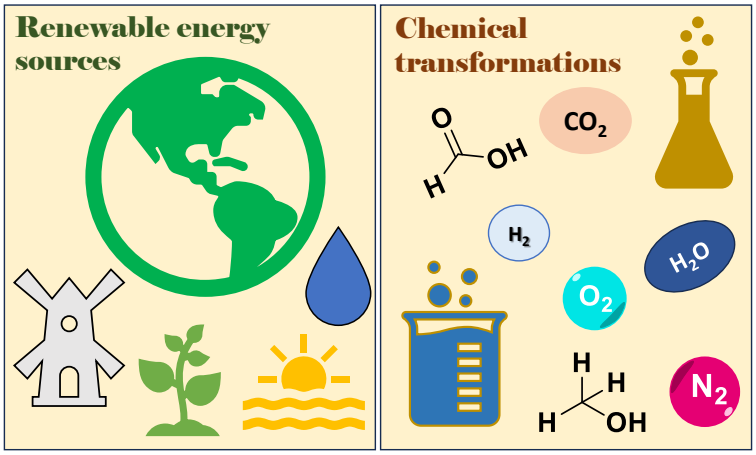

Figure 1.1 Energy production from renewable energy sources and chemical transformations as an alternative

The activation of small molecules, such as water (H_2O), formic acid (HCOOH), and carbon dioxide (CO_2), is of critical importance in renewable energy pathways, as these abundant and readily accessible compounds serve as key intermediates and carriers in sustainable energy cycles.[11] Efficient activation of H_2O is crucial for water splitting, a process that generates hydrogen, a clean and high-energy fuel, using renewable sources.[12] Similarly, formic acid is increasingly recognized as a safe, easily handled, and transportable material for hydrogen storage, capable of releasing hydrogen gas during the dehydrogenation process under mild and feasible conditions.[13] Carbon dioxide, a significant greenhouse gas, represents both a critical challenge and an opportunity as a valuable resource.[14] The catalytic transformation of CO_2 into valuable fuels and chemicals via hydrogenation or electrochemical reduction offers a promising route for completing the carbon cycle and mitigating CO_2 levels in the atmosphere.[15] Transition metal complexes and catalytic systems that can selectively activate these small molecules are indispensable for achieving high efficiency and sustainability in energy conversion and storage (Figure 1.2).[16–18] Consequently, the activation of small molecules is central to many renewable energy strategies, facilitating the production of clean fuels, reducing greenhouse gas emissions, and advancing circular energy systems, as well as carbon utilization processes.[19,20]

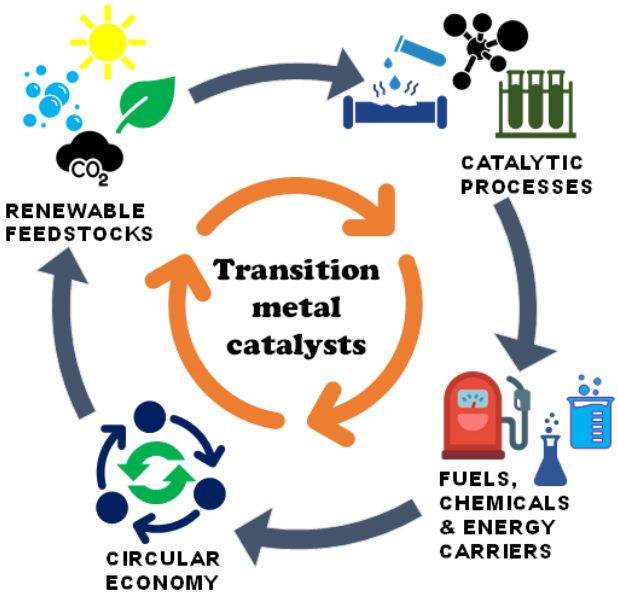

Figure 1.2 Utilization of transition metal catalysts in various applications

Transition metal catalysis is fundamental to modern chemical science, facilitating a vast array of chemical transformations with high efficiency, selectivity, and atom economy.[21] The unique ability of transition metals to access multiple oxidation states and coordinate with various substrates allows them to mediate complex reactions under mild conditions.[22] Central to the success of these catalytic systems is the design of the ligand, as it significantly influences the electronic and steric properties of the metal center.[23] The rational tailoring of ligand frameworks, such as pincer, *N*-heterocyclic carbene (NHC), phosphine, or bipyridine-based ligands, enables tuning of the reactivity, stability, and selectivity of metal catalysts.[24] In most cases, ligands also influence various essential processes either by being involved in the catalytic mechanism or by influencing the electronic and steric environment, such as substrate activation, bond formation or cleavage, and catalyst regeneration.[25,26] Recent advances in catalysis chemistry, integrating ligand design, have led to the development of a catalyst system that can activate stable bonds, operate in water or environmentally friendly solvents, and facilitate reactions crucial for energy-related processes, including hydrogen production, carbon dioxide reduction, and the dehydrogenation of formic acid.[27,28] The synergetic connection between transition metal centers

and specifically engineered ligands continues to advance the field of catalysis, leading to more sustainable and effective chemical processes.[29]

1.2 Ligand Design and Its Impact on Catalytic Applications

The concept of ligand-centered design has become a powerful strategy in developing selective and efficient catalytic systems, particularly in the realm of homogeneous catalysis.[30] Ligand modification is crucial for designing transition metal catalysts to enhance their reactivity, selectivity, and stability.[31] Electronic tuning modulates the electron-donating or electron-withdrawing nature of the ligands, thereby influencing the electron density at the metal center and affecting substrate activation and the stabilization of intermediates.[32] Steric modification controls the spatial environment around the metal center, minimizing unnecessary side reactions and improving selectivity.[33] Cooperative effects involve functional groups that are capable of participating in the catalytic cycle through hydrogen bonding or proton transfer, thereby enabling metal-ligand cooperation (MLC).[34] Rather than serving as a stabilizing framework for the metal center, ligand-engineering makes the ligand an active participant in the catalytic process.[35] The incorporation of proton-responsive or redox-active sites in ligands can facilitate metal-ligand cooperation, enabling processes such as proton-coupled electron transfer (PCET) or bond activation.[36,37] The ligand-centered approach specifically targets the construction of next-generation catalysts with improved catalytic selectivity.[38-40]

Building on the concept of ligand-centered design, the relationship between a structure and its catalytic performance or selectivity is both significant and complex.[41] Even minor modifications to the ligand framework, such as the type of donor atoms, the rigidity of the backbone, steric hindrance, or the inclusion of functional groups, can markedly influence the electronic environment and spatial arrangement around the metal center.[41-42] For instance, electron-rich ligands enhance the nucleophilicity of the metal center,[43] while the sterically demanding ligands can shield specific coordination sites and enforce regio- or

stereoselectivity.[44] Moreover, ligands equipped with cooperative sites, such as acidic or basic functionalities, can engage in concerted mechanisms that lower activation barriers and boost the reaction efficiency.[44]

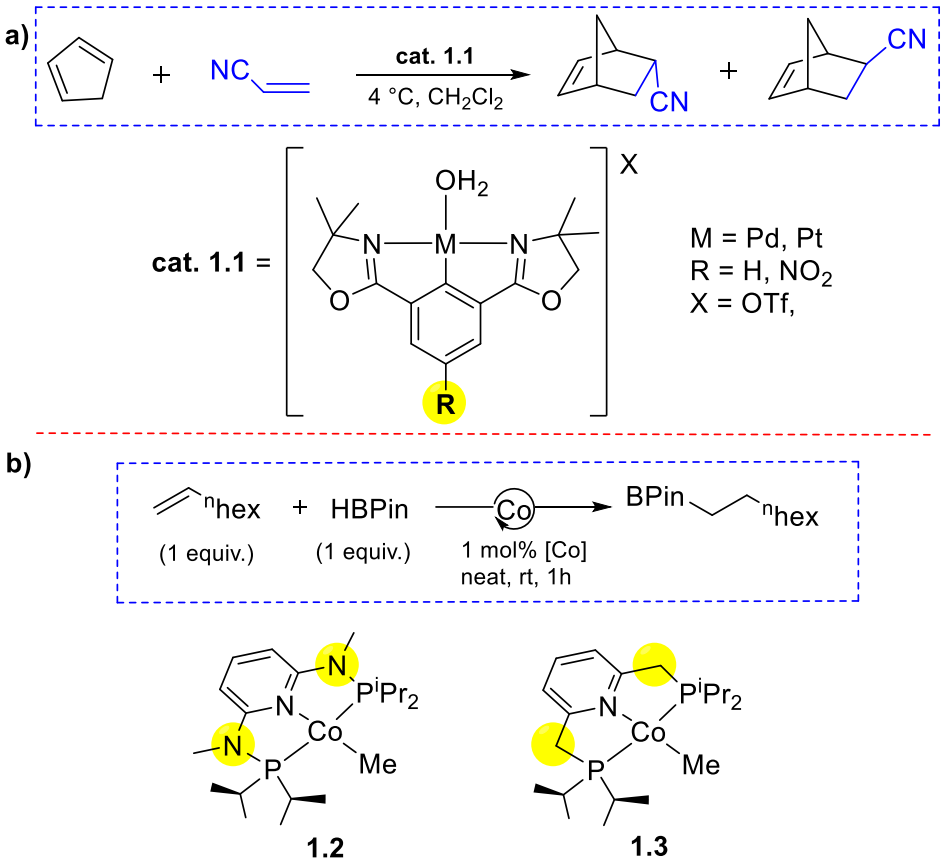

Scheme 1.1 Metal complexes showing the effect of tuning ligand design on the catalytic reactivity

For example, the catalyst **1.1**, synthesized by Fossey et al., catalyzed the Diels-Alder reaction involving nitriles. The substitution of the nitro group at the *p*-position (R) of the platinum complex lowers the catalytic activity due to the higher Lewis acidity.[45] In 2023, Chirik et al. demonstrated that a slight change in the ligand moiety within the Co-PNP scaffold altered the reactivity of the catalyst. Classical bis(phosphinomethyl)pyridine ^{i}PrPNP **1.3** was replaced by more rigid 2,6-diaminopyridine-derived ^{i}PrPNMeNP, where CH_2 spacers are replaced by *N*-Me linkers **1.2**, and the catalyst performance enhances in alkene hydroboration (Scheme 1.1).[46]

1.3 Pincer Ligand Frameworks as Modular Scaffolds for Catalyst Design

Pincer ligands are a distinct class of tridentate chelating ligands that bind in a meridional manner to the metal center, imparting high thermodynamic and kinetic stability to the resulting complexes.[47] The rigid coordination framework not only ensures that the metal is firmly bound but also allows systematic adjustments in both the electronic and steric environments around the metal center.[48] As depicted schematically (Figure 1.3a), the donor atoms (X, Y, Z) and substituents on the ancillary ligands (R, L) allow precise control of the electron density, hemilability, trans influence, and steric congestion, which in turn directly govern the reactivity and catalytic performance of the complexes. This modularity makes pincer ligands highly adaptable frameworks for tuning metal-ligand cooperation in catalytic processes.[34]

Pincer ligands are classified into two main structural categories: palindromic and non-palindromic. Palindromic pincer ligands are symmetrical and can adapt various charge states, such as neutral, anionic, dianionic, or trianionic, depending on the central donor atom.[49] The central donor atom (X), which can be a neutral or anionic group such as O, -NR, -C(phenyl), or imidylidene unit, strongly influences the electronic characteristics of the ligand framework.[50] The symmetry of the ligands often results in consistent binding to the metal centre and provides a predictable distribution of electron density throughout the ligand structure (Figure 1.3b).[51]

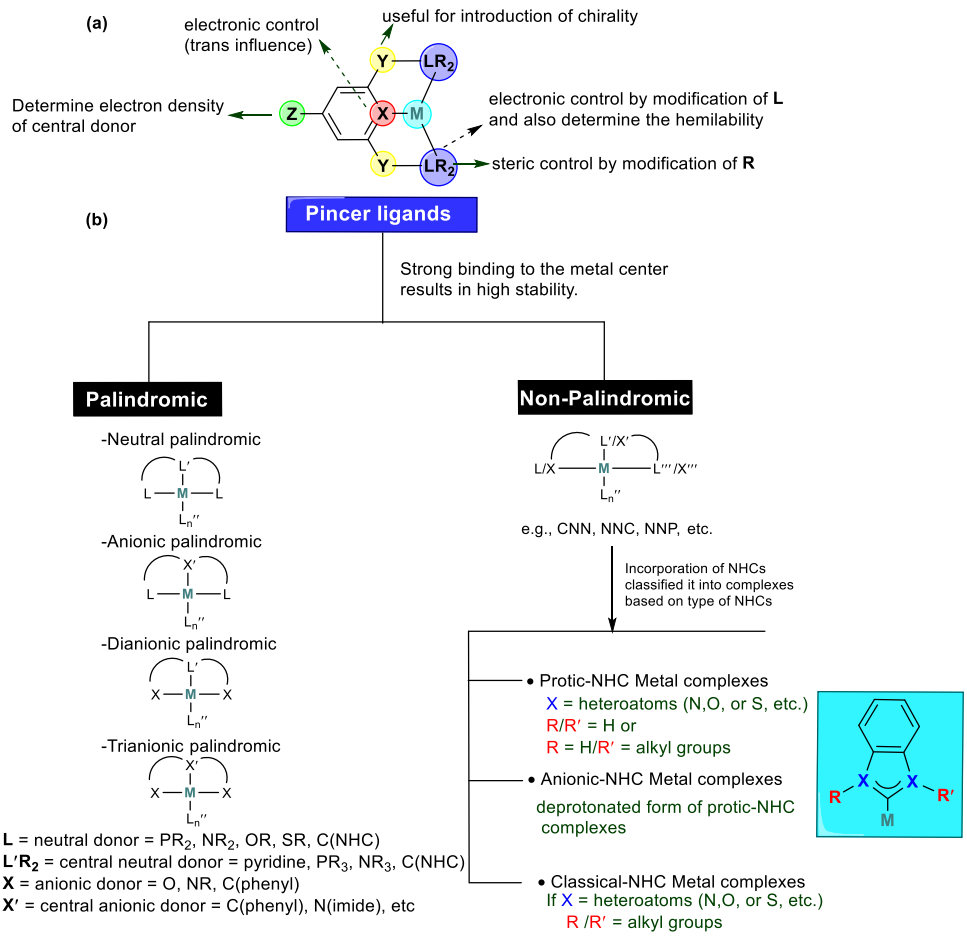

Figure 1.3 (a) Schematic representation of a pincer framework **(b)** Diversification of pincer ligands and incorporation of NHCs in a non-palindromic ligand.

Conversely, non-palindromic pincer ligands lack overall symmetry, resulting in an asymmetric environment at the metal center.[52] This asymmetry is particularly advantageous for inducing chirality and designing catalysts with directional electronic and steric effects. These non-palindromic systems facilitate the integration of NHCs, giving access to a diverse range of metal-NHC complexes that can broadly grouped as: (i) protic-NHC metal complexes in which a heteroatom (N, O, S, etc.) adjacent to the carbene center having atleast one proton enabling additional donor flexibility and MLC; (ii) anionic-NHC complexes, derived from deprotonation of protic NHCs provides enhanced electron donation to the metal; and (iii) classical NHC complexes, where the carbene carbon is surrounded by heteroatoms and stabilised by alkyl or aryl groups.[53–55]

The structural diversity arising from symmetry (palindromic vs. non-palindromic architectures), together with variations in the carbene donor, endows pincer ligands with exceptional tunability. Consequently, these ligands serve as a fine platform for transition metal catalysis, where the catalytic performance, selectivity, and stability can be precisely manipulated by adjusting the steric and electronic influences at the metal center.

1.4 *N*-Heterocyclic Carbenes (NHCs) in Catalysis

N-heterocyclic carbenes are a versatile class of ligands extensively used in transition metal catalysis owing to their strong σ-donating capacity, excellent thermal and chemical stabilities, and remarkable structural flexibility. In contrast to traditional phosphine ligands, NHCs are typically neutral two-electron donors that form strong metal-carbon bonds, substantially enhancing the stability of metal complexes even under harsh reaction conditions. This increases the electron density at the metal center and promotes difficult bond activation steps. [56–58] Furthermore, both the steric and electronic properties of NHCs can be adjusted by modifying the substituents on the nitrogen atoms or by altering the heterocyclic backbone, allowing for fine control over the catalytic activity and selectivity. These properties make NHC ligands highly valuable in a diverse range of applications, from organometallic synthesis to environmentally benign, green, and energy-related catalytic transformations (Figure 1.4).[59–61]

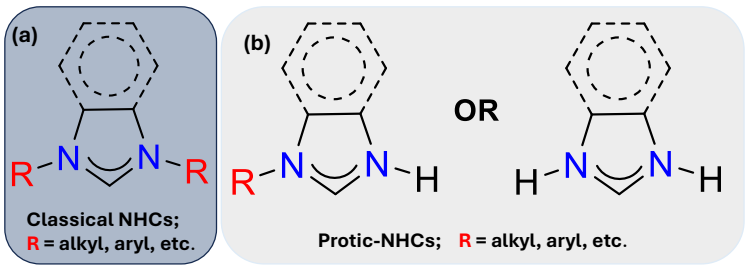

Figure 1.4 A general structure for *N*-heterocyclic carbene in azole rings (a) Classical NHCs (b) Protic-NHCs bearing NH, NR- and NH, NH substituents

A notable example illustrating the impact of incorporating NHCs on catalytic efficiency is the Grubbs' catalyst series. The Grubb's first- and second-generation catalysts differ from each other in terms of ligand decomposition. 1st generation Grubbs catalyst (G1) has two PCy_3 ligands, whereas in the 2nd generation Grubbs catalyst (G2), NHC (SIMes) replaces one of the PCy_3 ligands, leading to the highest overall reactivity and a stronger σ-donation ability, which requires a lower activation energy (Scheme 1.2).[62] The evolution of NHC ligands has significantly broadened their utility in coordination chemistry and catalysis. Classical NHCs, renowned for their strong σ-donating and minimal π-accepting properties, have been utilized to form stable metal-carbene complexes, exhibiting excellent catalytic performance and durability. Nonetheless, the limitation in reactivity control and functional diversity led to the design of more sophisticated NHCs.[63] Among these, protic-NHCs (pNHCs) have emerged as a new class of ligands, marked by an acidic *N*-H proton on the heterocyclic backbone.[64]

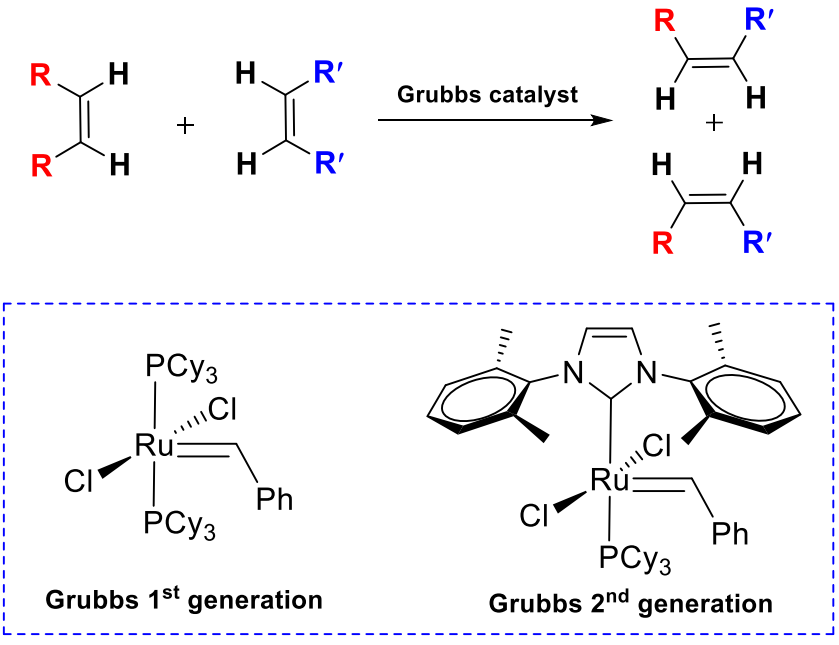

Scheme 1.2 Grubbs catalysts demonstrate the effect of NHCs insertion in the ligand platform

1.4.1 Significance of Protic *N*-heterocyclic carbenes: Protic-NHCs possess several unique and distinctive features that distinguish them from classical-NHC ligands owing to the presence of an *N*-H

functionality on the heterocyclic ring. This *N*-H group endows the ligand with a protic nature, enabling it to participate in hydrogen bonding and proton transfer reactions. This capability enables pNHCs to engage in metal-ligand cooperation, in which the metal center and ligand collaborate to activate substrates and facilitate crucial bond transformations.[65] This cooperative behavior is particularly valuable in reactions involving the activation of small molecules, such as H_2, HCOOH, and CO_2. The *N*-H site not only expands the range of catalytic pathways available to pNHC-based complexes but also enhances their reactivity and selectivity under mild conditions.[66] The multifunctional nature of pNHCs as next-generation ligands for the development of efficient, environmentally benign catalytic systems aimed at addressing global energy and sustainability challenges. [67,68]

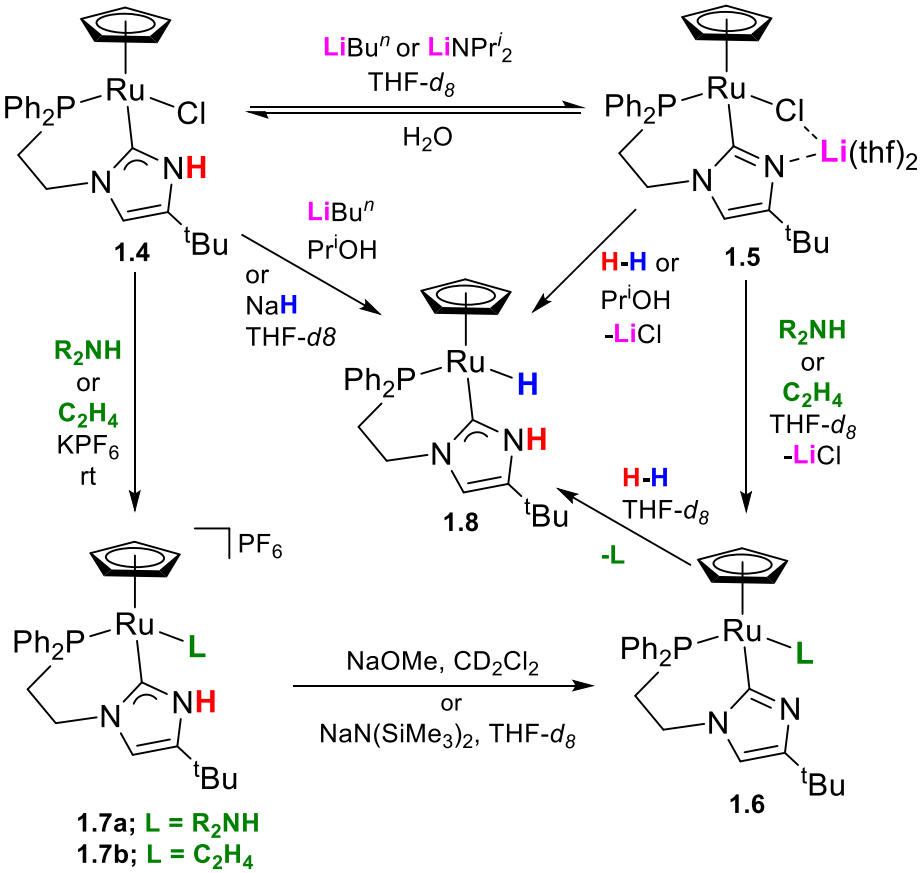

Scheme 1.3 Reactivity of a protic-NHC Ruthenium complex

The incorporation of pNHC into the ligand leads to structural changes that introduce additional functionality, allowing the ligand to participate in bond activation through proton transfer or hydrogen bonding, [69]

thereby broadening the scope of NHC-based catalysts.[70] The integration of pNHCs into established ligand platforms, such as bidentate and tridentate systems, enables significant advancements in transformation through the synergistic effects of the metal center and proton-responsive components.[71–73] For example, Grotjahn et al. reported catalyst **1.4**, which, when combined with lithium bases, resulted in an anionic imidazolyl complex **1.5**. Lithium adduct **1.5** reacted with dihydrogen or ^{i}PrOH to give hydrido-pNHC complex **1.8**, while complex **1.4** gave amine- or ethylene-coordinated complexes **1.7a** and **1.7b**, respectively. Overall, the complex **1.4** showed the significance of the presence of pNHC (Scheme 1.3).[74]

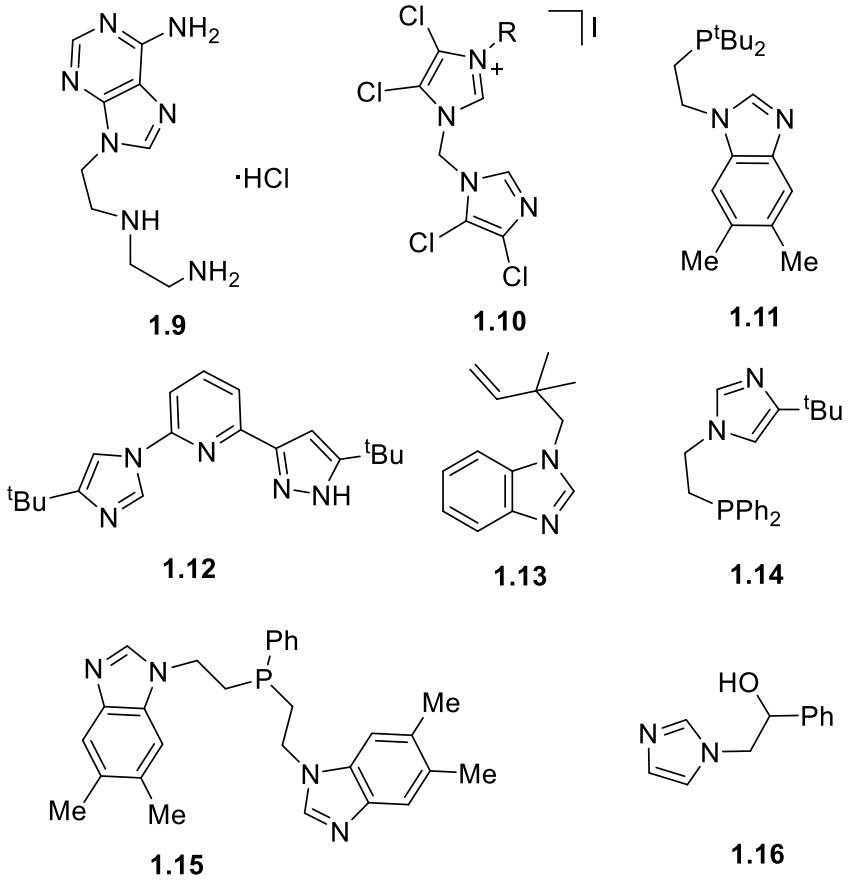

Figure 1.5 Representative examples of bidentate and tridentate pNHC precursors

In 1997, Houlton et al. reported ligand **1.9**, which has a purine/pyrimidine nucleus with a multidentate -NH and -NH_2 chelating group (Fig. 1.5).[75] They proposed that this type of chelation

subsequently restricts the sites where the metal ion can attach to the nucleobase. Peris and co-workers synthesized an azolium/azole-based bis(dichloroimidazolylidene) ligand **1.10** in 2006.[76] The new ligand was explored with Rh and Ir, affording well-characterized complexes that differ from their nonchlorinated analogues, and their catalytic activity in the hydrosilylation of terminal acetylenes and the cyclization of acetylenic acids showed marked deviations from that of bis-(NHC) nonchlorinated counterparts. In 2011, Hahn synthesized an *N*-alkylphosphine-substituted benzimidazole ligand **1.11**, which varied based on the alkylation of phosphine.[77] Ikariya and Kuwata reported a CNN-type ligand **1.12** bearing protic-NHCs, specifically 2-(imidazol-1-yl)-6-(pyrazol-3-yl)pyridine, in 201 k6.[63] In 2002, Ellman and Bergman reported a pNHC complex chelated with an olefin-tethered bidentate pNHC ligand **1.13**.[78] In 2008, Grotjahn reported the P^C-chelated pNHC precursor **1.14**, which was based on imidazole.[79] Furthermore, Cossairt and coworkers synthesized a tripodal ligand featuring an NHC-phosphine-NHC backbone (CPC ligand **1.15**) coordinated to a metal center.[80] Incorporating pNHCs enhances the complexity and versatility of the ligand system, affecting the electronic properties, coordination behavior, and applications of the metal complexes. Also, Olivan and Yus have used 2-(1*H*-imidazol-1-yl)-1-phenylethan-1-ol as a ligand **1.16** for synthesizing an osmium complex with $OsH_6(P^iPr_3)_2$ metal precursor.[81]

1.5 Metal ligand cooperativity

Metal-ligand cooperation in pincer NHC complexes has garnered significant attention because it combines the strong σ-donor ability of NHCs with the high tunability of the steric and electronic environments of the pincer system.[82] In particular, pincer-type architectures containing protic-NHCs have emerged as versatile frameworks for promoting cooperative reactivity in metal complexes.[83] Unlike classical "innocent" NHC ligands, pNHCs contain a strategically positioned *N*-H group that acts as an internal proton-responsive site. The *N*-H functionality allows the ligand to engage directly in bond activation

through reversible deprotonation-protonation cycles, thereby complementing the electronic role of the metal center.[84] In such systems, the pNHC unit can undergo metal-ligand cooperative transformations, such as heterolytic H_2 splitting, proton shuttling, or stabilization of reactive intermediates. The cooperative pathways of pNHC complexes not only expand the reaction scope of pincer catalysts but also enable challenging transformations, including the dehydrogenation of alcohols, formic acid dehydrogenation, CO_2 hydrogenation, and *N*-methylation reactions, under relatively mild conditions.[85–87] Additionally, the rigidity of the pincer backbone provides geometrical stability, whereas the protic site introduces dynamic reactivity, offering an exceptional balance between robustness and adaptability. Collectively, pNHC-pincer complexes represent a new generation of cooperative catalysts, where the interplay between the metal center and the protic carbene drives high activity, selectivity, and sustainability in a broad scope of catalytic applications. [88–90]

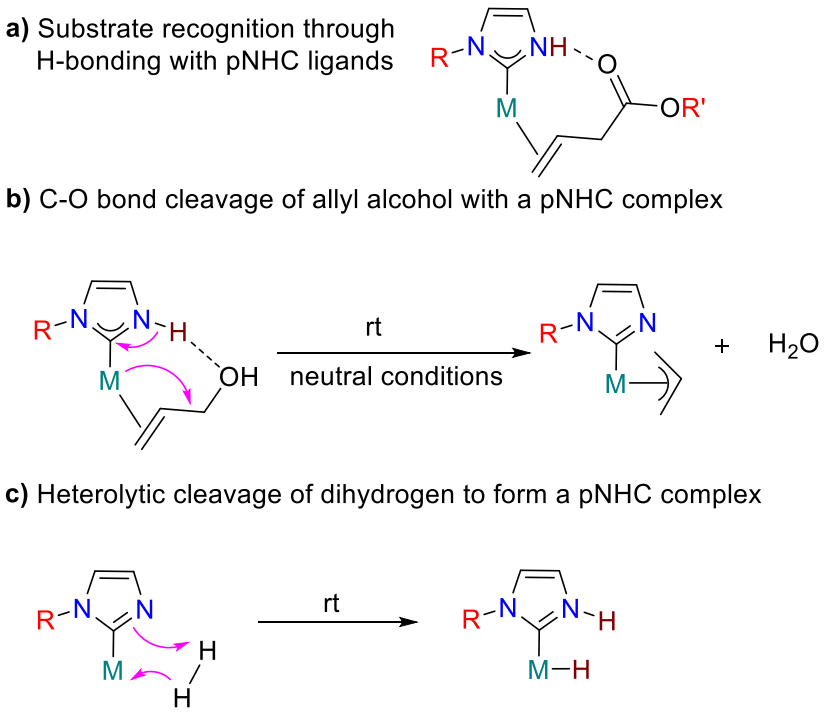

Figure 1.6 Schematic representation of metal-ligand cooperation in protic-NHC pincer complexes: **(a)** substrate recognition via H-bonding interactions involving the *N*-H functionality of the ligand; **(b)** cooperative C-O bond cleavage of allyl alcohol, facilitated by the

interplay of metal center and the ligand; and **(c)** heterolytic cleavage of H_2, where the hydride is attached to the metal and the ligand accepts a proton, exemplifying the bifunctional activation of small molecules.

As illustrated in Figure 1.6, pNHCs play multiple roles, ranging from substrate recognition to direct participation in bond activation processes.[65,69] In the first case (Figure 1.6a), the NH moiety acts as a hydrogen-bond donor, enabling substrate recognition. The H-bonding ability not only increases the substrate affinity towards the metal but also guides the orientational fate of the incoming molecule, thereby enhancing selectivity by lowering the activation barriers.[65] A notable example is the cleavage of the C-O bond of allyl alcohol under neutral conditions (Figure 1.6b). Here, the NH group of the pNHC participates in a cooperative mechanism in which the metal coordinates to the hydroxyl group while the ligand simultaneously assists in proton transfer.[91] Therefore, dual engagement facilitates facile C-O bond breaking and water elimination as a byproduct, yielding an olefin.

Another striking application of MLC is the heterolytic cleavage of dihydrogen (Figure 1.6c).[79] The metal center binds the hydride of the H_2 molecule, while the proton is accepted by the naked *N*-atom of the ligand, leading to the formation of the pNHC carbene site. The cooperative cleavage of H_2 highlights the bifunctional character of pNHC pincers, where the metal acts as a Lewis acidic site, and the ligand NH serves as a Brønsted basic site.[92] This synergistic pathway enables mild and efficient H_2 activation, which is crucial for catalysis in hydrogenation, dehydrogenation, and hydrogen storage. Collectively, all the examples underscore the multifaceted role of pNHC-pincer complexes in catalysis.[93] The ligand not only stabilizes the metal through its strong σ-donation but also introduces the dynamic reactivity via its protic functionality. [94,95]

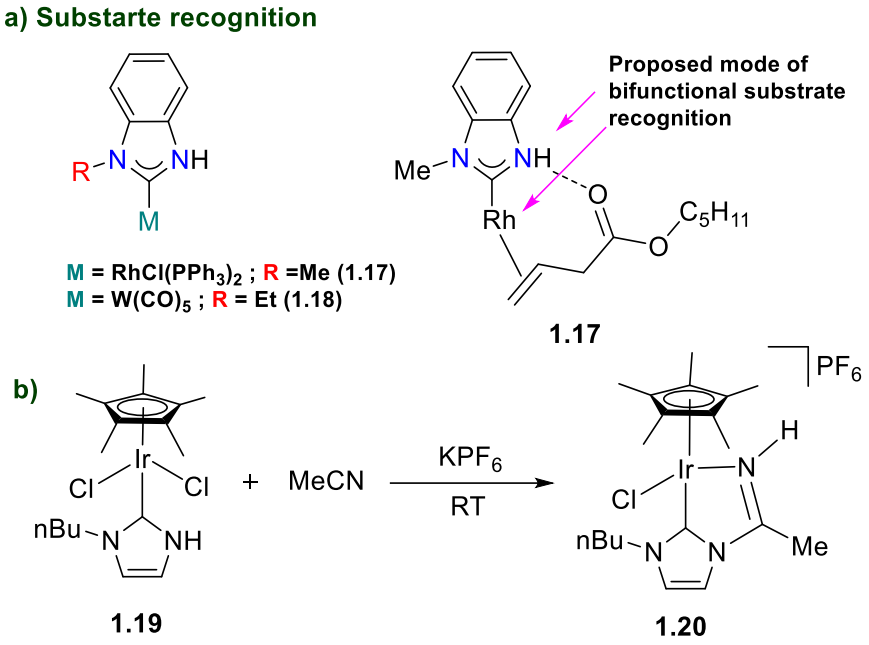

Scheme 1.4 Illustration of metal-ligand cooperation in protic-NHC complexes: **(a)** substrate recognition via bifunctional H-bonding between the NH group of the ligand and the coordinated substrate; **(b)** a stable pNHC-Ir complex, demonstrating the dual role of the protic carbene in metal coordination and proton-responsive reactivity.

Scheme 1.4 illustrates the role of protic NHC ligands in substrate recognition and their cooperative reactivity. As shown in Scheme 1.4a, the presence of the NH moiety in pNHC frameworks enables substrate recognition through hydrogen bonding in proximity to the metal center.[61] For example, Rh- (**1.17**) and W-based (**1.18**) pNHC complexes have been reported to engage in noncovalent interactions with oxygenated substrates, where the NH group donates a hydrogen bond. Simultaneously, the metal coordinates to the reactive site of the substrate.[96] This dual interaction facilitates the proper alignment and activation of the substrate, lowering the kinetic barrier for bond activation and enhancing the catalytic efficiency. The bifunctional recognition is a hallmark feature of MLC in pNHC systems, distinguishing them from classical-NHC ligands that lack proton-responsive functionality.[97] Scheme 1.4b illustrates another example of cooperative behavior, where a pNHC precursor undergoes coordination with a metal center under mild conditions to form a new stable complex

1.20. In this case, the NH group can interact with Lewis basic ligand MeCN, while the carbene carbon binds strongly to the metal, providing both electronic stabilization and a potential site for proton transfer.[66] Together, the examples mentioned in Scheme 1.4 emphasize the versatility of pNHC, not only in stabilizing metal complexes but also in directly engaging with substrates through Hydrogen Bonding and proton shuttling, providing highly cooperative and efficient catalytic processes.[98]

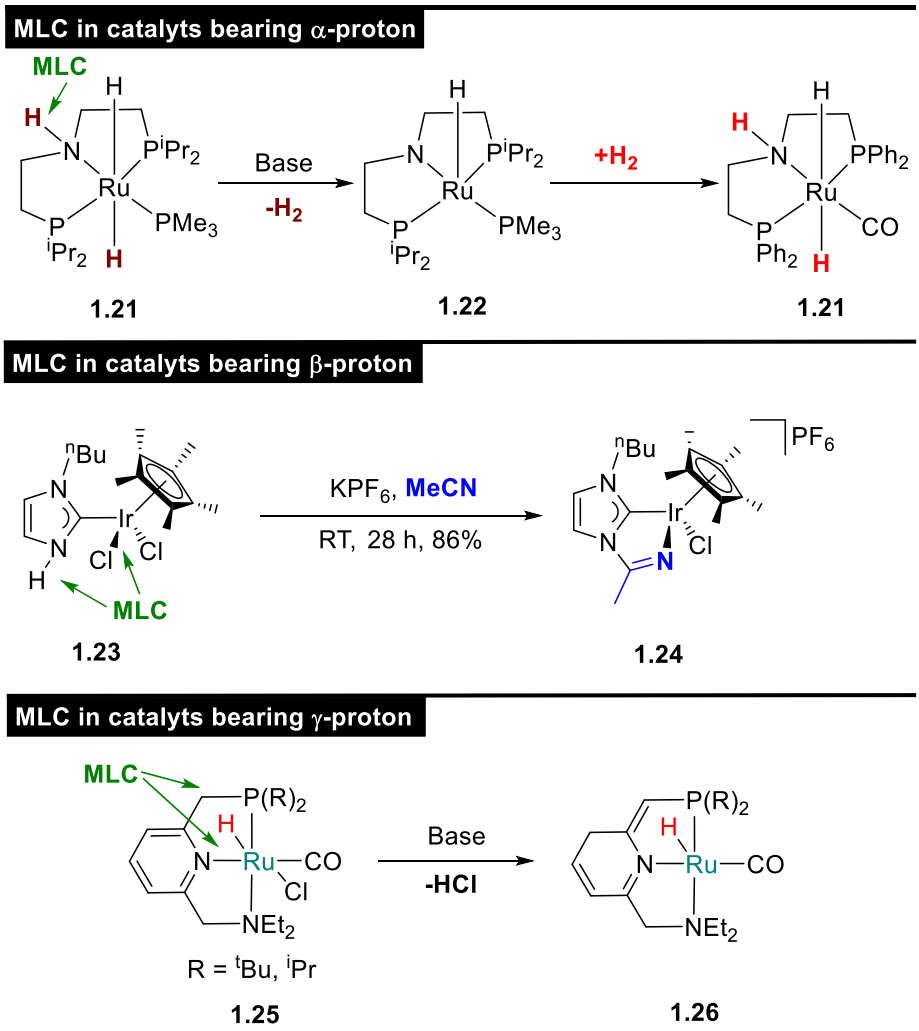

Figure 1.7 Selected examples of MLC catalysts with protic functionalization.

MLC involving α-, β-, and γ-protons describes a class of catalytic mechanisms in which a ligand-bound proton adjacent to the metal center participates directly in substrate activation.[99] In α-proton-assisted MLC, the proton is located on the carbon directly attached to the heteroatom

coordinated to the metal center.[100] The α-protons can undergo reversible deprotonation, aromatization-dearomatization, and metal-alkyl or metal-carbene interconversion that facilitates bond activation steps. In β-proton MLC, the proton is one atom away, which commonly participates in β-hydride elimination, β-H transfer, or hydrogen-shuttling mechanisms that regenerate the active catalyst, allowing transformations such as the dehydrogenation of alcohols and amines.[69] The γ-protons, located three positions away, are less acidic but can show remote MLC, where ligand flexibility enables proton shuttling over longer distances, which is essential in bifunctional frameworks and systems that resemble enzymatic proton relays.[101] Together, α, β, and γ-proton MLC provide tunable pathways for bond cleavage and formation without the need for external additives, such as bases or acids, improving catalyst efficiency and selectivity.[102]

Figure 1.7 illustrates the examples of α, β, and γ-proton MLC. Schneider et al. reported a Ru-amino complex, **1.21**, which partially eliminated H_2 to obtain **1.22** via α-proton MLC. Upon the quantitative addition of dihydrogen in solution under an H_2 atmosphere, **1.22** yields **1.21** again.[103] Metal-mediated NHCs are a good example of β-proton metal-ligand cooperation. Lammertsma et al. demonstrated the displacement of chloride on Iridium (III) of the complex **1.23**, which facilitated the nucleophilic attack of the NHCH group on the coordinated acetonitrile molecule, yielding a formal hydroamination product **1.24**.[104] Milstein et al. in 2006 prepared a new complex by deprotonating the γ-proton of the previously synthesized [(PNP)RuHCl(CO)] and releasing a dihydrogen molecule. The dearomatized complex, **1.26**, showed efficiency towards the hydrogenation of esters to alcohols involving MLC.[105]

1.6 Key Catalytic Applications Explored

1.6.1 Electrochemical Water Oxidation

The controllable catalytic activity and selectivity achieved through ligand design are crucial in advanced energy-related applications, such as artificial photosynthesis and the hydrogen economy.[106] For artificial

photosynthesis, catalysts should have the efficiency to drive multielectron, proton-coupled transformations, such as water splitting (Scheme 1.5) and CO_2 reduction, to mimic natural photosynthetic systems.[107] Ligand-centered catalyst design directly supports the development of sustainable, scalable technologies for clean energy generation, storage, and utilization, cornerstones of a low-carbon future.[108,109] Despite significant investigation into ligand-centered design for artificial photosynthesis and hydrogen-based energy systems, challenges related to catalyst stability and overpotential remain issues for the practical implementation of catalytic systems.[110]

$$\mathbf{2H_2O\ (\mathit{l})} \longrightarrow \mathbf{2H_2(\mathit{g})\ +\ O_2(\mathit{g})}$$

OER

$$2H_2O\ (\mathit{l}) \longrightarrow O_2(\mathit{g}) + 4H^+(\mathit{aq}) + 4e^-$$

HER

$$4H^+(\mathit{aq}) + 4e^- \longrightarrow 2H_2(\mathit{g})$$

Scheme 1.5 General reaction for Water splitting

Many transition metal catalysts used in water oxidation or hydrogen evolution suffer degradation under prolonged electrochemical conditions, resulting in a loss of activity and short operational lifetimes.[111] Ligands also decompose, oxidize, or detach from the metal center, especially in the presence of reactive intermediates or high-energy species.[112] Efficient catalysis often requires high overpotentials and additional energy input exceeding the thermodynamic requirements.[113] To address these challenges, the development of robust, redox-active ligands that can operate at low overpotentials through improved charge transfer kinetics is required.[114]

To address the challenges of catalyst stability and high overpotentials, pincer complexes have emerged as effective systems for improving the efficiency and durability of catalysis. Protic and redox-active ligands can facilitate proton and electron transfers, improving efficiency and selectivity under mild conditions. pNHCs facilitate more efficient proton

and electron transfer during key catalytic steps. Cooperative behavior can lower activation barriers, reduce overpotential, and enhance energy efficiency. Moreover, the strong σ-donating nature of pNHCs stabilizes the metal center and maintains the active oxidation state of the metal during catalysis, even under harsh reaction conditions. [115,116] As a result, pNHC metal complexes offer a promising platform for next-generation catalysts, characterized by high activity, low energy input, and long-term operational stability, thereby enabling sustainable energy applications.[117–119]

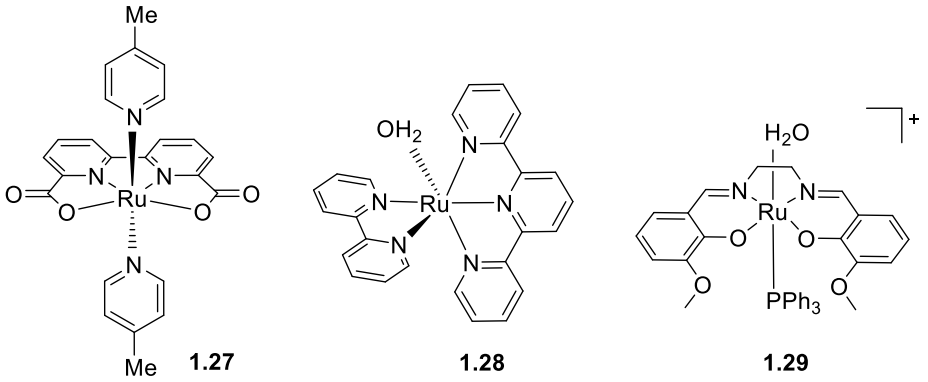

Figure 1.8 Selected examples of catalysts for electrochemical water oxidation.

Ruthenium catalysts involved in electrochemical water oxidation rely on high-valent Ru-oxo or oxyl intermediates via sequential proton-coupled electron-transfer (PCET) steps, which enable the challenging $4e^-$ oxidation of H_2O to O_2.[120,121] Meyer and his co-workers established a few single-site Ru polypyridyl catalysts that undergo PCET to form Ru^V=O species, which are capable of O-O bond formation via water nucleophilic attack (WNA) or peroxidic intermediates (**1.27**).[122] In contrast, Sun et al. demonstrated that the Ru-bda complexes operate through a bimolecular oxyl radical coupling (I2M) pathway and even isolated a rare seven-coordinate **1.28**.[123] Recently, Dutta and collaborators stabilized the Ru^V=O intermediate using a Schiff-base ligand **1.29**, confirming the I2M mechanism (Figure 1.8).[124]

1.6.2. Formic acid dehydrogenation

Among other hydrogen storage strategies, formic acid dehydrogenation has been observed as a practical and safe method for on-demand hydrogen generation, particularly in fuel cells and portable energy systems.[125] Formic acid (HCOOH) is a non-toxic liquid at room temperature and easy to handle, which makes it an attractive hydrogen carrier in comparison to gaseous H_2.[126,127] It can decompose into CO_2 and H_2 under mild conditions, catalyzed by efficient and selective systems (Figure 1.9).[128] The NHC-based metal complexes have demonstrated remarkable performance. Integrating pNHC complexes into formic acid dehydrogenation systems advances the field of homogeneous catalysis and addresses the needs in the hydrogen economy by enabling clean, controllable, and sustainable hydrogen delivery.[129]

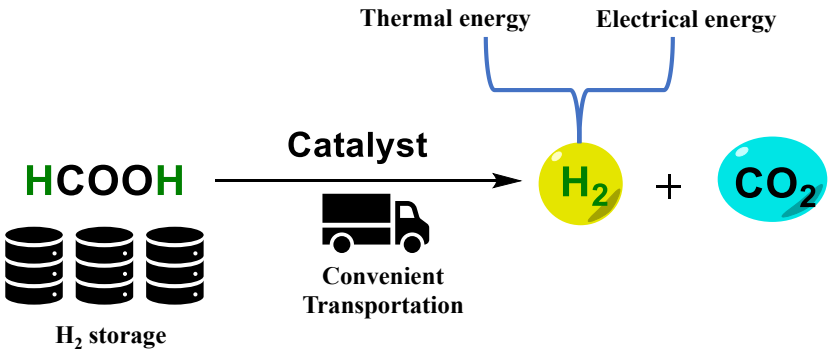

Figure 1.9 Schematic representation of the formic acid dehydrogenation process

To address the challenges of selectivity, reaction rates, and CO-free hydrogen generation, protic *N*-heterocyclic carbene (pNHC) complexes have emerged as highly promising candidates for low-temperature formic acid dehydrogenation.[130] Low-temperature activity is advantageous for portable and on-demand hydrogen generation, where the thermal energy input is limited and operational safety is crucial.[131,132] Additionally, the strong σ-donating and proton-responsive nature of pNHCs can stabilize key reaction intermediates, minimize catalyst degradation, and suppress side reactions such as CO formation.

These features not only improve the efficiency and longevity of the catalyst but also ensure high selectivity toward clean hydrogen production. [133–135]

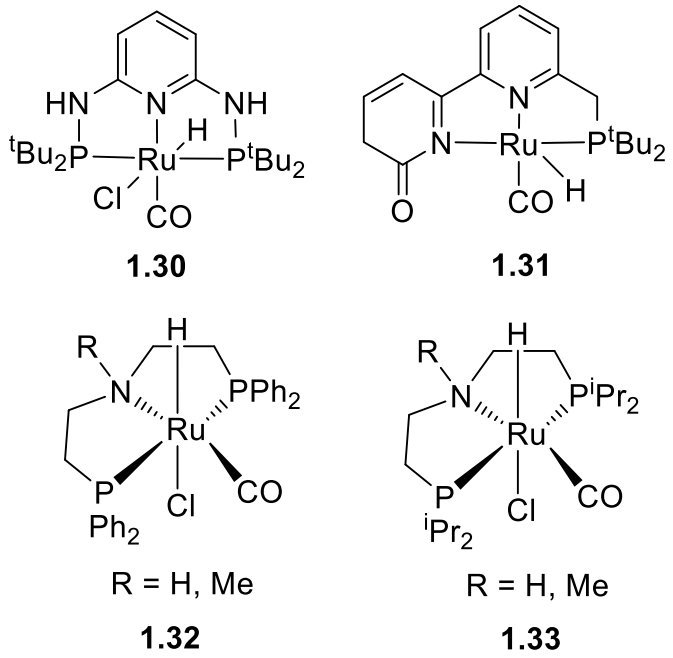

Figure 1.10 Selected examples of catalysts for formic acid dehydrogenation

Ruthenium pincer complexes have emerged as some of the most efficient catalysts for formic acid dehydrogenation, as demonstrated by several research groups, showing MLC and ligand design can enhance hydrogen-release efficiency.[130] Huang and collaborators presented a Ru(II)-PN^3-pincer complex **1.30** for base-free FADH with high activity (TOF up to 7000 h^{-1}) and remarkable longevity.[136] In parallel, Vlugt et al. developed a Ru-PNN(O) platform **1.31**, demonstrating base-free, robust catalysis over multiple cycles with the clean evolution of H_2/CO_2, and achieved TOFs of 35 h^{-1}, while showcasing the key role of ligand-assisted hydride transfer.[137] Prakash and Olah presented an amine-free reversible hydrogen-storage system, Ru-PNP catalyst **1.32**, which enables over 90% efficiency in both CO_2 hydrogenation and formate dehydrogenation.[138] Beller et al. demonstrated that Ru-PNP complexes (**1.33**) with *N*-methylated ligands significantly outperform their NH analogues, achieving turnover frequencies (TOFs) as high as 8981 h^{-1} at

pH 4.5, highlighting how ligand alkylation accelerates the rate-determining protonation step in formic acid activation (Figure 1.10).[139]

1.6.3. *N*-Methylation of Anilines

In parallel with hydrogen generation applications, pNHC-based catalysts have also demonstrated significance in facilitating the *N*-methylation of anilines, a crucial transformation in fine chemical synthesis and pharmaceutical production.[140,141] Traditional methods for *N*-methylation used toxic reagents, such as methyl halides or dimethyl sulfate, which generate hazardous waste and require harsh conditions.[142] In contrast, the use of a sustainable C1 source, such as methanol for *N*-methylation under mild conditions, offers a cleaner and atom-economical alternative. The tunable reactivity, high selectivity, and functional group tolerance of pNHC-containing complexes make them powerful tools for efficient and environmentally benign *N*-methylation protocols, highlighting the broad applicability of pNHCs in modern-day catalysis. [143–145]

The green strategies for *N*-methylation have gained significant attraction, particularly for employing sustainable reagents such as methanol, formic acid, and even CO_2 as C1 sources.[146] These reagents are non-toxic, readily available, and serve as both the methylating agent and hydrogen source in catalytic systems, thereby enhancing atom economy and minimizing waste products. Transition metal complexes bearing pNHCs have proven to be effective in facilitating such transformations under mild conditions. The pNHC ligands can stabilize intermediates, facilitate proton transfer, and suppress over-alkylation or competing methylation of other functional groups.[147]

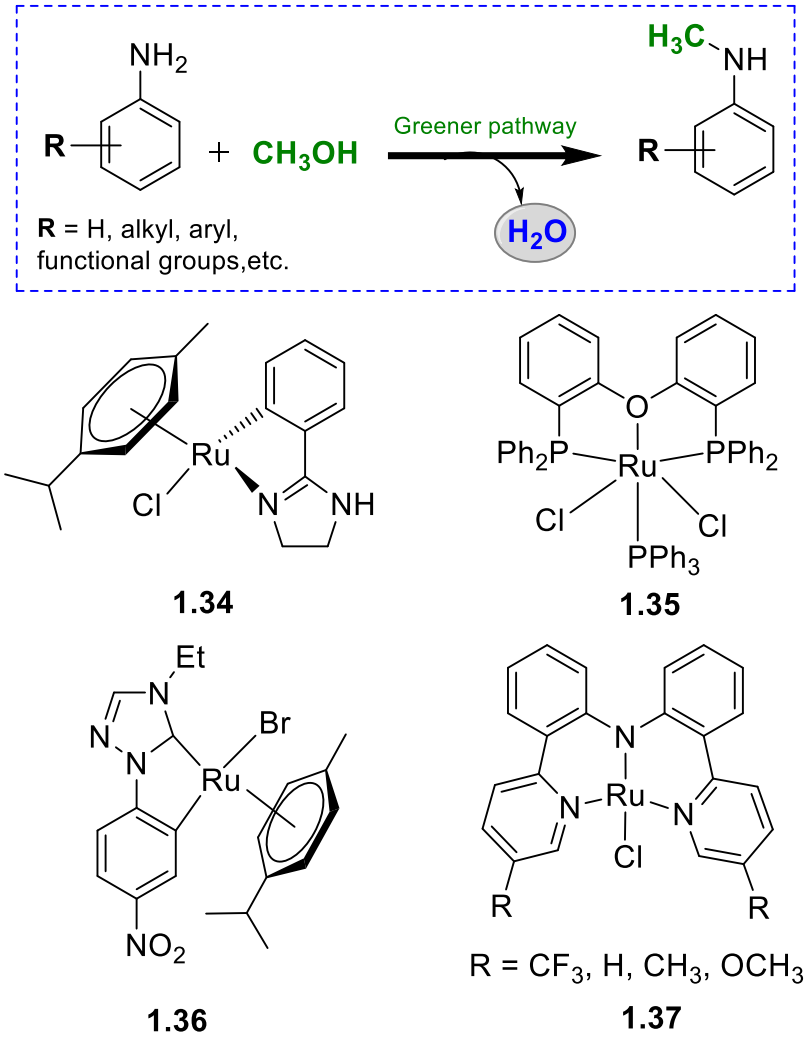

Scheme 1.6 Selected examples of catalysts for *N*-methylation of anilines.

Beller and co-workers reported Ru(C-N)(p-cymene) complexes, particularly complex 9 (**1.34**), efficiently methylate aniline under mild conditions (60 °C, NaOH) to deliver an 88% yield at only 0.4 mol% catalyst loading.[148] Additionally, Gong and Zhao reported a catalyst, (DPEPhos)$RuCl_2PPh_3$ (**1.35**), which enables broad-scope aniline methylation with greater than 99% conversion under weak-base conditions.[149] Rit and Illam also developed electronically tunable Ru^{II}-NHC cyclometalated complexes, where complex (**1.36**) achieved high efficiency in the selective mono-*N*-methylation of various amines via a borrowing hydrogen pathway.[150] Recently, Lin & Hao introduced an air-stable NNN-pincer Ru complex bearing an electron-donating OMe substituent, delivering a 94% yield of *N*-methylaniline at 110 °C (**1.37**) (Scheme 1.6).[151]

1.7. Research gap

Designing ligands is crucial in various catalytic applications, as even minor structural changes can significantly impact the reactivity and stability of the resulting complexes, thereby facilitating the identification of preferred reaction pathways. Numerous studies highlight the role of ligands through metal-ligand cooperation, which boosts catalytic efficiency via proton-responsive sites, particularly in the case of pNHC ligands.

- Rational ligand design plays a pivotal role in tailoring transition-metal catalysts for diverse chemical transformations. However, systematic comparative studies investigating the influence of α-, β-, and γ-N substitutions, as well as variations in carbene analogues within ligand frameworks, remain significantly underexplored.
- Direct comparisons of complexes based on ligands with variations at different positions and a single complex with multiple tunable sites are also underexplored.
- This gap presents a significant opportunity to develop next-generation pincer catalysts with optimized ligand variations for sustainable processes, linking catalytic optimization with detailed mechanistic insights.

1.8 Scope of the thesis

This study investigated a ligand system with the potential for modification at various positions. A common ligand framework was studied deeply by substituting at different positions. Building on the previously synthesized complex **[Ru-A]** by our group,[152] this work showed the design of a series named Carbene Pyridine Amino Pyridine (CPAP). The complex demonstrates its effectiveness in activating small molecules, indicating potential for hemilability. All the characteristics of the complex are essential for exploring the various catalytic applications. By substituting at different positions, various catalytic applications were

employed to assess the impact of substitution on the ligand, which resulted in the formation of corresponding complexes. These applications were utilized to clearly demonstrate the effect and examine the versatility of the complexes.

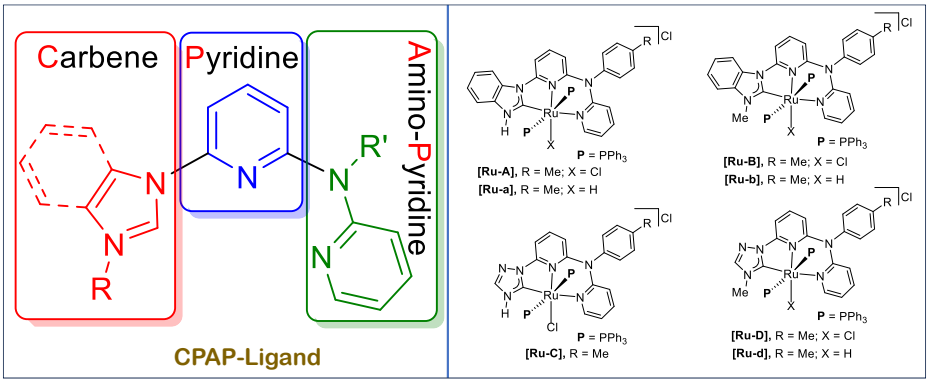

Figure 1.11 Demonstration of previously synthesized complexes based on a series of ligands called CPAP [152,153]

1.9 Objectives of the thesis

- Systematic modification of our unsymmetrical CPAP ligand platform to investigate the effect of substituent and azole moieties.
- To synthesize a series of Ru-complexes with new CPAP ligands.
- Explore the reactivity of these complexes and catalytic applications, and analyse the effect of various structural modifications.
- To establish the structure-property relationship of the complexes with CPAP ligands.

1.10 Organization of the Thesis

In Chapter 1, a survey of ligand design and transition metal complexes containing protic and classical NHCs, along with their applications, is presented, accompanied by a relevant literature review.

In Chapter 2, the synthesis and characterization of Ru(II) bis(pincer) complexes based on β-N substitution, suitable for electrochemical water oxidation, are discussed.

In Chapter 3, the Selective *N*-methylation of anilines using Ru(II) pincer complexes with varying carbene-containing azole moieties has been studied.

In Chapter 4, Ru(II)-pincer complexes based on γ-NH substitution were tested for formic acid dehydrogenation.

In Chapter 5, a fluorescence study was conducted to investigate the effect of γ-N substitution on the corresponding complex.

In Chapter 6, a summary of the thesis is provided, detailing the key achievements and outlining the future directions for further research.

1.11 References

[1] Chu, S., and Majumdar, A. (2012). Opportunities and challenges for a sustainable energy future. Nature, 488, 294–303. (https://doi.org/10.1038/nature11475)

[2] Yang, G., Zha, D., Cao, D., and Zhang, G. (2024). Time for a change: Rethinking the global renewable energy transition from the Sustainable Development Goals and the Paris Climate Agreement. The Innov,5, 100582. (https://doi.org/10.1016/j.xinn.2024.100582)

[3] Owusu, P.A., and Asumadu-Sarkodie, S. (2016). A review of renewable energy sources, sustainability issues and climate change mitigation. Cogent Eng., 3, 1167990. (https://doi.org/10.1080/23311916.2016.1167990)

[4] Gajdzik, B., Wolniak, R., Nagaj, R., Žuromskaitė-Nagaj, B., and Grebski, W.W. (2024). The Influence of the Global Energy Crisis

on Energy Efficiency: A Comprehensive Analysis. Energies, 17, 947. (https://doi.org/10.3390/en17040947)

[5] Sthel, M.S., Tostes, J.G.R., and Tavares, J.R. (2013). Current energy crisis and its economic and environmental consequences: Intense human cooperation. NS 05, 244–252. (https://doi.org/10.4236/ns.2013.52A036)

[6] Olabi, A.G., and Abdelkareem, M.A. (2022). Renewable energy and climate change. Renew. Sustain. Energy Rev., 158, 112111. (https://doi.org/10.1016/j.rser.2022.112111)

[7] Gielen, D., Boshell, F., Saygin, D., Bazilian, M.D., Wagner, N., and Gorini, R. (2019). The role of renewable energy in the global energy transformation. Energy Strategy Rev., 24, 38–50. (https://doi.org/10.1016/j.esr.2019.01.006)

[8] Hassan, Q., Viktor, P., J. Al-Musawi, T., Mahmood Ali, B., Algburi, S., Alzoubi, H.M., Khudhair Al-Jiboory, A., Zuhair Sameen, A., Salman, H.M., and Jaszczur, M. (2024). The renewable energy role in the global energy Transformations. Renew. Energy Focus, 48, 100545. (https://doi.org/10.1016/j.ref.2024.100545)

[9] Artz, J., Müller, T.E., Thenert, K., Kleinekorte, J., Meys, R., Sternberg, A., Bardow, A., and Leitner, W. (2018). Sustainable Conversion of Carbon Dioxide: An Integrated Review of Catalysis and Life Cycle Assessment. Chem. Rev. 118, 434–504. (https://doi.org/10.1021/acs.chemrev.7b00435)

[10] Jessop, P.G., Ikariya, T., and Noyori, R. (1994). Homogeneous Hydrogenation of Carbon Dioxide. Nature, 368, 231-233. (https://doi:10.1038/368231a0)

[11] Melese, A., Wubet, W., Hussen, A., Temesgen, A., and Mulate, K. (2025). Review on activation of small molecules (dihydrogen, carbon dioxide, and dinitrogen) by various transition metal

complexes. J. Chem. Res., 49, 17475198251313648. (https://doi.org/10.1177/17475198251313648)

[12] Kazemi, A., Manteghi, F., and Tehrani, Z. (2024). Metal Electrocatalysts for Hydrogen Production in Water Splitting. ACS Omega, acsomega.3c07911. (https://doi.org/10.1021/acsomega.3c07911)

[13] Sordakis, K., Tang, C., Vogt, L.K., Junge, H., Dyson, P.J., Beller, M., and Laurenczy, G. (2018). Homogeneous Catalysis for Sustainable Hydrogen Storage in Formic Acid and Alcohols. Chem. Rev., 118, 372–433. (https://doi.org/10.1021/acs.chemrev.7b00182)

[14] Quan, Y., Zhu, J., and Zheng, G. (2021). Electrocatalytic Reactions for Converting CO_2 to Value-Added Products. Small Sci., 1, 2100043. (https://doi.org/10.1002/smsc.202100043)

[15] Enthaler, S., Von Langermann, J., and Schmidt, T. (2010). Carbon dioxide and formic acid—the couple for environmental-friendly hydrogen storage? Energy Environ. Sci. 3, 1207. (https://doi.org/10.1039/b907569k)

[16] Maurya, Y., Singh, A., Kumar, V., Ul Nisa, M., and Chatterjee, S. (2024). First row transition metal catalyzed small molecule activation for sustainable organic transformation: Synergy between nature and chemist's toolbox. Tetrahedron Lett., 142, 155066. (https://doi.org/10.1016/j.tetlet.2024.155066)

[17] Singh, T., Jalwal, S., and Chakraborty, S. (2022). Homogeneous First-row Transition-metal-catalyzed Carbon Dioxide Hydrogenation to Formic Acid/Formate, and Methanol. Asian J Org Chem, 11, e202200330. (https://doi.org/10.1002/ajoc.202200330)

[18] Milani, B., Licini, G., Clot, E., and Albrecht, M. (2016). Small molecule activation. Dalton Trans., 45, 14419–14420. (https://doi.org/10.1039/C6DT90140A)

[19] Pal, R., Ghara, M., and Chattaraj, P.K. (2022). Activation of Small Molecules and Hydrogenation of CO2 Catalyzed by Frustrated Lewis Pairs. Catalysts, 12, 201. (https://doi.org/10.3390/catal12020201)

[20] Zhang, W., Lai, W., and Cao, R. (2017). Energy-Related Small Molecule Activation Reactions: Oxygen Reduction and Hydrogen and Oxygen Evolution Reactions Catalyzed by Porphyrin- and Corrole-Based Systems. Chem. Rev., 117, 3717–3797. (https://doi.org/10.1021/acs.chemrev.6b00299)

[21] Leenders, S.H.A.M., Gramage-Doria, R., De Bruin, B., and Reek, J.N.H. (2015). Transition metal catalysis in confined spaces. Chem. Soc. Rev., 44, 433–448. (https://doi.org/10.1039/C4CS00192C)

[22] Ganley, J.M., Joe, C.L., and Simmons, E.M. (2025). Development of Robust, Efficient and Scalable Transition Metal Catalyzed Transformations: Translation of Reactions from Micromole to Multi-Kilogram Scale Processes. ACS Catal., 15, 8317–8336. (https://doi.org/10.1021/acscatal.5c00836)

[23] Bellini, R., van der Vlugt, J.I., and Reek, J.N.H. (2012). Supramolecular Self-Assembled Ligands in Asymmetric Transition Metal Catalysis. Isr. J. Chem., 52, 613–629. (https://doi.org/10.1002/ijch.201200002)

[24] Govindan, K., Jayaram, A., Seenivasan, V.T., Venkatachalam, G., and Lin, W. (2024). Transition-Metal Catalyzed Synthesis of N - Heterocycles using Solvent-Carbon (C1) Synthons. ChemCatChem, 16, e202400658. (https://doi.org/10.1002/cctc.202400658)

[25] Feichtner, K.-S., and Gessner, V.H. (2018). Cooperative bond activation reactions with carbene complexes. Chem. Commun., 54, 6540–6553. https://doi.org/10.1039/C8CC02198H.

[26] Eremin, D.B., Denisova, E.A., Yu. Kostyukovich, A., Martens, J., Berden, G., Oomens, J., Khrustalev, V.N., Chernyshev, V.M., and Ananikov, V.P. (2019). Ionic Pd/NHC Catalytic System Enables Recoverable Homogeneous Catalysis: Mechanistic Study and Application in the Mizoroki–Heck Reaction. Chem. Eur. J., 25, 16564–16572. https://doi.org/10.1002/chem.201903221.

[27] Roy, B.C., Jaseer, E.A., Mousa, A.H., and Maity, N. (2026). Advances in efficient homogeneous catalytic hydrogenation of CO2 to formic acid: Bridging carbon utilization with renewable hydrogen storage. Renew. Sustain. Energy Rev., 226, 116371. https://doi.org/10.1016/j.rser.2025.116371.

[28] Kumar, N.S., and Adhikary, A. (2024). Transition metal pincer catalysts for formic acid dehydrogenation: a mechanistic perspective. Front. Chem., 12, 1452408. https://doi.org/10.3389/fchem.2024.1452408.

[29] Arevalo, R., and Chirik, P.J. (2019). Enabling Two-Electron Pathways with Iron and Cobalt: From Ligand Design to Catalytic Applications. J. Am. Chem. Soc., 141, 9106–9123. https://doi.org/10.1021/jacs.9b03337.

[30] Younus, H.A., Su, W., Ahmad, N., Chen, S., and Verpoort, F. (2015). Ruthenium Pincer Complexes: Synthesis and Catalytic Applications. Adv Synth Catal, 357, 283–330. https://doi.org/10.1002/adsc.201400777.

[31] Lawrence, M.A.W., Green, K.-A., Nelson, P.N., and Lorraine, S.C. (2018). Review: Pincer ligands Tunable, versatile and applicable. Polyhedron, 143, 11–27. (https://doi.org/10.1016/j.poly.2017.08.017)

[32] Lundgren, R.J., and Stradiotto, M. (2016). Key Concepts in Ligand Design: An Introduction. In Ligand Design in Metal Chemistry, M. Stradiotto and R. J. Lundgren, eds. (Wiley), pp. 1–14. (https://doi.org/10.1002/9781118839621.ch1)

[33] Stradiotto, M. (2016). Ligand Design in Metal Chemistry: Reactivity and Catalysis 1st ed. (John Wiley & Sons, Incorporated).

[34] Peris, E., and Crabtree, R.H. (2018). Key factors in pincer ligand design. Chem. Soc. Rev., 47, 1959–1968. (https://doi.org/10.1039/C7CS00693D)

[35] Durand, D.J., and Fey, N. (2019). Computational Ligand Descriptors for Catalyst Design. Chem. Rev., 119, 6561–6594. (https://doi.org/10.1021/acs.chemrev.8b00588)

[36] Ding, D., Mou, T., Feng, M., and Jiang, X. (2016). Utility of Ligand Effect in Homogenous Gold Catalysis: Enabling Regiodivergent π-Bond-Activated Cyclization. J. Am. Chem. Soc., 138, 5218–5221. (https://doi.org/10.1021/jacs.6b01707)

[37] Garrido-Barros, P., Moonshiram, D., Gil-Sepulcre, M., Pelosin, P., Gimbert-Suriñach, C., Benet-Buchholz, J., and Llobet, A. (2020). Redox Metal–Ligand Cooperativity Enables Robust and Efficient Water Oxidation Catalysis at Neutral pH with Macrocyclic Copper Complexes. J. Am. Chem. Soc., 142, 17434–17446. (https://doi.org/10.1021/jacs.0c06515)

[38] Milstein, D. (2015). Metal–ligand cooperation by aromatization–dearomatization as a tool in single bond activation. Phil. Trans. R. Soc. A., 373, 20140189. (https://doi.org/10.1098/rsta.2014.0189)

[39] Ramspoth, T.-F., Kootstra, J., and Harutyunyan, S.R. (2024). Unlocking the potential of metal ligand cooperation for enantioselective transformations. Chem. Soc. Rev., 53, 3216–3223. (https://doi.org/10.1039/D3CS00998J)

[40] Khusnutdinova, J.R., and Milstein, D. (2015). Metal–Ligand Cooperation. Angew Chem Int Ed, 54, 12236–12273. (https://doi.org/10.1002/anie.201503873)

[41] Mahmudov, K.T., and Pombeiro, A.J.L. (2023). Control of Selectivity in Homogeneous Catalysis through Noncovalent Interactions. Chem. Eur. J., 29, e202203861. (https://doi.org/10.1002/chem.202203861)

[42] Yu, H., Zhai, Y., Dai, G., Ru, S., Han, S., and Wei, Y. (2017). Transition-Metal-Controlled Inorganic Ligand-Supported Non-Precious Metal Catalysts for the Aerobic Oxidation of Amines to Imines. Chem. Eur. J., 23, 13883–13887. (https://doi.org/10.1002/chem.201703185)

[43] Shimbayashi, T., and Fujita, K. (2020). Recent Advances in Homogeneous Catalysis via Metal–Ligand Cooperation Involving Aromatization and Dearomatization. Catalysts, 10, 635. (https://doi.org/10.3390/catal10060635)

[44] Chen, X., Jiang, H., Hou, B., Gong, W., Liu, Y., and Cui, Y. (2017). Boosting Chemical Stability, Catalytic Activity, and Enantioselectivity of Metal-Organic Frameworks for Batch and Flow Reactions. J. Am. Chem. Soc., 139, 13476–13482. (https://doi.org/10.1021/jacs.7b06459)

[45] Fossey, J.S., and Richards, C.J. (2004). Synthesis of 2,6-Bis(2-oxazolinyl)phenylplatinum(II) NCN Pincer Complexes by Direct Cyclometalation. Catalysts for Carbon−Carbon Bond Formation. Organometallics, 23, 367–373. (https://doi.org/10.1021/om0305162)

[46] Lee, B., Pabst, T.P., Hierlmeier, G., and Chirik, P.J. (2023). Exploring the Effect of Pincer Rigidity on Oxidative Addition Reactions with Cobalt(I) Complexes. Organometallics, 42, 708–718. https://doi.org/10.1021/acs.organomet.3c00079.

[47] Van Koten, G., and Gossage, R.A. eds. (2016). The Privileged Pincer-Metal Platform: Coordination Chemistry & Applications (Springer International Publishing) (https://doi.org/10.1007/978-3-319-22927-0)

[48] Asay, M., and Morales-Morales, D. (2015). Non-symmetric pincer ligands: complexes and applications in catalysis. Dalton Trans., 44, 17432–17447. (https://doi.org/10.1039/C5DT02295A)

[49] O'Reilly, M.E., and Veige, A.S. (2014). Trianionic pincer and pincer-type metal complexes and catalysts. Chem. Soc. Rev., 43, 6325–6369. (https://doi.org/10.1039/C4CS00111G)

[50] Sarkar, S., McGowan, K.P., Culver, J.A., Carlson, A.R., Koller, J., Peloquin, A.J., Veige, M.K., Abboud, K.A., and Veige, A.S. (2010). NCN Trianionic Pincer Ligand Precursors: Synthesis of Bimetallic, Chelating Diamide, and Pincer Group IV Complexes. Inorg. Chem., 49, 5143–5156. (https://doi.org/10.1021/ic100232s)

[51] Zafar, M., Subramaniyan, V., Tibika, F., and Tulchinsky, Y. (2024). Cationic ligands – from monodentate to pincer systems. Chem. Commun., 60, 9871–9906. (https://doi.org/10.1039/D4CC01489H)

[52] Deng, Q.-H., Melen, R.L., and Gade, L.H. (2014). Anionic Chiral Tridentate *N*-Donor Pincer Ligands in Asymmetric Catalysis. Acc. Chem. Res., 47, 3162–3173. (https://doi.org/10.1021/ar5002457)

[53] Zhao, D., Candish, L., Paul, D., and Glorius, F. (2016). *N*-Heterocyclic Carbenes in Asymmetric Hydrogenation. ACS Catal., 6, 5978–5988. (https://doi.org/10.1021/acscatal.6b01736)

[54] Wang, W., Cui, L., Sun, P., Shi, L., Yue, C., and Li, F. (2018). Reusable *N*-Heterocyclic Carbene Complex Catalysts and Beyond: A Perspective on Recycling Strategies. Chem. Rev., 118, 9843–9929. (https://doi.org/10.1021/acs.chemrev.8b00057)

[55] Kong, L., Morvan, J., Pichon, D., Jean, M., Albalat, M., Vives, T., Colombel-Rouen, S., Giorgi, M., Dorcet, V., Roisnel, T., et al. (2020). From Prochiral *N*-Heterocyclic Carbenes to Optically Pure Metal Complexes: New Opportunities in Asymmetric Catalysis. J. Am. Chem. Soc., 142, 93–98. (https://doi.org/10.1021/jacs.9b12698)

[56] He, F., Zois, K.P., Tzeli, D., Danopoulos, A.A., and Braunstein, P. (2024). *N*-heterocyclic carbenes as bridgehead donors in metal pincer complexes. Coord. Chem. Rev., 514, 215757. (https://doi.org/10.1016/j.ccr.2024.215757)

[57] Doddi, A., Peters, M., and Tamm, M. (2019). *N*-Heterocyclic Carbene Adducts of Main Group Elements and Their Use as Ligands in Transition Metal Chemistry. Chem. Rev., 119, 6994–7112. (https://doi.org/10.1021/acs.chemrev.8b00791)

[58] César, V., Bellemin-Laponnaz, S., and Gade, L.H. (2004). Chiral *N*-heterocyclic carbenes as stereodirecting ligands in asymmetric catalysis. Chem. Soc. Rev., 33, 619–636. (https://doi.org/10.1039/B406802P)

[59] Aktas, H., Slootweg, J.C., Schakel, M., Ehlers, A.W., Lutz, M., Spek, A.L., and Lammertsma, K. (2009). *N*-Heterocyclic Carbene-Functionalized Ruthenium Phosphinidenes: What a Difference a Twist Makes. J. Am. Chem. Soc., 131, 6666–6667. (https://doi.org/10.1021/ja901540h)

[60] Kausamo, A., Tuononen, H.M., Krahulic, K.E., and Roesler, R. (2008). *N*-Heterocyclic Carbenes with Inorganic Backbones: Electronic Structures and Ligand Properties. Inorg. Chem., 47, 1145–1154. (https://doi.org/10.1021/ic7020929)

[61] Ramasamy, B., and Ghosh, P. (2016). The Developing Concept of Bifunctional Catalysis with Transition Metal *N*-Heterocyclic

Carbene Complexes. Eur J Inorg Chem, 2016, 1448–1465. (https://doi.org/10.1002/ejic.201501429)

[62] Stewart, I.C., Benitez, D., O'Leary, D.J., Tkatchouk, E., Day, M.W., Goddard, W.A., and Grubbs, R.H. (2009). Conformations of *N*-Heterocyclic Carbene Ligands in Ruthenium Complexes Relevant to Olefin Metathesis. J. Am. Chem. Soc., 131, 1931–1938. (https://doi.org/10.1021/ja8078913)

[63] Toda, T., Yoshinari, A., Ikariya, T., and Kuwata, S. (2016). Protic *N*-Heterocyclic Carbene Versus Pyrazole: Rigorous Comparison of Proton- and Electron-Donating Abilities in a Pincer-Type Framework. Chem. Eur. J., 22, 16675–16683. (https://doi.org/10.1002/chem.201602552)

[64] Kuwata, S., and Ikariya, T. (2014). Metal–ligand bifunctional reactivity and catalysis of protic *N*-heterocyclic carbene and pyrazole complexes featuring β-NH units. Chem. Commun., 50, 14290–14300. (https://doi.org/10.1039/C4CC04457F)

[65] Hahn, F.E. (2013). Substrate Recognition and Regioselective Catalysis with Complexes Bearing NR,NH-NHC Ligands. ChemCatChem, 5, 419–430. (https://doi.org/10.1002/cctc.201200567)

[66] Wang, M.H., and Scheidt, K.A. (2016). Cooperative Catalysis and Activation with *N*-Heterocyclic Carbenes. Angew Chem Int Ed, 55, 14912–14922. (https://doi.org/10.1002/anie.201605319)

[67] Jacobs, E., and Nguyen, T.V. (2025). *N*-Heterocyclic Carbenes and *N*-Heterocycles as Synthetic Reagents and Building Blocks. Chem. Eur. J., 31, e202402339. (https://doi.org/10.1002/chem.202402339)

[68] Ramasamy, B., and Ghosh, P. (2016). The Developing Concept of Bifunctional Catalysis with Transition Metal *N*-Heterocyclic

Carbene Complexes. Eur J Inorg Chem, 2016, 1448–1465. (https://doi.org/10.1002/ejic.201501429)

[69] Kuwata, S., and Hahn, F.E. (2018). Complexes Bearing Protic *N*-Heterocyclic Carbene Ligands. Chem. Rev., 118, 9642–9677. (https://doi.org/10.1021/acs.chemrev.8b00176)

[70] Jahnke, M.C., and Hahn, F.E. (2015). Complexes Bearing Protic *N* -Heterocyclic Carbenes: Synthesis and Applications. Chem. Lett., 44, 226–237. (https://doi.org/10.1246/cl.141052)

[71] Evans, K.J., and Mansell, S.M. (2020). Functionalised *N*-Heterocyclic Carbene Ligands in Bimetallic Architectures. Chem. Eur. J, 26, 5927–5941. (https://doi.org/10.1002/chem.201905510)

[72] Wang, H., Wen, J., and Zhang, X. (2021). Chiral Tridentate Ligands in Transition Metal-Catalyzed Asymmetric Hydrogenation. Chem. Rev., 121, 7530–7567. (https://doi.org/10.1021/acs.chemrev.1c00075)

[73] Santini, C., Marinelli, M., and Pellei, M. (2016). Boron-Centered Scorpionate-Type NHC-Based Ligands and Their Metal Complexes. Eur J Inorg Chem, 2016, 2312–2331. (https://doi.org/10.1002/ejic.201600133)

[74] Miranda-Soto, V., Grotjahn, D.B., Cooksy, A.L., Golen, J.A., Moore, C.E., and Rheingold, A.L. (2011). A Labile and Catalytically Active Imidazol-2-yl Fragment System. Angew Chem Int Ed, 50, 631–635. (https://doi.org/10.1002/anie.201005100)

[75] Price, C., Elsegood, M.R.J., Clegg, W., Rees, N.H., and Houlton, A. (1997). Evidence for Directed Metalation: A Structural Intermediate in the Formation of a Novel C-bound Adenine Complex of Ruthenium. Angew. Chem. Int. Ed., Engl. 36, 1762–1764. (https://doi.org/10.1002/anie.199717621)

[76] Viciano, M., Mas-Marzá, E., Sanaú, M., and Peris, E. (2006). Synthesis and Reactivity of New Complexes of Rhodium and Iridium with Bis(dichloroimidazolylidene) Ligands. Electronic and Catalytic Implications of the Introduction of the Chloro Substituents in the NHC Rings. Organometallics, 25, 3063–3069. (https://doi.org/10.1021/om060174a)

[77] Naziruddin, A.R., Hepp, A., Pape, T., and Hahn, F.E. (2011). Synthesis of Rhodium(I) Complexes Bearing Bidentate NH,NR-NHC/Phosphine Ligands. Organometallics, 30, 5859–5866. (https://doi.org/10.1021/om200689r)

[78] Tan, K.L., Bergman, R.G., and Ellman, J.A. (2002). Intermediacy of an *N*-Heterocyclic Carbene Complex in the Catalytic C−H Activation of a Substituted Benzimidazole. J. Am. Chem. Soc., 124, 3202–3203. (https://doi.org/10.1021/ja017351d)

[79] Miranda-Soto, V., Grotjahn, D.B., DiPasquale, A.G., and Rheingold, A.L. (2008). Imidazol-2-yl Complexes of Cp*Ir as Bifunctional Ambident Reactants. J. Am. Chem. Soc., 130, 13200–13201. (https://doi.org/10.1021/ja804713u)

[80] Johnson, M.C., Rogers, D., Kaminsky, W., and Cossairt, B.M. (2021). CO_2 Hydrogenation Catalyzed by a Ruthenium Protic *N*-Heterocyclic Carbene Complex. Inorg. Chem., 60, 5996–6003. (https://doi.org/10.1021/acs.inorgchem.1c00417)

[81] Eguillor, B., Esteruelas, M.A., García-Raboso, J., Oliván, M., Oñate, E., Pastor, I.M., Peñafiel, I., and Yus, M. (2011). Osmium NHC Complexes from Alcohol-Functionalized Imidazoles and Imidazolium Salts. Organometallics, 30, 1658–1667. (https://doi.org/10.1021/om101173e)

[82] Wodrich, M.D., and Hu, X. (2017). Natural inspirations for metal–ligand cooperative catalysis. Nat Rev Chem, 2, 0099. (https://doi.org/10.1038/s41570-017-0099)

[83] Gunanathan, C., and Milstein, D. (2011). Metal–Ligand Cooperation by Aromatization–Dearomatization: A New Paradigm in Bond Activation and “Green” Catalysis. Acc. Chem. Res., 44, 588–602. (https://doi.org/10.1021/ar2000265)

[84] A. Mata, J., and Poyatos, M. (2011). Recent Developments in the Applications of Palladium Complexes Bearing *N*-Heterocyclic Carbene Ligands. COC, 15, 3309–3324. (https://doi.org/10.2174/138527211797247969)

[85] Filonenko, G.A., Conley, M.P., Copéret, C., Lutz, M., Hensen, E.J.M., and Pidko, E.A. (2013). The impact of Metal–Ligand Cooperation in Hydrogenation of Carbon Dioxide Catalyzed by Ruthenium PNP Pincer. ACS Catal., 3, 2522–2526. (https://doi.org/10.1021/cs4006869)

[86] Eijsink, L.E., Perdriau, S.C.P., De Vries, J.G., and Otten, E. (2016). Metal–ligand cooperative activation of nitriles by a ruthenium complex with a de-aromatized PNN pincer ligand. Dalton Trans., 45, 16033–16039. (https://doi.org/10.1039/C6DT02478E)

[87] Asay, M., and Morales-Morales, D. (2015). Non-symmetric pincer ligands: complexes and applications in catalysis. Dalton Trans., 44, 17432–17447. (https://doi.org/10.1039/C5DT02295A)

[88] I, M., R, S., B, I., Mt, H., and E, D. (2009). Recent Advances in the Use of Unsymmetrical Palladium Pincer Complexes. COC, 13, 878–895. (https://doi.org/10.2174/138527209788452144)

[89] Anaby, A., Butschke, B., Ben-David, Y., Shimon, L.J.W., Leitus, G., Feller, M., and Milstein, D. (2014). B–H Bond Cleavage via Metal–Ligand Cooperation by Dearomatized Ruthenium Pincer Complexes. Organometallics, 33, 3716–3726. (https://doi.org/10.1021/om500311a)

[90] Van Koten, G., and Gossage, R.A. eds. (2016). The Privileged Pincer-Metal Platform: Coordination Chemistry & Applications (Springer International Publishing) (https://doi.org/10.1007/978-3-319-22927-0)

[91] Araki, K., Kuwata, S., and Ikariya, T. (2008). Isolation and Interconversion of Protic *N*-Heterocyclic Carbene and Imidazolyl Complexes: Application to Catalytic Dehydrative Condensation of N -(2-Pyridyl)benzimidazole and Allyl Alcohol. Organometallics, 27, 2176–2178. (https://doi.org/10.1021/om800285n)

[92] Eisenstein, O., and Crabtree, R.H. (2013). Outer sphere hydrogenation catalysis. New J. Chem., 37, 21–27. (https://doi.org/10.1039/C2NJ40659D)

[93] Fogler, E., Garg, J.A., Hu, P., Leitus, G., Shimon, L.J.W., and Milstein, D. (2014). System with Potential Dual Modes of Metal–Ligand Cooperation: Highly Catalytically Active Pyridine-Based PNNH–Ru Pincer Complexes. Chem. Eur. J, 20, 15727–15731. (https://doi.org/10.1002/chem.201405295)

[94] Feller, M., Diskin-Posner, Y., Shimon, L.J.W., Ben-Ari, E., and Milstein, D. (2012). N–H Activation by Rh(I) via Metal–Ligand Cooperation. Organometallics, 31, 4083–4101. (https://doi.org/10.1021/om300248r)

[95] Zak, I.L., Gadekar, S.C., and Milo, A. (2021). Designing the Secondary Coordination Sphere in Small-Molecule Catalysis. Synlett, 32, 329–336. (https://doi.org/10.1055/s-0040-1707326)

[96] Meier, N., Hahn, F.E., Pape, T., Siering, C., and Waldvogel, S.R. (2007). Molecular Recognition Utilizing Complexes with NH,NR-Stabilized Carbene Ligands. Eur J Inorg Chem, 2007, 1210–1214. (https://doi.org/10.1002/ejic.200601258)

[97] Chernyshev, V.M., Denisova, E.A., Eremin, D.B., and Ananikov, V.P. (2020). The key role of R–NHC coupling (R = C, H, heteroatom) and M–NHC bond cleavage in the evolution of M/NHC complexes and formation of catalytically active species. Chem. Sci., 11, 6957–6977. (https://doi.org/10.1039/D0SC02629H)

[98] Wang, X., Chen, H., and Li, X. (2007). Ir(III)-Induced C-Bound to *N*-Bound Tautomerization of a *N*-Heterocyclic Carbene. Organometallics, 26, 4684–4687. (https://doi.org/10.1021/om700498w)

[99] Ebner, F., Sigmund, L.M., and Greb, L. (2020). Metal–Ligand Cooperativity of the Calix[4]pyrrolato Aluminate: Triggerable C−C Bond Formation and Rate Control in Catalysis. Angew Chem Int Ed, 59, 17118–17124. (https://doi.org/10.1002/anie.202007717)

[100] Krishnakumar, V., Chatterjee, B., and Gunanathan, C. (2017). Ruthenium-Catalyzed Urea Synthesis by N–H Activation of Amines. Inorg. Chem., 56, 7278–7284. (https://doi.org/10.1021/acs.inorgchem.7b00962)

[101] Zhang, J., Leitus, G., Ben-David, Y., and Milstein, D. (2005). Facile Conversion of Alcohols into Esters and Dihydrogen Catalyzed by New Ruthenium Complexes. J. Am. Chem. Soc., 127, 10840–10841. (https://doi.org/10.1021/ja052862b)

[102] Li, H., Gonçalves, T.P., Lupp, D., and Huang, K.-W. (2019). PN^3 (P)-Pincer Complexes: Cooperative Catalysis and Beyond. ACS Catal., 9, 1619–1629. (https://doi.org/10.1021/acscatal.8b04495)

[103] Käß, M., Friedrich, A., Drees, M., and Schneider, S. (2009). Ruthenium Complexes with Cooperative PNP Ligands: Bifunctional Catalysts for the Dehydrogenation of Ammonia–Borane. Angew Chem Int Ed, 48, 905–907. (https://doi.org/10.1002/anie.200805108)

[104] Rong, M.K., Chirila, A., Franciolus, D., Lutz, M., Nieger, M., Ehlers, A.W., Slootweg, J.C., and Lammertsma, K. (2019). Protic NHC Iridium Complexes with β-H Reactivity–Synthesis, Acetonitrile Insertion, and Oxidative Self-Activation. Organometallics, 38, 4543–4553. (https://doi.org/10.1021/acs.organomet.9b00584)

[105] Zhang, J., Leitus, G., Ben-David, Y., and Milstein, D. (2006). Efficient Homogeneous Catalytic Hydrogenation of Esters to Alcohols. Angew Chem Int Ed, 45, 1113–1115. (https://doi.org/10.1002/anie.200503771)

[106] Oliveira, A.M., Beswick, R.R., and Yan, Y. (2021). A green hydrogen economy for a renewable energy society. Curr Opin Chem Eng, 33, 100701. (https://doi.org/10.1016/j.coche.2021.100701)

[107] Zahran, Z.N., Tsubonouchi, Y., Mohamed, E.A., and Yagi, M. (2019). Recent Advances in the Development of Molecular Catalyst-Based Anodes for Water Oxidation toward Artificial Photosynthesis. ChemSusChem, 12, 1775–1793. (https://doi.org/10.1002/cssc.201802795)

[108] Briand, G.G. (2023). Redox-active ligands – a viable route to reactive main group metal compounds. Dalton Trans., 52, 17666–17678. (https://doi.org/10.1039/D3DT03100D)

[109] Yan, J., Ye, F., Dai, Q., Ma, X., Fang, Z., Dai, L., and Hu, C. (2023). Recent progress in carbon-based electrochemical catalysts: From structure design to potential applications. Nano Res. Energy, 2, e9120047. (https://doi.org/10.26599/NRE.2023.9120047)

[110] Xie, Y., Shaffer, D.W., Lewandowska-Andralojc, A., Szalda, D.J., and Concepcion, J.J. (2016). Water Oxidation by Ruthenium Complexes Incorporating Multifunctional Bipyridyl

Diphosphonate Ligands. Angew Chem Int Ed, 55, 8067–8071. (https://doi.org/10.1002/anie.201601943)

[111] Falch, A., and Babu, S.P. (2021). A Review and Perspective on Electrocatalysts Containing Cr for Alkaline Water Electrolysis: Hydrogen Evolution Reaction. Electrocatalysis, 12, 104–116. (https://doi.org/10.1007/s12678-020-00634-7)

[112] Bofill, R., García-Antón, J., Escriche, L., Sala, X., and Llobet, A. (2013). Water Oxidation. In Comprehensive Inorganic Chemistry II (Elsevier), pp. 505–523. (https://doi.org/10.1016/B978-0-08-097774-4.00821-4)

[113] Dau, H., Limberg, C., Reier, T., Risch, M., Roggan, S., and Strasser, P. (2010). The Mechanism of Water Oxidation: From Electrolysis via Homogeneous to Biological Catalysis. ChemCatChem, 2, 724–761. (https://doi.org/10.1002/cctc.201000126)

[114] Zhang, L., Mathew, S., Hessels, J., Reek, J.N.H., and Yu, F. (2021). Homogeneous Catalysts Based on First-Row Transition-Metals for Electrochemical Water Oxidation. ChemSusChem, 14, 234–250. (https://doi.org/10.1002/cssc.202001876)

[115] Burling, S., Paine, B.M., Nama, D., Brown, V.S., Mahon, M.F., Prior, T.J., Pregosin, P.S., Whittlesey, M.K., and Williams, J.M.J. (2007). CH Activation Reactions of Ruthenium *N*-Heterocyclic Carbene Complexes: Application in a Catalytic Tandem Reaction Involving CC Bond Formation from Alcohols. J. Am. Chem. Soc., 129, 1987–1995. (https://doi.org/10.1021/ja065790c)

[116] Burling, S., Mahon, M.F., Powell, R.E., Whittlesey, M.K., and Williams, J.M.J. (2006). Ruthenium Induced C−N Bond Activation of an *N*-Heterocyclic Carbene: Isolation of C- and *N*-Bound Tautomers. J. Am. Chem. Soc., 128, 13702–13703. (https://doi.org/10.1021/ja065582k)

[117] Díez-González, S., and Nolan, S. (2007). *N*-Heterocyclic Carbene-Copper(I) Complexes in Homogeneous Catalysis. Synlett, 2007, 2158–2167. (https://doi.org/10.1055/s-2007-985577)

[118] Kumar, A., and Ghosh, P. (2012). Studies of the Electronic Properties of *N*-Heterocyclic Carbene Ligands in the Context of Homogeneous Catalysis and Bioorganometallic Chemistry. Eur J Inorg Chem, 2012, 3955–3969. (https://doi.org/10.1002/ejic.201200622)

[119] Zhang, L., and Hou, Z. (2013). *N*-Heterocyclic carbene (NHC)–copper-catalysed transformations of carbon dioxide. Chem. Sci., 4, 3395. (https://doi.org/10.1039/c3sc51070k)

[120] Gagliardi, C.J., Vannucci, A.K., Concepcion, J.J., Chen, Z., and Meyer, T.J. (2012). The role of proton coupled electron transfer in water oxidation. Energy Environ. Sci., 5, 7704. (https://doi.org/10.1039/c2ee03311a)

[121] Ishizuka, T., Kotani, H., and Kojima, T. (2016). Characteristics and reactivity of ruthenium–oxo complexes. Dalton Trans., 45, 16727–16750. (https://doi.org/10.1039/C6DT03024F)

[122] Duan, L., Fischer, A., Xu, Y., and Sun, L. (2009). Isolated Seven-Coordinate Ru(IV) Dimer Complex with $[HOHOH]^-$ Bridging Ligand as an Intermediate for Catalytic Water Oxidation. J. Am. Chem. Soc., 131, 10397–10399. (https://doi.org/10.1021/ja9034686)

[123] Concepcion, J.J., Zhong, D.K., Szalda, D.J., Muckerman, J.T., and Fujita, E. (2015). Mechanism of water oxidation by $[Ru(bda)(L)_2]$: the return of the "blue dimer." Chem. Commun., 51, 4105–4108. (https://doi.org/10.1039/C4CC07968J)

[124] Phapale, D., Sharma, V., Saini, A., Sharma, S., Kumar, P., Kumar, R., Shanmugam, M., Draksharapu, A., Dutta, A., McInnes,

E.J.L., et al. (2024). Capturing the Elusive [Ru^{V}═O]$^{+}$ Intermediate in Water Oxidation. ACS Catal., 14, acscatal.4c01623. (https://doi.org/10.1021/acscatal.4c01623)

[125] Guan, C., Pan, Y., Zhang, T., Ajitha, M.J., and Huang, K. (2020). An Update on Formic Acid Dehydrogenation by Homogeneous Catalysis. Chem. Asian J., 15, 937–946. (https://doi.org/10.1002/asia.201901676)

[126] Onishi, N., Kanega, R., Kawanami, H., and Himeda, Y. (2022). Recent Progress in Homogeneous Catalytic Dehydrogenation of Formic Acid. Molecules, 27, 455. (https://doi.org/10.3390/molecules27020455)

[127] Eppinger, J., and Huang, K.-W. (2017). Formic Acid as a Hydrogen Energy Carrier. ACS Energy Lett., 2, 188–195. (https://doi.org/10.1021/acsenergylett.6b00574)

[128] Iglesias, M., and Oro, L.A. (2018). Mechanistic Considerations on Homogeneously Catalyzed Formic Acid Dehydrogenation. Eur J Inorg Chem, 2018, 2125–2138. (https://doi.org/10.1002/ejic.201800159)

[129] Celaje, J.J.A., Lu, Z., Kedzie, E.A., Terrile, N.J., Lo, J.N., and Williams, T.J. (2016). A prolific catalyst for dehydrogenation of neat formic acid. Nat Commun, 7, 11308. (https://doi.org/10.1038/ncomms11308)

[130] Aufricht, P., Nori, V., Rabell, B., Piccirilli, L., Koranchalil, S., W. Larsen, R., Nielsen, M.T., and Nielsen, M. (2025). Formic acid dehydrogenation catalysed by a novel amino-di(*N*-heterocyclic carbene) based Ru-CNC pincer complex. Chem. Commun., 61, 3986–3989. (https://doi.org/10.1039/D4CC05164E)

[131] Kumar, N., Aepuru, R., Lee, S.-Y., and Park, S.-J. (2025). Advances in Catalysts for Hydrogen Production: A Comprehensive

Review of Materials and Mechanisms. Nanomaterials 15, 256. (https://doi.org/10.3390/nano15040256)

[132] Bulushev, D.A. (2021). Progress in Catalytic Hydrogen Production from Formic Acid over Supported Metal Complexes. Energies, 14, 1334. (https://doi.org/10.3390/en14051334)

[133] Siemeling, U., Färber, C., Bruhn, C., Leibold, M., Selent, D., Baumann, W., Von Hopffgarten, M., Goedecke, C., and Frenking, G. (2010). *N*-heterocyclic carbenes which readily add ammonia, carbon monoxide and other small molecules,. Chem. Sci., 1, 697. (https://doi.org/10.1039/c0sc00451k)

[134] Reyes, E., Uria, U., Carrillo, L., and Vicario, J. (2016). Enantioselective Cascade Reactions under *N*-Heterocyclic Carbene Catalysis. Synthesis 49, 451–471. (https://doi.org/10.1055/s-0036-1589470)

[135] Cavell, K. (2008). *N*-Heterocyclic carbenes/imidazolium salts as substrates in catalysis: the catalytic 2-substitution and annulation of heterocyclic compounds. Dalton Trans., 6676. (https://doi.org/10.1039/b811449h)

[136] Pan, Y., Pan, C., Zhang, Y., Li, H., Min, S., Guo, X., Zheng, B., Chen, H., Anders, A., Lai, Z., et al. (2016). Selective Hydrogen Generation from Formic Acid with Well-Defined Complexes of Ruthenium and Phosphorus–Nitrogen PN^3 -Pincer Ligand. Chem. Asian J., 11, 1357–1360. (https://doi.org/10.1002/asia.201600169)

[137] De Boer, S.Y., Korstanje, T.J., La Rooij, S.R., Kox, R., Reek, J.N.H., and Van Der Vlugt, J.I. (2017). Ruthenium PNN(O) Complexes: Cooperative Reactivity and Application as Catalysts for Acceptorless Dehydrogenative Coupling Reactions. Organometallics, 36, 1541–1549. (https://doi.org/10.1021/acs.organomet.7b00111)

[138] Kothandaraman, J., Czaun, M., Goeppert, A., Haiges, R., Jones, J., May, R.B., Prakash, G.K.S., and Olah, G.A. (2015). Amine-Free Reversible Hydrogen Storage in Formate Salts Catalyzed by Ruthenium Pincer Complex without pH Control or Solvent Change. ChemSusChem, 8, 1442–1451. (https://doi.org/10.1002/cssc.201403458)

[139] Agapova, A., Alberico, E., Kammer, A., Junge, H., and Beller, M. (2019). Catalytic Dehydrogenation of Formic Acid with Ruthenium-PNP-Pincer Complexes: Comparing N-Methylated and NH-Ligands. ChemCatChem, 11, 1910–1914. (https://doi.org/10.1002/cctc.201801897)

[140] Obora, Y. (2014). Recent Advances in α - Alkylation Reactions using Alcohols with Hydrogen Borrowing Methodologies. ACS Catal., 4, 3972–3981. (https://doi.org/10.1021/cs501269d)

[141] Zhang, F., Chen, K., Min, X., Yang, W., Su, M., and Cao, Z. (2024). Catalysis-Controlled Selective N -mono or N -di-methylation of Anilines: A Review on Synthesis of N -methyl or N , N -dimethyl anilines. ChemistrySelect 9, e202304621. (https://doi.org/10.1002/slct.202304621)

[142] Kurul, F., Doruk, B., and Topkaya, S.N. (2025). Principles of green chemistry: building a sustainable future. Discov. Chem., 2, 68. (https://doi.org/10.1007/s44371-025-00152-9)

[143] Toyooka, G., Tuji, A., and Fujita, K. (2018). Efficient and Versatile Catalytic Systems for the *N*-Methylation of Primary Amines with Methanol Catalyzed by *N*-Heterocyclic Carbene Complexes of Iridium. Synthesis, 50, 4617–4626. (https://doi.org/10.1055/s-0037-1610252)

[144] Paul, B., and Kundu, S. (2024). The use of methanol as a C1 building block. Nat Protoc, 19, 2358–2385. (https://doi.org/10.1038/s41596-024-00978-0)

[145] Yu, X., Cui, X., Jing, H., Qian, B., Yuan, H., and Shi, F. (2024). Recent Development in Synthesis of N-Methylamines with Amines and Methanol. ChemCatChem, 16, e202400291. (https://doi.org/10.1002/cctc.202400291)

[146] Sarki, N., Goyal, V., Natte, K., and Jagadeesh, R.V. (2021). Base Metal-Catalyzed C-Methylation Reactions Using Methanol. Adv Synth Catal, 363, 5028–5046. (https://doi.org/10.1002/adsc.202100762)

[147] Onishi, N., Kanega, R., Fujita, E., and Himeda, Y. (2019). Carbon Dioxide Hydrogenation and Formic Acid Dehydrogenation Catalyzed by Iridium Complexes Bearing Pyridyl-pyrazole Ligands: Effect of an Electron-donating Substituent on the Pyrazole Ring on the Catalytic Activity and Durability. Adv Synth Catal, 361, 289–296. (https://doi.org/10.1002/adsc.201801323)

[148] Piehl, P., Amuso, R., Spannenberg, A., Gabriele, B., Neumann, H., and Beller, M. (2021). Efficient methylation of anilines with methanol catalysed by cyclometalated ruthenium complexes. Catal. Sci. Technol., 11, 2512–2517. (https://doi.org/10.1039/D0CY02210A)

[149] Gao, C., Li, Y., Wang, M., Gong, D., and Zhao, L. (2023). Ru(II)-Catalyzed *N*-Methylation of Amines Using Methanol as the C1 Source. ACS Omega, 8, 36597–36603. (https://doi.org/10.1021/acsomega.3c06260)

[150] Illam, P.M., and Rit, A. (2022). Electronically tuneable orthometalated Ru^{II} –NHC complexes as efficient catalysts for C–C and C–N bond formations via borrowing hydrogen strategy. Catal. Sci. Technol., 12, 67–74. (https://doi.org/10.1039/D1CY01767E)

[151] Bai, M., Zhang, S., Lin, Z., Hao, Z., Han, Z., Lu, G.-L., and Lin, J. (2024). Ruthenium Complexes with NNN-Pincer Ligands for *N*-

Methylation of Amines Using Methanol. Inorg. Chem., 63, 11821–11831. (https://doi.org/10.1021/acs.inorgchem.4c01561)

[152] Nath, S., Yadav, E., Raghuvanshi, A., and Singh, A.K. (2023). Ru(II) Complexes with Protic- and Anionic-Naked-NHC Ligands for Cooperative Activation of Small Molecules**. Chem Eur J, 29, e202301971. (https://doi.org/10.1002/chem.202301971)

[153] Nath, S., and Singh, A.K. (2025). Substrate-assisted product release in hydrogenation of LOHCs facilitated by hemilabile pyridine in Ru(II)–NNC pincer complexes and enhanced activity of proton-responsive protic-NHC ligands. Catal. Sci. Technol., 15, 2999–3008. (https://doi.org/10.1039/D5CY00209E)

CHAPTER 2

Ru(II)-Bis(pincer) Complexes for Electrochemical Water Oxidation

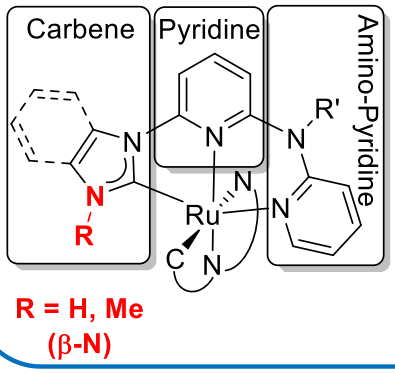

This chapter investigates the influence of β-Nitrogen substitution in the CPAP ligand framework. Our objective is to understand the effect of varying the β-N substitution from hydrogen to methyl on the catalytic efficiency. To evaluate these effects, electrochemical water oxidation has been employed as the model catalytic application.

2.1 Introduction

The water oxidation process is crucial in converting solar energy into chemical energy in photosynthesis.[1–6] The oxygen evolution reaction (OER) is the key bottleneck in converting solar and electrical energy into chemical fuels.[7–13] Electrochemical water oxidation offers a practical and energy-efficient route,[14–18] though it is both thermodynamically unfavourable and kinetically demanding, requiring highly effective catalysts for the $4H^+/4e^-$ extraction.[19–21]A significant increase in studies has produced promising water oxidation catalysis,[22–24] including transition-metal oxides and mixed-metal oxides,[25,26] with extensive research on Ru, Ir, and 3d metals.[27–37]

Since the discovery of Meyer's "blue dimer" in 1982,[38] various ruthenium complexes have been proven to be efficient water oxidation catalysts,[47-52] primarily involving high-valent oxo species.[38] Notably, the Ru=O species was observed in the tris(2-pyridylmethyl)amine (TPA) complex,[39] where ruthenium transitions were between Ru(II) and Ru(IV) redox states.[39,40] The trinuclear Ru(bda) complex, being the most efficient catalyst for water oxidation, has shown the highest TON of 1.8 million reported to date.[41] Proton-coupled electron transfer (PCET)[42–46] is a crucial step in the context of water oxidation, which helps prevent charge buildup, enabling the conversion of water to oxygen, as seen in Photosystem II (PSII).[47] Thus, integrating the PCET-

facilitating feature is a key to catalyst design for electrochemical processes. [48–56]

Bis-pincer complexes have garnered attention for their diverse photophysical, photochemical, and electrochemical applications.[57] The coordinatively saturated nature imparts high stability and effective photosensitising and electrochemical properties.[58–60] For example, the polypyridine Ru complex $[Ru(tpy)_2]^{2+}$ is well recognised in oxidation, photocatalysis, and photosensitization.[61–63] The incorporation of stronger donors, *N*-heterocyclic carbenes (NHCs), in bis(pincer) complexes has also been reported.[64–68] Although complexes like $[Ru(bpy)_3]^{2+}$ and $[Ru(tpy)_2]^{2+}$ exhibit photosensitizer properties, their electrochemical applications are limited.[61,69–71] For electrocatalytic applications, designing coordinatively saturated complexes that can generate vacant sites under electrochemical conditions is a popular design strategy.[60,72]

We recently reported an unsymmetrical NNC pincer ligand that enables access to both protic and classical NHC complexes.[73,74] A comparison of protic and classical NHC in the heterolytic splitting of H_2 and the activation of small molecules confirmed their proton-responsive nature.[73] In this study, we present homoleptic ruthenium(II)-bis(pincer) complexes featuring either protic or classical NHC donors based on β-N substitution of the CPAP ligand framework. Here, coordinatively saturated Ru(II)-bis(pincer) complexes with the possibility of a hemilabile pyridine [75] and bearing proton-responsive protic-NHCs are investigated for electrochemical water oxidation.

2.2 Results and discussion

2.2.1 Synthesis of ligands (L1, L2·HI, L3 and L4·HI)

The protic-NHC complexes were based on the previously reported CNN pincer ligand **L1**, which is {6-(1*H*-benzimidazole-1-yl)-*N*-(pyridin-2-yl)-*N*-(*p*-tolyl)pyridin-2-amine} used as a model.[73] Ligand **L1** is a part of the CPAP series, having a benzimidazolylidene group with β-NH

functionality. To explore analogues of **L1**, the imidazole-based CNN pincer ligand **L3**, {6-(1*H*-imidazol-1-yl)-*N*-(pyridin-2-yl)-*N*-(*p*-tolyl)pyridin-2-amine}, was synthesized through a multistep process.

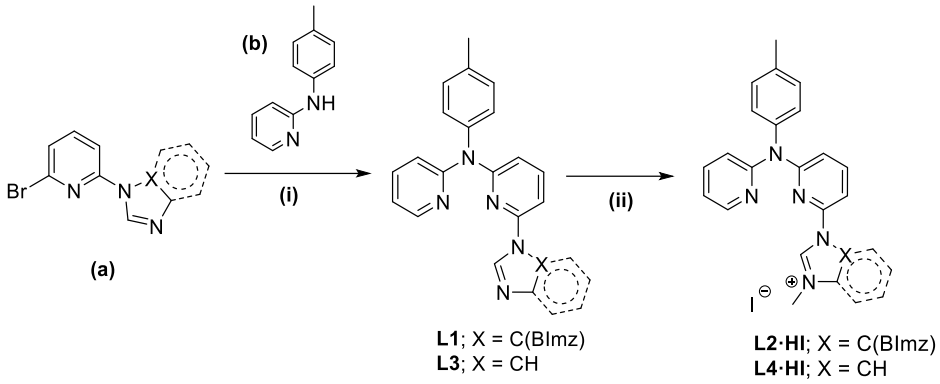

Scheme 2.1. Synthesis of ligands (**L1, L2·HI, L3,** and **L4·HI**) (**i**) $Pd(OAc)_2$, dppf, NaO^tBu, toluene, 110 °C, 24 h (**ii**) CH_3I, toluene, 110 °C, 24 h

Initially, the Ullmann C-N coupling reaction was applied to react 2,6-dibromopyridine with benzimidazole (for **L1**) and imidazole (for **L3**). These intermediates underwent Pd-catalyzed Buchwald-Hartwig cross-coupling with *N*-(*p*-tolyl)pyridine-2-amine to form the desired ligands (Scheme 2.1). ^1H, $^{13}C\{^1H\}$ NMR spectroscopy, LCMS, and HRMS have been used to fully characterize these ligands. In the case of **L3**, the ortho-pyridyl proton resonates at δ 8.36 ppm in the ^1H NMR spectrum, along with other aromatic protons in the range of 6.83-8.07 ppm and methyl protons at δ 2.38 ppm. The $^{13}C\{^1H\}$ and DEPT-135 NMR spectra display respective signals, confirming the structure of the ligand. Additionally, the LCMS(ESI^+) supports the formation of **L3** ligand with a corresponding peak for $[M+H]^+$at m/z = 328.1636 (calculated for $C_{20}H_{17}N_5$: 328.1557). The HRMS shows the peak for $[M+H]^+$ at m/z = 328.1563 (calculated for $C_{20}H_{17}N_5$: 328.1557).

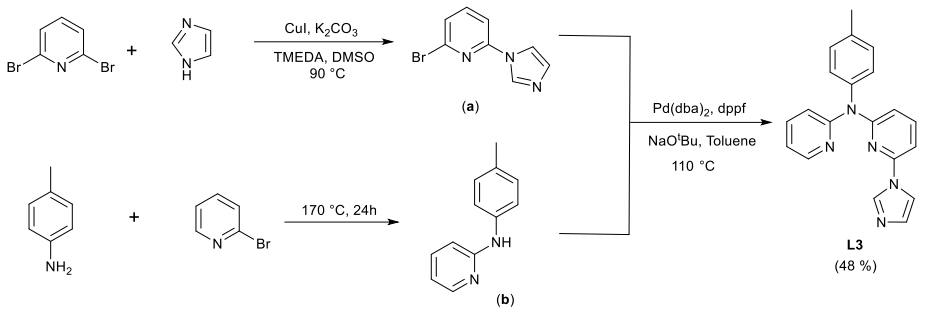

Scheme 2.2 Synthetic procedure for ligand **L3**

To synthesize the classical NHC complexes, methylated derivatives of the ligands **L1** and **L3** were prepared by treating them with methyl iodide in toluene, producing the corresponding salts **L2·HI** and **L4·HI** (Scheme 2.3). These were characterized by ^{1}H NMR, $^{13}C\{^{1}H\}$ NMR spectroscopy, and HRMS. **L2·HI** has already been reported. For **L4·HI**, the ^{1}H NMR spectrum shows a peak at δ 10.87 ppm for the proton flanked by two nitrogen atoms, whereas the methyl protons appear at δ 4.32 and δ 2.48 ppm. The methyl carbon signals are observed at δ 37.7 and δ 21.3 ppm. Additionally, the HRMS data also shows a corresponding peak for the ligand at m/z = 342.1722 (calculated for $C_{21}H_{20}N_5$: 342.1713).

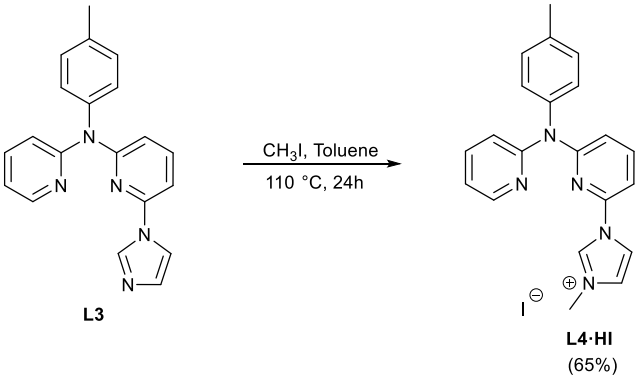

Scheme 2.3 Synthetic procedure for ligand **L4·HI**

2.2.2 Preparation of Ru(II)-bis(pincer) complexes

The homoleptic Ru(II)-bis(pincer) complexes **Ru1-Ru4** were synthesized from $RuCl_3 \cdot 3H_2O$ in a single step using ligand precursors in a 1:2 molar ratio in ethylene glycol (Scheme 2.4). Ligand precursors **L1**, **L2·HI, L3**, and **L4·HI**, capable of forming pNHC and classical NHC

donors, were chosen to compare their electronic and cooperative properties. Ligands with a benzimidazolylidene core (**L1** and **L2·HI**) have been previously reported by our group. [73,74] Therefore, the detailed characterization is confined to new ligands with an imidazolylidene core, **L3** and **L4·HI**, only. Ligands **L1** and **L3** produced bis(pincer)-protic-NHC complexes **Ru1** and **Ru3** via metal-assisted tautomerization from the azole to the pNHC form, while their methylated forms, **L2·HI** and **L4·HI,** resulted in bis(pincer)-classical-NHC complexes **Ru2** and **Ru4**. This straightforward process yielded ruthenium complexes featuring CNN-type ligands in good yields (60-65%). All these complexes are air- and moisture-stable and were thoroughly characterized using NMR spectroscopy, mass spectrometry, and single-crystal X-ray diffraction. These octahedral complexes, featuring two unsymmetrical NNC pincer ligands, are expected to be inherently chiral. However, their chiral resolution was not within the scope of this study.

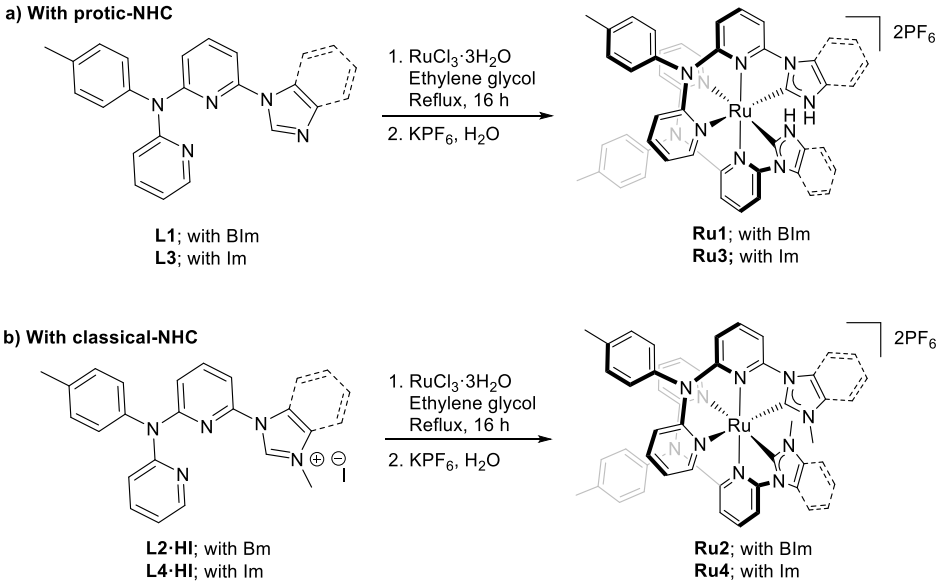

Scheme 2.4 Synthesis of complexes **Ru1-Ru4**

The bis(pincer)-pNHC complex (**Ru1**) was confirmed by NMR spectroscopy, showing a characteristic signal at δ 13.28 for two *N*-H protons (Figure 2.1) and at δ 203.6 ppm for $C_{carbene}$ (Figure 2.2). HRMS $(ESI)^+$ showed a peak for $[M\text{-}2PF_6\text{-}H]^+$ at m/z 855.2264 (calculated for $C_{48}H_{38}N_{10}Ru$: 855.2253), along with a signal at m/z 428.1192 for $[M\text{-}2PF_6]^{2+}$ (calculated for $C_{48}H_{38}N_{10}Ru$: 428.1163). The methylated

analogue, **Ru2**, showed a signal for the *N*-CH_3 group at δ 3.08 in the ^1H NMR spectrum. A signal for the carbene carbon was observed at δ 203.5 in the $^{13}C\{^1H\}$ NMR spectrum. The HRMS $(ESI)^+$ for **Ru2** showed a peak at m/z 442.1320 for $[M\text{-}2PF_6]^{2+}$ (calculated for $C_{50}H_{42}N_{10}Ru$: 442.1339).

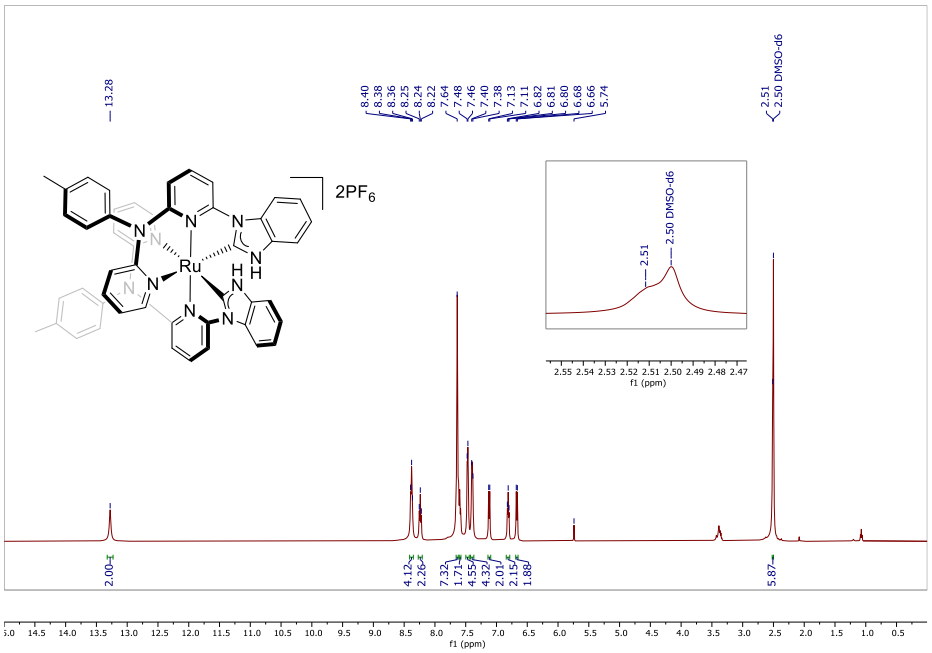

Figure 2.1. ^1H NMR spectrum of **Ru1** in DMSO-d_6.

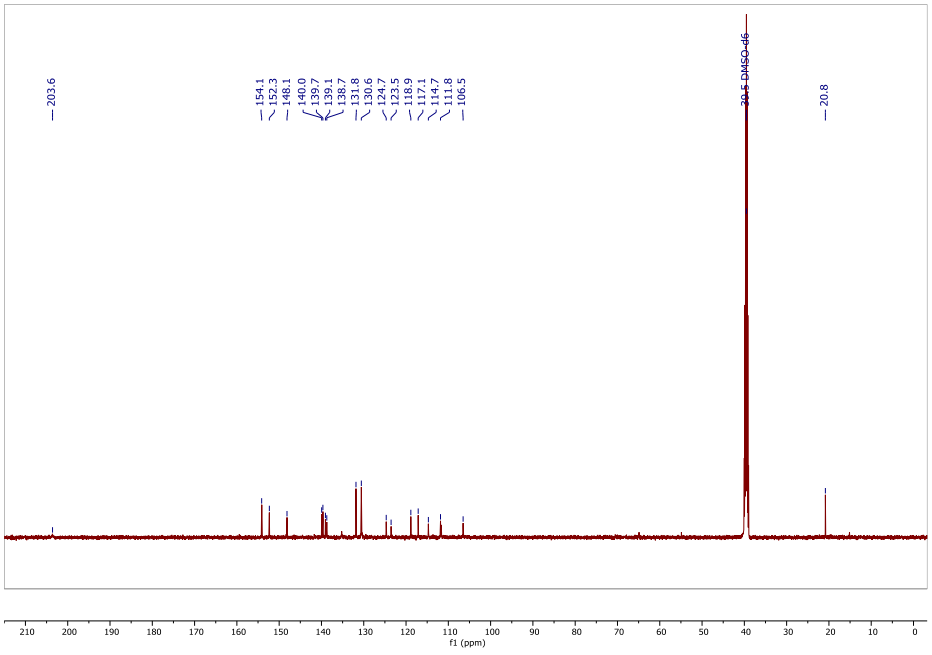

Figure 2.2. $^{13}C\{^1H\}$ NMR spectrum of **Ru1** in DMSO-d_6.

Similarly, the protic-imidazolylidene complex (**Ru3**) and its classical analogue (**Ru4**) exhibited comparable characterization data. The distinguishing feature of **Ru3** was the presence of a signal for the *N*-H proton at δ 12.48 ppm, which was absent in **Ru4** due to the methylation of the nitrogen in the imidazole ring, which displayed a set of *N*-methyl protons at δ 2.83 ppm. In the $^{13}C\{^{1}H\}$ spectrum, the carbene carbon peaks were observed at δ 191.5 ppm for **Ru3** and δ 190.5 ppm for **Ru4**. HRMS $(ESI)^{+}$ analysis of **Ru3** revealed a $[M\text{-}2PF_6\text{-}H]^{+}$ peak at m/z 755.1968 (calculated for $C_{40}H_{34}N_{10}Ru$: 755.1938) and a $[M\text{-}2PF_6]^{2+}$ signal at m/z 378.1031 (calculated for $C_{40}H_{34}N_{10}Ru$: 378.1005). For **Ru4**, the $[M\text{-}2PF_6]^{2+}$ peak was detected at m/z 392.1191 (calculated for $C_{42}H_{38}N_{10}Ru$: 392.1162).

2.2.3 Molecular structures of Ru1-Ru4 complexes

Single crystals suitable for X-ray diffraction were obtained for all four homoleptic Ru(II)-bis(pincer) complexes. The obtained single-crystal X-ray diffraction data confirmed the presence of both enantiomers in the lattice (only one enantiomer is depicted in Figure 2.3). Complexes **Ru1**, **Ru3**, and **Ru4** crystallized in the monoclinic system, adopting the $P2_1/c$ space group, whereas complex **Ru2** crystallized in an orthorhombic crystal system with a non-centrosymmetric Fdd2 space group. The crystallographic parameters are listed in Tables 2.1 and 2.2.

All the complexes exhibited distorted octahedral geometries. Replacing the hydrogen on the β-NH group in **Ru1** and **Ru3** with a methyl group to form complexes **Ru2** and **Ru4** did not result in any structural rearrangements (Figure 2.3). The Ru1-$C1_{NHC}$ bond distance of 1.955(3) Å in complex **Ru1** is comparable to the bond distances previously reported by our group for similar ligand frameworks. [73,74] **Ru2**, which has a classical-NHC, has a comparatively longer Ru1-$C1_{NHC}$ bond distance of 1.977(5) Å. However, the difference between Ru1-$C1_{NHC}$ bond distances of the imidazolylidene-based protic-NHC complex **Ru3** (1.976(6) Å) and its classical analogue **Ru4** (1.986(4) Å) is less prominent. Similar variations are observed in the Ru1-N5 bond

distances across the complexes, with values of 2.152(3) Å, 2.130(5) Å, 2.130(5) Å, and 2.128(3) Å for **Ru1**, **Ru2**, **Ru3**, and **Ru4**, respectively.

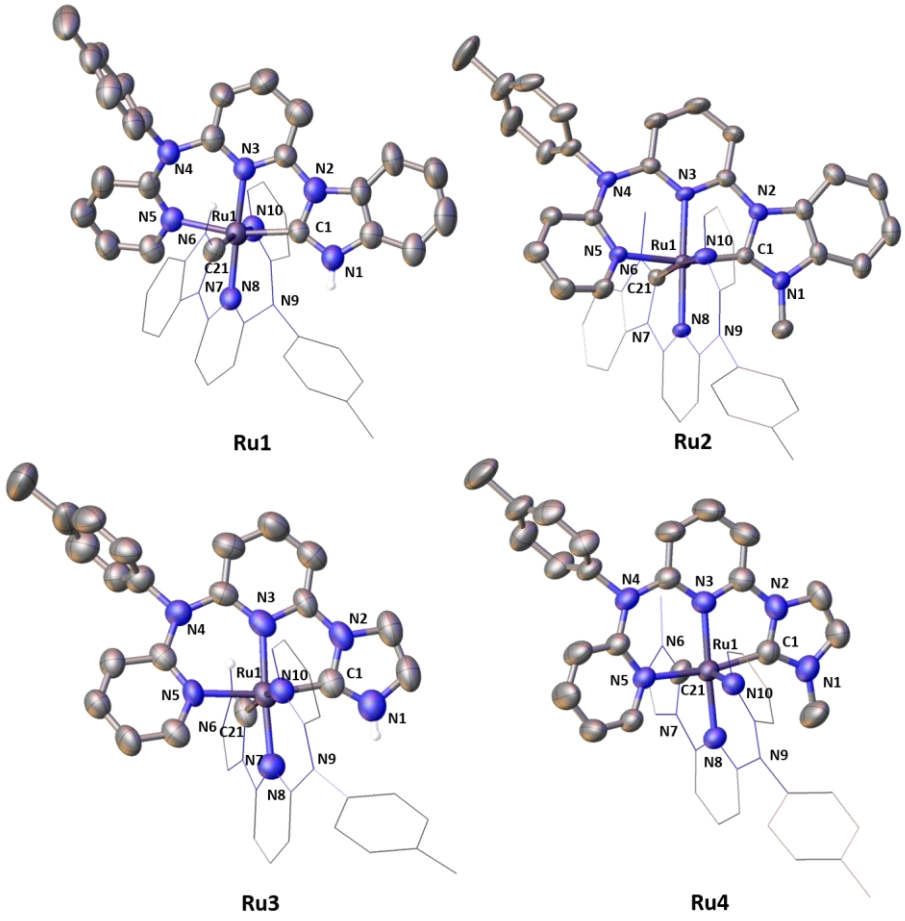

Figure 2.3 Molecular structures of **Ru1-Ru4** obtained from SCXRD. For each complex, one of the two identical pincer ligands is shown as a wireframe for clarity. All hydrogen atoms (except *N*-H) and two PF_6 counterions in each structure are omitted for clarity. Only one enantiomer of the dicationic complex is shown. Selected bond distances (Å) and angles (°): **Ru1**; Ru1-C1= 1.955(3), Ru1-C21 = 1.969(3), Ru1-N5= 2.152(3), Ru1-N3 = 2.039(3), Ru1-N8 = 2.042(3), C1-Ru1-N5 166.45(12); C2-Ru1-N10 166.33(12), N3-Ru1-N8 175.80(10). **Ru2**; Ru1-C1 = 1.977(5), Ru1-C21 = 1.987(5), Ru1-N5 = 2.130(5), Ru1-N3 = 2.048(5), Ru1-N8 = 2.057(5), C1-Ru1-N5 167.5(2); C21-Ru1-N10 169.4(2), N3 Ru1 N8 175.34(17). **Ru3**; Ru1-C1 = 1.976(6), Ru1-C21 = 1.980(5), Ru1-N5 = 2.130(5), Ru1-N3 = 2.046(5), Ru1-N8 = 2.048(5), Ru1-N10 = 2.132(5); C1-Ru1-N5 169.6(2), C21-Ru1-N10 167.7(2), N3-Ru1-N8 173.4(2). **Ru4**; Ru1-C1 = 1.986(4), Ru1-C21 = 1.979(4), Ru1-

N5 = 2.128(3), Ru1-N3 = 2.058(3), Ru1-N8 = 2.059(3), Ru1-N10 = 2.134(3); C1-Ru1-N5 168.81(15), C21-Ru1-N10 167.93(15), N3-Ru1-N8 174.23(12).

Table 2.1 Crystal data and structural refinement parameters for complexes **Ru1** and **Ru2**

	Ru1	**Ru2**
Empirical formula	$C_{50}H_{41}F_{12}N_{11}P_2Ru$	$C_{50}H_{42}F_{12}N_{10}P_2Ru$
Formula weight	1186.95	1173.94
Temperature/K	298.0	298.0
Crystal system	Monoclinic	Orthorhombic
Space group	$P2_1/c$	Fdd2
a/Å	11.9599(2)	43.0211(5)
b/Å	20.2681(3)	39.0729(5)
c/Å	21.1006(3))	12.23240(10)
α/°	90	90
β/°	98.1720(10)	90
γ/°	90	90
Volume/Å^3	98.1720(10)	20562.2(4)
Z	4	16
ρ_{calc}g/cm^3	1.557	1.517
μ/mm^{-1}	0.466	0.457
F(000)	2400.0	9504.0
Radiation	MoKα (λ = 0.71073)	Mo Kα (λ = 0.71073)
2Θ range for data collection/°	6.278 to 58.322	5.882 to 58.408
Reflections collected	68386	114746
Independent reflections	12238 [R_{int} = 0.0402, R_{sigma} = 0.0276]	13113 [R_{int} = 0.0672, R_{sigma} = 0.0372]
Data/restraints/parameters	12238/0/688	13113/1/680
Goodness-of-fit on F^2	1.074	1.047
Final R indexes [I>=2σ (I)]	R1 = 0.0558, wR2 = 0.1483	R1 = 0.0528, wR2 = 0.1464
Final R indexes [all data]	R1 = 0.0686, wR2 = 0.1609	R1 = 0.0638, wR2 = 0.1580

Table 2.2 Crystal data and structural refinement parameters for complexes **Ru3** and **Ru4**

	Ru3	**Ru4**
Empirical formula	$C_{80}H_{74}F_{24}N_{20}O_3P_4Ru_2$	$C_{44}H_{46}F_{12}N_{10}O_2P_2Ru$
Formula weight	2256.79	1137.92
Temperature/K	298.0	298.0
Crystal system	Monoclinic	Monoclinic
Space group	P2/c	$P2_1/c$
a/Å	27.8763(8)	19.0017(5)
b/Å	15.6815(5)	16.2654(3)

c/Å	24.6159(7)	18.3386(4)
α/°	90	90
β/°	115.772(4)	116.342(3)
γ/°	90	90
Volume/Å^3	9690.3(6)	5079.4(2)
Z	4	4
ρ_{calc}g/cm^3	1.547	1.488
μ/mm^{-1}	0.485	0.463
F(000)	4580.0	2312.0
Radiation	MoKα (λ = 0.71073)	MoKα (λ = 0.71073)
2Θ range for data collection/°	5.908 to 51.364	5.718 to 58.464
Reflections collected	111328	111596
Independent reflections	18359 [R_{int} = 0.0894, R_{sigma} = 0.0637]	13053 [R_{int} = 0.1130, R_{sigma} = 0.0711]
Data/restraints/parameters	18359/0/1211	13053/0/608
Goodness-of-fit on F^2	1.063	1.048
Final R indexes [I>=2σ (I)]	R1 = 0.0823, wR2 = 0.2241	R1 = 0.0635, wR2 = 0.1677
Final R indexes [all data]	R1 = 0.1298, wR2 = 0.2679	R1 = 0.1161, wR2 = 0.1985

2.2.4 Electrochemical analysis. To evaluate the electrochemical water oxidation reaction (WOR) capacity of complexes **Ru1**-**Ru4**, cyclic voltammetry (CV) experiments were conducted to examine the redox behavior of each complex. The experiments were performed using distilled, dried, and degassed acetonitrile under a nitrogen atmosphere. The complex **Ru1**, which features a protic benzimidazole group in its ligand, exhibited two distinct redox processes. A reversible redox event at 1.37 V vs. Ag/AgCl/3 M KCl corresponds to the oxidation of Ru(III) to Ru(IV), whereas a small and less prominent hump observed at 1.78 V represents the oxidation of Ru(IV) to Ru(V) (Figure 2.4). The redox event corresponding to the Ru(II)/Ru(III) couple at approximately 0.8 V was not prominently observed in the cyclic voltammograms; however, it was evident in the differential pulse voltammetry (DPV) measurements (Figure 2.5). The peak for Ru(II) to Ru(III) in the CV became clearly recognizable in the presence of water.

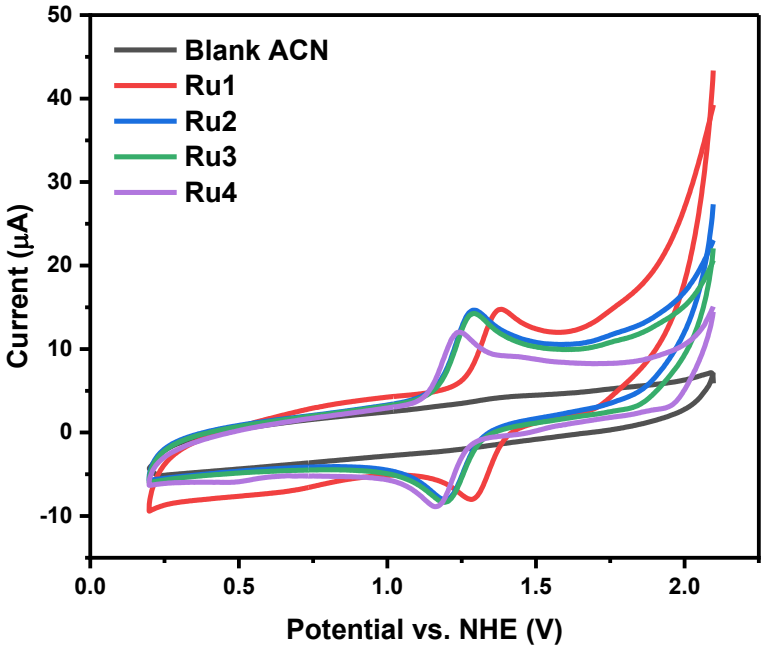

Figure 2.4 Cyclic Voltammograms of all complexes (**Ru1**-**Ru4**) (0.5 mM) in dry ACN using 0.1 M $TBAPF_6$ as the supporting electrolyte at room temperature. A glassy carbon (GC) electrode (diameter 3 mm) was used as the working electrode, a Pt wire as the counter electrode, and an Ag/AgCl/3 M KCl as the reference electrode at a scan rate of 50 mV/s.

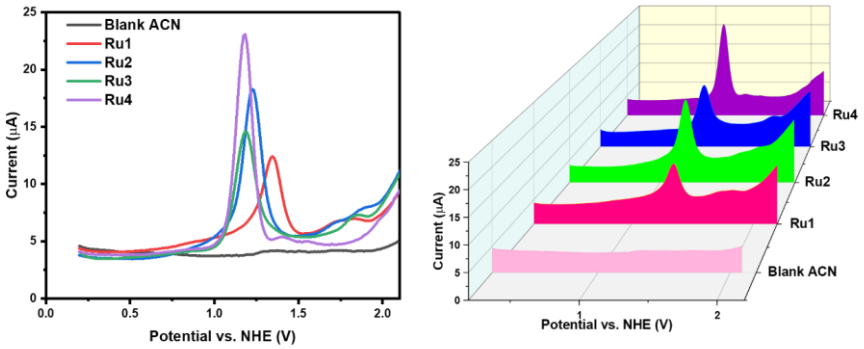

Figure 2.5 Differential Pulse voltammograms for all complexes (**Ru1**-**Ru4**)

For complex **Ru2**, with a classical NHC ligand, two redox processes were identified. Similar to **Ru1**, a reversible process was observed at 1.30 V, while an irreversible oxidation occurred at 1.77 V. The low oxidation potential of **Ru2** compared to that of **Ru1** clearly demonstrates

the behavior of the two attached ligands based on their electron-donating capabilities. The **L1** ligand in **Ru1** has a protic benzimidazolylidene unit, whereas the **L2** ligand of **Ru2** has a methylated benzimidazolylidene unit. The presence of a methyl group in **L2** increases the electron density on the ligand owing to the positive electron-donating effect of the methyl substituent, resulting in a lower oxidation potential than that of **Ru1**. Under similar conditions, complex **Ru3** displayed a reversible redox wave at 1.29 V and a second wave at approximately 1.70 V. However, the broadening of the oxidation and reduction waves makes it difficult to discern the reversibility of these events. **Ru3** has a lower oxidation potential than **Ru1,** which can be understood based on the donor strengths of the NHCs arising from different types of azole rings. The imidazolylidene unit is, in general, a better donor and a poorer π-acceptor than the bezimidazolylidene unit, exhibiting moderate donor and better π-acceptor abilities.[76] Complex **Ru4**, the classical NHC analog of complex **Ru3**, exhibited only one set of redox waves at 1.24 V during CV analysis and the lowest oxidation potential among all four complexes due to a combination of better electron donation properties of classical over protic-NHC as well as the imidazole over benzimidazole moiety.[76] All CV measurements for the complexes were recorded at scan rates ranging from 20 to 1000 mV/s, showing a linear relationship with the square root of the scan rate ($\nu^{1/2}$), confirming that the processes are diffusion-controlled under these conditions (Figure 2.6).

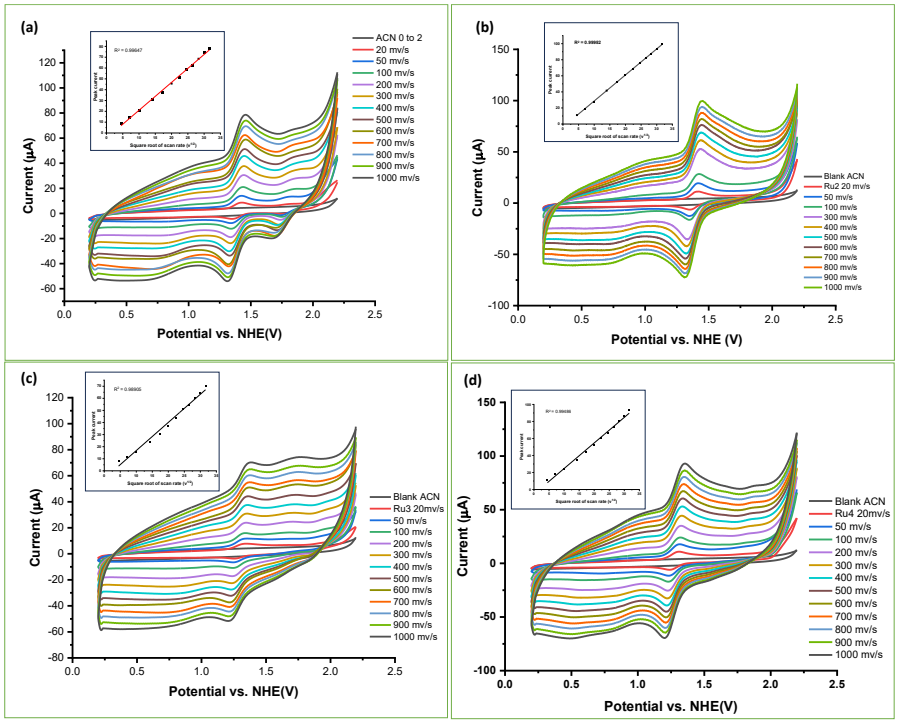

Figure 2.6 Cyclic Voltammogram of Complexes at different scan rates. Plots of the peak current and the square root of the number of scans (inset) for **(a)** Ru1, **(b)** Ru2, **(c)** Ru3, and **(d)** Ru4 in acetonitrile solution.

To precisely determine the peak positions in terms of voltage for all the complexes, differential pulse voltammetry (DPV) experiments were performed. For complex **Ru1,** the peaks observed at 0.8 V, 1.34 V, and 1.74 V confirmed the original voltages for the two oxidation processes. In the case of **Ru2**, the DPV experimental results confirmed the presence of three oxidation processes at 0.7 V (clearer after the addition of water) and 1.23 V, which were associated with redox transitions. Additionally, a peak at 1.80 V was observed in the DPV of **Ru2**, which could be due to Ru(V/IV), as acetonitrile solvent oxidation generally occurs at 2.5 V. For **Ru3**, the identification of two distinct voltages, 1.18 V and 1.82 V, is attributed to the Ru(IV/III) and Ru(V/IV) transitions, respectively. For **Ru4**, transitions were observed at 1.24 V, accompanied by a very small hump at approximately 1.7 V for the Ru(III) to Ru (IV) and Ru(IV) to Ru(V) transitions, respectively. In both **Ru3** and **Ru4**, the Ru(II) to Ru(III) transitions were observed after the addition of water.

2.2.5 Electrochemical experiments at low temperature: The cyclic voltammograms recorded at room temperature have generally shown two transitions. The observation of Ru(IV) to Ru(V) was not clear due to either the instability of the high-valent Ru(V) species or the fast oxidation of ACN at room temperature. To slow down these processes and determine the exact value for the Ru(IV)/Ru(V) redox couple, we performed electrochemical experiments at a low temperature, i.e., -30 °C. After analyzing the data, we found that for **Ru1**, the low temperature led to improved reversibility of the Ru(IV) to Ru(V) couple at approximately 1.8 V, possibly due to its greater reactivity, even at low temperatures (Figure 2.7).

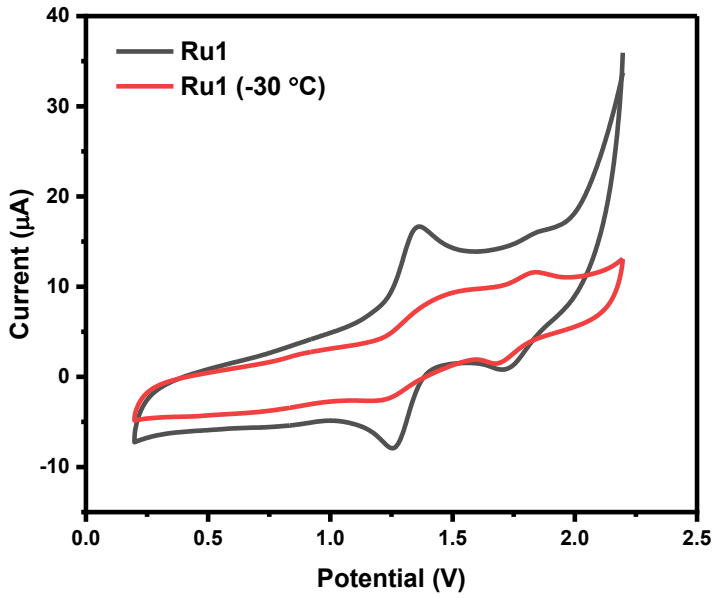

Figure 2.7 Cyclic Voltammogram of **Ru1** complex in dry ACN using 0.1 M $TBAPF_6$ as electrolyte at room temperature and at low temperature (-30 °C)

The cyclic voltammograms for all other complexes were also recorded at -30 °C. Among them, only in the case of **Ru3**, we can clearly observe the redox wave attributed to Ru(IV) to Ru(V), which was not visible in the initial electrochemical experiments at room temperature. Under these low-temperature conditions, the cyclic voltammogram of **Ru3** clearly showed three redox waves, at around 1.2 V, 1.6 V, and 1.75

V, featuring Ru(II)/Ru(III), Ru(III)/Ru(IV), and Ru(IV)/Ru(V) redox waves, respectively (Figure 2.8). The low-temperature experiments for the complexes **Ru2** and **Ru4** were not fruitful in detecting a prominent oxidation potential for the Ru(IV)/Ru(V) redox wave.

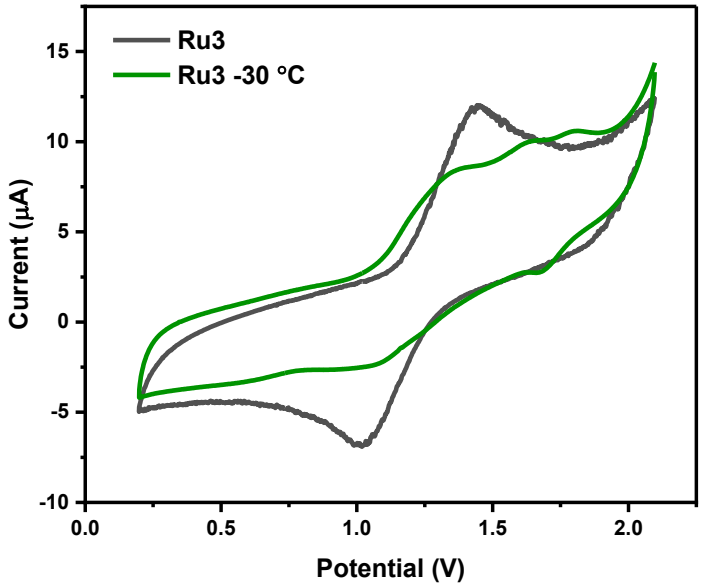

Figure 2.8 Cyclic Voltammogram of **Ru3** complex in dry ACN using 0.1 M $TBAPF_6$ as electrolyte at room temperature and at low temperature (-30 °C)

2.2.6 Water oxidation reaction (WOR). The electrochemical properties of all complexes (**Ru1**-**Ru4**) for the water oxidation reaction were investigated using a 0.5 mM catalyst. The potential measurements were conducted against an Ag/AgCl reference electrode and converted to the normal hydrogen electrode (NHE) potential using the equation E(NHE) = E(Ag/AgCl) + 0.199 V. Scans were performed in the range of 0 to 2 V at a constant scan rate of 50 mV/s. Due to the insolubility of the complexes in water, an acetonitrile solution of the catalyst has been used, with the addition of water for electrochemical water oxidation. Water was added incrementally in 20 μL portions to the electrochemical cell, containing 10 mL of a 0.5 mM catalyst solution in acetonitrile, to a total volume of 2000 μL. A distinct change in the electrochemical response was observed upon the addition of 200 μL of water, which was identified

as the optimal water concentration for subsequent studies. We used 200 µL of water for all studies. Further addition of water led to a progressive increase in the anodic peak current, accompanied by a shift in potential consistent with the onset of the water oxidation reaction (Figure 2.9). The appearance of gas bubbles at the electrode surface during these measurements provided visual confirmation of gas evolution.

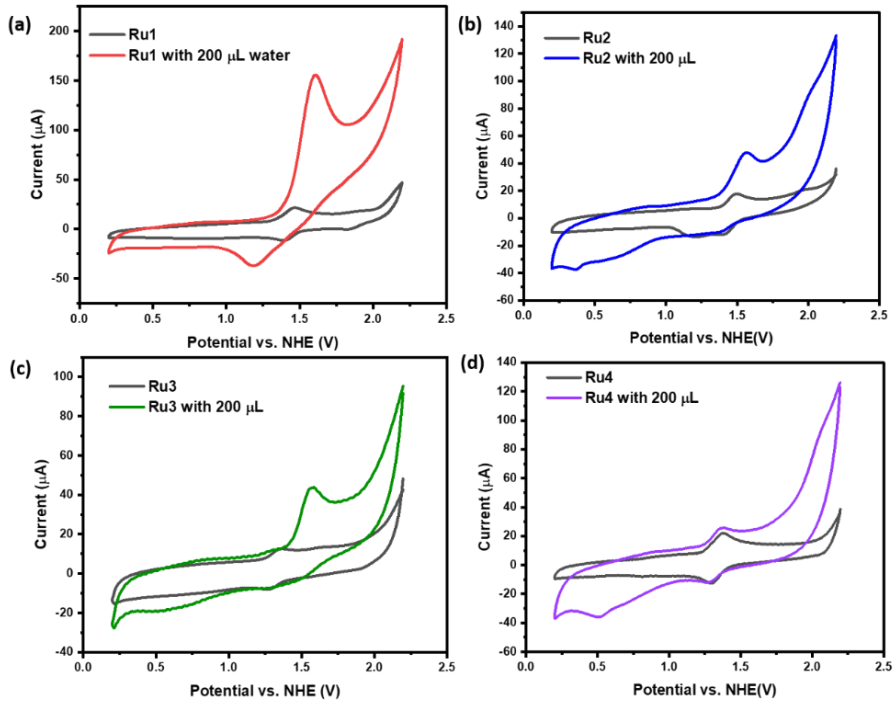

Figure 2.9. Cyclic Voltammograms of all the complexes (**Ru1**-**Ru4**) showing the electrochemical behavior before and after the addition of 200 µL of water

In the acetonitrile solution of **Ru1**, the successive addition of water led to a potential shift from 1.37 V to 1.60 V, accompanied by a more than sevenfold increase in current (from 21.4 µA to 155.4 µA), indicating electrocatalytic water oxidation.[21,77] Simultaneously, a new irreversible wave was observed at -0.45 V vs. NHE, corresponding to the $O_2/O_2^{\bullet-}$ couple, following scans through the catalytic anodic wave under an inert atmosphere (Figure 2.10).[32] Additionally, a prominent shift was noted in the DPV results, where a new wave appeared at 1.51 V, resulting in a reduction of the wave previously observed at 1.34 V. In addition, a wave for Ru(III/II) was observed at 0.8 V. Similarly, **Ru2** exhibited an

increase in current with the successive addition of water. Initially, the potential was 1.48 V, which shifted to 1.56 V, while the potential at 1.95 V shifted to 2.07 V, indicating a broad irreversible oxidation wave. The DPV showed a slight shift in potential from 1.43 V to 1.45 V and from 1.89 V to 1.91 V, with current increases of 30 µA and 74 µA, respectively. For **Ru3**, a notable potential shift was observed from 1.35 V to 1.56 V, along with an increase in the current from 12 µA to 43 µA and the appearance of a potential wave at Ru(II) to Ru(III). In contrast, **Ru4** exhibited a shift from 1.37 V to a lower potential of 1.35 V. Analyzing all the observed shifts and increase in current following water addition, we can conclude that **Ru1**, which contains a protic-benzimidazolylidene group, demonstrates more efficient electrochemical water oxidation compared to the other complexes.

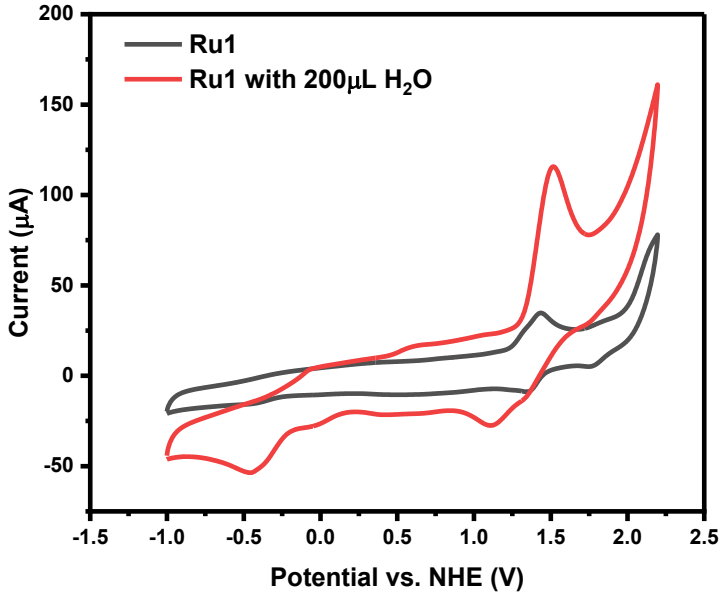

Figure 2.10 Cyclic Voltammogram of **Ru1** complex in dry ACN using 0.1 M $TBAPF_6$ as electrolyte at room temperature

Among all the complexes, the benzimidazolylidene-containing **Ru1** and **Ru2** complexes demonstrated superior performance compared to their imidazolylidene analogs, **Ru3** and **Ru4**. The enhanced catalytic activity of **Ru1** and **Ru2** compared to **Ru3** and **Ru4** could be due to the better π-acceptor ability of benzimidazolylidene-based ligands,[78]

facilitating the binding of the aqua ligand and further stabilizing the other intermediates (e.g., Ru=O) during the reaction.[79,80] Despite being coordinatively saturated complexes, all the bis(pincer) complexes **Ru1-Ru4** contain a potentially hemilabile pyridine [75] with a six-membered metallacycle, which can generate a vacant site for the binding of an aqua ligand. Moreover, both protic-NHC complexes, **Ru1** and **Ru3**, demonstrated slightly better performance than their classical counterparts, **Ru2** and **Ru4,** indicating the potential role of protic-NHCs in PCET. The NMR data showed that **Ru1** has a more acidic proton (δ 13.48) than **Ru3** (δ 12.48), which further supports the better reactivity of the benzimidazolylidene-based protic-NHC of **Ru1** due to its potential role in PCET than its imidazolylidene-based protic-NHC analogue (**Ru3**).

To further evaluate the catalytic performance and determine the kinetic parameters for each ruthenium-based complex (**Ru1-Ru4**), we performed a Foot-of-the-Wave Analysis (FOWA), a robust method that provides a means to extract the observed rate constant (K_{obs}) from the rising portion of the catalytic wave. This analysis is particularly effective for water oxidation and proton-coupled electron transfer (PCET) processes, where a clear catalytic plateau is not always attainable. By plotting the Tafel plot between the log of current density and overpotential, we observed a change in electron transfer for one redox process, specifically associated with the Ru(IV)/Ru(III) couple, near 1. In our case, the graph obtained with x =1, that is, for the WNA mechanism, showed greater linearity than the graph with x = 3/2. Therefore, we calculated the slope values by linear fitting of the graph plotted between i/i_p vs. $1/\{1 + e [(f(E-E°)]\}$, assuming the WNA mechanism. The obtained K_{obs} value for the same graph was 0.32 s^{-1} for **Ru1**. The K_{obs} values for **Ru2**, **Ru3**, and **Ru4** were 0.11, 0.023, and 0.06, respectively. Based on the established water nucleophilic attack (WNA) mechanism, and supported by the rigidity of the pincer ligand framework (which disfavors bimolecular I2M pathways), we propose that the catalytic cycle involves the sequential oxidation of Ru(II) to Ru(V),

forming a Ru(V)=O species as the probable active intermediate responsible for O-O bond formation and subsequent O_2 release.

2.2.7 FOWA analysis of Ru1-Ru4 for WNA mechanism. For a one-electron catalytic process, applying the Randles-Sevcik method to calculate the turnover frequency (TOF) can lead to overestimations and mask the true kinetic behavior of the system. To address these challenges, we utilized the foot of the wave technique, which provides a more accurate representation of the catalytic kinetics.

$$\frac{i}{i_p} = \frac{4\times22\cdot4\sqrt{\frac{RT}{Fv}k_{obs}}}{\left[1+e^{\frac{F(E_0-E)}{RT}}\right]^{a}} \quad \text{.....Eq.(1)}$$

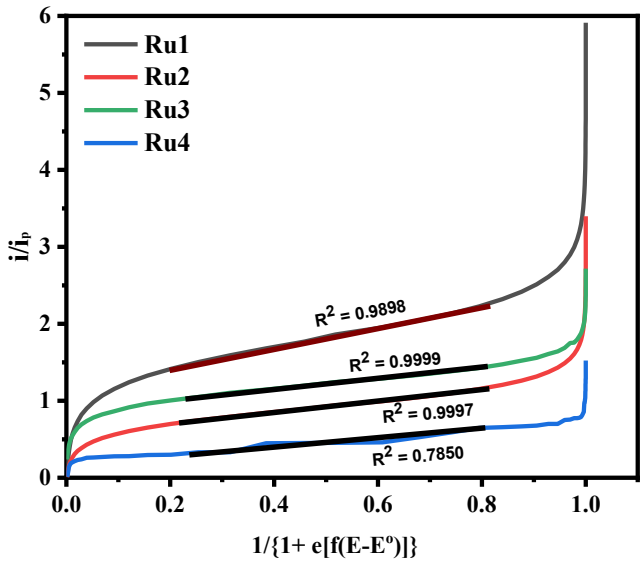

Figure 2.11 A plot of i/i_p vs. $1/\{1 + e [(f(E-E°)]\}$ where f = nF/RT, assuming WNA mechanism for the electrochemical water oxidation using all the complexes **Ru1**-**Ru4**. The black line in each curve indicates the data points used for the FOWA analysis.

As proposed earlier, for the WNA or I2M mechanistic pathway, the value of "x" in eq. (1) is 1 or 3/2, respectively. The rate (kobs) (or TOF) of the reaction was calculated from the slope of the linear plot obtained between

i/i_p and $\frac{1}{\left[1+e^{F(E_0-E_{cat})/RT}\right]}$[a]. This equation can be written in the form of a linear equation, y = mx, where x varies from 0 to 1. FOWA analysis of the electrochemical OER revealed that complex **Ru1** follows the Water Nucleophilic Attack (WNA) mechanism, as indicated by the slope value (Figure 2.11).

2.2.8 Chronoamperometry: To gain insight into the efficiency of all the catalysts, we performed chronoamperometry experiments over various periods. Initially, for **Ru1**, only 2 h of the experiment were set, which resulted in a graph showing a constant current (Figure 2.12). Subsequently, all complexes were subjected to 8-hour chronoamperometry experiments to calculate the charge derived/apparent TON and TOF values (Figure 2.13). Herein, with our complexes, the apparent TON and TOF are in sync with our experimental findings regarding the efficiency of different complexes. **Ru1** showed the highest TON value of 159264 and TOF of 5.53 s^{-1} (calculated for a peak potential of 1.56 V with an overpotential of 330 mV), while **Ru4** had the lowest values, 47774 and 1.65 s^{-1}, respectively. **Ru2** and **Ru3** have 62560, 2.17 s^{-1} and 49856, 1.65 $s^{-1,}$ respectively.

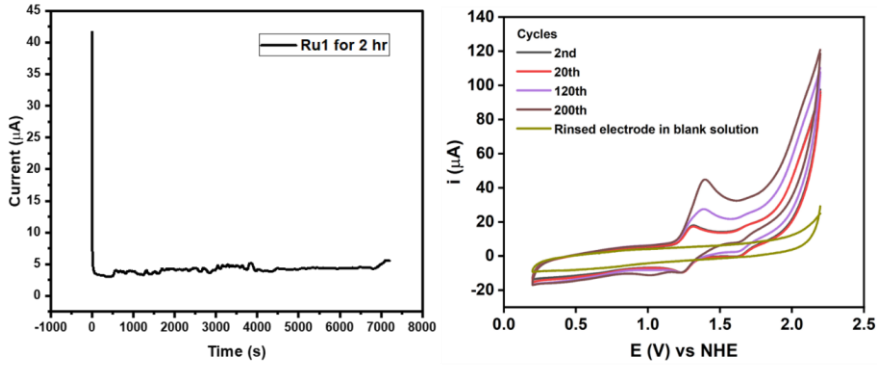

Figure 2.12 (**a**) A chronoamperometry experiment was conducted for 2 hours at 1.56 V vs. NHE using **Ru1** to evaluate the long-term stability of the catalyst for the oxygen evolution reaction (OER). (**b**) Cyclic voltammograms (CVs) recorded up to 200 cycles at a scan rate of 50 mV/s, showing further increase in current after the 100th cycle, likely due to the formation of more active species. Further investigation with a

rinsed electrode in a fresh blank solution showed no catalytic current, ruling out electrodeposition on the working electrode surface. This indicates that the current increase observed after the 100th cycle was due to the full activation of the catalyst.

To assess the TON, the first charge was calculated by integrating the area under the obtained curve or by integrating the current over time (as Q = I × t). Assuming that all the charge is utilized in water oxidation, as the ACN solvent does not oxidize at this potential, the total charge was converted to the number of moles of electrons transferred. It was then divided by the number of moles of the catalyst to obtain the final value of TON.

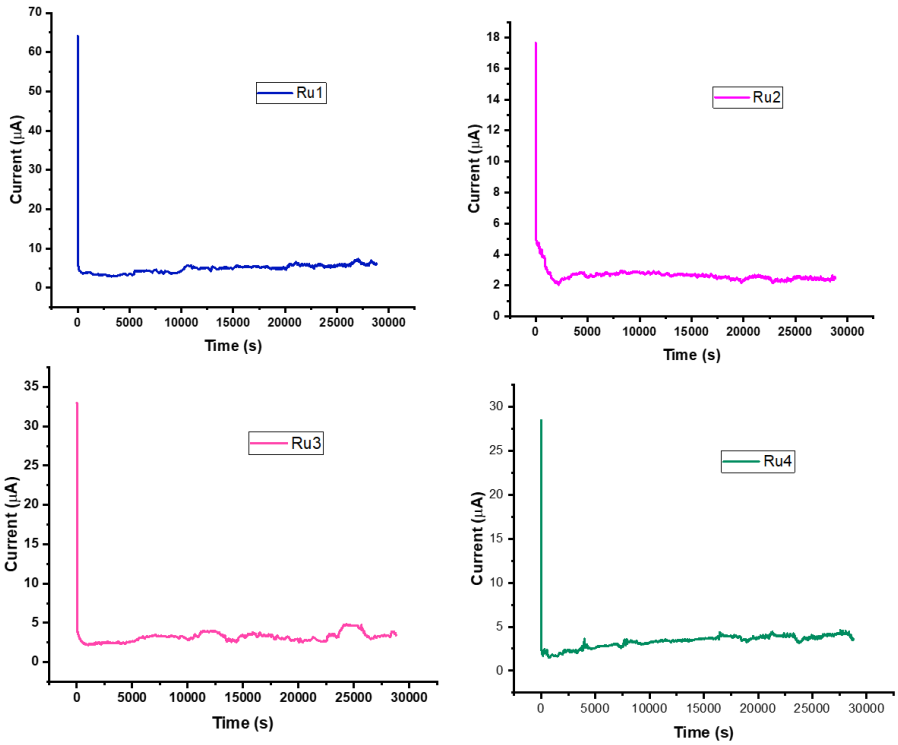

Figure 2.13 Chronoamperometry measurements of **Ru1-Ru4** for an 8 h period at a potential of 1.56 V vs. NHE

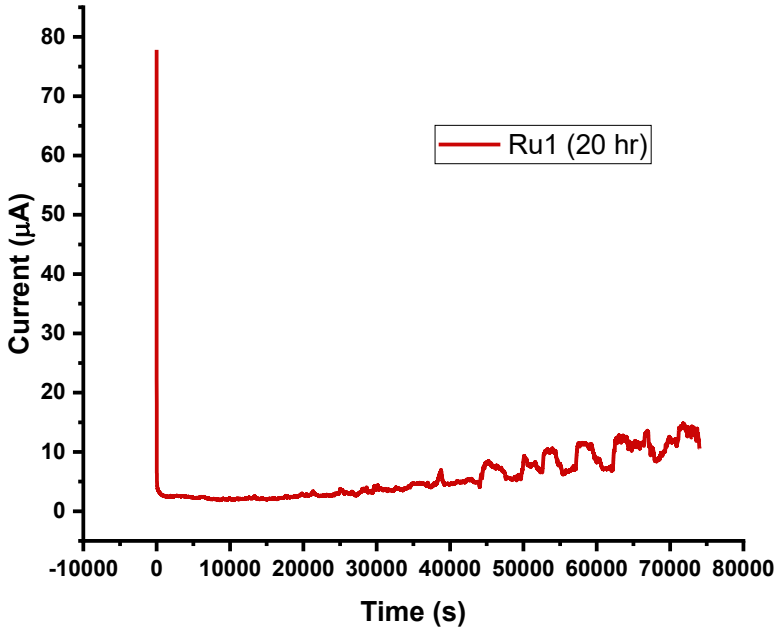

Figure 2.14 Chronoamperometry measurements of complex **Ru1** for a 20 h period

Ru1 on performing a chronoamperometry experiment at the onset potential, that is, 1.37 V, gave a TON of 62560 and TOF of 2.17 s^{-1}. Furthermore, a longer experiment at the peak potential of 1.56 V for 20 hours using the **Ru1** catalyst was conducted to assess its long-term stability and efficiency (Figure 2.14), yielding a TON value of 322,560 and a TOF of 4.48 s^{-1}. After 20 h of the chronoamperometry experiment, a slight increase in the current was observed. To confirm this observation, we performed cyclic voltammetry after 20 h of chronoamperometry and found a similar increase in current, which was due to the generation of active species during the process (Figure 2.15). Using **Ru1**, CVs were recorded for up to 200 cycles at a scan rate of 50 mV/s. The increase in current was suspected to be a consequence of the formation of more active species as the reaction progressed. To rule out nanoparticle formation or electrodeposition, further investigations were conducted using a rinsed electrode in a fresh blank solution. No catalytic current was observed with the rinsed electrode, eliminating the possibility of electrodeposition onto the surface of the working electrode.

To further ensure the absence of any nanoparticle generation in the system, we performed Dynamic Light Scattering (DLS) for **Ru1** and **Ru2,** taking them as representatives of each series of protic and classical NHC complexes. No variation was observed either before or after the addition of 200 µL of water, indicating the absence of any particles in the solution.

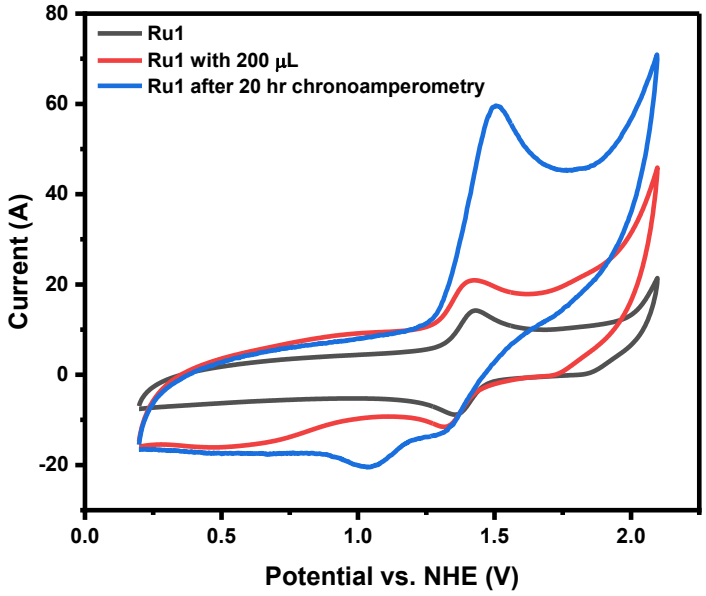

Figure 2.15 Cyclic Voltammograms showcasing the catalyst behavior before and after the 20 h chronoamperometry

2.2.9 pH-dependent electrochemical analysis. The **Ru1** catalyst was evaluated for water oxidation in a mixed H_2O/CH_3CN solvent system by adjusting the pH using aqueous acid, base, or citric acid and NaH_2PO_4 buffer. The highest catalytic current was observed in 1 M HCl. This enhanced activity can be attributed to two main factors: (1) acidic conditions provide a high concentration of protons, which facilitates fast proton-coupled electron transfer (PCET), a key step in water oxidation;[81] (2) the Ru center more readily reaches higher oxidation states at low pH, which is essential for O-O bond formation in the catalytic cycle.[82] When buffer solutions with a pH between 2.6 and 8 were used, the current decreased, likely due to reduced proton availability, which slows down the PCET process. In CH_3CN, even small

decreases in proton concentration can significantly impact catalytic efficiency.[83] The lowest current was recorded in 1 M NaOH, where the formation of high-valent Ru intermediates is thermodynamically less favorable, making the O-O bond formation step the rate-limiting stage.[84] Although CH_3CN is an aprotic solvent, the addition of water (via buffer or acid) allows limited proton mobility. This mixed solvent system is known to support molecular catalysis while providing a broad electrochemical window.[80] Overall, these results demonstrate that pH has a strong influence on the catalytic performance of **Ru1**, even in a H_2O/CH_3CN medium (Figure 2.16).

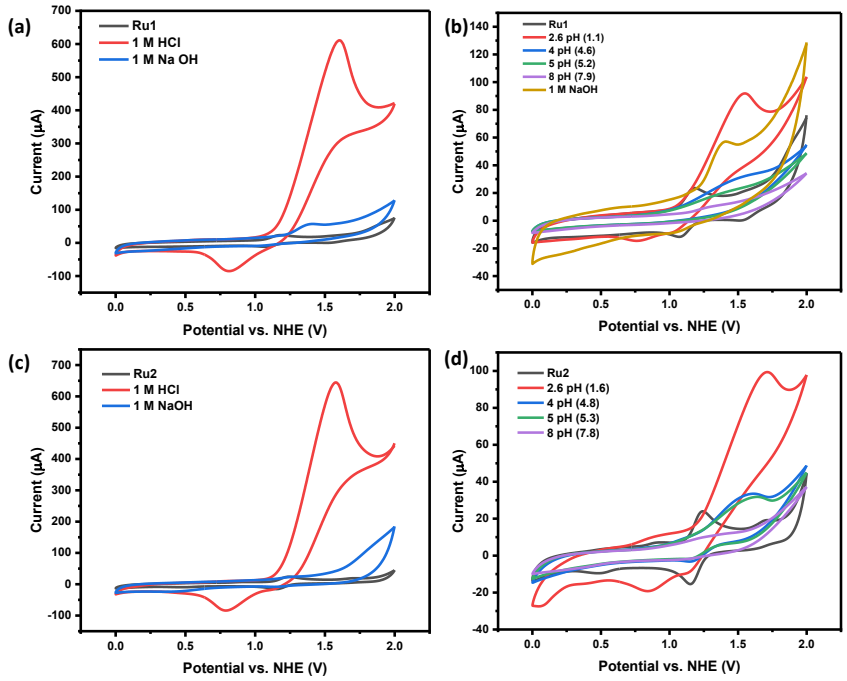

Figure 2.16 Cyclic voltammograms of **Ru1** and **Ru2** in H_2O/CH_3CN with added aqueous acid (1M HCl), basic (1M NaOH), and buffer solutions (Citric acid + NaH_2PO_4), showing pH-dependent OER activity.

2.3 Conclusion

In summary, a series of homoleptic ruthenium(II) bis(pincer) complexes (**Ru1**-**Ru4**) was synthesized and thoroughly characterized using NMR spectroscopy, mass spectrometry, and single-crystal X-ray diffraction. These complexes exhibited catalytic activity towards electrochemical

water oxidation under homogeneous conditions, proceeding via the water nucleophilic attack (WNA) mechanism. Notably, protic-NHC complexes bearing a β-NH substituent on the CPAP ligand framework demonstrated superior catalytic performance compared to their *N*-methylated analogues, underscoring the critical role of the *N*-H functionality in facilitating proton-coupled electron transfer (PCET) processes. To gain further mechanistic insights, low-temperature electrochemical studies (at -30 °C) were conducted, enabling the observation of the Ru(IV)/Ru(V) redox transformation, a key step in the catalytic cycle. Among the complexes investigated, **Ru1**, featuring a benzimidazolylidene-based protic-NHC ligand, emerged as the most efficient catalyst for electrochemical water oxidation. Chronoamperometric measurements confirmed the long-term stability and sustained catalytic activity of **Ru1** over a 20 h period. Furthermore, the catalyst has exhibited enhanced performance under acidic conditions relative to basic media, highlighting the influence of proton availability on catalytic efficiency. This set of complexes offers insights into the applicability of protic NHC ligands in electrochemical water oxidation for the first time. Further investigations to understand the mechanistic details of these processes are currently underway.

2.4 Experimental Section

2.4.1 General Experimental Information

All synthesis experiments for preparing ligands and complexes were conducted under a nitrogen atmosphere using standard Schlenk line techniques. Solvents were purified following established protocols under nitrogen and stored over 4 Å molecular sieves within an N_2 glove box. Reagents were purchased from commercial suppliers and used without additional purification, although many chemicals were purified according to standard methods. The metal precursor $RuCl_3 \cdot 3H_2O$ was obtained commercially and used without further purification. NMR spectra were recorded at room temperature and pressure using a Bruker Avance 400 MHz spectrometer (400 MHz for ^{1}H, 100 MHz for ^{13}C, and 162 MHz for ^{31}P) and a 500 MHz spectrometer (500 MHz for ^{1}H, 125

MHz for ^{13}C, and 202 MHz for ^{31}P). Deuterated solvents, including dimethyl sulfoxide and chloroform, were employed for NMR analysis, with chemical shift values (δ) reported in parts per million relative to the residual solvent signals. The resonance peaks for ^{1}H in $CDCl_3$ are at δ 7.26 and in DMSO-d_6 at δ 2.50 ppm; for ^{13}C, $CDCl_3$ appears at δ 77.0 and DMSO-d_6 at δ 40.45 ppm. High-resolution mass spectrometry (HRMS) was performed using a Bruker micrOTOF-QII mass spectrometer. X-ray diffraction studies were performed using a dual-core Agilent Technology (Oxford Diffraction) Super Nova CCD system.

2.4.2 Synthesis of complex Ru1. Ligand **L1** (57.66 mg, 0.1529 mmol) and $RuCl_3 \cdot 3H_2O$ (20 mg, 0.0764 mmol) were added to an oven-dried Schlenk tube charged with a magnetic stir bar. Ethylene glycol was then added as a solvent, and the Schlenk tube was immersed in a preheated oil bath. The reaction was carried out overnight (i.e., for 18 h). After the completion of the reaction, an aqueous solution of KPF_6 was added to the reaction mixture, and a yellow precipitate was formed, which was further washed with water and then with ether. After drying the yellow powder (87 mg, 0.046 mmol, 61% yield), spectroscopic characterizations were performed. ESI-MS calculated for $C_{48}H_{38}N_{10}Ru$, $[M]^{2+}$=428.1163, obtained = 428.1192; $[M\text{-}H]^{+}$ = 855.2253, obtained = 855.2291. **^{1}H NMR** (500 MHz, DMSO-d_6, 25 °C) δ 13.28 (s, 2H), 8.38 (t, *J* = 7.6 Hz, 4H), 8.24 (t, *J* = 8.4 Hz, 2H), 7.64 (s, 4H), 7.59 (d, *J* = 8.0 Hz, 2H), 7.47 (d, *J* = 6.1 Hz, 2H), 7.39 (d, *J* = 9.5 Hz, 4H), 7.12 (d, *J* = 8.7 Hz, 4H), 6.81 (t, *J* = 6.6 Hz, 4H), 6.67 (d, *J* = 8.9 Hz, 4H), 2.51 (s, 6H). **^{13}C{^{1}H} NMR** (126 MHz, DMSO-d_6, 25 °C) δ 203.6, 154.1, 152.3, 148.1, 140.0, 139.7, 139.1, 138.7, 131.8, 130.6, 124.7, 123.5, 118.9, 117.1, 114.7, 111.8, 106.5, 20.8. **^{31}P{^{1}H} NMR** (202 MHz, DMSO-d_6, 25 °C) δ 144.1

2.4.3 Synthesis of complex Ru2. In an oven-dried Schlenk tube charged with a magnetic stir bar, ligand **L2·HI** (79.38 mg, 0.1529 mmol) and $RuCl_3 \cdot 3H_2O$ (20 mg, 0.0764 mmol) were added after ethylene glycol was added as a solvent, and the Schlenk tube was dipped in a preheated oil bath. This reaction was carried out overnight (i.e., 18h). After the completion of the reaction, an aqueous solution of KPF_6 was added to

the reaction mixture, and a yellow precipitate (62 mg, 0.052 mmol, 69% yield) was crushed out, which was further washed with water and then ether. After drying the yellow powder, spectroscopic characterizations were performed. ESI-MS calculated for $C_{50}H_{42}N_{10}Ru$, $[M]^{2+}$= 442.1320, obtained = 442.1349. **^{1}H NMR** (500 MHz, DMSO) δ 8.51 – 8.40 (m, 4H), 8.26 (t, *J* = 8.5 Hz, 2H), 7.59 (d, *J* = 8.2 Hz, 8H), 7.53 – 7.45 (m, 6H), 7.02 (d, *J* = 8.7 Hz, 2H), 6.89 (t, *J* = 6.6 Hz, 4H), 6.52 (d, *J* = 8.9 Hz, 4H), 3.05 (s, 6H), 2.48 (s, 6H). **^{13}C{^{1}H} NMR** (126 MHz, DMSO) δ 203.5, 154.5, 154.3, 153.3, 148.9, 140.3, 139.5, 136.9, 132.8, 131.3, 130.4, 125.0, 124.5, 119.5, 118.0, 114.7, 112.7, 111.5, 107.6, 67.5, 55.4, 32.2, 25.6, 21.3.

2.4.4 Synthesis of 6-(1*H*-imidazol-1-yl)-*N*-(pyridin-2-yl)-*N*-(*p*-tolyl)pyridin-2-amine (L3) (Scheme 2.2). To an oven-dried two-neck round-bottom flask connected to a condenser and equipped with a magnetic stirrer bar, 2-bromo-6-(1*H*-imidazole-1-yl)pyridine (a) (2.24 g, 10 mmol) and *N*-(p-tolyl)pyridin-2-amine (b) (2.39 g, 13 mmol) were added. Along with this, $Pd(dba)_2$ (0.23 g, 0.4 mmol), dppf (0.221 g, 0.4 mmol), and NaO^tBu (1.15 g,12 mmol) were added under a nitrogen atmosphere. DMSO (20 ml) was used as the solvent, and the mixture was heated for 18h at 90 °C. After completion of the reaction, the reaction mixture was extracted using a brine solution and DCM. The organic layer contained the desired product; therefore, the aqueous layer was discarded. The organic layer was evaporated to obtain a white powder and purified by Column Chromatography. The obtained product (1.57 g, 48 %) was characterized using LC-MS, HRMS, and NMR spectroscopy. **^{1}H NMR** (500 MHz, $CDCl_3$, 25 °C) δ 8.36 (d, *J* = 7.0 Hz, 1H), 8.07 (s, 1H), 7.63 – 7.56 (m, 1H), 7.39 (s, 1H), 7.26 (s, 1H), 7.22 (d, *J* = 8.4 Hz, 3H), 7.15 (s, 1H), 7.13 (d, *J* = 2.7 Hz, 2H), 7.11 (s, 1H), 7.08 (s, 1H), 7.02 – 6.96 (m, 1H), 6.85 (t, *J* = 8.2 Hz, 1H), 2.38 (s, 3H).**^{13}C{^{1}H} NMR** (126 MHz, $CDCl_3$, 25 °C) δ 157.5, 157.2, 148.5, 147.3, 141.5, 140.0, 137.6, 136.4, 135.1, 130.6, 130.4, 128.0, 119.1, 118.4, 116.0, 112.1, 103.9, 21.2.

2.4.5 Synthesis of 3-methyl-1-(6-(pyridin-2-yl(*p*-tolyl)amino)pyridin-2-yl)-1*H*-imidazol-3-ium (Scheme 2.3). L3 (1 g, 3.05 mmol) was taken in a pressure tube and dissolved in toluene. After obtaining a homogeneous solution of the ligand, methyl iodide (190 µL, 3.05 mmol) was added to the solution. This solution was heated at 110 °C for 24 h to obtain a yellow powder, which was crushed out of the toluene solution. This powder was filtered and washed with toluene (3x) followed by ether (3x). The obtained yellow powder (0.93 g, 1.98 mmol, 65% yield) was confirmed to be the desired product by LC-MS and NMR spectroscopy. **^{1}H NMR** (500 MHz, $CDCl_3$, 25 °C) δ 10.87 (s, 1H), 8.47 (d, *J* = 5.2 Hz, 1H), 7.85 (t, *J* = 8.0 Hz, 1H), 7.80 (s, 1H), 7.76 (d, *J* = 9.8 Hz, 1H), 7.54 (s, 1H), 7.21 (d, *J* = 8.2 Hz, 3H), 7.18 (s, 1H), 7.15 (t, *J* = 8.7 Hz, 3H), 4.32 (s, 4H), 2.48 (s, 5H).**^{13}C{^{1}H} NMR** (126 MHz, $CDCl_3$, 25 °C) δ 157.2, 157.1, 148.7, 137.0, 134.9, 130.8, 127.9, 126.8, 123.7, 119.9, 118.8, 115.1, 106.1, 37.7, 21.3.

2.4.6 Synthesis of complex Ru3. In an oven-dried Schlenk tube charged with a magnetic stir bar, ligand **L3** (50.01 mg, 0.1529 mmol) and $RuCl_3 \cdot 3H_2O$ (20 mg, 0.0764 mmol) were added, followed by ethylene glycol as a solvent, and the Schlenk tube was dipped in a pre-heated oil bath. The reaction was carried out overnight (i.e., for 18 h). After the completion of the reaction, an aqueous solution of KPF_6 was added to the reaction mixture, and a yellow precipitate was crushed, washed with water, and then with ether. After drying the yellow powder (50.4 mg, 0.048 mmol, 63% yield), spectroscopic characterizations were performed. ESI-MS calculated for $C_{40}H_{34}N_{10}Ru$, $[M]^{2+}$=378.1005, obtained =378.1031. **^{1}H NMR** (500 MHz, DMSO-d_6, 25 °C) δ 12.48 (s, 2H), 8.40 (s, 2H), 8.07 (t, *J* = 8.3 Hz, 2H), 7.96 (d, *J* = 7.9 Hz, 4H), 7.62 (d, *J* = 8.2 Hz, 4H), 7.58 (d, *J* = 8.2 Hz, 6H), 7.55 (s, 2H), 7.41 (d, *J* = 6.0 Hz, 4H), 7.38 (s, 2H), 2.50 (s, 6H). **^{13}C{^{1}H} NMR** (126 MHz, DMSO-d_6, 25 °C) δ 191.5, 153.9, 151.9, 148.4, 140.0, 137.7, 131.9, 130.5, 120.8, 118.5, 117.0, 116.5, 114.1, 105.3, 20.9.

2.4.7 Synthesis of complex Ru4. In an oven-dried Schlenk tube charged with a magnetic stir bar, ligand **L4·HI** (71.28 mg, 0.1529 mmol) and

$RuCl_3 \cdot 3H_2O$ (20 mg, 0.0764 mmol) were added after ethylene glycol was added as a solvent, and the Schlenk tube was dipped in a preheated oil bath. This reaction was carried out overnight (i.e., 18h). After the completion of the reaction, an aqueous solution of KPF_6 was added to the reaction mixture, and a yellow precipitate was crushed, washed with water, and then with ether. After drying the yellow powder (56 mg, 0.052 mmol, 68% yield), spectroscopic characterizations were performed. ESI-MS- calculated for $C_{40}H_{34}N_{10}Ru$, $[M]^{2+}$=392.1162, obtained =392.1191. **^{1}H NMR** (500 MHz, DMSO-d_6, 25 °C) δ 8.44 (d, *J* = 2.3 Hz, 1H), 8.09 (t, *J* = 8.4 Hz, 1H), 8.00 (d, *J* = 8.0 Hz, 1H), 7.57 (d, *J* = 8.4 Hz, 2H), 7.54 (ddd, *J* = 9.0, 7.1, 1.9 Hz, 1H), 7.47 (d, *J* = 8.2 Hz, 1H), 7.40 (dd, *J* = 5.9, 2.1 Hz, 1H), 7.35 (d, *J* = 2.3 Hz, 1H), 6.81 (t, *J* = 6.5 Hz, 1H), 6.75 (d, *J* = 8.8 Hz, 1H), 6.42 (d, *J* = 8.4 Hz, 1H), 2.83 (s, 3H), 2.46 (s, 3H).**^{13}C{^{1}H} NMR** (126 MHz, DMSO-d_6, 25 °C) δ 190.5, 153.6, 152.2, 148.5, 139.9, 139.9, 138.8, 138.4, 132.5, 130.0, 118.8, 117.5, 117.2, 113.7, 105.8, 34.7, 20.8.

2.4.8 X-ray crystallography

Single crystals of complexes **Ru1**, **Ru2**, **Ru3**, and **Ru4**, suitable for X-ray crystallographic analysis, were obtained by layering the corresponding solutions in acetonitrile with diethyl ether (1:3, v/v) at -4°C. X-ray diffraction studies were conducted using an Agilent dual-core SuperNova CCD system (Oxford Diffraction) with monochromated Mo-Kα radiation (λ = 0.71073 Å). Unit cell determination, data collection, reduction, and empirical absorption corrections were processed with the CrysAlisPro65 software. The graphical interface Olex 2-1.5 was used for structural visualization.[85] The structures were solved using direct methods via SHELXT,[86] revealing all non-disordered, non-hydrogen atoms, which were refined anisotropically. The structural model was refined by full-matrix least-squares minimization on F^2, utilizing ShelXL [87] within the Olex2 graphical interface. Hydrogen atoms were placed in fixed positions during the final stages of refinement. The crystallographic data corresponding to Cambridge Crystallographic Data Centre (CCDC) entries 2416267-2416270 (for **Ru2**, **Ru4**, **Ru3**, and **Ru1**,

respectively) are available free of charge through the joint CCDC/Fachinformationszentrum Karlsruhe Access Structures service. These data can also be requested by emailing deposit@ccdc.cam.ac.uk.

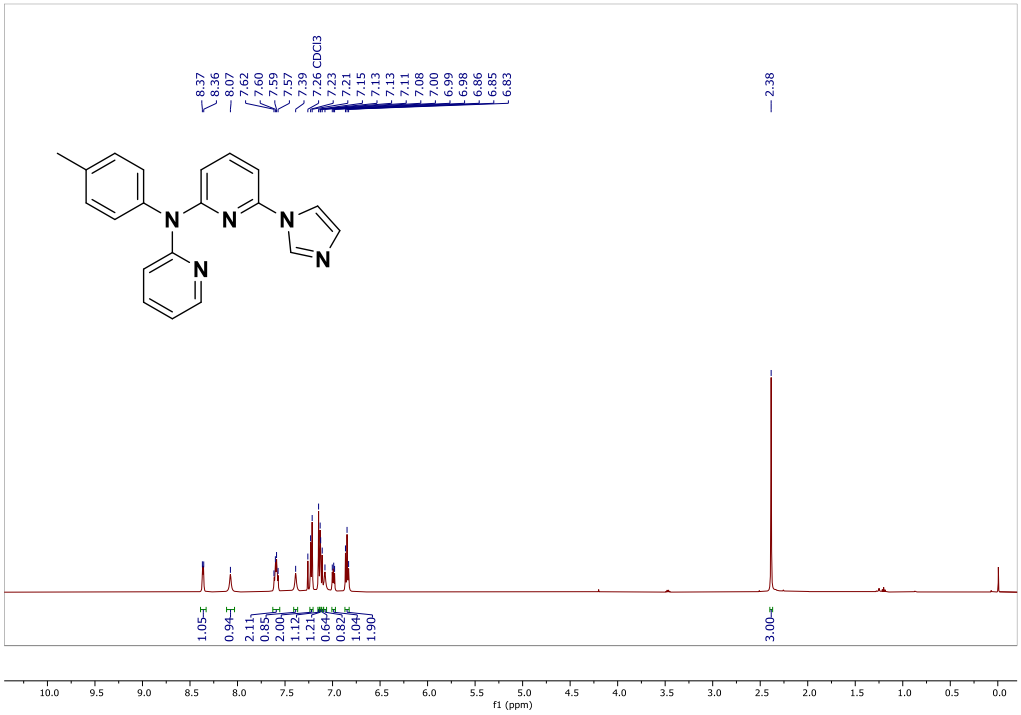

Figure 2.17 ^{1}H NMR of ligand **L3**

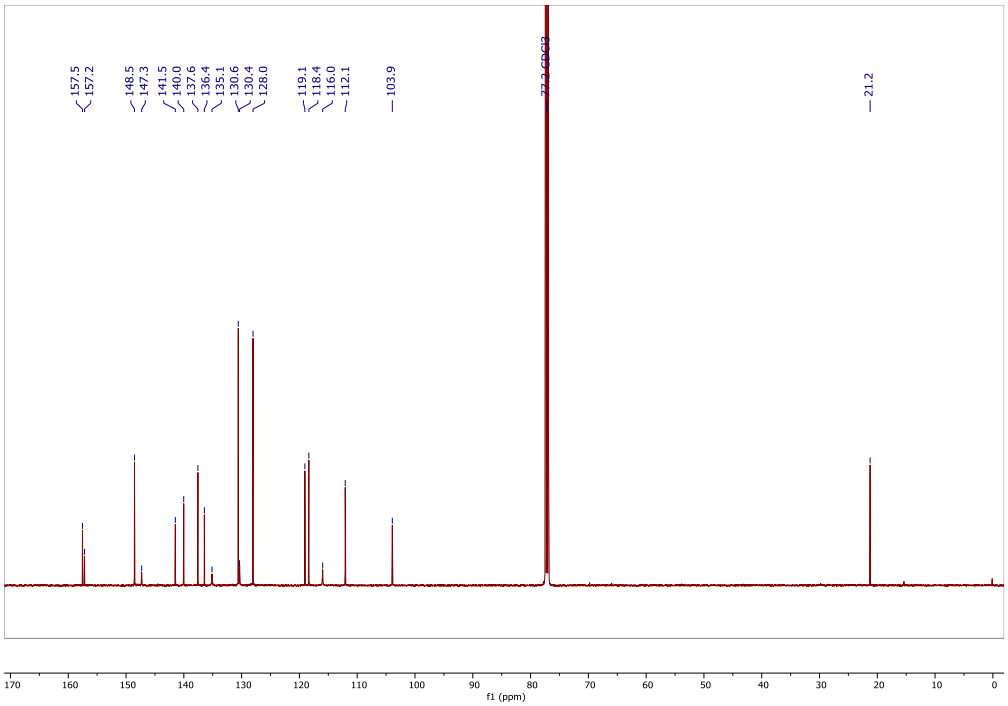

Figure 2.18 ^{13}C{^{1}H} NMR of ligand **L3**

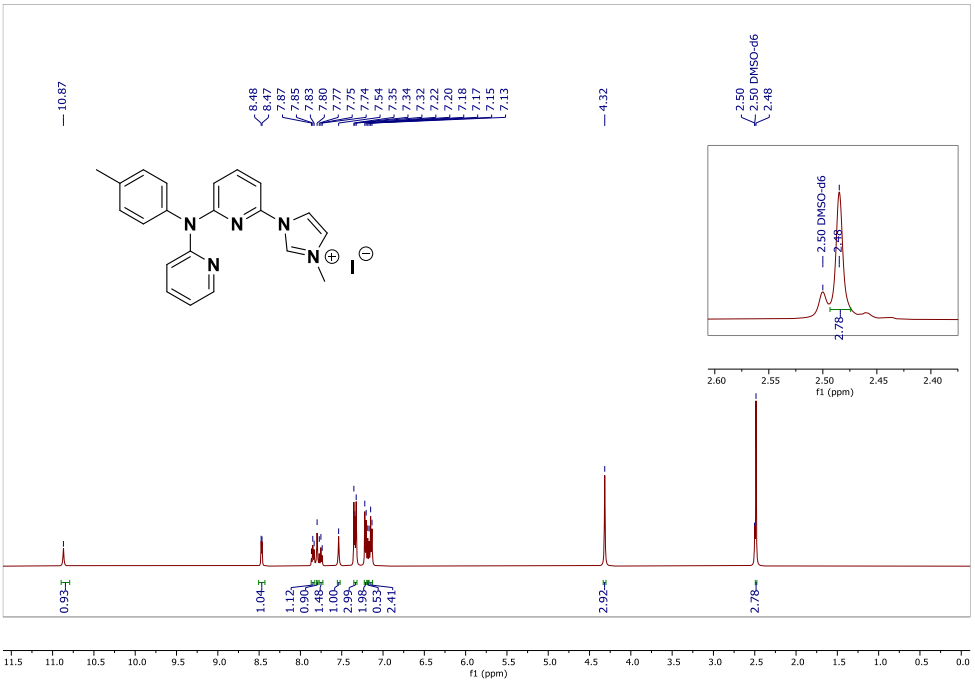

Figure 2.19 ^{1}H NMR of **L4·HI**

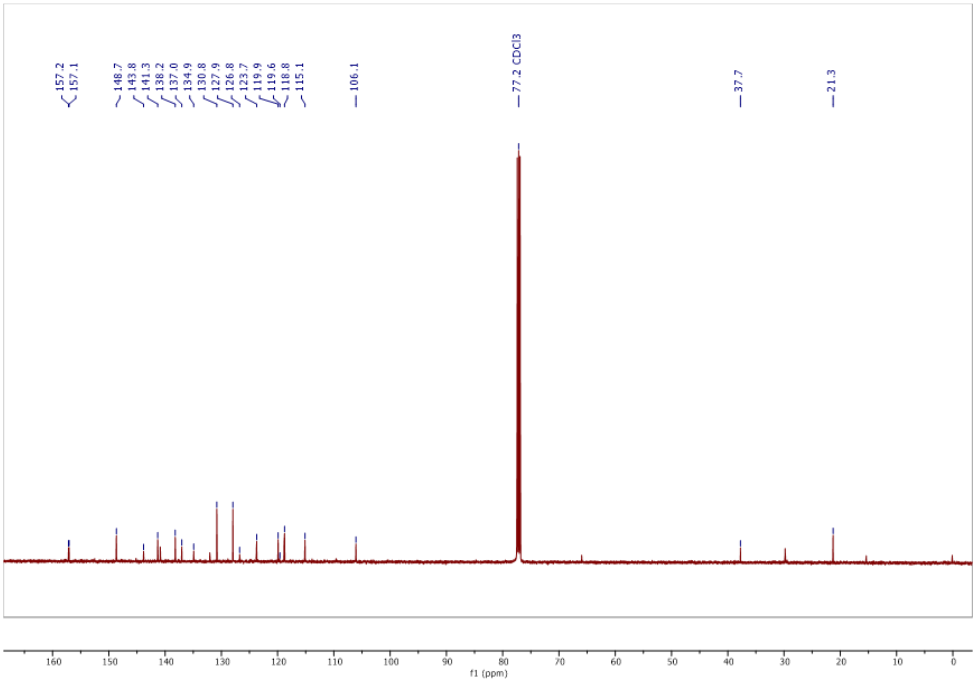

Figure 2.20 ^{13}C{^{1}H} NMR of **L4·HI**

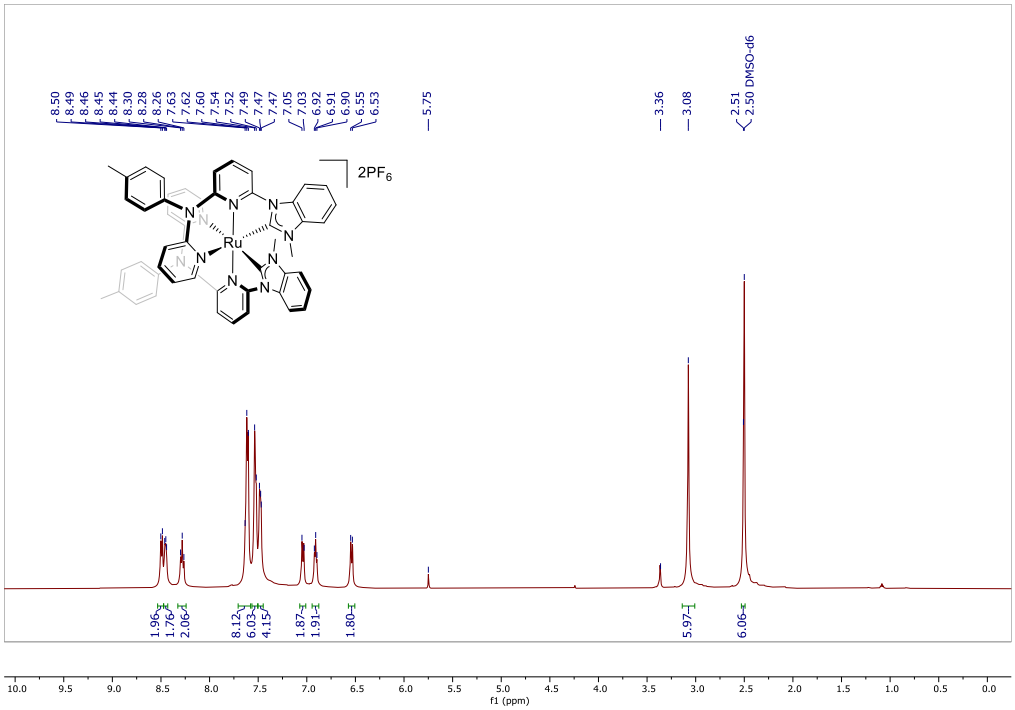

Figure 2.21 ^{1}H NMR of **Ru2**

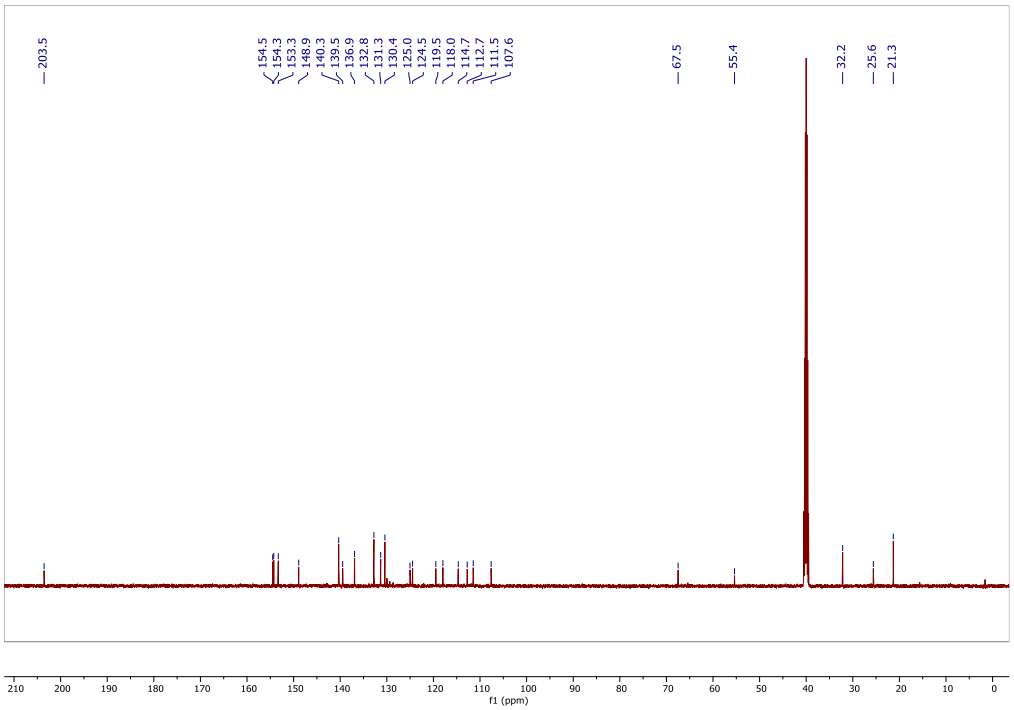

Figure 2.22 ^{13}C{^{1}H} NMR of **Ru2**

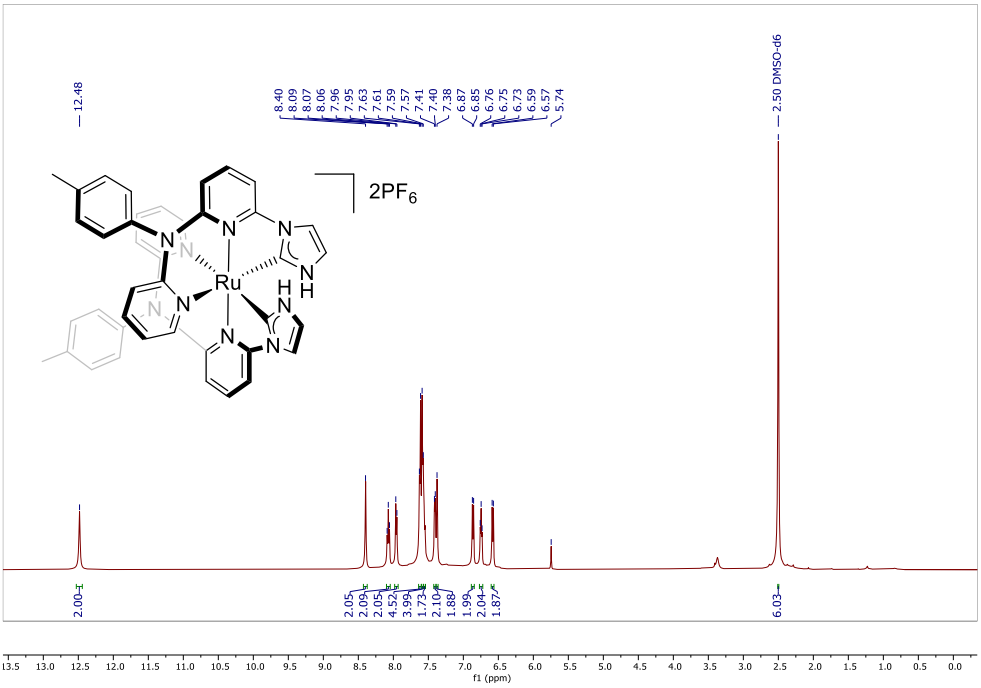

Figure 2.23 ^{1}H NMR of **Ru3**

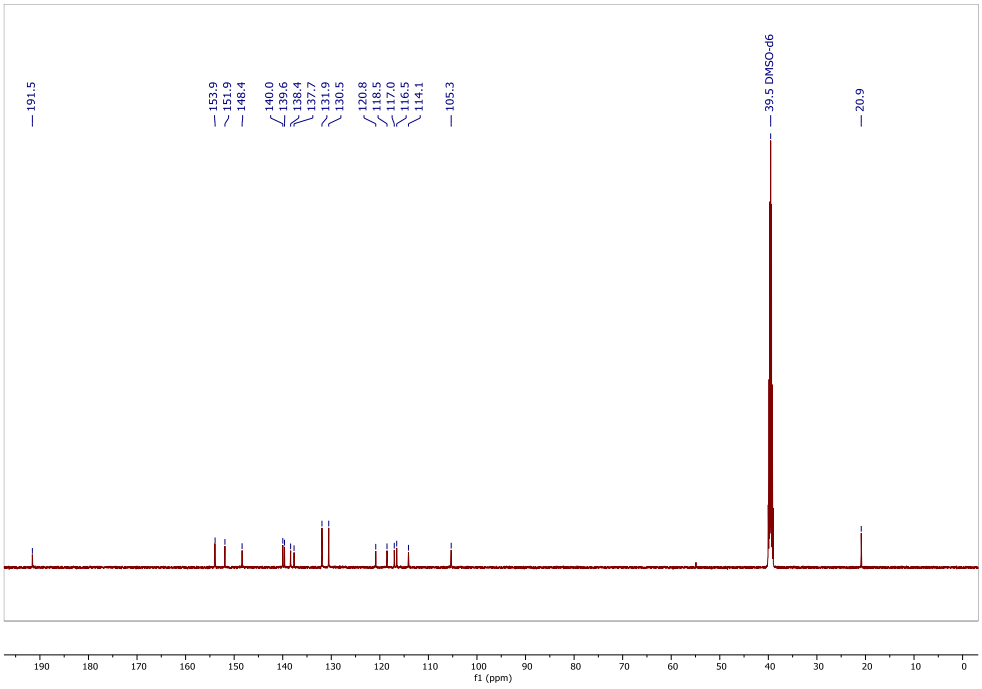

Figure 2.24 ^{13}C{^{1}H} NMR of **Ru3**

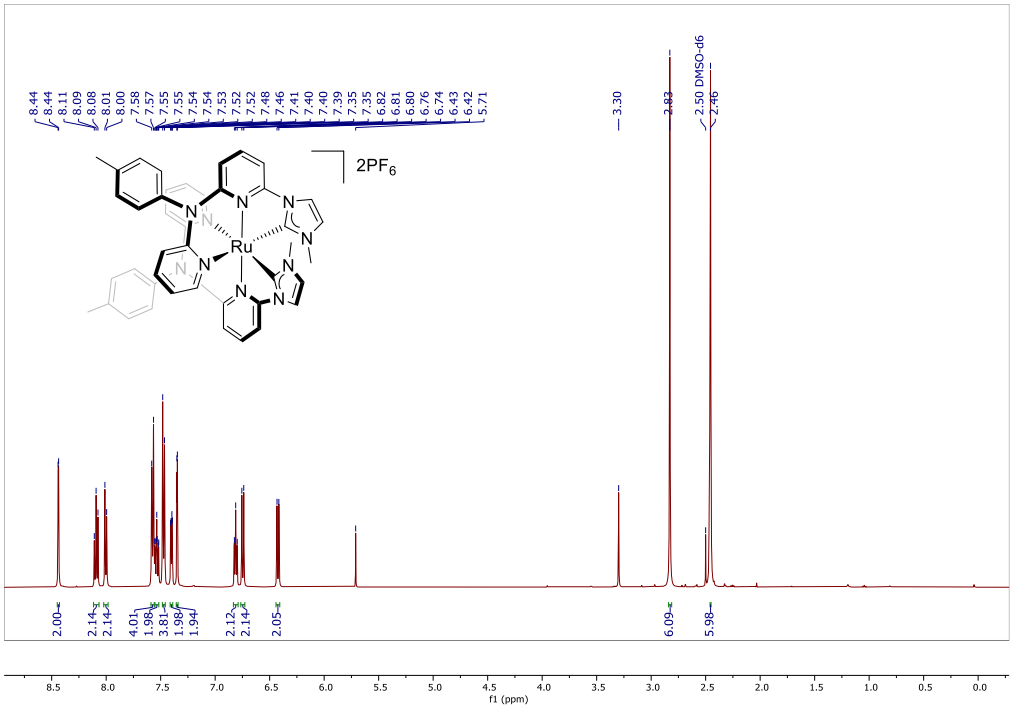

Figure 2.25 ^{1}H NMR of **Ru4**

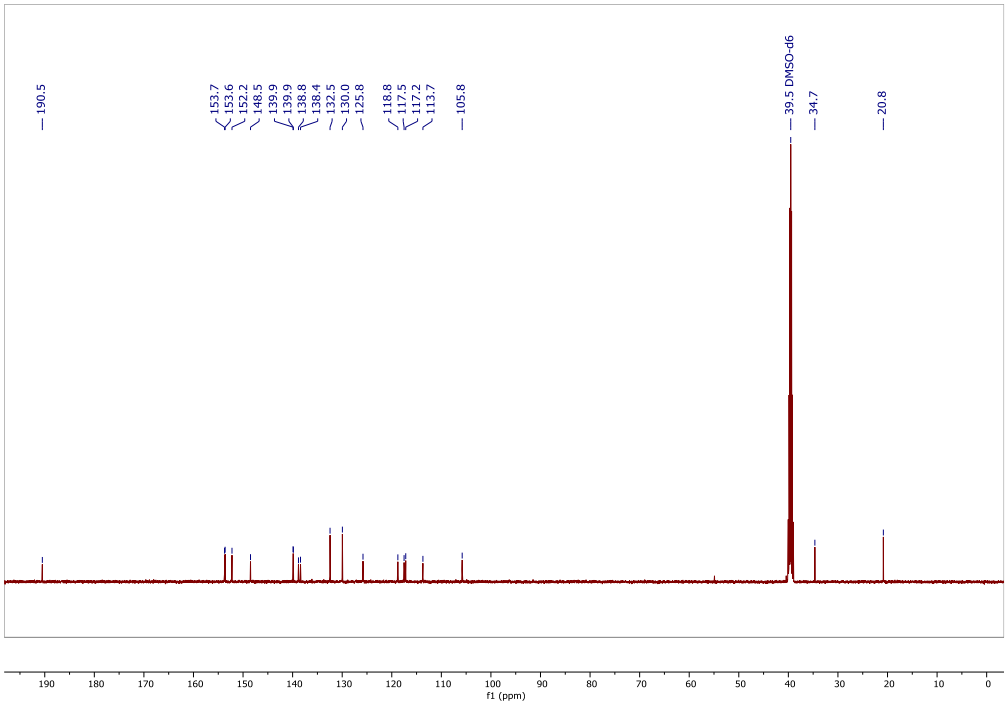

Figure 2.26 ^{13}C{^{1}H} NMR of **Ru4**

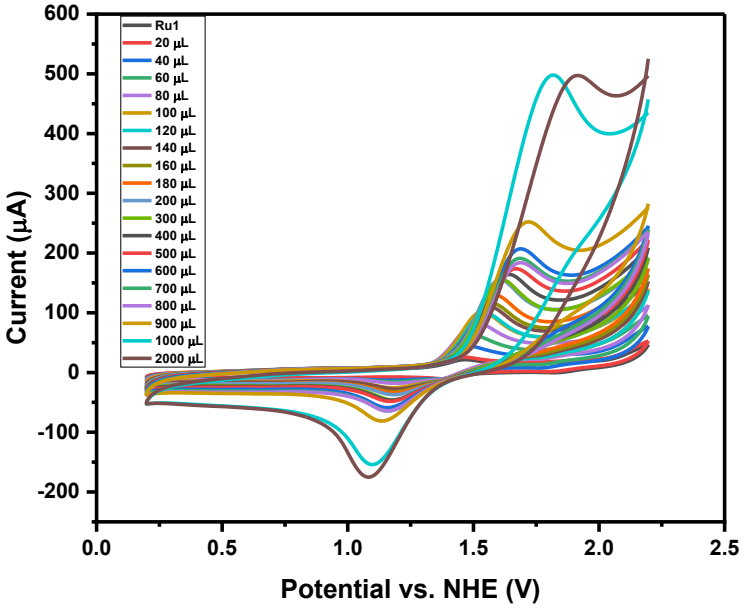

Figure 2.27 Cyclic voltammograms of **Ru1** recorded in CH_3CN (0.1 M $TBAPF_6$) after the successive addition of water in 20 µL increments up to a total volume of 2000 µL.

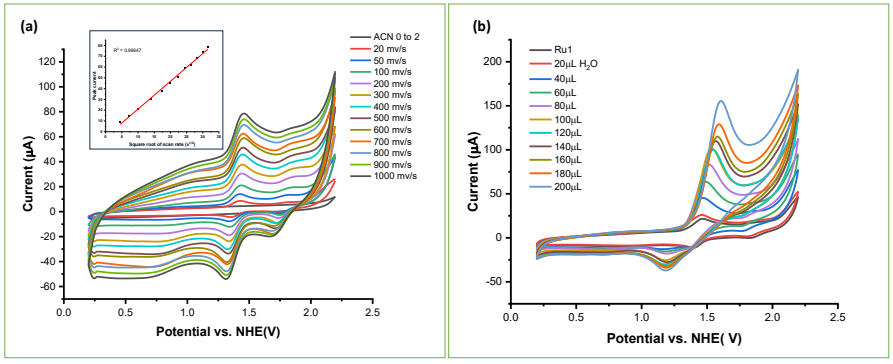

Figure 2.28 (a) Cyclic Voltammogram of Complex **Ru1** at different scan rates. Linear plot of the peak current (I_{pa}) and the square root of the scan rate of complex **Ru1** (in the inset). **(b) Ru1** in acetonitrile solution upon gradual addition of H_2O. A glassy carbon (GC) electrode (diameter 3 mm) was used as the working electrode, a Pt wire as the counter electrode, and an Ag/AgCl/3 M KCl as the reference electrode at a scan rate of 50 mV/s.

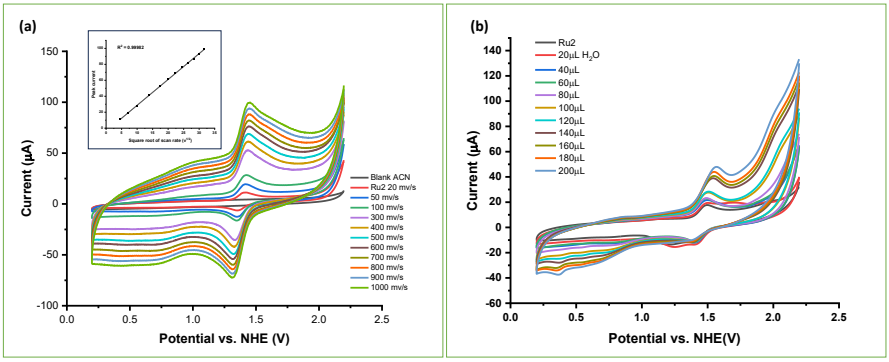

Figure 2.29 (a) Cyclic Voltammogram of Complex **Ru2** at different scan rates. The plot of the peak current and the square root of the scans (in the inset). **(b) Ru2** in acetonitrile solution upon gradual addition of H_2O. A glassy carbon (GC) electrode (diameter 3 mm) was used as the working electrode, a Pt wire as the counter electrode, and an Ag/AgCl/1 M KCl as the reference electrode at a scan rate of 50 mV/s.

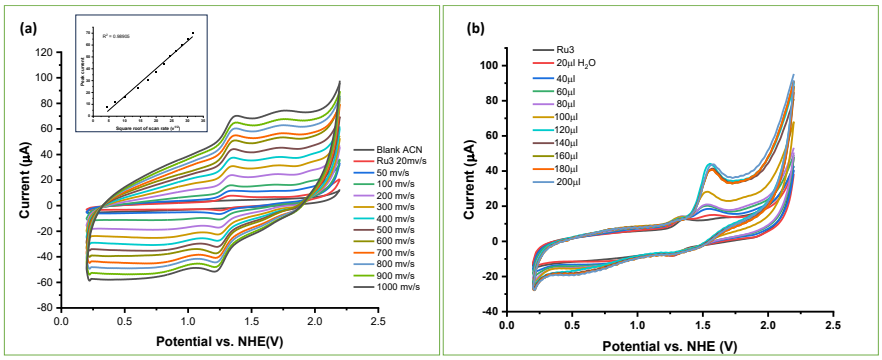

Figure 2.30 (a) Cyclic voltammograms of Complex **Ru3** at different scan rates. The plot of the peak current and the square root of the scans (in the inset). **(b) Ru3** in acetonitrile solution upon gradual addition of H_2O. A glassy carbon (GC) electrode (diameter 3 mm) was used as the working electrode, a Pt wire as the counter electrode, and an Ag/AgCl/1 M KCl as the reference electrode at a scan rate of 50 mV/s.

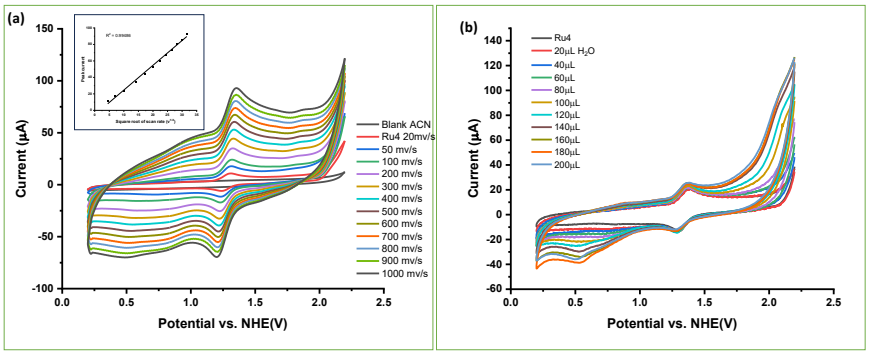

Figure 2.31 (a) Cyclic voltammograms of Complex **Ru4** at different scan rates. Plot of the peak current and the square root of the number of scans (inset). **(b) Ru4** in acetonitrile solution upon gradual addition of H_2O. A glassy carbon (GC) electrode (diameter 3 mm) was used as the working electrode, a Pt wire as the counter electrode, and an Ag/AgCl/1 M KCl as the reference electrode at a scan rate of 50 mV/s.

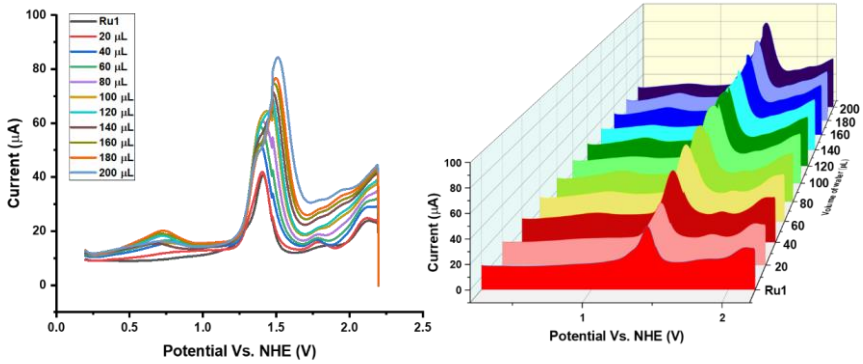

Figure 2.32 Differential Pulse voltammograms for **Ru1** in **(a)** graphical form and **(b)** 3D waterfall view.

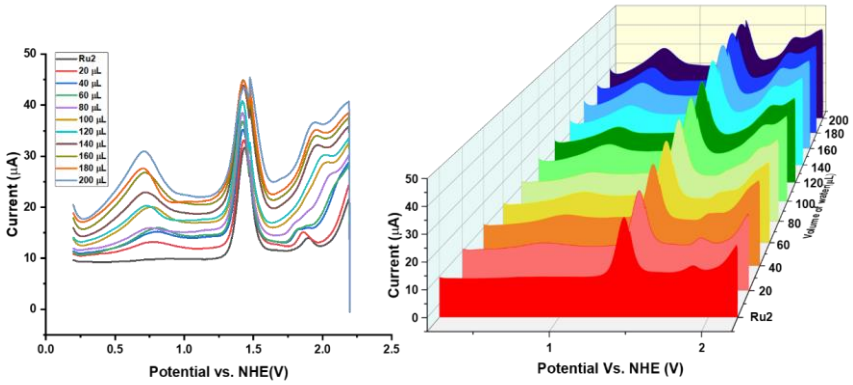

Figure 2.33 Differential Pulse voltammograms for **Ru2** in **(a)** graphical form and **(b)** 3D waterfall view.

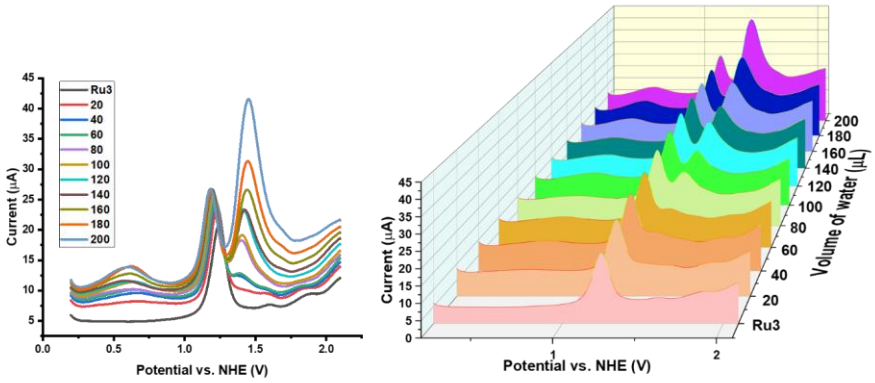

Figure 2.34 Differential Pulse voltammograms for **Ru3** in **(a)** graphical form and **(b)** 3D waterfall view.

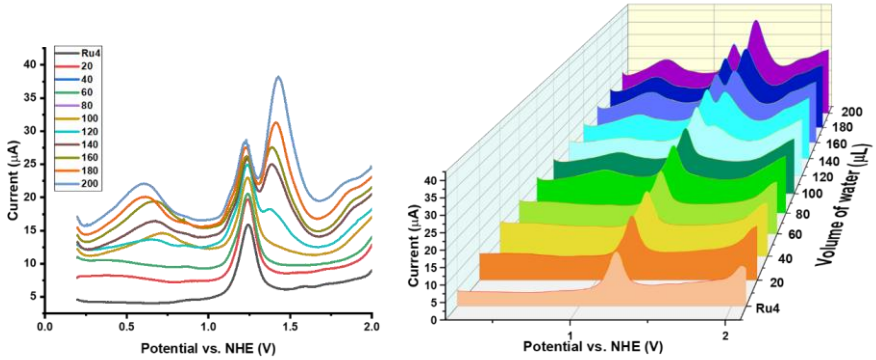

Figure 2.35 Differential Pulse voltammograms for **Ru4** in **(a)** graphical form and **(b)** 3D waterfall view.

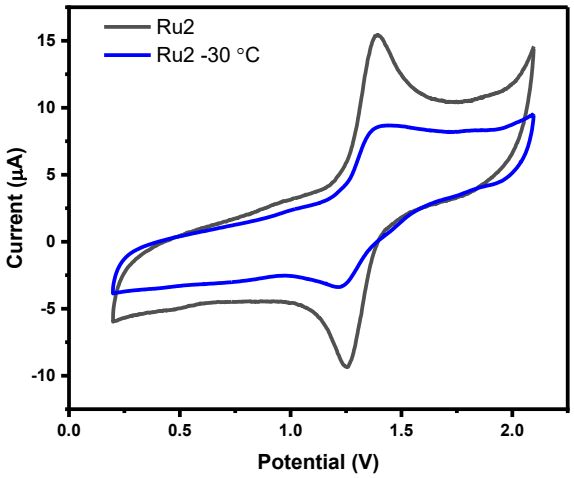

Figure 2.36 Cyclic Voltammogram of **Ru2** complex in dry ACN using 0.1 M $TBAPF_6$ as electrolyte at room temperature and at low temperature (-30 °C).

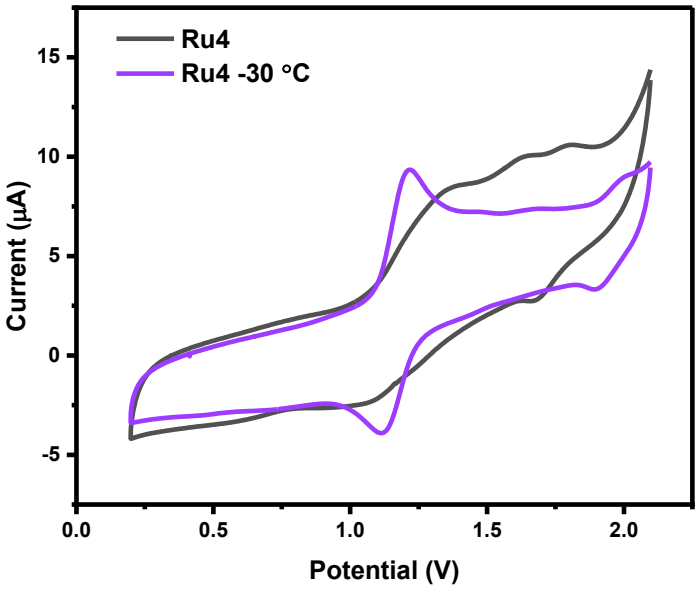

Figure 2.37 Cyclic Voltammogram of **Ru4** complex in dry ACN using 0.1 M $TBAPF_6$ as electrolyte at room temperature and at low temperature (-30 °C).

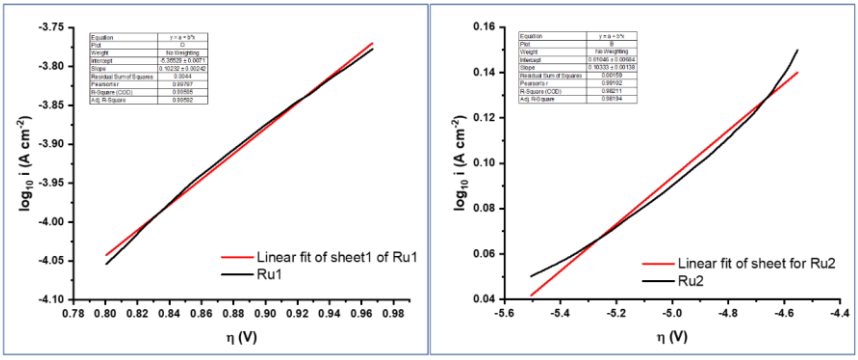

Figure 2.38 Tafel plots of complexes **Ru1** and **Ru2**

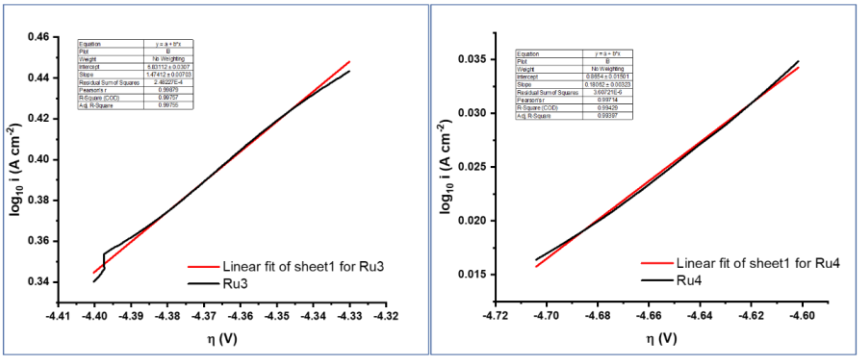

Figure 2.39 Tafel plots of complexes **Ru3** and **Ru4**

Realtime Size Plot S/N : 409614

User	: Common	Group	: Amrendra K Singh	Repetition	: 1/1
Date	: 23-10-2024	File Name	: 23.10.24		
Time	: 14:29:20	Sample Information	: Ru1		
SOP Name	: Ekta Yadava			Security	: No Security

Version 5.22 /

Realtime Size Plot

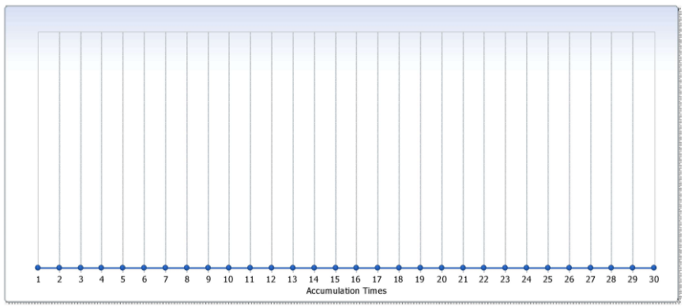

Realtime Size Table S/N : 409614

User	: Common	Group	: Amrendra K Singh	Repetition	: 1/1
Date	: 23-10-2024	File Name	: 23.10.24		
Time	: 14:29:20	Sample Information	: Ru1		
SOP Name	: Ekta Yadava			Security	: No Security

Version 5.22 /

Accum. times	Diameter (realtime) (nm)	Mean Diameter (nm)	Intensity (cps)	Elapsed Time (sec)
1	0.0	0.0	2841	0
2	0.0	0.0	2818	3
3	0.0	0.0	2819	5
4	0.0	0.0	2920	7
5	0.0	0.0	3210	9
6	0.0	0.0	3222	12
7	0.0	0.0	2965	14
8	0.0	0.0	2956	16
9	0.0	0.0	2957	18
10	0.0	0.0	2972	21
11	0.0	0.0	2792	23
12	0.0	0.0	2967	25
13	0.0	0.0	3191	27
14	0.0	0.0	3115	30
15	0.0	0.0	3021	32
16	0.0	0.0	2911	34
17	0.0	0.0	2817	36
18	0.0	0.0	2918	39
19	0.0	0.0	2851	41
20	0.0	0.0	3101	43
21	0.0	0.0	3087	46
22	0.0	0.0	3101	48
23	0.0	0.0	2914	50
24	0.0	0.0	2791	52
25	0.0	0.0	2927	54
26	0.0	0.0	2931	57
27	0.0	0.0	2955	59
28	0.0	0.0	3044	61
29	0.0	0.0	3144	64
30	0.0	0.0	3283	66

Figure 2.40 Dynamic Light Scattering (DLS) data for **Ru1** prior to the addition of water.

Realtime Size Plot S/N : 409614

User	: Common	Group	: Amrendra K Singh	Repetition	: 1/1
Date	: 23-10-2024	File Name	: 23.10.24		
Time	: 14:36:42	Sample Information	: Ru2		
SOP Name	: Ekta Yadava			Security	: No Security

Version 5.22 /

Realtime Size Plot

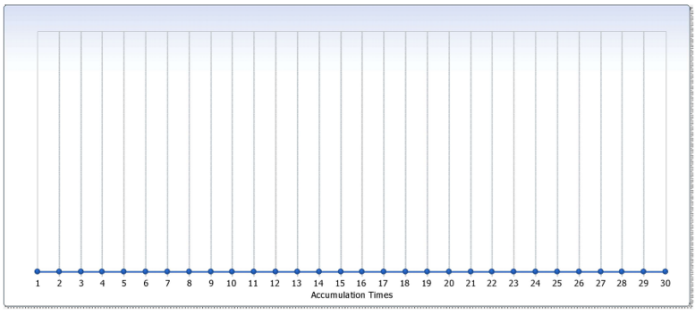

Realtime Size Table S/N : 409614

User	: Common	Group	: Amrendra K Singh	Repetition	: 1/1
Date	: 23-10-2024	File Name	: 23.10.24		
Time	: 14:36:42	Sample Information	: Ru2		
SOP Name	: Ekta Yadava			Security	: No Security

Version 5.22 /

Accum. times	Diameter (realtime) (nm)	Mean Diameter (nm)	Intensity (cps)	Elapsed Time (sec)
1	0.0	0.0	4070	0
2	0.0	0.0	3910	2
3	0.0	0.0	4073	5
4	0.0	0.0	4086	7
5	0.0	0.0	3881	9
6	0.0	0.0	4044	12
7	0.0	0.0	4018	14
8	0.0	0.0	4062	16
9	0.0	0.0	4295	18
10	0.0	0.0	4401	20
11	0.0	0.0	4436	23
12	0.0	0.0	4300	25
13	0.0	0.0	4118	27
14	0.0	0.0	4177	29
15	0.0	0.0	4068	32
16	0.0	0.0	3974	34
17	0.0	0.0	3998	36
18	0.0	0.0	4353	38
19	0.0	0.0	4268	41
20	0.0	0.0	4231	43
21	0.0	0.0	4622	45
22	0.0	0.0	4130	48
23	0.0	0.0	4397	50
24	0.0	0.0	4178	52
25	0.0	0.0	4103	54
26	0.0	0.0	4020	57
27	0.0	0.0	4238	59
28	0.0	0.0	4291	61
29	0.0	0.0	4355	63
30	0.0	0.0	4191	66

Figure 2.41 Dynamic Light Scattering (DLS) data for **Ru1** after the addition of 200 µL of water.

Realtime Size Plot S/N : 409614

User	: Common	Group	: Amrendra K Singh	Repetition	: 1/1
Date	: 23-10-2024	File Name	: 23.10.24		
Time	: 14:50:50	Sample Information	: RuEY74b		
SOP Name	: Ekta Yadava			Security	: No Security

Version 5.22 /

Realtime Size Plot

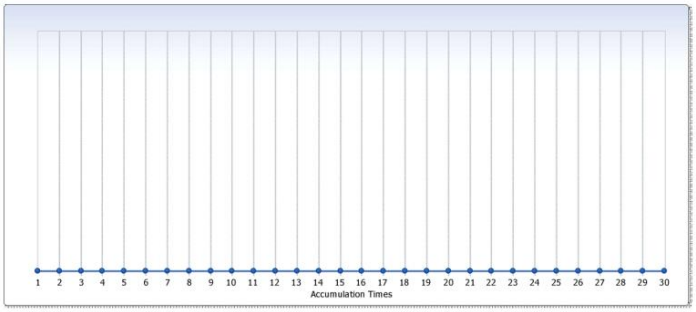

SOP Name : Ekta Yadava Security : No Security

Version 5.22 /

Accum. times	Diameter (realtime) (nm)	Mean Diameter (nm)	Intensity (cps)	Elapsed Time (sec)
1	0.0	0.0	2841	0
2	0.0	0.0	2818	3
3	0.0	0.0	2819	5
4	0.0	0.0	2920	7
5	0.0	0.0	3210	9
6	0.0	0.0	3222	12
7	0.0	0.0	2965	14
8	0.0	0.0	2956	16
9	0.0	0.0	2957	18
10	0.0	0.0	2972	21
11	0.0	0.0	2792	23
12	0.0	0.0	2967	25
13	0.0	0.0	3191	27
14	0.0	0.0	3115	30
15	0.0	0.0	3021	32
16	0.0	0.0	2911	34
17	0.0	0.0	2817	36
18	0.0	0.0	2918	39
19	0.0	0.0	2851	41
20	0.0	0.0	3101	43
21	0.0	0.0	3087	46
22	0.0	0.0	3101	48
23	0.0	0.0	2914	50
24	0.0	0.0	2791	52
25	0.0	0.0	2927	54
26	0.0	0.0	2931	57
27	0.0	0.0	2955	59
28	0.0	0.0	3044	61
29	0.0	0.0	3144	64
30	0.0	0.0	3283	66

Figure 2.42 Dynamic Light Scattering (DLS) data for **Ru2** prior to the addition of water.

Realtime Size Plot S/N : 409614

User	: Common	Group	: Amrendra K Singh	Repetition	: 1/1
Date	: 23-10-2024	File Name	: 23.10.24		
Time	: 14:57:50	Sample Information	: RuEY74W		
SOP Name	: Ekta Yadava			Security	: No Security

Version 5.22 /

Realtime Size Plot

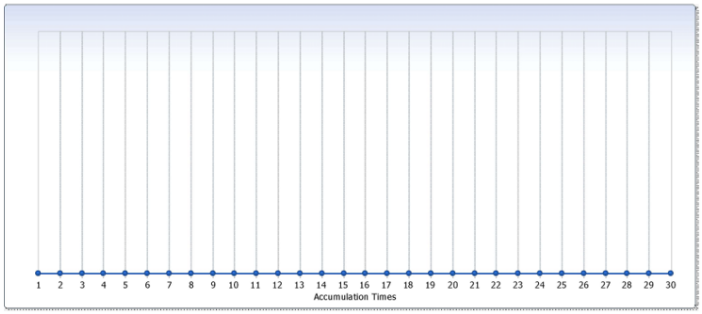

Realtime Size Table S/N : 409614

User	: Common	Group	: Amrendra K Singh	Repetition	: 1/1
Date	: 23-10-2024	File Name	: 23.10.24		
Time	: 14:57:50	Sample Information	: RuEY74W		
SOP Name	: Ekta Yadava			Security	: No Security

Version 5.22 /

Accum. times	Diameter (realtime) (nm)	Mean Diameter (nm)	Intensity (cps)	Elapsed Time (sec)
1	0.0	0.0	4318	3
2	0.0	0.0	4350	5
3	0.0	0.0	4527	7
4	0.0	0.0	4209	9
5	0.0	0.0	4714	12
6	0.0	0.0	4150	14
7	0.0	0.0	3941	18
8	0.0	0.0	4170	20
9	0.0	0.0	4194	23
10	0.0	0.0	4053	25
11	0.0	0.0	4292	31
12	0.0	0.0	4310	33
13	0.0	0.0	4563	37
14	0.0	0.0	3812	39
15	0.0	7.1	3928	42
16	0.0	0.0	3888	44
17	0.0	0.0	3976	46
18	0.0	0.0	4571	48
19	0.0	0.0	4550	51
20	0.0	0.0	4568	53
21	0.0	0.0	3809	58
22	0.0	0.0	3821	60
23	0.0	0.0	3770	62
24	0.0	0.0	3875	64
25	0.0	0.0	3811	67
26	0.0	0.0	4342	69
27	0.0	0.0	4685	73
28	0.0	0.0	3931	76
29	0.0	0.0	4526	78
30	0.0	0.0	3935	80

Figure 2.43 Dynamic Light Scattering (DLS) data for **Ru2** after the addition of 200 µL of water.

2.5 References

[1] Song, H., Luo, S., Huang, H., Deng, B., and Ye, J. (2022). Solar-Driven Hydrogen Production: Recent Advances, Challenges, and Future Perspectives. ACS Energy Lett., *7*, 1043–1065. (https://doi.org/10.1021/acsenergylett.1c02591)

[2] El-Khouly, M.E., El-Mohsnawy, E., and Fukuzumi, S. (2017). Solar energy conversion: From natural to artificial photosynthesis. J. Photochem. Photobiol. C Photochem. Rev, *31*, 36–83. (https://doi.org/10.1016/j.jphotochemrev.2017.02.001)

[3] Zhang, B., Zhang, S.-X., Yao, R., Wu, Y.-H., and Qiu, J.-S. (2021). Progress and prospects of hydrogen production: Opportunities and challenges. J. Electron. Sci. Technol., *19*, 100080. (https://doi.org/10.1016/j.jnlest.2021.100080)

[4] Kärkäs, M.D., Verho, O., Johnston, E.V., and Åkermark, B. (2014). Artificial Photosynthesis: Molecular Systems for Catalytic Water Oxidation. Chem. Rev., *114*, 11863–12001. (https://doi.org/10.1021/cr400572f)

[5] Chen, Y., Xu, B., Yao, R., Chen, C., and Zhang, C. (2022). Mimicking the Oxygen-Evolving Center in Photosynthesis. Front. Plant Sci., *13*, 929532. (https://doi.org/10.3389/fpls.2022.929532)

[6] Ye, S., Ding, C., and Li, C. (2019). Artificial photosynthesis systems for catalytic water oxidation. In Advances in Inorganic Chemistry (Elsevier), pp. 3–59. (https://doi.org/10.1016/bs.adioch.2019.03.007)

[7] Li, J., Zeng, J., Zhao, F., Sun, X., Wang, S., and Lu, X.F. (2024). A Review on Highly Efficient Ru-Based Electrocatalysts for Acidic Oxygen Evolution Reaction. Energy Fuels, *38*, 11521–11540. (https://doi.org/10.1021/acs.energyfuels.4c02080)

[8] Singh, A.K., and Roy, L. (2024). Evolution in the Design of Water Oxidation Catalysts with Transition-Metals: A Perspective on Biological, Molecular, Supramolecular, and Hybrid Approaches. ACS Omega, *9*, 9886–9920. (https://doi.org/10.1021/acsomega.3c07847)

[9] Lyons, M.E.G., Doyle, R.L., Browne, M.P., Godwin, I.J., and Rovetta, A.A.S. (2017). Recent developments in electrochemical water oxidation. Curr. Opin. Electrochem., *1*, 40–45. (https://doi.org/10.1016/j.coelec.2016.12.005)

[10] Ruan, Z., Dong, J., Wang, J., Qi, Z., Chen, X., Liang, X., and Lin, J. (2024). Efficient electrochemical water oxidation catalyzed by N_4-coordinated nickel complexes under neutral conditions. Sustainable Energy Fuels, *8*, 1769–1774. (https://doi.org/10.1039/D4SE00303A)

[11] Roger, I., and Symes, M.D. (2016). First row transition metal catalysts for solar-driven water oxidation produced by electrodeposition. J. Mater. Chem. A, *4*, 6724–6741. (https://doi.org/10.1039/C5TA09423B)

[12] Gagliardi, C.J., Vannucci, A.K., Concepcion, J.J., Chen, Z., and Meyer, T.J. (2012). The role of proton coupled electron transfer in water oxidation. Energy Environ. Sci., *5*, 7704. (https://doi.org/10.1039/c2ee03311a)

[13] Greife, P., Schönborn, M., Capone, M., Assunção, R., Narzi, D., Guidoni, L., and Dau, H. (2023). The electron–proton bottleneck of photosynthetic oxygen evolution. Nature, *617*, 623–628. (https://doi.org/10.1038/s41586-023-06008-5)

[14] Wang, S., Lu, A., and Zhong, C.-J. (2021). Hydrogen production from water electrolysis: role of catalysts. Nano Converg., *8*, 4. (https://doi.org/10.1186/s40580-021-00254-x)

[15] Shaghaghi, Z., Mohammad-Rezaei, R., and Jafari, S. (2022). Efficient electrochemical water oxidation mediated by different substituted manganese-salophen complexes. J. Electroanal. Chem., *922*, 116733. (https://doi.org/10.1016/j.jelechem.2022.116733)

[16] Liu, T., Fan, L., Yang, H., Wang, L., Fan, X., and Sun, L. (2024). Coordination-Adaptive Molecular Platform for Catalytic Water Oxidation. Artif. Photosynth., aps.4c00005. (https://doi.org/10.1021/aps.4c00005)

[17] Chen, Q.-F., Zhang, X., Shi, J., Zhan, J., Xie, F., Zhang, H.-T., Deng, J., Liu, J., Li, M., Shao, Y., et al. (2024). In Situ Revelation of the Dynamic Evolution of Molecular Water Oxidation Catalysts. CCS Chem, 1–12. (https://doi.org/10.31635/ccschem.024.202403935)

[18] Den Boer, D., and Hetterscheid, D.G.H. (2023). Correlations between the Electronic Structure and Energetics of the Catalytic Steps in Homogeneous Water Oxidation Catalysis. J. Am. Chem. Soc., *145*, 23057–23067. (https://doi.org/10.1021/jacs.3c05741)

[19] Liao, R.-Z., Kärkäs, M.D., Laine, T.M., Åkermark, B., and Siegbahn, P.E.M. (2016). On the mechanism of water oxidation catalyzed by a dinuclear ruthenium complex: a quantum chemical study. Catal. Sci. Technol., *6*, 5031–5041. (https://doi.org/10.1039/C6CY00083E)

[20] Das, B., Orthaber, A., Ott, S., and Thapper, A. (2015). Water oxidation catalysed by a mononuclear Co^{II} polypyridine complex; possible reaction intermediates and the role of the chloride ligand. Chem. Commun., *51*, 13074–13077. (https://doi.org/10.1039/C5CC04148A)

[21] Das, B., Toledo-Carrillo, E.A., Li, G., Ståhle, J., Thersleff, T., Chen, J., Li, L., Ye, F., Slabon, A., Göthelid, M., et al. (2023). Bifunctional and regenerable molecular electrode for water

electrolysis at neutral pH. J. Mater. Chem. A, *11*, 13331–13340. (https://doi.org/10.1039/D3TA00071K)

[22] Costentin, C. (2020). Proton-Coupled Electron Transfer Catalyst: Heterogeneous Catalysis. Application to an Oxygen Evolution Catalyst. ACS Catal., *10*, 7958–7967. (https://doi.org/10.1021/acscatal.0c02532)

[23] Gao, J., Liu, Y., Liu, B., and Huang, K.-W. (2022). Progress of Heterogeneous Iridium-Based Water Oxidation Catalysts. ACS Nano, *16*, 17761–17777. (https://doi.org/10.1021/acsnano.2c08519)

[24] Das, B., Toledo-Carrillo, E.A., Li, L., Ye, F., Chen, J., Slabon, A., Verho, O., Eriksson, L., Göthelid, M., Dutta, J., et al. (2022). Cobalt Electrocatalyst on Fluorine Doped Carbon Cloth – a Robust and Partially Regenerable Anode for Water Oxidation. ChemCatChem, *14*, e202200538. (https://doi.org/10.1002/cctc.202200538)

[25] Song, F., Bai, L., Moysiadou, A., Lee, S., Hu, C., Liardet, L., and Hu, X. (2018). Transition Metal Oxides as Electrocatalysts for the Oxygen Evolution Reaction in Alkaline Solutions: An Application-Inspired Renaissance. J. Am. Chem. Soc., *140*, 7748–7759. (https://doi.org/10.1021/jacs.8b04546)

[26] Wu, W., Huang, Z.-H., and Lim, T.-T. (2014). Recent development of mixed metal oxide anodes for electrochemical oxidation of organic pollutants in water. Applied Catalysis A: General *480*, 58–78. (https://doi.org/10.1016/j.apcata.2014.04.035)

[27] Liu, T., Li, G., Shen, N., Wang, L., Timmer, B.J.J., Kravchenko, A., Zhou, S., Gao, Y., Yang, Y., Yang, H., et al. (2022). Promoting Proton Transfer and Stabilizing Intermediates in Catalytic Water Oxidation via Hydrophobic Outer Sphere Interactions. Chem Eur J, *28*, e202104562. (https://doi.org/10.1002/chem.202104562)

[28] Yang, J., Wang, L., Zhan, S., Zou, H., Chen, H., Ahlquist, M.S.G., Duan, L., and Sun, L. (2021). From Ru-bda to Ru-bds: a step forward to highly efficient molecular water oxidation electrocatalysts under acidic and neutral conditions. Nat Commun, *12*, 373. (https://doi.org/10.1038/s41467-020-20637-8)

[29] Das, B., Rahaman, A., Shatskiy, A., Verho, O., Kärkäs, M.D., and Åkermark, B. (2021). The Impact of Ligand Carboxylates on Electrocatalyzed Water Oxidation. Acc. Chem. Res., *54*, 3326–3337. (https://doi.org/10.1021/acs.accounts.1c00298)

[30] Sinha, W., Mizrahi, A., Mahammed, A., Tumanskii, B., and Gross, Z. (2018). Reactive Intermediates Involved in Cobalt Corrole Catalyzed Water Oxidation (and Oxygen Reduction). Inorg. Chem., *57*, 478–485. (https://doi.org/10.1021/acs.inorgchem.7b02696)

[31] Matheu, R., Ertem, M.Z., Gimbert-Suriñach, C., Sala, X., and Llobet, A. (2019). Seven Coordinated Molecular Ruthenium–Water Oxidation Catalysts: A Coordination Chemistry Journey: Focus Review. Chem. Rev., *119*, 3453–3471. (https://doi.org/10.1021/acs.chemrev.8b00537)

[32] Das, P.K., Bhunia, S., Chakraborty, P., Chatterjee, S., Rana, A., Peramaiah, K., Alsabban, M.M., Dutta, I., Dey, A., and Huang, K.-W. (2021). Electrocatalytic Water Oxidation by a Phosphorus–Nitrogen O═PN^3 -Pincer Cobalt Complex. Inorg. Chem., *60*, 614–622. (https://doi.org/10.1021/acs.inorgchem.0c02376)

[33] Wang, Y., Tseng, Y., Kumbhar, S.V., Chang, H., Yang, T., Lu, I., and Wang, Y. (2025). Overcoming the Tradeoff Between Reaction Rate and Overpotential in Dinuclear Cobalt Complex Catalyzed Electrochemical Water Oxidation. Chem Eur J, e202403583. (https://doi.org/10.1002/chem.202403583)

[34] Duan, L., Bozoglian, F., Mandal, S., Stewart, B., Privalov, T., Llobet, A., and Sun, L. (2012). A molecular ruthenium catalyst with

water-oxidation activity comparable to that of photosystem II. Nature Chem, *4*, 418–423. (https://doi.org/10.1038/nchem.1301)

[35] Xie, Y., Shaffer, D.W., Lewandowska-Andralojc, A., Szalda, D.J., and Concepcion, J.J. (2016). Water Oxidation by Ruthenium Complexes Incorporating Multifunctional Bipyridyl Diphosphonate Ligands. Angew Chem Int Ed, *55*, 8067–8071. (https://doi.org/10.1002/anie.201601943)

[36] Timmer, B.J.J., Kravchenko, O., Liu, T., Zhang, B., and Sun, L. (2021). Off-Set Interactions of Ruthenium–bda Type Catalysts for Promoting Water-Splitting Performance. Angew Chem Int Ed, *60*, 14504–14511. (https://doi.org/10.1002/anie.202101931)

[37] Li, G., and Ahlquist, M.S.G. (2022). Computational comparison of $Ru(bda)(py)_2$ and $Fe(bda)(py)_2$ as water oxidation catalysts. Dalton Trans., *51*, 8618–8624. (https://doi.org/10.1039/D2DT01150F)

[38] Gersten, S.W., Samuels, G.J., and Meyer, T.J. (1982). Catalytic oxidation of water by an oxo-bridged ruthenium dimer. J. Am. Chem. Soc., *104*, 4029–4030. (https://doi.org/10.1021/ja00378a053)

[39] Radaram, B., Ivie, J.A., Singh, W.M., Grudzien, R.M., Reibenspies, J.H., Webster, C.E., and Zhao, X. (2011). Water Oxidation by Mononuclear Ruthenium Complexes with TPA-Based Ligands. Inorg. Chem., *50*, 10564–10571. (https://doi.org/10.1021/ic200050g)

[40] Ishizuka, T., Sugimoto, H., Itoh, S., and Kojima, T. (2022). Recent progress in oxidation chemistry of high-valent ruthenium-oxo and osmium-oxo complexes and related species. Coord Chem Rev, *466*, 214536. (https://doi.org/10.1016/j.ccr.2022.214536)

[41] Schindler, D., Gil-Sepulcre, M., Lindner, J.O., Stepanenko, V., Moonshiram, D., Llobet, A., and Würthner, F. (2020). Efficient

Electrochemical Water Oxidation by a Trinuclear Ru(bda) Macrocycle Immobilized on Multi-Walled Carbon Nanotube Electrodes. Adv. Energy Mater., *10*, 2002329. (https://doi.org/10.1002/aenm.202002329)

[42] Franceschi, P., Rossin, E., Goti, G., Scopano, A., Vega-Peñaloza, A., Natali, M., Singh, D., Sartorel, A., and Dell'Amico, L. (2023). A Proton-Coupled Electron Transfer Strategy to the Redox-Neutral Photocatalytic CO_2 Fixation. J. Org. Chem., *88*, 6454–6464. (https://doi.org/10.1021/acs.joc.2c02952)

[43] Costentin, C. (2008). Electrochemical Approach to the Mechanistic Study of Proton-Coupled Electron Transfer. Chem. Rev., *108*, 2145–2179. (https://doi.org/10.1021/cr068065t)

[44] Nocera, D.G. (2022). Proton-Coupled Electron Transfer: The Engine of Energy Conversion and Storage. J. Am. Chem. Soc., *144*, 1069–1081. (https://doi.org/10.1021/jacs.1c10444)

[45] Huynh, M.H.V., and Meyer, T.J. (2007). Proton-Coupled Electron Transfer. Chem. Rev., *107*, 5004–5064. (https://doi.org/10.1021/cr0500030)

[46] Rosenthal, J., and Nocera, D.G. (2007). Role of Proton-Coupled Electron Transfer in O–O Bond Activation. Acc. Chem. Res., *40*, 543–553. (https://doi.org/10.1021/ar7000638)

[47] Meyer, T.J., Huynh, M.H.V., and Thorp, H.H. (2007). The Possible Role of Proton-Coupled Electron Transfer (PCET) in Water Oxidation by Photosystem II. Angew Chem Int Ed, *46*, 5284–5304. (https://doi.org/10.1002/anie.200600917)

[48] Schneider, J., Bangle, R.E., Swords, W.B., Troian-Gautier, L., and Meyer, G.J. (2019). Determination of Proton-Coupled Electron Transfer Reorganization Energies with Application to Water

Oxidation Catalysts. J. Am. Chem. Soc., *141*, 9758–9763. (https://doi.org/10.1021/jacs.9b01296)

[49] Liu, T., and Sun, L. (2023). Proton transfer regulating in catalytic water oxidation by Ru-complexes: second coordination sphere and beyond. Sci. Bull., *68*, 854–856. (https://doi.org/10.1016/j.scib.2023.04.012)

[50] Matheu, R., Ertem, M.Z., Benet-Buchholz, J., Coronado, E., Batista, V.S., Sala, X., and Llobet, A. (2015). Intramolecular Proton Transfer Boosts Water Oxidation Catalyzed by a Ru Complex. J. Am. Chem. Soc., *137*, 10786–10795. (https://doi.org/10.1021/jacs.5b06541)

[51] Kessinger, M., Soudackov, A.V., Schneider, J., Bangle, R.E., Hammes-Schiffer, S., and Meyer, G.J. (2022). Reorganization Energies for Interfacial Proton-Coupled Electron Transfer to a Water Oxidation Catalyst. J. Am. Chem. Soc., *144*, 20514–20524. (https://doi.org/10.1021/jacs.2c09672)

[52] Kundu, A., Dey, S.K., Dey, S., Anoop, A., and Mandal, S. (2020). Mononuclear Ruthenium-Based Water Oxidation Catalyst Supported by Anionic, Redox-Non-Innocent Ligand: Heterometallic O–O Bond Formation via Radical Coupling Pathway. Inorg. Chem., *59*, 1461–1470. (https://doi.org/10.1021/acs.inorgchem.9b03258)

[53] Karak, S., Stepanenko, V., Addicoat, M.A., Keßler, P., Moser, S., Beuerle, F., and Würthner, F. (2022). A Covalent Organic Framework for Cooperative Water Oxidation. J. Am. Chem. Soc., *144*, 17661–17670. (https://doi.org/10.1021/jacs.2c07282)

[54] Singh, A.K., and Roy, L. (2024). Evolution in the Design of Water Oxidation Catalysts with Transition-Metals: A Perspective on Biological, Molecular, Supramolecular, and Hybrid Approaches.

ACS Omega, *9*, 9886–9920. (https://doi.org/10.1021/acsomega.3c07847)

[55] Hunter, B.M., Gray, H.B., and Müller, A.M. (2016). Earth-Abundant Heterogeneous Water Oxidation Catalysts. Chem. Rev., *116*, 14120–14136. (https://doi.org/10.1021/acs.chemrev.6b00398)

[56] Blakemore, J.D., Crabtree, R.H., and Brudvig, G.W. (2015). Molecular Catalysts for Water Oxidation. Chem. Rev., *115*, 12974–13005. (https://doi.org/10.1021/acs.chemrev.5b00122)

[57] Katipamula, S., White, N.M., and Waldie, K.M. (2023). Controlled-potential electrolysis for evaluating molecular electrocatalysts. Chem Catalysis, *3*, 100561. (https://doi.org/10.1016/j.checat.2023.100561)

[58] Yu, C.-H., Zhu, C., Ji, X., Hu, W., Xie, H., Bhuvanesh, N., Fang, L., and Ozerov, O.V. (2020). Palladium bis-pincer complexes with controlled rigidity and inter-metal distance. Inorg. Chem. Front., *7*, 4357–4366. (https://doi.org/10.1039/D0QI01111H)

[59] Zhu, C., Ang, N.W.J., Meyer, T.H., Qiu, Y., and Ackermann, L. (2021). Organic Electrochemistry: Molecular Syntheses with Potential. ACS Cent. Sci., *7*, 415–431. (https://doi.org/10.1021/acscentsci.0c01532)

[60] Wang, L., and Wang, L. (2022). Ligands modification strategies for mononuclear water splitting catalysts. Front. Chem., *10*, 996383. (https://doi.org/10.3389/fchem.2022.996383)

[61] Jakubikova, E., Chen, W., Dattelbaum, D.M., Rein, F.N., Rocha, R.C., Martin, R.L., and Batista, E.R. (2009). Electronic Structure and Spectroscopy of $[Ru(tpy)_2]^{2+}$, $[Ru(tpy)(bpy)(H_2O)]^{2+}$, and $[Ru(tpy)(bpy)(Cl)]^{+}$. Inorg. Chem., *48*, 10720–10725. (https://doi.org/10.1021/ic901477m)

[62] Brown, C.M., Arsenault, N.E., Cross, T.N.K., Hean, D., Xu, Z., and Wolf, M.O. (2020). Structural, electrochemical and photophysical behavior of Ru(II) complexes with large bite angle sulfur-bridged terpyridyl ligands. Inorg. Chem. Front., *7*, 117–127. (https://doi.org/10.1039/C9QI01009B)

[63] Mishima, K., Kinoshita, T., Hayashi, M., Jono, R., Segawa, H., and Yamashita, K. (2016). Theoretical investigation of [Ru(tpy)2]2+, [Ru(tpy)(bpy)(H_2 O)]2+ and [Ru(tpy)(bpy)(Cl)]+ complexes in acetone revisited: Inclusion of strong spin–orbit couplings to quantum chemistry calculations. J. Theor. Comput. Chem., *15*, 1650001. (https://doi.org/10.1142/S0219633616500012)

[64] Ryan, R.T., Stevens, K.C., Calabro, R., Parkin, S., Mahmoud, J., Kim, D.Y., Heidary, D.K., Glazer, E.C., and Selegue, J.P. (2020). Bis-tridentate *N*-Heterocyclic Carbene Ru(II) Complexes are Promising New Agents for Photodynamic Therapy. Inorg. Chem., *59*, 8882–8892. (https://doi.org/10.1021/acs.inorgchem.0c00686)

[65] Kim, Hyeong-Mook, Jeong, Daero, Noh, Hee Chang, and Chung, Young Keun (2014). Manipulation of Absorption Maxima by Controlling Oxidation Potentials in Bis(tridentate) Ru(II) *N*-Heterocyclic Carbene Complexes. Bull. Korean Chem. Soc., *35*, 448–456. (https://doi.org/10.5012/BKCS.2014.35.2.448)

[66] Fang, Y.-Q., Taylor, N.J., Laverdière, F., Hanan, G.S., Loiseau, F., Nastasi, F., Campagna, S., Nierengarten, H., Leize-Wagner, E., and Van Dorsselaer, A. (2007). Ruthenium(II) Complexes with Improved Photophysical Properties Based on Planar 4‘-(2-Pyrimidinyl)-2,2‘:6‘,2‘ ‘-terpyridine Ligands. Inorg. Chem., *46*, 2854–2863. (https://doi.org/10.1021/ic0622609)

[67] Torres, J., Carrión, M.C., Leal, J., Castañeda, G., Manzano, B.R., and Jalón, F.A. (2019). Homoleptic ruthenium complexes with *N*-heterocyclic carbene ligands as photosensitizers in the

photocatalytic generation of H2 from water. J. Organomet. Chem. *898*, 120880. (https://doi.org/10.1016/j.jorganchem.2019.120880)

[68] Zhang, Y.-M., Shao, J.-Y., Yao, C.-J., and Zhong, Y.-W. (2012). Cyclometalated ruthenium(ii) complexes with a bis-carbene CCC-pincer ligand. Dalton Trans., *41*, 9280. (https://doi.org/10.1039/c2dt31015e)

[69] Homanen, P., Haukka, M., Pakkanen, T.A., Pursiainen, J., and Laitinen, R.H. (1996). Ruthenium(II) Bipyridine Complexes: Synthesis and Characterization of $Ru(bpy)(CO)_2$ $(SCN)_2$, $Ru(dmbpy)(CO)_2$ Cl_2 , and $Ru(dmbpy)(CO)_2$ (NCS)H (bpy = 2,2‘-Bipyridine; dmbpy = 6,6‘-Dimethyl-2,2‘-bipyridine). Organometallics, *15*, 4081–4084. (https://doi.org/10.1021/om9602724)

[70] Villani, E., Sakanoue, K., Einaga, Y., Inagi, S., and Fiorani, A. (2022). Photophysics and electrochemistry of ruthenium complexes for electrogenerated chemiluminescence. J. Electroanal. Chem. *921*, 116677. (https://doi.org/10.1016/j.jelechem.2022.116677)

[71] Siewert, B., Langerman, M., Hontani, Y., Kennis, J.T.M., Van Rixel, V.H.S., Limburg, B., Siegler, M.A., Talens Saez, V., Kieltyka, R.E., and Bonnet, S. (2017). Turning on the red phosphorescence of a [Ru(tpy)(bpy)(Cl)]Cl complex by amide substitution: self-aggregation, toxicity, and cellular localization of an emissive ruthenium-based amphiphile. Chem. Commun., *53*, 11126–11129. (https://doi.org/10.1039/C7CC02989F)

[72] Kaeffer, N., and Leitner, W. (2022). Electrocatalysis with Molecular Transition-Metal Complexes for Reductive Organic Synthesis. JACS Au, *2*, 1266–1289. (https://doi.org/10.1021/jacsau.2c00031)

[73] Nath, S., Yadav, E., Raghuvanshi, A., and Singh, A.K. (2023). Ru(II) Complexes with Protic- and Anionic-Naked-NHC Ligands

for Cooperative Activation of Small Molecules**. Chem Eur J, *29*, e202301971. (https://doi.org/10.1002/chem.202301971)

[74] Nath, S., Yadav, E., Raghuvanshi, A., and Singh, A.K. (2023). Mechanistic insights and comparative analysis of Ru(II)–NNC pincer complexes with anionic-, protic-, and classical-NHCs for transfer hydrogenation of ketones. Catal. Sci. Technol., *13*, 7085–7099. (https://doi.org/10.1039/D3CY01383A)

[75] Nath, S., and Singh, A.K. (2025). Substrate-assisted product release in hydrogenation of LOHCs facilitated by hemilabile pyridine in Ru(II)–NNC pincer complexes and enhanced activity of proton-responsive protic-NHC ligands. Catal. Sci. Technol., *15*, 2999–3008. (https://doi.org/10.1039/D5CY00209E)

[76] Teng, Q., and Huynh, H.V. (2014). Determining the Electron-Donating Properties of Bidentate Ligands by ^{13}C NMR Spectroscopy. Inorg. Chem., *53*, 10964–10973. (https://doi.org/10.1021/ic501325j)

[77] Maji, S., López, I., Bozoglian, F., Benet-Buchholz, J., and Llobet, A. (2013). Mononuclear Ruthenium–Water Oxidation Catalysts: Discerning between Electronic and Hydrogen-Bonding Effects. Inorg. Chem., *52*, 3591–3593. (https://doi.org/10.1021/ic3028176)

[78] Tanjedrew, N., Thammanatpong, K., Surawatanawong, P., Chakthranont, P., Chantarojsiri, T., Unjarern, T., and Kiatisevi, S. (2024). Tunable Metal-Free Imidazole-Benzimidazole Electrocatalysts for Oxygen Reduction in Aqueous Solutions. Chem Eur J, *30*, e202302854. (https://doi.org/10.1002/chem.202302854)

[79] Khan, S., and Naskar, S. (2022). Chemical and electrochemical water oxidation catalyzed by heteroleptic Ru(III) complexes of anionic 2,6 pyridine dicarboxylate ligand: Experimental and

theoretical study. Polyhedron, *222*, 115898. (https://doi.org/10.1016/j.poly.2022.115898)

[80] Phapale, D., Sharma, V., Saini, A., Sharma, S., Kumar, P., Kumar, R., Shanmugam, M., Draksharapu, A., Dutta, A., McInnes, E.J.L., et al. (2024). Capturing the Elusive $[Ru^{V}=O]^{+}$ Intermediate in Water Oxidation. ACS Catal., *14*, acscatal.4c01623. (https://doi.org/10.1021/acscatal.4c01623)

[81] Koper, M.T.M. (2013). Theory of multiple proton–electron transfer reactions and its implications for electrocatalysis. Chem. Sci., *4*, 2710. (https://doi.org/10.1039/c3sc50205h)

[82] Wada, T., Nishimura, S., Mochizuki, T., Ando, T., and Miyazato, Y. (2017). Mechanism of Water Oxidation Catalyzed by a Dinuclear Ruthenium Complex Bridged by Anthraquinone. Catalysts, *7*, 56. (https://doi.org/10.3390/catal7020056)

[83] Duan, L., Xu, Y., Tong, L., and Sun, L. (2011). Ce^{IV} - and Light-Driven Water Oxidation by $[Ru(terpy)(pic)_3]^{2+}$ Analogues: Catalytic and Mechanistic Studies. ChemSusChem, *4*, 238–244. (https://doi.org/10.1002/cssc.201000313)

[84] Trotochaud, L., Ranney, J.K., Williams, K.N., and Boettcher, S.W. (2012). Solution-Cast Metal Oxide Thin Film Electrocatalysts for Oxygen Evolution. J. Am. Chem. Soc., *134*, 17253–17261. (https://doi.org/10.1021/ja307507a)

[85] Dolomanov, O.V., Bourhis, L.J., Gildea, R.J., Howard, J.A.K., and Puschmann, H. (2009). *OLEX2*: a complete structure solution, refinement and analysis program. J Appl Crystallogr, *42*, 339–341. (https://doi.org/10.1107/S0021889808042726)

[86] Sheldrick, G.M. (2015). *SHELXT* – Integrated space-group and crystal-structure determination. Acta Crystallogr A Found Adv ,*71*, 3–8. (https://doi.org/10.1107/S2053273314026370)

[87] Sheldrick, G.M. (2008). A short history of *SHELX*. Acta Crystallogr A Found Crystallogr, *64*, 112–122. (https://doi.org/10.1107/S0108767307043930)

CHAPTER 3

Microwave-Accelerated Catalysis with Ru(II)-pNHC Complexes for Selective *N*-Methylation of Anilines Using Methanol as a Sustainable C1 Source

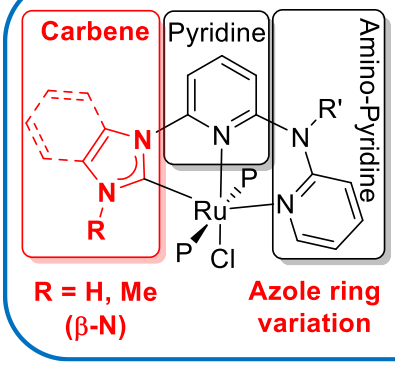

In this chapter, we focus on the structural variation of azole moieties. Modifying the azole group alters the electronic properties of carbene, leading to a noticeable difference in catalytic efficiency. Additionally, the effect of β-Nitrogen substitution in the CPAP ligand framework has also been examined. To assess the catalytic efficiency, we employed the N-methylation of aniline using methanol under both thermal-assisted and microwave conditions to study the effect of microwave irradiation on catalytic performance.

3.1 Introduction

The formation of sustainable and efficient C-N bonds remains a major focus in modern catalysis, due to the importance of amine functionalities in pharmaceuticals, agrochemicals, fine chemicals, and functional materials.[1–6] The *N*-methylated amines are a valuable class of compounds, as they serve as key intermediates and structural motifs that modulate biological activity, lipophilicity, and pharmacokinetic behavior.[7-12] Traditional *N*-methylation methods rely on hazardous and waste-generating alkylating agents, such as methyl iodide, dimethyl sulfate, or formaldehyde, which pose serious environmental and safety concerns.[13–17] In contrast, the use of methanol as a benign and renewable C1 feedstock, coupled with hydrogen-borrowing (or autotransfer) catalysis, provides a highly atom-economical and environmentally friendly alternative for selective *N*-methylation, generating only water as the stoichiometric byproduct.[18–27]

Recently, transition-metal catalysts have emerged as versatile platforms for C-N bond formation, particularly Ru-NHC systems due to their exceptional stability, tunable electronic properties, and robust metal-ligand cooperativity, which promote bifunctional pathways that enhance both activity and selectivity.[23,28–34] These properties of pNHC make them ideally suited for *N*-methylation of anilines using methanol, a benign and sustainable C1 source activated through a borrowing hydrogen mechanism (Figure 3.1).[26,35,36] Cooperative pincer-type

scaffolds effectively modulate the electronic environment of the metal center, lower activation barriers, and improve catalytic turnover.[37–40] Bai et al. reported NNN-pincer Ru complexes that display remarkable activity, with OMe-substituted derivatives showing a superior substrate scope.[41] Beller's group demonstrated highly efficient cyclometalated Ru complexes,[28] while Pirani and Eshghi showcased a caffeine-derived Ru-NHC system combining excellent mono-selectivity with green credentials.[42] Srimani et al. introduced an acridine-based SNS-Ru catalyst that promotes robust *N*-methylation under mild conditions.[43] Collectively, these studies underscore the versatility of Ru-NHC and Ru-pincer architectures as powerful, sustainable platforms for selective *N*-methylation transformations using methanol (Figure 3.2).[43-45]

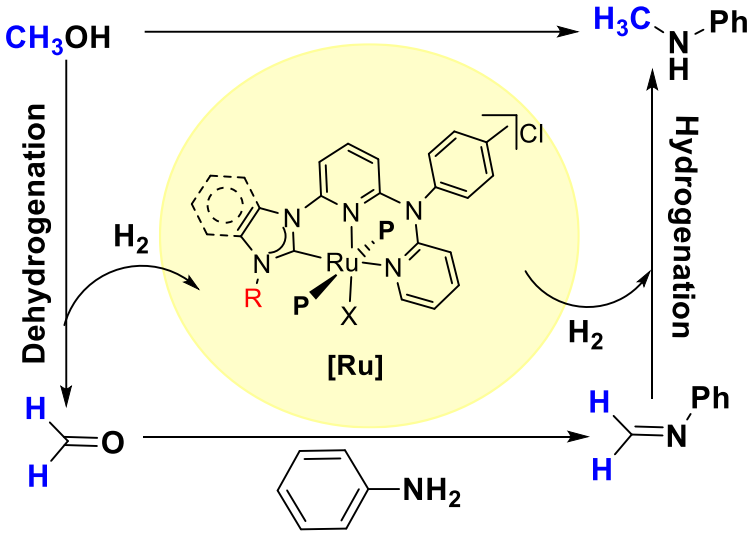

Figure 3.1 A general hydrogen borrowing reaction mechanism for *N*-methylation of amines with methanol.

Microwave-assisted organic synthesis (MAOS) has revolutionized synthetic chemistry by offering a rapid, energy-efficient, and sustainable alternative to conventional heating methods.[47–51] Unlike traditional protocols, which often require prolonged heating, harsh conditions, and yield limitations, microwave irradiation enables rapid reaction rates, higher selectivity, cleaner profiles, and improved energy efficiency.[52,53] Reports have demonstrated that microwave-assisted *N*-alkylation, employing alcohols as sustainable C1 sources, enables the efficient synthesis of alkylated amines in excellent yields within only a few

minutes.[54–57] This strategy offers broad substrate tolerance and significantly simplifies the product isolation. The studies highlight the advantages of microwave irradiation over conventional thermal conditions, particularly in terms of reaction acceleration and operational simplicity.[58,59] However, the inability to sufficiently lower the reaction temperature remains a limitation, underscoring the need for further investigation and methodological refinement.[60] Collectively, this methodology exemplifies the principles of green chemistry, providing a superior alternative to traditional approaches in both academic and industrial contexts.[61,62] Notably, Crabtree and co-workers demonstrated microwave-assisted *N*-methylation of anilines using methanol and an iridium catalyst,[63] yet the distinct benefits of microwave irradiation-such as milder reaction conditions, shorter reaction times, and improved energy utilization-remain insufficiently explored.

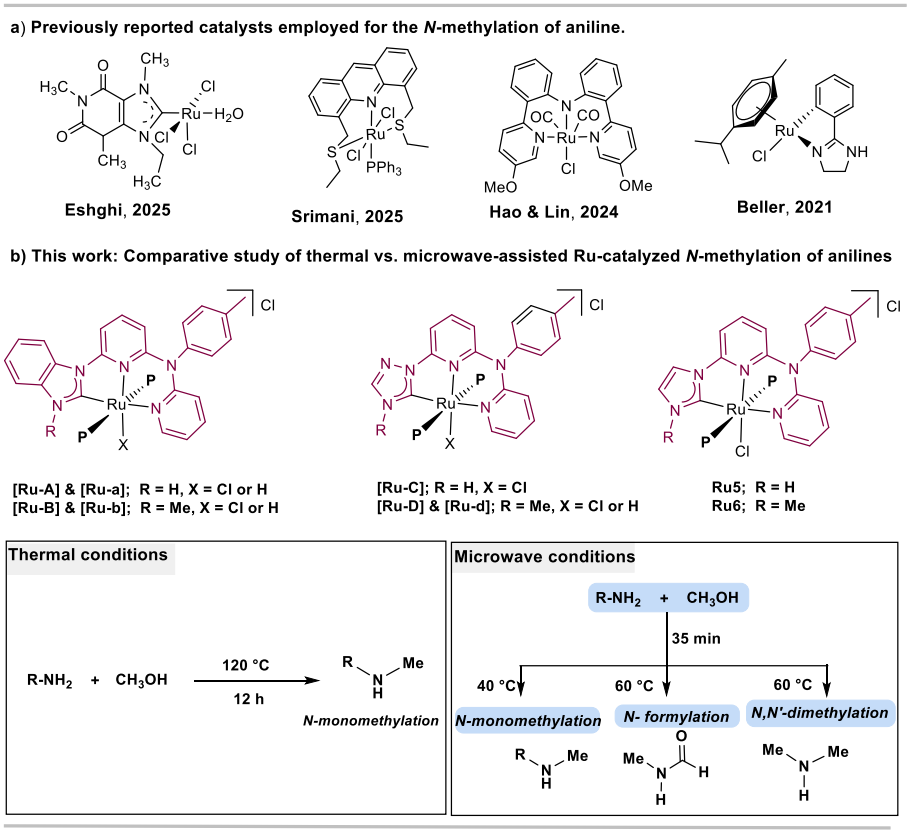

Figure 3.2 (**a**) Selected examples of reported catalysts for *N*-methylation of anilines. (**b**) Comparative study of **[Ru-A]-[Ru-d]** and **Ru5-Ru6** complexes under thermal and microwave conditions, demonstrating enhanced efficiency under microwave-assisted catalysis

Herein, we report a systematic investigation of ruthenium (II) complexes bearing unsymmetrical protic and classical NHC pincer ligands, elucidating their structural features, electronic properties, and catalytic efficiency in the sustainable *N*-methylation of anilines using methanol as a green C1 source. Building on our previous work on Ru-pNHC systems, [**Ru-A]-[Ru-d]**,[64-66] a new pair of complexes (**Ru5** and **Ru6**) incorporating an imidazolylidene core was synthesized and thoroughly characterized by multinuclear NMR and high-resolution mass spectrometry. These complexes form a set that differs based on the azole moiety. A direct comparison is made between complexes bearing benzimidazolylidene, triazolylidene, and imidazolylidene moieties that are capable of generating carbenes.

The protic NHC complex **Ru5**, in particular, displayed enhanced activity, inspiring a broader catalytic screening of [**Ru-A]-[Ru-d]** under both thermal and microwave-assisted conditions. The comparative study revealed that microwave irradiation dramatically improved reaction efficiency and selectivity under milder conditions, enabling rapid and quantitative *N*-methylation within minutes. The methodology exhibited broad substrate scope, excellent functional group tolerance, and scalability to the gram scale, underscoring its synthetic practicality. Detailed mechanistic studies, supported by control experiments, NMR, and mass spectrometric analyses, established a hydrogen-borrowing pathway mediated by a Ru-hydride intermediate, with methanol serving as the exclusive source of both methyl and hydrogen donors. Collectively, these findings highlight the synergistic role of ligand design and microwave-assisted catalysis in achieving efficient, atom-economical, and environmentally benign *N*-alkylation processes.

3.2 Results and discussion

A series of ruthenium complexes bearing an unsymmetrical ligand framework, previously developed by our group, has been systematically investigated to elucidate their structural features and catalytic potential across diverse catalytic applications.[64–66] In continuation of our efforts

toward the design of efficient homogeneous catalysts, we examined our previously reported ruthenium pincer complexes [**Ru-A]-[Ru-d]** (Figure 3.2),[64,65] which have demonstrated remarkable activity in hydrogenation reactions.[66] Notably, the protic benzimidazolylidene complex [**Ru-A]** exhibited better catalytic performance, thereby motivating the incorporation of an imidazolylidene core into the ligand scaffold to afford two new complexes, **Ru5** and **Ru6**, derived from recently developed imidazole-based ligands.[34]

The protic-imidazolylidene complex **Ru5** was synthesized via the reaction of 6-(1*H*-imidazol-1-yl)-*N*-(pyridin-2-yl)-*N*-(*p*-tolyl)pyridin-2-amine (**L3**) with $RuCl_2(PPh_3)_3$ in methanol. In contrast, the corresponding methylated analogue **Ru6** was obtained from the imidazolium salt precursor 3-methyl-1-(6-(pyridin-2-yl(*p*-tolyl)amino)pyridin-2-yl)-1*H*-imidazol-3-ium iodide (**L4·HI**) derived from **L3**, and $RuCl_2(PPh_3)_3$ through a transmetalation pathway involving the *in situ* formation of a silver-carbene intermediate in the presence of Ag_2O (Scheme 3.1).

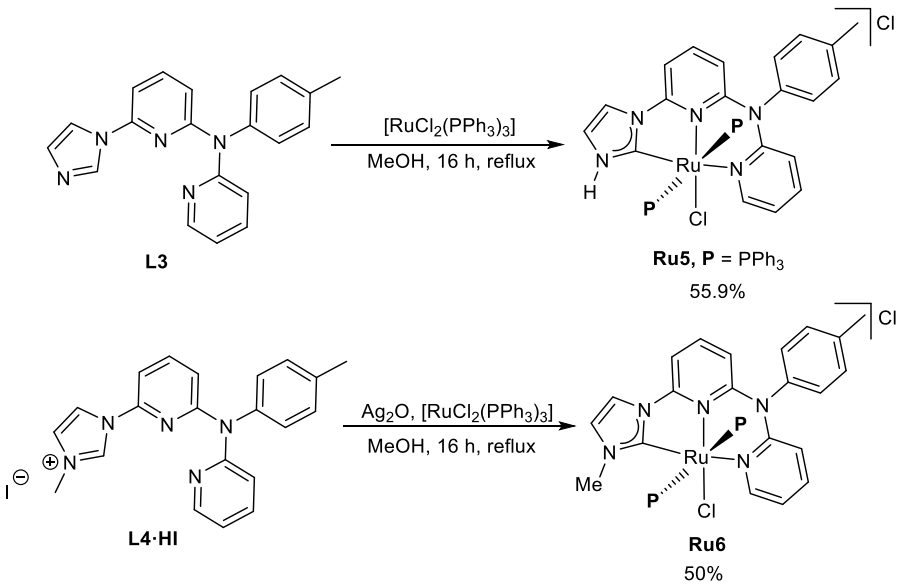

Scheme 3.1 Synthesis of Ru(II) pNHC complex **Ru5** and Ru(II) classical-NHC complex **Ru6**.

The formation of complexes **Ru5** and **Ru6** was confirmed by multinuclear NMR spectroscopy (^1H, ^{13}C, and ^{31}P) and high-resolution mass spectrometry. The ^1H NMR spectrum of **Ru5** displays distinct

resonances at δ 13.45 ppm (monophosphine) and δ 13.23 ppm (bisphosphine), which are attributed to the NH proton (Figure 3.3). These chemical shifts are in close agreement with those previously reported for analogous systems by our group. The dynamic equilibrium resulting from the DMSO-d_6 solvent is a key feature of this type of system, which we have already explained in our previous reports.[64] To verify the dynamic nature of such systems, a few experiments were conducted in the previous report using CuI and PPh_3, which confirmed the presence of both mono- and bisphosphine complexes.[64] The $^{31}P\{^1H\}$ NMR spectrum of **Ru5** reveals three resonances at δ 32.4 ppm corresponding to the coordinated monophosphine species, δ 23.9 ppm assigned to the bisphosphine complex, and a signal at δ - 6.0 ppm arising from free PPh_3 (Figure. 3.5). In the $^{13}C\{^1H\}$ NMR spectrum, a characteristic Ru-$C_{carbene}$ doublet signal at δ 187.8 ppm (J = 3.1 Hz) is observed, indicative of a metal-bound carbene carbon in the monophosphine species (Figure. 3.4). Furthermore, high-resolution ESI^+ mass spectrometry shows a prominent ion peak at m/z 726.1149, corresponding to $[M\text{-}Cl\text{-}PPh_3]^+$, which is the consistent with calculated mass for the proposed cationic fragment.

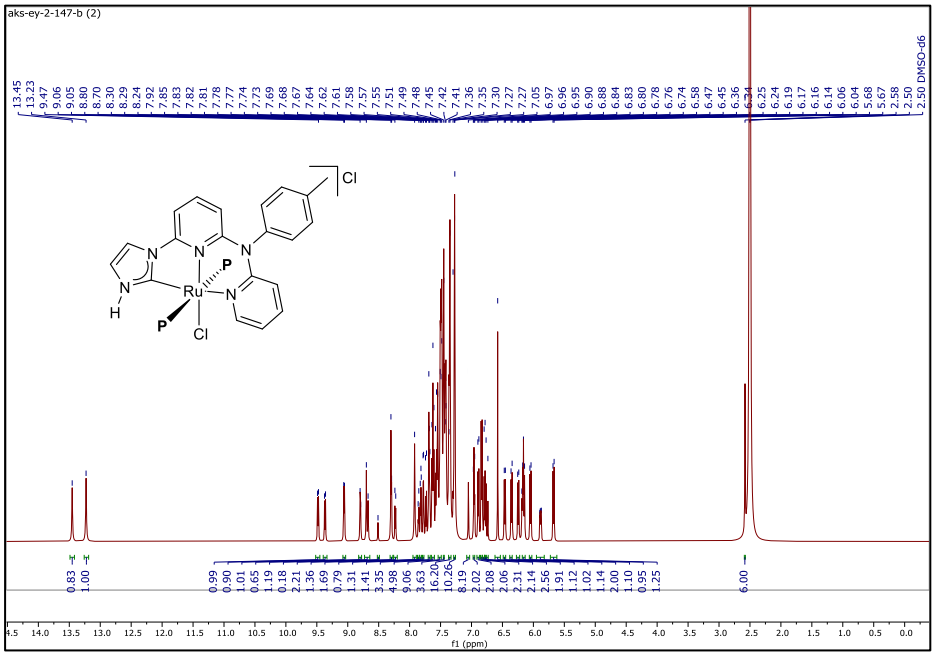

Figure 3.3 ^1H NMR of **Ru5** in DMSO-d_6

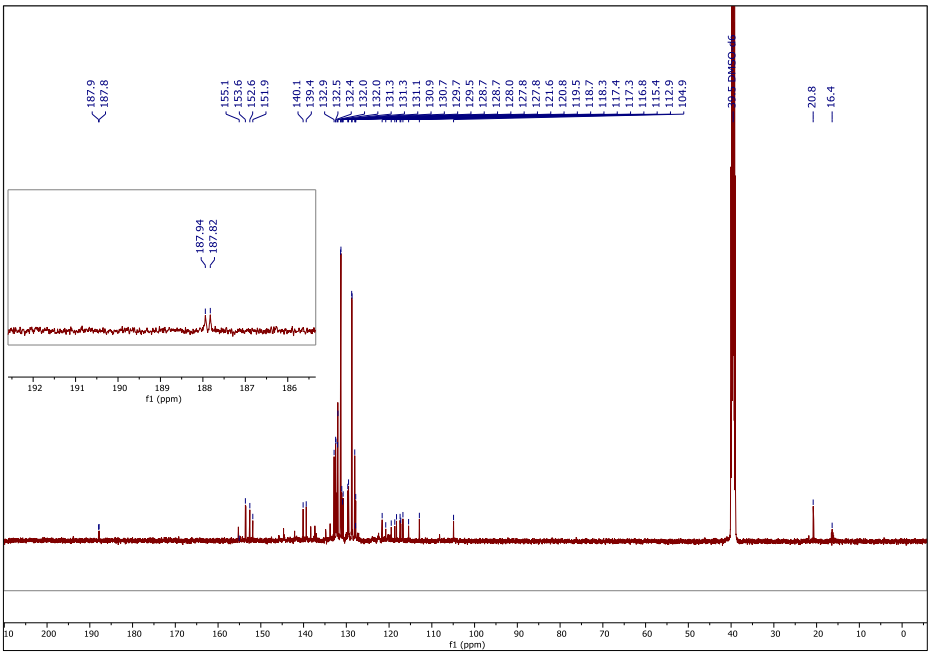

Figure 3.4 ^{13}C NMR of **Ru5** in DMSO-d_6

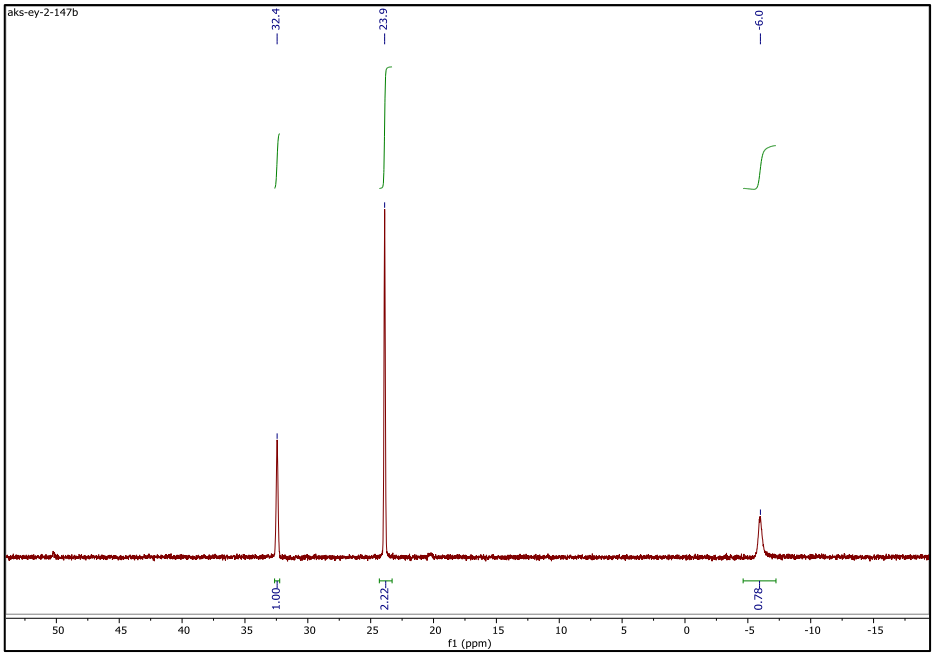

Figure 3.5 ^{31}P NMR of **Ru5** in DMSO-d_6

The *N*-methylated complex **Ru6** exhibits two well-resolved downfield doublets in its ^{1}H NMR spectrum at δ 9.43 and 9.39 ppm, corresponding to the ortho-protons of the pyridyl moiety in the mono- and bisphosphine species, respectively (Figure 3.6). The *p*-tolyl methyl resonances are observed at δ 2.43 and 2.33 ppm, while the *N*-CH_3 proton signals appear at δ 4.09 and 3.95 ppm for the mono- and bisphosphine

forms, respectively (Figure 3.6). In the $^{13}C\{^{1}H\}$ NMR spectrum, a characteristic Ru-$C_{carbene}$ doublet signal at δ 185.8 ppm (J = 14.0 Hz) is observed. The $^{31}P\{^{1}H\}$ NMR spectrum displays two sharp singlets at δ 33.3 and 25.1 ppm, characteristic of the mono- and bisphosphine complexes, along with an additional signal at δ -6.0 ppm, corresponding to free PPh_3, based on the ratio of mono-, bisphosphine, and free phosphine (Figure 3.8).

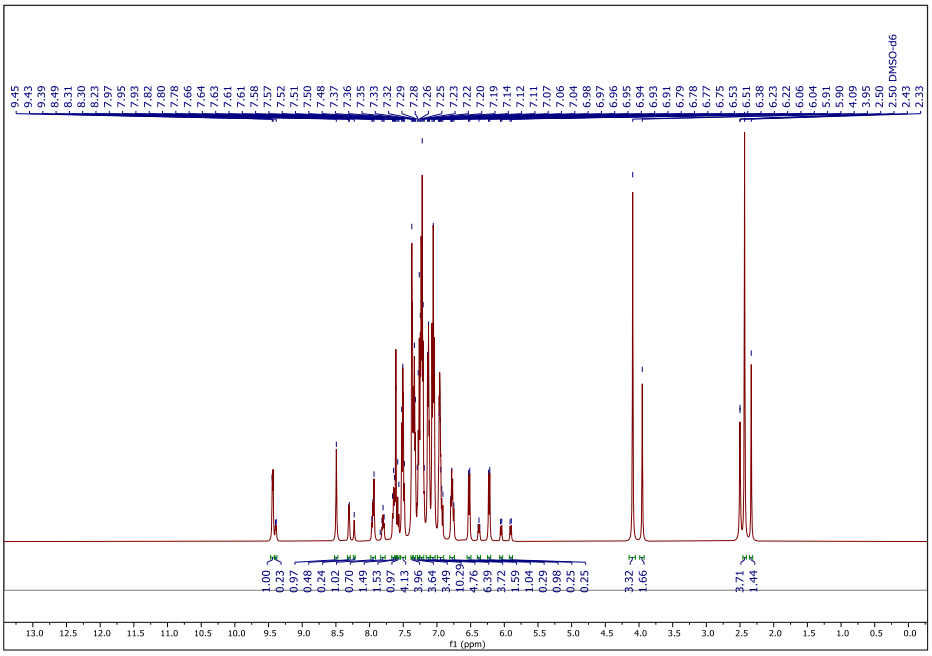

Figure 3.6 ^{1}H NMR of **Ru6**

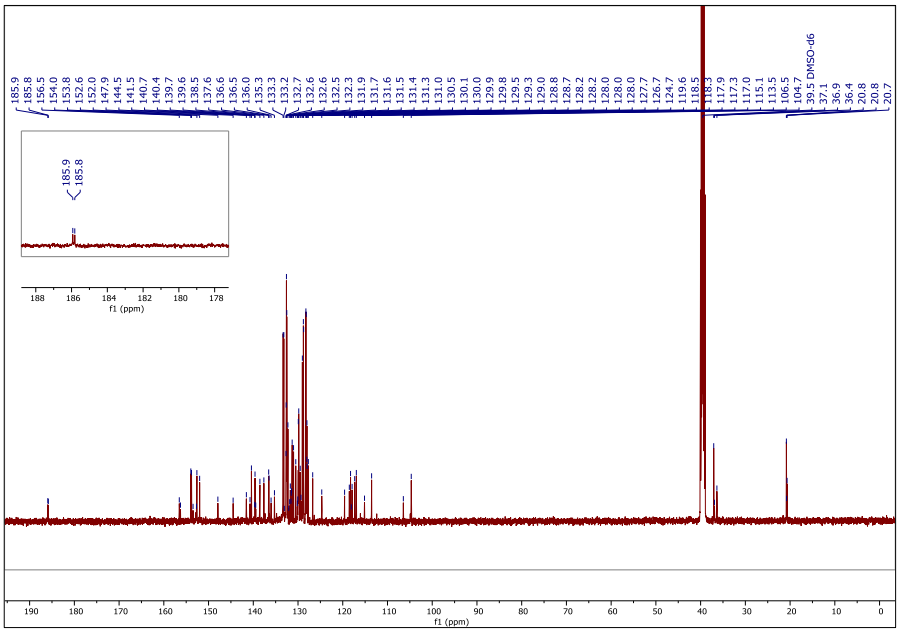

Figure 3.7 ^{13}C NMR of **Ru6**

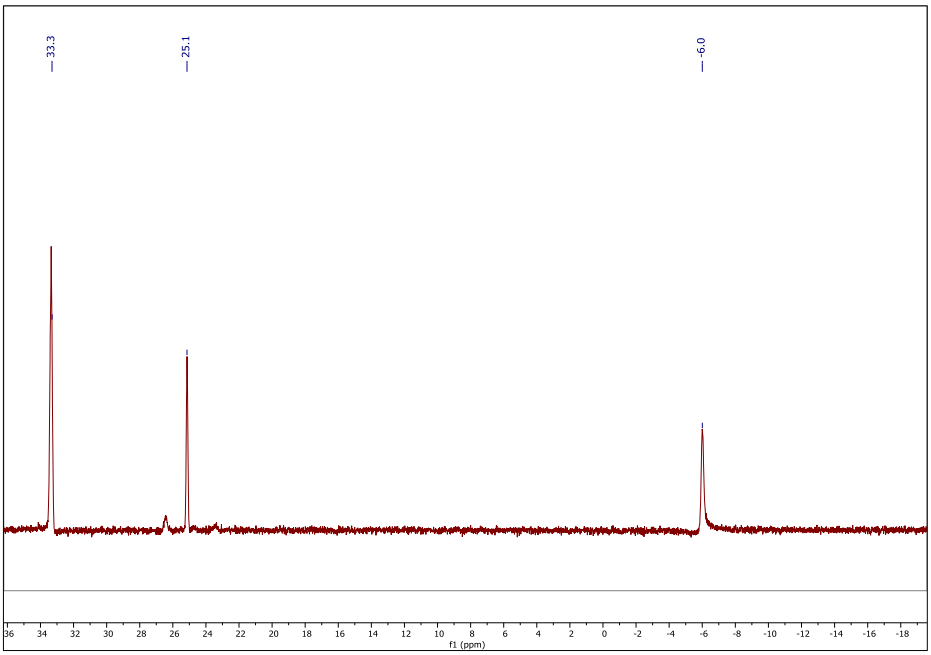

Figure 3.8 ^{31}P NMR of **Ru6**

High-resolution ESI$^+$ mass spectrometry confirms the molecular composition, revealing a prominent ion peak at m/z = 740.1317 with the expected isotopic distribution pattern, consistent with the [M-Cl-PPh_3]$^+$ fragment.

3.2.1 Reaction optimization and comparative evaluation of thermal and microwave-assisted *N*-methylation of anilines. To evaluate the catalytic potential of these complexes, we selected the *N*-methylation of anilines as a model transformation, given the widespread importance of amines and their methylated derivatives in pharmaceuticals and industry.[67] In this context, we systematically compared thermal and microwave-assisted *N*-methylation of anilines to assess efficiency, sustainability, and scalability.

3.2.1.1 Thermal *N*-methylation of anilines. We initiated our study by optimizing the reaction conditions for the *N*-methylation of aniline using methanol as an economical and environmentally benign methylating agent, employing the newly synthesized protic-imidazolylidene ruthenium complex, **Ru5**, as the precatalyst. Initially, the effect of various inorganic bases on the *N*-methylation of aniline was evaluated using **Ru5** as the precatalyst (Table 3.1, entries 1-6). When aniline was

treated with methanol at 110 °C using **Ru5** (1 mol%) and KO^{t}Bu (0.1 mol%) as base, a moderate conversion of 52% to *N*-methylaniline was achieved after 24 h, as determined by GC analysis. In contrast, weaker bases such as Cs_2CO_3 and K_2CO_3 afforded no significant improvement in yield (Table 3.1, entries 5-6). Extending the reaction time under these conditions improved the yield to 63% (Table 3.1, entry 7). However, increasing the methanol volume to 1.5 mL caused a significant decline in yield to 52% (Table 3.1, entry 8). Increasing the base loading further enhanced the conversion of 1 (Table 3.1, entry 9), and raising the reaction temperature under optimized conditions boosted the yield to 96% (Table 3.1, entry 10). Notably, prolonging the reaction time to 30 h afforded a conversion of > 99% (Table 3.1, entry 11). Under the same conditions, **Ru6** also exhibited catalytic activity, albeit slightly lower than that of **Ru5** (Table 3.1, entry 12). Screening a series of complexes**, [Ru-A]-[Ru-d]**, under optimized conditions revealed that **[Ru-A]** exhibited superior catalytic activity, achieving a conversion of >99% in 24 hours (Table 3.1, entries 13-19). Notably, reducing the catalyst loading of **[Ru-A]** did not affect the conversion (Table 3.1, entry 20), and lowering the base loading to 0.5 mmol still resulted in >99% conversion (Table 3.1, entries 21-22). Interestingly, shortening the reaction time to 12 h also maintained complete conversion of 1 (Table 3.1, entry 23).

Table 3.1 Optimization of thermal *N*-methylation of anilines catalyzed by ruthenium complexes[a]

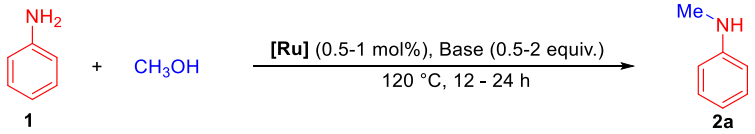

1 2a

#	[Ru] (mol%)	Base (mmol)	Additives (mol%)	Solvent (ml)	Temp (°C)	Time (h)	Conversion [b] (%)
1.	**Ru5(1)**	KO^{t}Bu (1)	-	1	110	24	52
2.	**Ru5 (1)**	NaO^{t}Bu (1)	-	1	110	24	49
3.	**Ru5 (1)**	NaOH (1)	-	1	110	24	25
4.	**Ru5 (1)**	KOH (1)	-	1	110	24	50

5.	**Ru5 (1)**	Cs_2CO_3 (1)	-	1	110	24	22
6.	**Ru5 (1)**	K_2CO_3 (1)	-	1	110	24	20
7.	**Ru5 (1)**	KO^{t}Bu (1)	-	1	110	30	63
8.	**Ru5 (1)**	KO^{t}Bu (1)	-	1.5	110	24	52
9.	**Ru5 (1)**	KO^{t}Bu (2)	-	1	110	24	86
10.	**Ru5 (1)**	KO^{t}Bu (2)	-	1	120	24	96
11.	**Ru5 (1)**	KO^{t}Bu (2)	-	1	120	30	>99
12.	**Ru6(1)**	KO^{t}Bu (2)	-	1	120	24	56
13.	**[Ru-A](1)**	KO^{t}Bu (2)	-	1	120	24	95
14.	**[Ru-a](1)**	KO^{t}Bu (2)	-	1	120	24	45
15.	**[Ru-B](1)**	KO^{t}Bu (2)	-	1	120	24	79
16.	**[Ru-b](1)**	KO^{t}Bu (2)	-	1	120	24	20
17.	**[Ru-C](1)**	KO^{t}Bu (2)	-	1	120	24	73
18.	**[Ru-D](1)**	KO^{t}Bu (2)	-	1	120	24	69
19.	**[Ru-d](1)**	KO^{t}Bu (2)	-	1	120	24	16
20.	**[Ru-A](0.5)**	KO^{t}Bu (2)	-	1	120	24	>99
21.	**[Ru-A](0.5)**	KO^{t}Bu (1)	-	1	120	24	>99
22.	**[Ru-A](0.5)**	KO^{t}Bu (0.5)	-	1	120	24	>99
23.	**[Ru-A](0.5)**	**KO^{t}Bu (0.5)**	**-**	**1**	**120**	**12**	**>99**
24.[c]	**Ru5 (1)**	NaOMe (1)	-	1	120	24	67
25.[c]	**Ru5 (1)**	NaOMe (1)	$NaBPh_4$ (10)	1	120	24	69
26.[c]	**Ru5 (1)**	NaOMe (1)	$NaBPh_4$ (20)	1	120	24	74
27.[c]	**Ru5 (1)**	NaOMe (1)	$NaBPh_4$ (40)	1	120	24	92
28.[c]	**Ru5 (1)**	NaOMe (1)	$NaBPh_4$ (50)	1	120	24	>99
29.[c]	**Ru5(1)**	NaOMe (1)	$NaBF_4$ (20)	1	120	24	27
30.	**Ru5(1)**	KO^{t}Bu (1)	$NaBPh_4$ (50)	1	120	24	98

[a]Reaction conditions: Methanol (1 mL, 0.0247 mol), cat. (0.5-1 mol%), and KO^{t}Bu (0.5 equiv. 0.5 mmol) at 120 °C for 12 h. Conversion[b] was obtained through GC-MS without using an internal standard. [c]*In situ*-generated NaOMe by the addition of Na metal in methanol.

To reduce the reliance on excess base, sodium metal was evaluated as an alternative, showing slightly higher activity than KO^{t}Bu

(Table 3.1, entry 24). To further enhance the catalytic efficiency of **Ru5**, the effects of various additives were systematically examined. Building on our previous study on sodium salt additives in amine *N*-alkylation,[68] $NaBPh_4$ significantly improved the conversion, achieving complete transformation at a 50 mol% loading (Table 3.1, entry 27), whereas $NaBF_4$ had a minimal effect (entry 29). Notably, the combination of $NaBPh_4$ with KO^tBu (1 mmol) further increased the product yield (entry 30). Among the screened complexes, **[Ru-A]** exhibited superior catalytic activity. The optimized conditions were 0.5 mol% **[Ru-A]**, 0.5 mmol KO^tBu, 1 mL methanol, and 4 Å molecular sieves at 120 °C under an Ar atmosphere. Molecular sieves were essential because the water generated as a byproduct adversely affected the reaction by shifting the equilibrium unfavorably.

The benzimidazolylidene-based complex (**[Ru-A]**) exhibited the highest catalytic activity among all the complexes in the series. The fused aromatic ring system of the benzimidazole moiety contributes to the increased rigidity, enhanced π-delocalization, and improved stability of the NHC ligand framework. Conversely, imidazolylidene-based complexes exhibit greater σ-donor strength but poor π-acceptor capacity, along with lower structural rigidity, which leads to weaker stabilization of catalytic intermediates.[69] Triazolylidene-based complexes, possessing the poorest σ-donor capacity among all with good π-acceptor ability, although often more electron-deficient, display distinct electronic and steric profiles that can reduce hydride formation efficiency and decelerate key steps in the catalytic cycle, thereby explaining their comparatively lower performance.[69]

The data in Table 1 show that the complexes bearing classical NHC ligands exhibit lower catalytic activity than those containing protic NHC ligands. This trend aligns with our mechanistic understanding: the protic carbene systems facilitate protonation due to their acidic *N*-H functionality, which forms an anionic NHC after deprotonation. This enhances the dissociation of PPh_3 compared to the classical NHC-containing complex, enabling more efficient catalytic steps.[65] PPh_3

dissociation is a key feature of the catalytic pathway, which is relatively slower in the classical NHC complex than in the anionic NHC complex, likely accounting for their reduced efficiency under similar reaction conditions.

3.2.1.2 Microwave-assisted *N*-methylation of anilines

To overcome the harsh conditions typically required for the *N*-methylation of anilines using methanol, we evaluated our most active catalyst, **[Ru-A],** under microwave (MW) irradiation for the *N*-methylation of aniline (Table 3.2). Initial experiments at 60 °C, conducted via GC-MS analysis, revealed the formation of *N*-methylaniline (**2a**), *N*-methyl-*N*-phenylformamide (**3a**), and *N*, *N*-dimethylaniline (**4a**), along with minor unidentified byproducts. Time-course studies spanning 1-40 min confirmed the progressive formation of these products (Table 3.2, entries 1-6). To improve selectivity, suppression of *N*-formylation and other side reactions was essential. Reducing the temperature to 50 °C reduced but did not eliminate the formation of **3a** and **4a** (Table 3.2, entry 7). Further lowering the temperature to 40 °C increased the selectivity toward *N*-methylaniline (**2a**) to 92%. Prolonging the reaction time proportionally increased the yield, achieving quantitative conversion within 35 min (Table 3.2, entry 14). Notably, at elevated reaction times and temperatures, selective dimethylation could not be achieved, as **3a** began to form preferentially under these conditions (Table 3.2, entry 15).

Microwave-assisted reactions heat up quickly and evenly. This means that energy is more evenly distributed in the reaction mixture than with regular heating. It reduces temperature differences and hot spots, accelerating important reaction steps. In our setup, it enhances catalyst activation and facilitates faster interactions between substrates and catalysts as molecules move more efficiently with controlled heating. Although the reaction path remains the same as that with thermal heating, microwaves accelerate the kinetics of the reactions, resulting in a higher conversion and a shorter time to achieve greater efficiency.

Table 3.2 Optimization for reaction conditions for microwave-assisted *N*-methylation of anilines catalysed by [Ru-A][a]

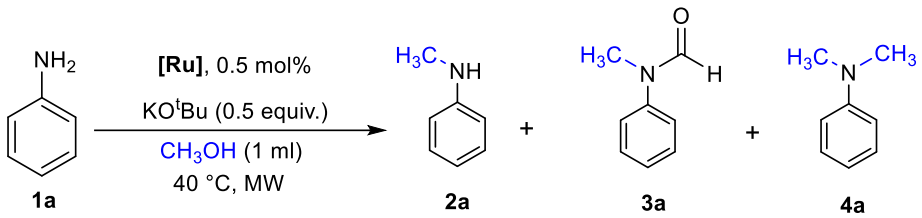

#	[Ru]	Temp (°C)	Time (min)	% Conversion (2a:3a:4a)[b]
1.	**[Ru-A]**	60	40	>99 (58:1:4)
2.	**[Ru-A]**	60	35	>99 (84:3:13)
3.	**[Ru-A]**	60	30	>99 (86:8:6)
4.	**[Ru-A]**	60	15	99 (90:3:6)
5.	**[Ru-A]**	60	5	99 (91:2:6)
6.	**[Ru-A]**	60	1	>99 (92:2:6)
7.	**[Ru-A]**	50	1	>99 (90:4:6)
8.	**[Ru-A]**	40	1	2 (2:n.d.:n.d.)
9.	**[Ru-A]**	40	5	17 (17:n.d.:n.d.)
10.	**[Ru-A]**	40	10	58 (58:n.d.:n.d.)
11.	**[Ru-A]**	40	15	68 (68:n.d.:n.d.)
12.	**[Ru-A]**	40	20	72 (72:n.d.:n.d.)
13.	**[Ru-A]**	40	25	77 (77:n.d.:n.d.)
14.	**[Ru-A]**	**40**	**35**	**>99** (>99:n.d.:n.d.)
15.	**[Ru-A]**	70	40	>99 (n.d.:55:45)

[a]Reaction conditions: Methanol (1 ml, 0.0247 mol), cat. (0.5-1 mol%), and KO^{t}Bu (0.5 equiv. 0.5 mmol) at 40 °C with 500 W. Conversion[b] was obtained through GC-MS without using an internal standard. n.d. = not detected.

The reaction profile for the **[Ru-A]**-catalyzed *N*-methylation of aniline, monitored by gas chromatography (GC) under optimized conditions, revealed the rapid consumption of aniline accompanied by the formation of *N*-methylaniline with >99% conversion. The hydrogen-transfer reduction of the transient imine intermediate, *N*-phenylmethanimine, appeared to proceed rapidly, as no trace of this species was detected during the course of the reaction. This observation

suggests that the reduction of the imine intermediate is not the rate-determining step in the overall catalytic process (Figure 3.9).

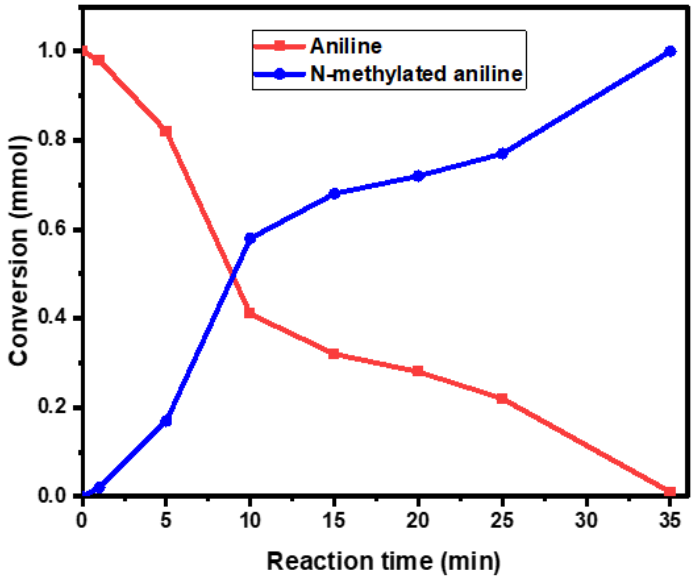

Figure 3.9 Reaction profile for the *N*-methylation of aniline using methanol as the methylating agent, monitored by GC. Reaction conditions: aniline (1.0 mmol), **[Ru-A]** (0.5 mol%), and KO^{t}Bu (0.5 equiv) in methanol (1.0 mL) at 40 °C.

3.2.2 Evaluation of substrate scopes under thermal and microwave conditions

Under the optimized reaction conditions, a broad range of aniline derivatives underwent smooth *N*-methylation to afford the corresponding *N*-methylanilines in good to excellent yields, regardless of the electronic nature of the substituents (Table 3.3). Both electron-donating (methyl, methoxy, and phenoxy) and electron-withdrawing (halogen) groups were well tolerated, demonstrating the versatility of the **[Ru-A]** catalytic system. Para-halogenated anilines (**2b-d**) furnished the desired products in excellent yields (94-95%), indicating that electron-withdrawing substituents such as chloro, bromo, and fluoro exerted negligible influence on the catalytic performance. Similarly, para-substituted electron-rich substrates (**2e-f**, **2h**) provided the corresponding *N*-methyl derivatives in good yields (90-95%). Notably, sterically encumbered di- and tri-substituted anilines (**2j-l**, **2n**) also underwent efficient

transformation, yielding isolated yields of 90-95%, which underscores the robustness of this transformation against both steric and electronic perturbations.

Interestingly, although meta- and para-substituted electron-donating anilines were efficiently converted, ortho-substituted derivatives afforded slightly lower yields, likely because steric hindrance influenced the catalyst-substrate interactions. Nevertheless, the products were obtained in synthetically useful yields, exemplified by **2m** (85%) and **2o** (79%). The methodology was further extended to heteroaromatic amines, with pyridine derivatives (**2p**-**r**) undergoing smooth transformations. Notably, 3-aminopyridine delivered a higher yield than 4-aminopyridine, a difference that may arise from variations in electronic distribution and steric orientation of the amino group. Substrates bearing strongly electron-donating substituents such as 3,5-dimethoxyaniline and *p*-phenoxy aniline were also well tolerated, affording excellent yields (93-95%) of corresponding products, **2s** and **2h**, respectively. Moreover, fused aromatic systems, including 1-naphthylamine and 8-aminoquinoline, provided the *N*-methylated products, **2t** and **2v** efficiently, underscoring the capacity of the catalytic system to accommodate extended π-systems. Importantly, the standard reaction conditions also proved compatible with sensitive functional groups such as hydroxyl (**2g)** and ester (**2w)** moieties, delivering the corresponding products in good to excellent yields without competitive side reactions. Collectively, these results highlight the broad functional group tolerance, regioselectivity, and synthetic utility of the Ru-catalysed *N*-methylation strategy. Despite yielding good results for most substrates, the corresponding products of a few substrates, *viz.*, **2g**, **2v**, **2y**, **2ac**, **2ad**, and **2af**, showed lower yields due to either being o-substituted or having another coordinating group in their structure. Interestingly, the yields of some of the products of their respective substrates (**2o**, **2z**, **2aa**, **2ab**) improved significantly under microwave irradiation.

The products **2aa-2af** were not isolated; instead, their conversions were determined by GC-MS analysis using bromobenzene as an internal standard for quantifying the yield of the desired products.

Among these, **2aa**, **2ab**, and **2ae** yielded good results under thermally assisted conditions; however, the isolation of pure products proved challenging, and repeated attempts to obtain them in a pure form were unsuccessful. Consequently, yield estimations for these substrates were performed exclusively under microwave-assisted conditions using the internal standard method. In contrast, products **2ac**, **2ad**, and **2af** showed no detectable conversion under thermal conditions; however, under microwave irradiation and standard conditions, a slight yield enhancement was observed. Extending the reaction time to 1 h resulted in a noticeable increase in yield, indicating that these substrates require longer reaction times for effective conversion. To probe the scope of the methodology, substrate **1a** was examined using ethanol instead of methanol as the alkylating agent under microwave conditions, yielding product **2ag** in an excellent 94% isolated yield. Secondary anilines, such as diphenylamine, remained unreactive under both thermal and microwave conditions. Furthermore, attempts to methylate the product **2ag** under standard conditions did not yield any additional conversion.

Even under microwave conditions, a few substrates produced very low yields, indicating that certain substrates resulted in moderate to low yields. However, this trend is consistent with those of other studies involving challenging *N*-methylation substrates. A key aim of our research was to assess the performance of our catalytic system under microwave irradiation compared with conventional thermal conditions. Our results consistently demonstrated that several substrates, which only achieved trace or minimal conversion with thermal heating, showed significantly improved yields when microwaves were used. This underscores the advantages and practical importance of using microwave irradiation for this transformation.

Table 3.3 Substrate scope for the *N*-methylation of anilines catalyzed by **[Ru-A]**[a]

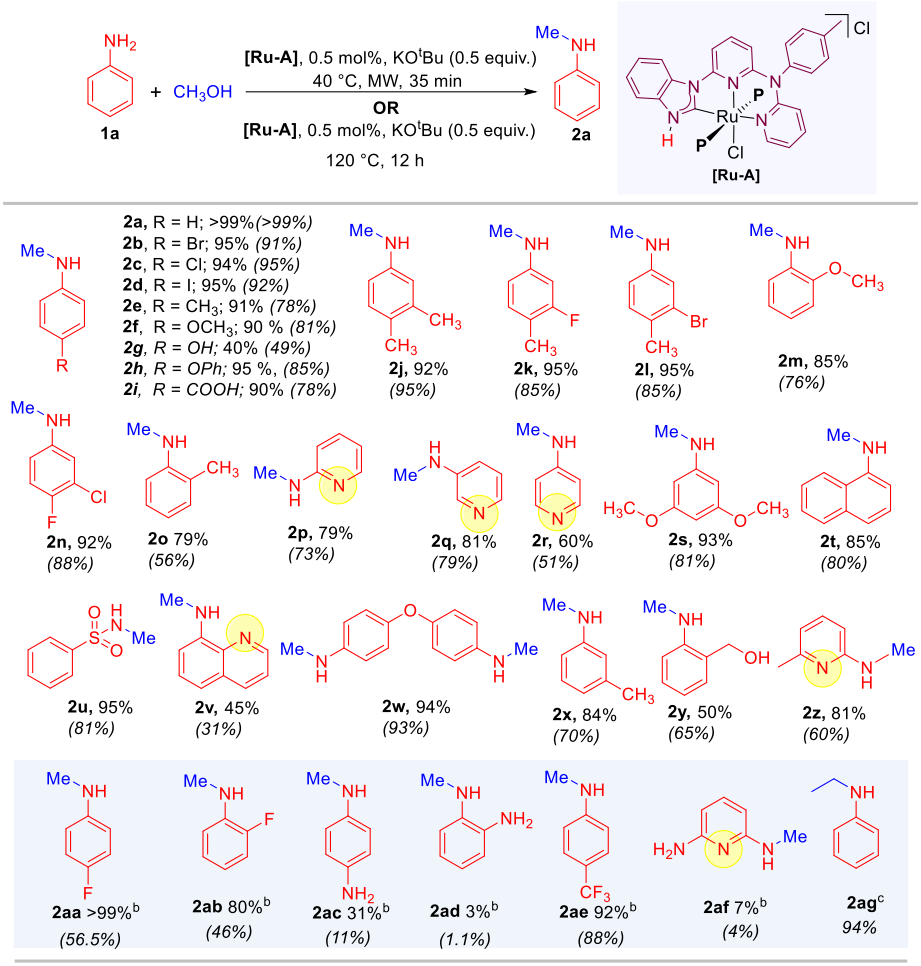

[a]Reaction conditions: Aniline derivative (1 mmol), methanol (1 ml, 0.0247 mol), catalyst (0.5 mol%), and KO^{t}Bu (0.5 equiv., 0.5 mmol) at 40 °C under microwave irradiation (500 W) or at 120 °C. Yields represent isolated products under microwave irradiation; values in parentheses indicate isolated yields under conventional thermal conditions. [b]Conversions and yields for **2aa-2af** were determined by GC-MS using bromobenzene as an internal standard. [c]Ethanol was used as the alkylating agent.

3.2.3 Gram-scale synthesis of *N*-methyl aniline

To establish the synthetic utility of this methodology, a gram-scale experiment was conducted for the *N*-methylation of aniline using methanol as the methylating agent (Scheme 3.2). The reaction was conducted on a 10 mmol scale under the optimized conditions with [**Ru-**

A] (0.5 mol%) and KO^{t}Bu (0.5 equiv) in methanol (10 ml) at 40 °C for 35 min under microwave irradiation, affording *N*-methylaniline in excellent yield. The transformation delivered 1.01 g (1.02 ml) of the product, corresponding to a 94% isolated yield, thereby confirming both the practicality and scalability of this catalytic system.

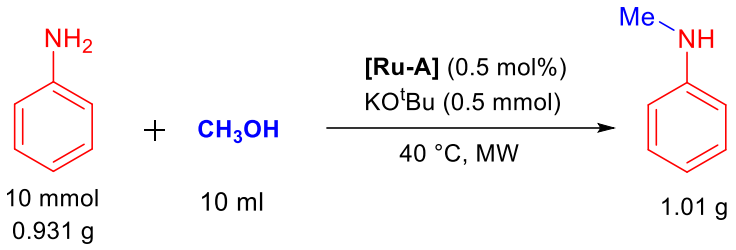

Scheme 3.2 Gram-scale reaction for the *N*-methylation of anilines.

3.2.4 Control Studies

To gain deeper mechanistic insight, a series of meticulously designed control experiments was performed (Figure 3.10). The control studies revealed the *in situ* generation of *N*-phenylmethanimine (m/z = 105.0578) from aniline and methanol under basic conditions. Upon subsequent treatment of this mixture with **[Ru-A]** at 80 °C in a Schlenk pressure tube, a mixture of aniline, *N*-methylaniline, and *N*-phenylmethanimine was obtained, thereby establishing the imine as a key catalytic intermediate in the methylation pathway (Figure 3.10a). To assess the potential role of formamides in the catalytic cycle, *N*-methyl-*N*-phenylformamide was subjected to standard reaction conditions, yielding *N*, *N*-dimethylaniline in an isolated yield of 80 %. This observation strongly suggests that formamide serves as a latent intermediate or reservoir under catalytic conditions (Figure 3.10b). In addition, *N*-phenylformamide also gives *N*-methylaniline in 91% isolated yield. Further support for the proposed mechanistic pathway was obtained from deuterium-labelling and complementary control experiments (Figure 3.10c). When CD_3OD was employed as the solvent under standard conditions, exclusive formation of *N*-methylaniline-d_3 (m/z = 110.0923) was observed, confirming selective incorporation of the -CD_3 group at nitrogen and unequivocally identifying methanol as the sole methyl source (Figure 3.10c).

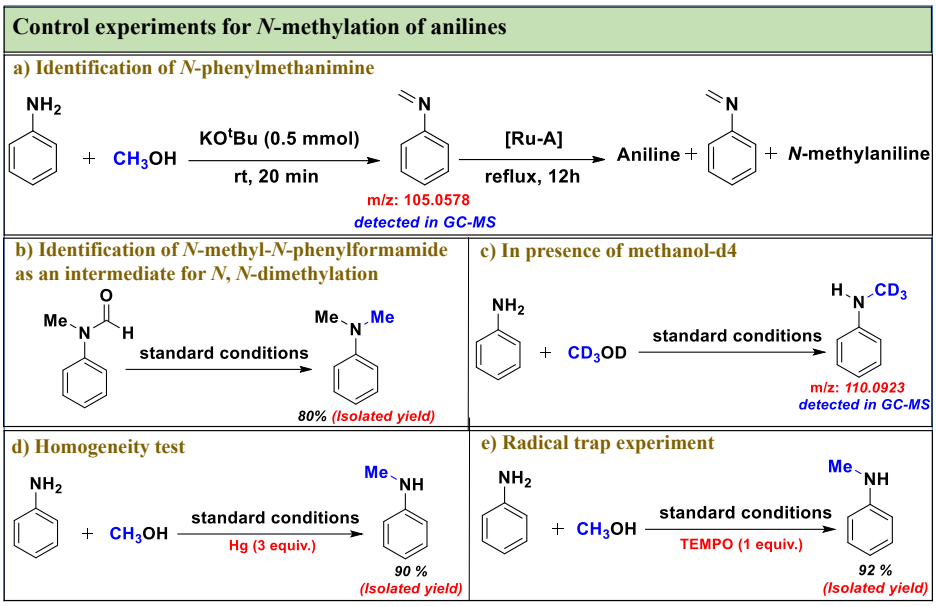

Figure 3.10 Control experiments elucidating the reaction pathway for **[Ru-A]**-catalyzed *N*-methylation of anilines. Standard condition: Aniline (1 mmol), methanol (1 ml, 0.0247 mol), catalyst (0.5 mol%), and KO^{t}Bu (0.5 equiv., 0.5 mmol) at 40 °C under microwave irradiation (500 W)

The nature of the active species was further examined by introducing metallic mercury (3 equiv.) under the optimized conditions. The reaction proceeded efficiently, affording *N*-methylaniline in 90% isolated yield, confirming that the active species is not significantly poisoned by Hg (0) (Figure 3.10d). Likewise, the addition of TEMPO (1 equiv.) as a radical scavenger did not suppress product formation, and *N*-methylaniline was obtained in an isolated yield of 92%, effectively ruling out the participation of a free-radical pathway in this methylation process (Figure 3.10e).

3.2.5 Mechanistic Studies

3.2.5.1 NMR analysis. To elucidate the intermediates involved in the catalytic mechanism and the potential pathway for the *N*-methylation of anilines, detailed NMR investigations were conducted (Figure 3.11). Initially, the ^{1}H, ^{13}C, and ^{31}P NMR spectra for **[Ru-A]** were analyzed. Stoichiometric treatment of **[Ru-A]** with KO^{t}Bu in a 1:1 ratio in DMSO-d_6 at room temperature resulted in complete conversion of **[Ru-A]** to **[Ru-A]′** within minutes, accompanied by a distinct color change from

yellow to orange-red. ^{1}H NMR analysis revealed the disappearance of the acidic *N*-H resonances at δ 14.15 and 13.97 ppm, confirming a clean transformation to **[Ru-A]′**. The subsequent addition of methanol, either at room temperature or upon heating at 60 °C for 2 h, did not lead to the reprotonation of **[Ru-A]′**. Instead, after heating, a Ru-hydride species was observed as a distinct triplet at δ -12.26 ppm (J_{PH} = 18.7 Hz), along with a signal for formaldehyde at δ 8.9 ppm, while the *N*-H signals remained absent. These observations unambiguously confirmed the formation of the Ru-H intermediate, providing strong evidence for a hydrogen-borrowing mechanism in the *N*-methylation process.

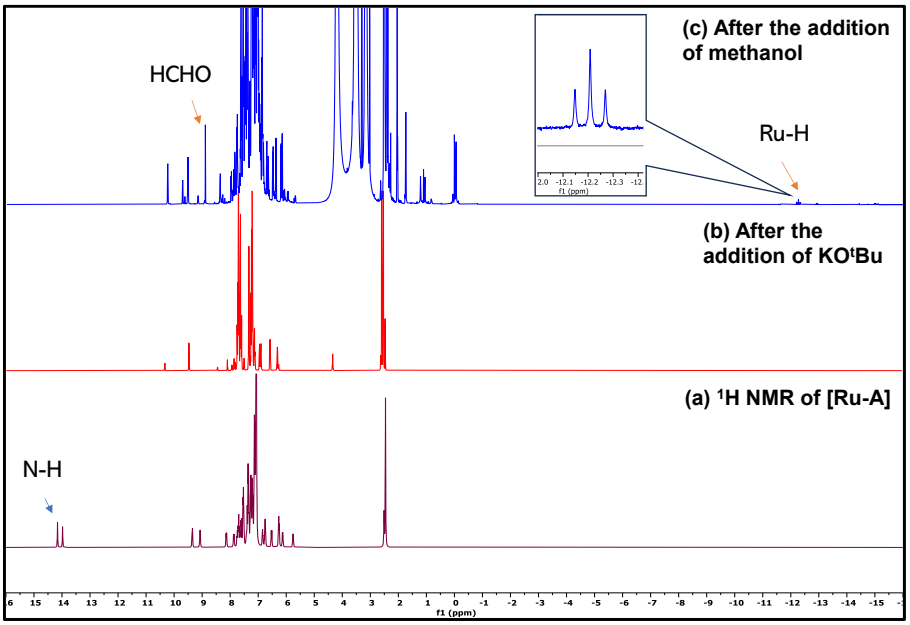

Figure 3.11 Mechanistic investigation using NMR experiments: ^{1}H NMR spectrum of (a) **[Ru-A]** and (b) after addition of 1 equiv. of base, KO^{t}Bu; (c) after subsequent addition of methanol.

3.2.5.2 Mass analysis. Mass spectrometric investigations of the catalytic mixture at various reaction intervals were performed to elucidate the intermediates involved in the *N*-methylation of aniline. At the early stage of the reaction, a signal at m/z = 812.1495 corresponding to $[M + CH_3OH + K]^+$ was detected, which can be attributed to the formation of the Ru-H species **3′**. As the reaction progressed, a highly intense peak at m/z = 1004.2985, assignable to the Ru-H derivative (**3′′**), was consistently observed at different time intervals. At the end of the *N*-methylation

process, a prominent signal at m/z = 878.2463 appeared, corresponding to the formation of species **5′**, confirming its role as the final catalytic intermediate in the transformation.

3.2.6 Proposed reaction mechanism

Based on NMR, mass spectrometric, and control experimental analyses, a plausible mechanistic pathway for the *N*-methylation of aniline was proposed (Figure 3.12). The catalytic cycle is initiated by the activation of the ruthenium pre-catalyst **[Ru-A]** through its interaction with the strong base KO^{t}Bu. Deprotonation of the NH moiety by the base affords the corresponding Ru-anionic-NHC complex (**[Ru-A]′**), which is the catalytically active species. Further involvement of the base in the presence of methanol facilitates the loss of the PPh_3 ligand to open a reactive site on the ruthenium center, along with the byproducts KCl salt and tert-butanol. This led to the formation of species **1′** on coordinating with the methanol and the formation of Ru-methoxide species. Species **1′** acts as a dehydrogenation catalyst for methanol. Specifically, the ruthenium-hydride species promotes the removal of hydrogen from methanol, yielding formaldehyde. In this process, a formaldehyde-bound ruthenium-hydride intermediate (species **2′**) is generated, which subsequently releases formaldehyde to regenerate the active hydride species **3′**. In the presence of phosphine, additional intermediate **3′′** is formed, as confirmed by mass spectrometric analysis. The regenerated hydride species is then capable of participating in subsequent catalytic transformations. Meanwhile, the in situ generated formaldehyde undergoes a condensation reaction with the primary amine present in the reaction mixture, leading to the formation of an imine intermediate with the elimination of water as a byproduct. The imine intermediate does not accumulate in the reaction mixture because the vacant coordination site on the ruthenium-hydride complex (**3′**) readily binds to the imine, resulting in the formation of species **4′**. Subsequently, the hydride ligand of the Ru-H bond in species **4′** is transferred from the ruthenium center to the imine carbon, thereby facilitating hydrogenation of the imine. In the presence of methanol, this process leads to the formation of species

5′, which was detected by mass spectrometric analysis. In species **5′**, a methanol molecule is coordinated to the ruthenium center and transfers its proton to the nitrogen atom of the coordinated aniline moiety. Following this protonation step, the *N*-methylated aniline is released from the metal center. This step is thermodynamically favored by an agostic interaction between the proton of the methoxide ligand and the ruthenium center, which provides additional stabilization. The release of the product restores the catalyst to its initial active form, thereby allowing the cycle to repeat (Figure 3.12).

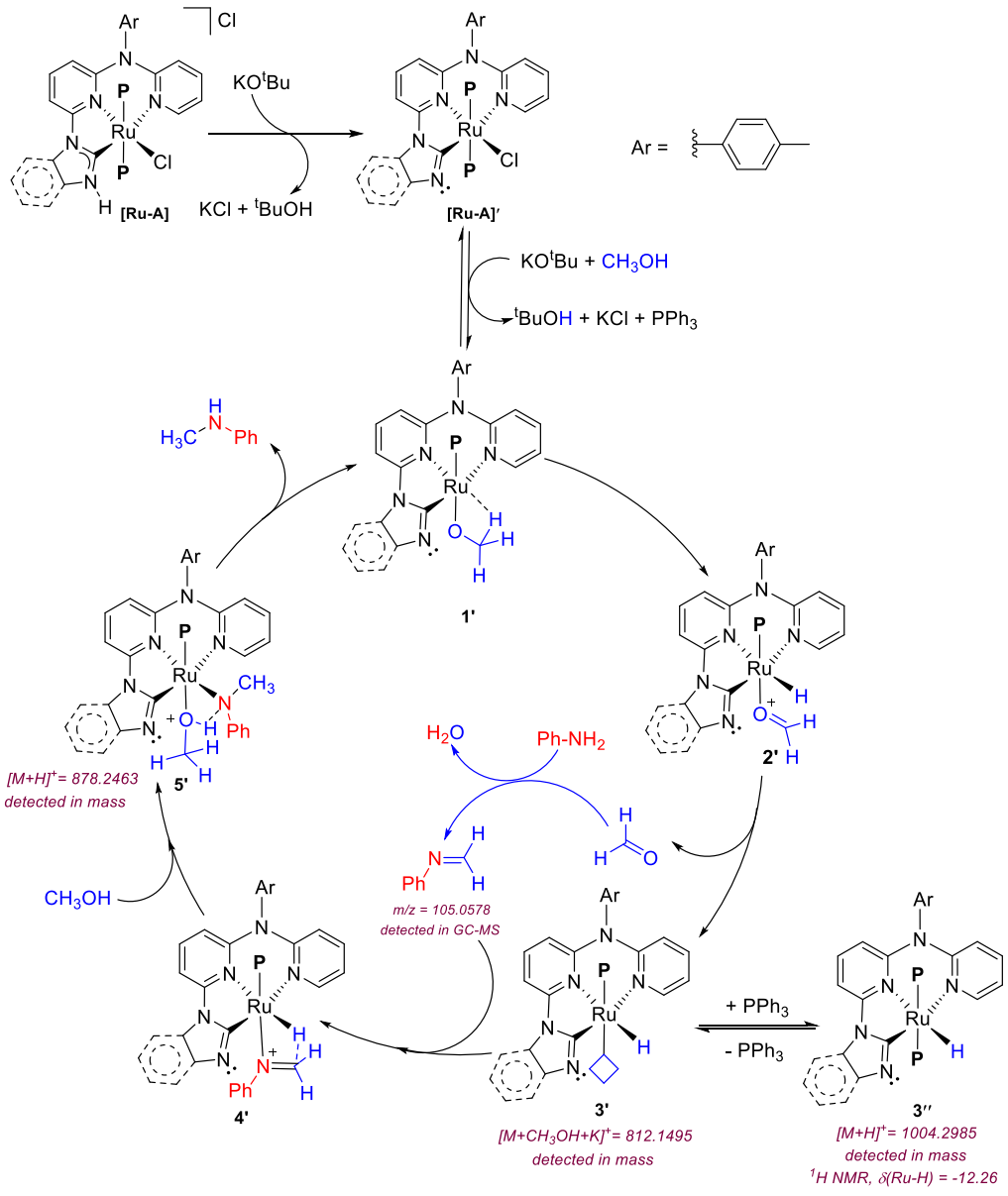

Figure 3.12 Proposed mechanism for the *N*-methylation of anilines catalyzed by **[Ru-A]** and **Ru5** using methanol.

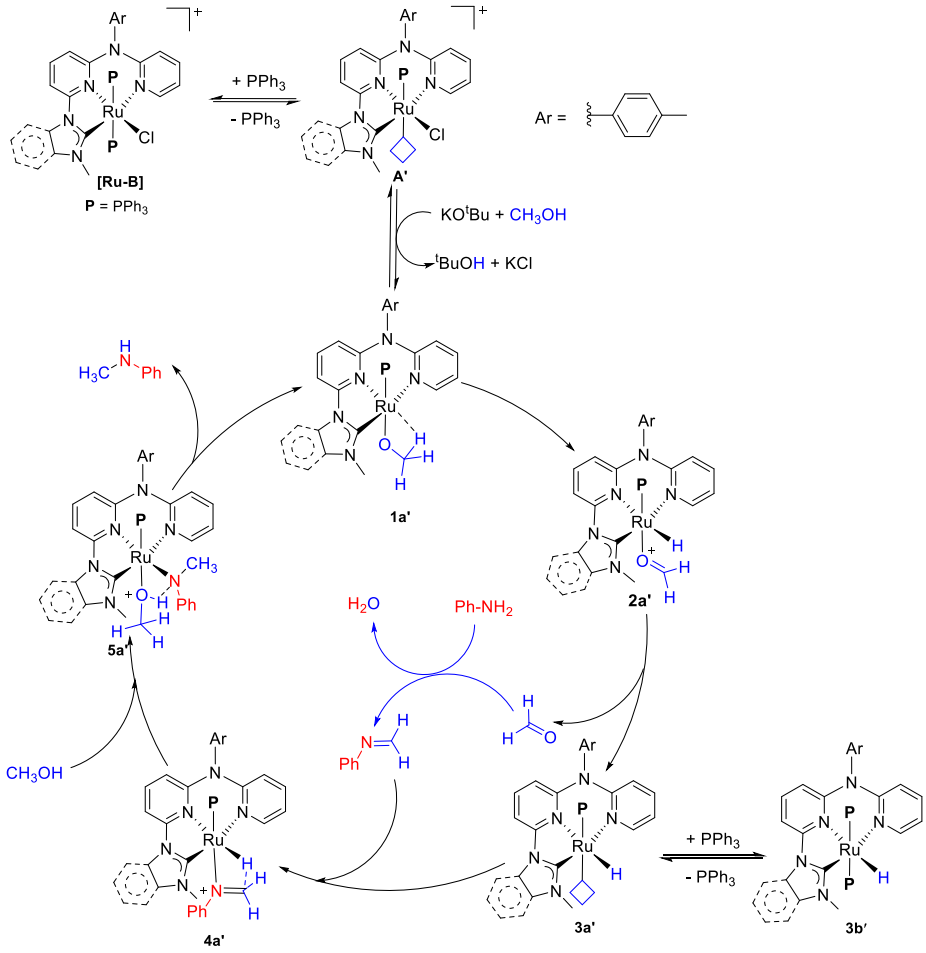

Figure 3.13 Proposed mechanism for the *N*-methylation of anilines catalyzed by Ru(II)-classical-NHC complexes [**Ru-B]** and **Ru6**.

In the catalytic cycle involving classical-NHC complexes, the process begins similarly with the phosphine ligand dissociation from the catalyst **[Ru-B]**, which is the classical counterpart of **[Ru-A]**, to form species **A′**. When a strong base, KO^{t}Bu, is added to a methanolic solution of **A′**, it produces a Ru-methoxy species, **1a′**, along with KCl salt and tert-butanol as byproducts. The species **1a′** catalyzes the dehydrogenation of methanol. Specifically, the ruthenium hydride species, **2a′**, facilitates the extraction of hydrogen from methanol, resulting in the production of formaldehyde. The removal of formaldehyde creates a vacant site, resulting in **3a′**. In the presence of phosphine, additional intermediates, such as **3b',** can form, as previously observed in protic-NHC complexes. The regenerated hydride species then participate in further catalytic reactions. Meanwhile, the formaldehyde generated in situ reacts with the primary amine in the mixture, forming an imine intermediate and

releasing water as a byproduct. This imine intermediate does not accumulate because the vacant coordination site on the ruthenium-hydride complex (**3a′**) quickly binds to it, forming species **4a′**. Subsequently, the hydride ligand of the Ru-H bond in species **4a′** transfers from the ruthenium center to the imine carbon, facilitating imine hydrogenation. In the presence of methanol, this resulted in species **5a′**. In species **5a′**, a methanol molecule coordinates to the ruthenium center and transfers its proton to the nitrogen atom of the coordinated aniline moiety. After protonation, *N*-methylated aniline is released from the metal center (Figure 3.13).

3.3 Conclusion

In summary, this study presents an evaluation of a series of unsymmetrical CNN-based Ru(II) complexes incorporating classical and protic-*N*-heterocyclic carbene (pNHC) ligands for the selective *N*-methylation of anilines using methanol as a sustainable C1 feedstock. A comparative analysis of benzimidazolylidene-, triazolylidene-, and newly synthesized imidazolylidene-derived complexes [**Ru-A]-[Ru-d**] established that the protic-benzimidazolylidene complex [**Ru-A]** exhibited better catalytic activity, delivering excellent yields under additive-free conditions. Detailed optimization under both thermal and microwave-assisted protocols highlighted pronounced structure-activity relationships, emphasizing the crucial role of ligand architecture in dictating reactivity and selectivity. Microwave irradiation significantly accelerated the transformation, yielding higher efficiency than conventional heating. Under optimized conditions, the catalytic system demonstrated a broad substrate scope, functional group tolerance, and high mono-methylation selectivity. Notably, the methodology was successfully extended to gram-scale synthesis, underscoring its practical significance. Mechanistic investigations revealed the involvement of imine and formamide intermediates in the hydrogen-borrowing pathway. This study establishes the synergistic role of the Ru-pNHC framework and microwave activation as a powerful paradigm for rapid, green, and

scalable *N*-methylation processes, paving the way for future developments in sustainable C-N bond-forming transformations.

3.4 Experimental Section

3.4.1 General Experimental Information

All synthesis experiments for preparing the complexes and thermal-assisted *N*-methylation reactions were conducted under a nitrogen atmosphere using standard Schlenk line techniques. Microwave-assisted reactions were performed in a MilestoneStart S microwave reactor equipped with a reflux condenser, magnetic stirrer for continuous agitation, and a non-contact infrared feedback system for real-time temperature monitoring and precise temperature regulation of the reaction mixture. In the MilestoneStart S microwave reactor, the temperature is typically monitored using an internal infrared (IR) sensor. In our study, the reaction temperature was maintained at 40 °C and verified by the internal IR sensor of the reactor, which continuously measured the temperature on the surface of the reaction vessel. Furthermore, the system automatically adjusted the microwave power to maintain this temperature constant, ensuring minimal fluctuations of ±1-2 °C.

Solvents were purified following established protocols under nitrogen and stored over 4 Å molecular sieves within an N_2 glove box. Reagents were purchased from commercial suppliers and used without additional purification, although many chemicals underwent purification according to standard methods. The metal precursor $RuCl_2(PPh_3)_3$ was prepared using a previously reported procedure. NMR spectra were recorded at room temperature and pressure using a Bruker Avance 400 MHz spectrometer (400 MHz for ^{1}H, 100 MHz for ^{13}C, and 162 MHz for ^{31}P) and a 500 MHz spectrometer (500 MHz for ^{1}H, 125 MHz for ^{13}C, and 202 MHz for ^{31}P). Deuterated solvents, including dimethyl sulfoxide and chloroform, were employed for NMR analysis, with chemical shift values (δ) reported in parts per million (ppm) relative to the residual solvent signals. The resonance peaks for ^{1}H in $CDCl_3$ are at δ 7.26 and

in DMSO-d_6 at δ 2.50 ppm; for ^{13}C, $CDCl_3$ appears at δ 77.0 and DMSO-d_6 at δ 40.45 ppm.

Electrospray ionization (ESI) and high-resolution mass spectrometry (HRMS) measurements were performed using a Bruker-Doltonics-micro TOF-QII spectrometer at 22 °C. GC-MS was performed using a Shimadzu QP2010 Ultra instrument. LCMS for a few samples was performed on an Xevo G3 QTOF mass spectrometer coupled with an Acquity H-class plus UPLC with a mass range of 20 to 1500 daltons in ESI+ ionization mode.

3.4.2 Synthesis of complex Ru5. An oven-dried Schlenk tube was charged with 6-(1*H*-imidazol-1-yl)-*N*-(pyridin-2-yl)-*N*-(*p*-tolyl)pyridin-2-amine (**L3**) (0.065 g, 0.2 mmol) in methanol (10 mL), and Ag_2O (0.0231 g, 0.1 mmol), followed by the addition of $RuCl_2(PPh_3)_3$ (0.191 g, 0.2 mmol). The resulting mixture was stirred at the reflux temperature for 12 h. After the completion of the reaction, the mother liquor was filtered through a short celite pad and reduced to 1-2 mL under reduced pressure. Diethyl ether was then added, and a yellow precipitate was obtained. Finally, after drying under high vacuum, the compound was obtained as a yellow powder. Yield 0.112 g (55.9%). **^{1}H NMR** (500 MHz, DMSO-d_6, 25 °C) δ 13.45 (s, 1H), 13.23 (s, 1H), 9.48 (d, J = 7.6 Hz, 1H), 9.37 (d, J = 7.8 Hz, 1H), 9.06 (d, J = 6.1 Hz, 1H), 8.80 (d, J = 4.6 Hz, 1H), 8.69 (d, J = 13.9 Hz, 1H), 8.30 (d, J = 5.3 Hz, 2H), 8.23 (d, J = 6.7 Hz, 1H), 7.92 (s, 2H), 7.86 (d, J = 5.3 Hz, 1H), 7.83 – 7.81 (m, 1H), 7.78 (d, J = 3.8 Hz, 1H), 7.74 (d, J = 8.1 Hz, 1H), 7.71 – 7.67 (m, 2H), 7.62 (t, J = 8.0 Hz, 3H), 7.59 – 7.54 (m, 4H), 7.52 – 7.47 (m, 10H), 7.45 (s, 5H), 7.42 (d, J = 6.0 Hz, 5H), 7.36 (d, J = 8.3 Hz, 8H), 7.31 – 7.25 (m, 7H), 7.05 (s, 1H), 6.95 (d, J = 5.6 Hz, 2H), 6.89 (d, J = 7.9 Hz, 1H), 6.84 (d, J = 8.1 Hz, 2H), 6.81 – 6.75 (m, 2H), 6.74 (s, 2H), 6.58 (s, 1H), 6.46 (d, J = 8.9 Hz, 1H), 6.35 (d, J = 8.7 Hz, 1H), 6.24 (d, J = 8.5 Hz, 1H), 6.20 – 6.12 (m, 3H), 6.05 (d, J = 8.9 Hz, 1H), 5.88 (dd, J = 8.9, 3.4 Hz, 1H), 5.67 (d, J = 8.7 Hz, 1H), 2.58 (s, 6H). **^{31}P NMR** (202 MHz, DMSO-d_6, 25 °C) δ -6.0, 23.9, 32.4. **^{13}C NMR** (126 MHz, DMSO-d_6, 25 °C) δ 187.9 (d, J = 14.7 Hz), 155.2, 153.6, 153.5, 152.6, 151.9, 140.1, 139.4, 132.9, 132.5, 132.4, 132.2, 132.0, 131.3, 131.1, 130.9, 130.75,

129.7, 129.5, 128.7, 128.6, 128.0, 127.9, 127.8, 20.8, 16.4. Calcd for $C_{56}H_{47}Cl_2N_5P_2Ru$: C, 65.69; H, 4.63; N, 6.84. Found: C, 65.13; H, 4.97; N, 7.01.

3.4.3 Synthesis of complex Ru6. An oven-dried Schlenk tube was charged with 3-methyl-1-(6-(pyridin-2-yl(*p*-tolyl)amino)pyridin-2-yl)-1*H*-imidazol-3-ium iodide (**L4·HI**) (0.094 g, 0.2 mmol) in methanol (10 mL), and Ag_2O (0.0231 g, 0.1 mmol), followed by the addition of $RuCl_2(PPh_3)_3$ (0.191 g, 0.2 mmol). The resulting mixture was stirred at the reflux temperature for 12 h. After the completion of the reaction, the mother liquor was filtered through a short celite pad and reduced to 1-2 mL under reduced pressure. Diethyl ether was then added, and a yellow precipitate was obtained. Finally, after drying under high vacuum, the compound was obtained as a yellow powder. Yield 0.104 g (50%). **^{1}H NMR** (500 MHz, DMSO-d_6, 25 °C) δ 9.44 (d, *J* = 6.0 Hz, 1H), 8.49 (s, 1H), 8.31 (d, *J* = 5.0 Hz, 0H), 8.23 (s, 0H), 7.94 (d, *J* = 8.1 Hz, 1H), 7.80 (t, *J* = 7.8 Hz, 0H), 7.64 (t, *J* = 7.6 Hz, 1H), 7.62 – 7.60 (m, 1H), 7.57 (d, *J* = 8.4 Hz, 0H), 7.55 – 7.47 (m, 3H), 7.37 (d, *J* = 4.9 Hz, 3H), 7.34 (d, *J* = 7.5 Hz, 2H), 7.27 (d, *J* = 7.8 Hz, 2H), 7.23 (q, *J* = 7.2, 6.6 Hz, 7H), 7.12 (t, *J* = 7.0 Hz, 4H), 7.06 (t, *J* = 8.9 Hz, 6H), 6.96 (dt, *J* = 8.5, 4.7 Hz, 3H), 6.92 (d, *J* = 8.2 Hz, 0H), 6.77 (q, *J* = 9.5, 8.0 Hz, 1H), 6.52 (d, *J* = 8.9 Hz, 1H), 6.38 (s, 0H), 6.22 (d, *J* = 8.7 Hz, 1H), 6.05 (d, *J* = 8.9 Hz, 0H), 5.91 (d, *J* = 8.7 Hz, 0H), 4.09 (s, 2H), 3.95 (s, 1H), 2.43 (s, 3H), 2.33 (s, 1H). **^{31}P NMR** (202 MHz, DMSO-d_6, 25 °C) δ -6.01, 24.42, 32.58. **^{13}C NMR** (126 MHz, DMSO-d_6, 25 °C) δ 185.9, 185.8, 156.5, 156.2, 153.9, 153.8, 152.6, 152.0, 147.9, 144.5, 141.5, 140.7, 140.4, 139.6, 138.6, 138.5, 137.6, 136.3, 136.2, 136.3, 135.3, 133.3, 133.2, 132.7, 132.6, 132.5, 132.4, 132.2, 131.8, 131.7, 131.6, 131.4, 131.3, 131,0, 130.5, 130.0, 129.8, 129.5, 129.3, 129.1, 128.8, 128.7, 128.2, 128.1, 128.03, 128.0, 127.9, 127.7, 126.7, 124.7, 119.6, 118.5, 118.3, 117.9, 117.3, 116.9, 115.1, 113.5, 106.4, 104.7, 37.1, 36.4, 20.8, 20.7.

3.4.4 General Procedure for *N*-methylation of Anilines with Methanol. In an oven-dried Schlenk pressure tube, aniline (91.30 μL, 1 mmol), methanol (1 mL, 0.0247 mol), [**Ru-A]** (5.36 mg, 0.5 mol%), and KO^{t}Bu (0.5 equiv., 56 mg) were added under nitrogen flow. During the

constant purging of nitrogen, the Schlenk pressure tube was sealed to prevent any interaction with moisture or air. Molecular sieves of size 4 Å were added to the Schlenk tube to absorb the water produced as a byproduct of the reaction. The reaction mixture was stirred with a magnetic stirring bar at 40 °C for 35 min under microwave irradiation. After completion of the reaction, the crude mixture was diluted with methanol and passed through a celite filter, followed by the preparation of a slurry by adding a small amount of silica and removal of the solvent under vacuum. The crude mixture was then purified by silica gel column chromatography (60-120 mesh size) using a hexane-ethyl acetate eluent to yield the *N*-methylated product.

3.4.5 Control experiments: (a) To identify the *N*-phenylmethanimine, we have performed the reaction containing methanol (1ml, 0.0247 mol), aniline (1 mmol, 91.30 µL), and KO^{t}Bu (0.5 equiv., 56 mg) at room temperature. The mixture was stirred for 20 min, and GC-MS was performed. A signal at m/z = 105.0578 was observed for *N*-phenylmethanimine. Subsequently, **[Ru-A]** was added to the Schlenk tube and refluxed for 12 h. The obtained GC-MS data contained signals for *N*-methylaniline, aniline, and *N*-phenylmethanimine**.**

(b) In a dried Schlenk pressure tube having 4 Å molecular sieves, [**Ru-A]** (5.36 mg, 0.005 mmol) was added, followed by the addition of 1ml of methanol and 0.5 equiv. of base, KO^{t}Bu (0.5 mmol, 56 mg). After stirring for 1-2 minutes, *N*-methyl-*N*-phenylformamide (1 mmol, 123.4 µL) was added under a nitrogen atmosphere, and the Schlenk pressure tube was sealed. The reaction mixture was cooled after heating in a microwave at 40 °C for 35 min. The reaction mixture was filtered, and the solvent was removed using a rotary evaporator. The product (98.9 µL, 91 %) was isolated by column chromatography (1% ethyl acetate-hexane mixture).

(c) Using the general procedure for *N*-methylation of anilines used in this work, the reaction was set up in a well-dried Schlenk pressure tube. 1 ml of CD_3OD was used instead of methanol. After heating the mixture under

microwave conditions for 35 min, GC-MS was performed. It showed a peak at m/z = 110.0923 for *N*-methylaniline-D3.

(d) In an oven-dried Schlenk pressure tube, aniline (1 mmol), methanol (1 ml), [**Ru-A]** (0.5 mol%), KO^{t}Bu (0.5 equiv.), and mercury (3 equiv., 3 mmol) were added under a gentle stream of nitrogen. The setup was then sealed and heated under microwave irradiation for 35 min at 40 °C. After the reaction was complete, the crude mixture was cooled to room temperature, followed by filtration through a Celite pad with several washes (3 mL of methanol) and then concentrated in vacuo. The residue was purified by column chromatography on silica gel to afford the desired product in 90 % yield.

(e) In an oven-dried Schlenk pressure tube, aniline (1 mmol), methanol (1 ml), [**Ru-A]** (0.5 mol%), KO^{t}Bu (0.5 equiv.), and TEMPO (1 equiv., 1 mmol) were added under a gentle stream of nitrogen. The setup was then sealed and heated under microwave irradiation for 35 min at 40 °C. After the reaction was complete, the crude mixture was cooled to room temperature, followed by filtration through a Celite pad with several washes (3 mL of methanol) and then concentrated in vacuo. The residue was purified by column chromatography on silica gel to afford the desired product in 92 % yield.

3.4.6 Characterization data for the substrates for *N*-Methylation of anilines:

(1) *N*-methylaniline (2a)

The compound was prepared as described in the general method (colourless liquid, 98 % isolated yield). ^{1}H NMR (500 MHz, $CDCl_3$, 25 °C) δ 7.28 (t, J = 7.2 Hz, 2H), 6.80 (t, J = 7.4 Hz, 1H), 6.64 (d, J = 8.5 Hz, 2H), 3.59 (s, 1H), 2.82 (s, 3H). ^{13}C NMR (126 MHz, $CDCl_3$, 25 °C) δ 149.3, 129.1, 117.0, 112.3, 30.5.

(2) 4-bromo-*N*-methylaniline (2b)

The compound was prepared as described in the general method (crystalline solid, 95 % isolated yield). ^{1}H NMR (500 MHz, $CDCl_3$) δ

7.27 (d, J = 8.9 Hz, 2H), 6.47 (d, J = 9.0 Hz, 2H), 3.49 (s, 1H), 2.79 (s, 3H). ^{13}C NMR (126 MHz, $CDCl_3$) δ 148.3, 131.9, 114.0, 108.8, 30.7.

(3) 4-chloro-*N*-methylaniline (2c)

The compound was prepared as described in the general method (white crystalline solid, 94 % isolated yield). ^{1}H NMR (500 MHz, $CDCl_3$) δ 7.14 (d, J = 8.9 Hz, 2H), 6.52 (d, J = 9.0 Hz, 2H), 3.66 (s, 1H), 2.81 (s, 3H). ^{13}C NMR (126 MHz, $CDCl_3$) δ 147.9, 129.0, 121.8, 113.5, 30.9.

(4) 4-iodo-*N*-methylaniline (2d)

The compound was prepared as described in the general method (brown crystalline solid, 95 % isolated yield). ^{1}H NMR (500 MHz, $CDCl_3$) δ 7.41 (d, J = 8.9 Hz, 2H), 6.37 (d, J = 8.9 Hz, 2H), 4.23 (s, 1H), 2.78 (s, 3H). ^{13}C NMR (126 MHz, $CDCl_3$) δ 148.9, 137.4, 129.2, 114.4, 30.5.

(5) *N*,4-dimethylaniline (2e)

The compound was prepared as described in the general method (Yellow liquid, 91 % isolated yield). ^{1}H NMR (500 MHz, $CDCl_3$) δ 7.24 (d, J = 8.4 Hz, 2H), 6.78 (d, J = 8.5 Hz, 2H), 3.72 (s, 1H), 3.03 (s, 3H), 2.49 (s, 3H). ^{13}C NMR (126 MHz, $CDCl_3$) δ 147.1, 129.7, 126.6, 112.7, 31.2, 20.4.

(6) 4-methoxy-*N*-methylaniline (2f)

The compound was prepared as described in the general method (light yellow crystalline solid, 90 % isolated yield). ^{1}H NMR (500 MHz, $CDCl_3$) δ 6.83 (d, J = 9.0 Hz, 2H), 6.61 (d, J = 6.1 Hz, 2H), 3.77 (s, 3H), 3.39 (s, 1H), 2.81 (s, 3H).^{13}C NMR (126 MHz, $CDCl_3$) δ 152.1, 143.7, 114.9, 113.7, 55.6, 31.6.

(7) 4-(methylamino)phenol (2g)

The compound was prepared as described in the general method (brownish solid, 40 % isolated yield). ^{1}H NMR (500 MHz, $CDCl_3$) δ 10.02 (s, 1H), 6.70 – 6.68 (m, 2H), 6.56 – 6.55 (m, 2H), 4.42 (s, 1H),

2.78 (s, 3H). ^{13}C NMR (126 MHz, $CDCl_3$) δ 148.5, 143.0, 116.3, 114.7, 32.1.

(8) *N*-methyl-4-phenoxyaniline (2h)

The compound was prepared as described in the general method (white powder, 95 % isolated yield). ^{1}H NMR (500 MHz, $CDCl_3$) δ 7.31 (t, J = 8.0 Hz, 2H), 7.06 (t, J = 7.3 Hz, 1H), 7.04 – 6.97 (m, 4H), 6.64 (d, J = 8.9 Hz, 2H), 3.55 (s, 1H), 2.86 (s, 3H). ^{13}C NMR (126 MHz, $CDCl_3$) δ 159.3, 147.5, 146.1, 129.6, 122.0, 121.3, 117.1, 113.4, 31.3.

(9) 4-(methylamino)benzoic acid (2i)

The compound was prepared as described in the general method (white crystalline solid, 90 % isolated yield). ^{1}H NMR (500 MHz, DMSO) δ 11.95 (s, 1H), 7.87 – 7.59 (m, 2H), 6.67 – 6.49 (m, 2H), 3.92 – 3.25 (m, 0H), 2.74 (d, J = 4.1 Hz, 3H). ^{13}C NMR (126 MHz, DMSO) δ 205.37, 191.19, 168.90, 154.49, 148.22, 66.91.

(10) *N*,3,4-trimethylaniline (2j)

The compound was prepared as described in the general method (Yellowish oily liquid, 94 % isolated yield). ^{1}H NMR (500 MHz, $CDCl_3$) δ 7.16 (d, J = 8.9 Hz, 1H), 7.00 (d, J = 8.1 Hz, 1H), 6.55 (d, J = 8.9 Hz, 1H), 6.44 (dd, J = 7.9, 2.7 Hz, 1H), 3.49 (s, 1H), 2.84 (s, 3H), 2.25 (s, 3H), 2.20 (s, 3H).^{13}C NMR (126 MHz, $CDCl_3$) δ 138.7, 138.0, 134.6, 130.8, 123.0, 119.5, 37.9, 19.6, 19.2.

(11) 3-fluoro-*N*,4-dimethylaniline (2k)

The compound was prepared as described in the general method (yellow liquid, 95 % isolated yield). ^{1}H NMR (500 MHz, $CDCl_3$) δ 7.32 (d, J = 6.8, 3.1 Hz, 1H), 7.24 (s, 1H), 7.21 (d, J = 8.1 Hz, 1H), 4.47 (s, 1H), 2.98 (s, 3H), 2.24 (s, 3H). ^{13}C NMR (126 MHz, $CDCl_3$) δ 162.2, 160.2, 132.9, 126.4, 118.1, 110.2, 38.0, 14.4.

(12) 3-bromo-*N*,4-dimethylaniline (2l)

The compound was prepared as described in the general method (Yellow liquid, 95 % isolated yield). ^{1}H NMR 1H NMR (500 MHz, $CDCl_3$) δ 7.04 (d, J = 8.2 Hz, 1H), 6.83 (s, 1H), 6.49 (d, J = 8.2 Hz, 1H), 2.79 (s,

3H), 2.33 (s, 3H). ^{13}C NMR (126 MHz, $CDCl_3$) δ 148.5, 131.0, 125.7, 125.4, 115.6, 112.0, 30.8, 21.7.

(13) 2-methoxy-*N*-methylaniline (2m)

The compound was prepared as described in the general method (white salt, 85 % isolated yield). ^{1}H NMR (500 MHz, $CDCl_3$) δ 10.95 (s, 2H), 7.62 (d, J = 7.8 Hz, 1H), 7.21 (t, J = 7.6 Hz, 1H), 6.84 (dt, J = 15.0, 7.6 Hz, 2H), 3.80 (s, 3H), 2.90 (s, 3H). ^{13}C NMR (126 MHz, $CDCl_3$) δ 152.1, 130.5, 125.4, 123.7, 120.9, 112.2, 56.2, 36.6.

(14) 3-chloro-4-fluoro-*N*-methylaniline (2n)

The compound was prepared as described in the general method (colorless liquid, 92 % isolated yield). ^{1}H NMR (500 MHz, $CDCl_3$) δ 6.93 (t, J = 8.9 Hz, 1H), 6.56 (dd, J = 6.1, 2.9 Hz, 1H), 6.40 (ddd, J = 9.0, 3.8, 2.9 Hz, 1H), 3.60 (s, 1H), 2.77 (s, 3H). ^{13}C NMR (126 MHz, $CDCl_3$) δ 151.7, 149.8, 146.4, 120.8, 116.8, 113.0, 111.7, 30.9.

(15) *N*,2-dimethylaniline (2o)

The compound was prepared as described in the general method (oily liquid, 79 % isolated yield). ^{1}H NMR (400 MHz, $CDCl_3$) δ 7.17 (t, J = 7.7 Hz, 1H), 7.07 (d, J = 7.4 Hz, 1H), 6.68 (t, J = 7.4 Hz, 1H), 6.64 (d, J = 8.0 Hz, 1H), 3.61 (s,1H), 2.92 (s, 3H), 2.16 (s, 3H). ^{13}C NMR (101 MHz, $CDCl_3$) δ 147.3, 130.0, 127.3, 122.1, 117.0, 109.3, 30.9, 17.5.

(16) *N*-methylpyridin-2-amine (2p)

The compound was prepared as described in the general method (light yellow liquid, 79 % isolated yield). ^{1}H NMR (500 MHz, $CDCl_3$) δ 8.02 (d, J = 4.1 Hz, 1H), 7.33 (ddd, J = 8.9, 7.1, 2.0 Hz, 1H), 6.48 (ddd, J = 7.3, 5.0, 1.1 Hz, 1H), 6.30 (d, J = 8.5 Hz, 1H), 4.97 (s, 1H), 2.82 (s, 3H). ^{13}C NMR (126 MHz, $CDCl_3$) δ 159.6, 148.0, 137.3, 112.4, 106.2, 28.9.

(17) *N*-methylpyridin-3-amine (2q)

The compound was prepared as described in the general method (Yellowish oily liquid, 81 % isolated yield). ^{1}H NMR (500 MHz, $CDCl_3$) δ 7.94 (d, J = 3.1 Hz, 1H), 7.83 (d, J = 4.9 Hz, 1H), 7.03 (dd, J = 8.4, 4.7

Hz, 1H), 6.82 (dd, J = 8.3, 1.6 Hz, 1H), 3.26 (s, 1H), 2.73 (s, 3H). ^{13}C NMR (126 MHz, $CDCl_3$) δ 145.7, 136.6, 134.0, 124.0, 118.7, 29.9.

(18) *N*-methylpyridin-4-amine (2r)

The compound was prepared as described in the general method (crystalline solid, 60 % isolated yield). ^{1}H NMR (500 MHz, $CDCl_3$) δ 8.02 (d, J = 4.7, 1.7 Hz, 2H), 6.32 (d, 2H), 5.28 (s, 1H), 2.70 (s, 3H). ^{13}C NMR (126 MHz, $CDCl_3$) δ 149.3, 107.0, 77.4, 28.9.

(19) 3,5-dimethoxy-*N*-methylaniline (2s)

The compound was prepared as described in the general method (crystalline solid, 93 % isolated yield). ^{1}H NMR (500 MHz, $CDCl_3$) δ 5.92 (s, 1H), 5.82 (s, 2H), 3.81 (s, 1H), 3.77 (s, 6H), 2.80 (s, 3H). ^{13}C NMR (126 MHz, $CDCl_3$) δ 161.7, 151.4, 91.1, 89.5, 55.0, 30.6.

(20) *N*-methylnaphthalen-1-amine (2t)

The compound was prepared as described in the general method (crystalline solid, 85 % isolated yield). ^{1}H NMR (500 MHz, $CDCl_3$) δ 7.68 (dd, J = 8.1, 1.7 Hz, 1H), 7.55 (d, J = 7.8 Hz, 1H), 7.33 (ddd, J = 8.2, 6.7, 1.4 Hz, 1H), 7.30 – 7.25 (m, 2H), 7.15 (d, J = 8.2 Hz, 1H), 6.45 (d, J = 7.6 Hz, 1H), 3.65 (s, 1H), 2.78 (s, 3H). ^{13}C NMR (126 MHz, $CDCl_3$) δ 144.5, 134.2, 128.6, 126.7, 125.7, 124.6, 123.4, 119.9, 117.2, 103.7, 30.9.

(21) *N*-methylbenzenesulfonamide (2u)

The compound was prepared as described in the general method (crystalline solid, 95 % isolated yield). ^{1}H NMR (400 MHz, DMSO-d_6) δ 7.95 – 7.93 (m, 1H), 7.65 (d, J = 7.3 Hz, 2H), 7.48 (s, 2H), 3.72 (s, 3H). ^{13}C NMR (101 MHz, DMSO-d_6) δ 144.2, 132.1, 129.2, 125.8, 28.9.

(22) *N*-methylquinolin-8-amine (2v)

The compound was prepared as described in the general method (white solid, 45 % isolated yield). ^{1}H NMR (500 MHz, $CDCl_3$) δ 8.55 (dd, J = 4.2, 1.8 Hz, 1H), 7.93 (dd, J = 8.2, 1.8 Hz, 1H), 7.29 – 7.19 (m, 2H), 6.90

(dd, J = 8.2, 1.3 Hz, 2H), 6.50 (dd, J = 7.6, 1.1 Hz, 1H), 2.89 (s, 3H). ^{13}C NMR (126 MHz, $CDCl_3$) δ 146.6, 145.8, 136.6, 129.4, 128.2, 121.5, 113.8, 112.7, 104.6, 29.8.

(23) 4-(4-aminophenoxy)-*N*-methylaniline (2w)

The compound was prepared as described in the general method (crystalline solid, 94 % isolated yield). ^{1}H NMR (500 MHz, $CDCl_3$) δ 6.94 (d, J = 8.9 Hz, 4H), 6.61 (d, J = 9.0 Hz, 4H), 3.61 (s, 2H), 2.82 (s, 6H). ^{13}C NMR (126 MHz, $CDCl_3$) δ 149.7, 145.1, 119.4, 113.3, 31.2.

(24) *N*,3-dimethylaniline (2x)

The compound was prepared as described in the general method (Oily liquid, 84 % isolated yield). ^{1}H NMR (500 MHz, $CDCl_3$) δ 7.25 (t, J = 8.1 Hz, 1H), 6.72 (d, J = 7.5 Hz, 1H), 6.58 – 6.53 (m, 2H), 3.68 (s, 1H), 2.89 (s, 3H), 2.46 (s, 3H). ^{13}C NMR (126 MHz, $CDCl_3$) δ 149.4, 138.7, 129.0, 117.9, 113.1, 109.5, 30.5, 21.5.

(25) (2-(methylamino)phenyl)methanol (2y)

The compound was prepared as described in the general method (white powder, 50 % isolated yield). ^{1}H NMR (500 MHz, $CDCl_3$) δ 7.51 – 7.43 (m, 2H), 7.40 (dd, J = 8.7, 6.6 Hz, 2H), 7.19 (td, J = 7.2, 1.9 Hz, 1H), 4.32 (s, 1H), 2.87 (s, 2H), 2.84 (s, 3H).^{13}C NMR (126 MHz, $CDCl_3$) δ 141.0, 140.2, 129.3, 127.2, 112.6, 110.5, 32.1, 22.8.

(26) *N*,6-dimethylpyridin-2-amine (2z)

The compound was prepared as described in the general method (yellowish oily liquid, 81 % isolated yield). ^{1}H NMR (500 MHz, $CDCl_3$) δ 7.40 – 7.29 (m, 1H), 6.41 (d, J = 7.3 Hz, 1H), 6.17 (d, J = 8.4 Hz, 1H), 2.85 (s, 3H), 2.35 (s, 3H). ^{13}C NMR (126 MHz, $CDCl_3$) δ 159.2, 156.3, 138.5, 112.0, 102.3, 29.3, 23.8.

(27) *N*-ethylaniline (4a)

The compound was prepared as described in the general method (colourless liquid, 94 % isolated yield). ^{1}H NMR (500 MHz, $CDCl_3$) δ

7.38 – 7.30 (m, 2H), 6.87 (t, J = 7.3 Hz, 1H), 6.75 (d, J = 7.3 Hz, 2H), 3.55 (s, 1H), 3.27 (q, J = 7.1 Hz, 2H), 1.37 (t, J = 7.2 Hz, 3H). ^{13}C NMR (126 MHz, $CDCl_3$) δ 148.4, 129.2, 117.1, 112.7, 38.4, 14.8.

(28) *N*-methyl-*N*-phenylformamide

The compound was prepared as described in the general method (pale liquid, 64 % isolated yield). ^{1}H NMR (500 MHz, DMSO-d_6) δ 7.63 (s, 1H), 6.64 – 6.54 (m, 2H), 6.49 – 6.41 (m, 1H), 6.34 (dd, J = 7.4, 1.9 Hz, 2H), 2.48 (s, 3H). ^{13}C NMR (126 MHz, DMSO-d_6) δ 162.2, 141.8, 129.4, 126.2, 122.1, 31.8.

(29) *N*, *N*-dimethylaniline

The compound was prepared as described in the general method (pale liquid, 96 % isolated yield). ^{1}H NMR (500 MHz, $CDCl_3$) δ 7.40 – 7.35 (m, 2H), 6.87 (d, J = 8.3 Hz, 2H), 6.85 (d, J = 7.2 Hz, 1H), 3.05 (s, 6H). ^{13}C NMR (126 MHz, $CDCl_3$) δ 150.7, 129.1, 116.7, 112.7, 40.6.

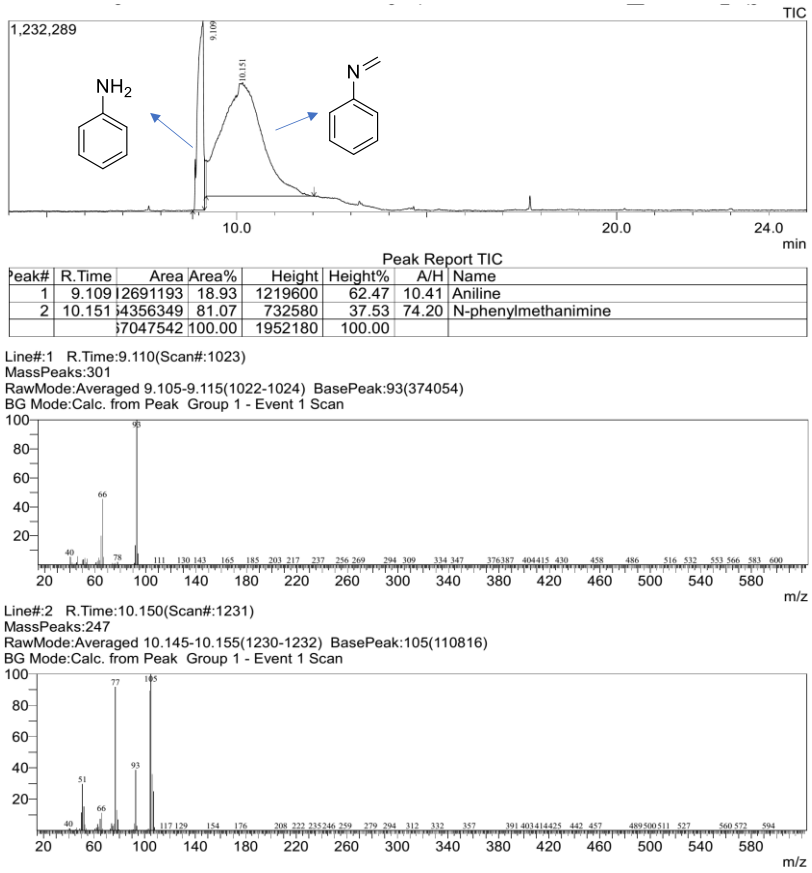

Figure 3.14 GC-MS for the identification of *N*-phenylmethanimine at room temperature

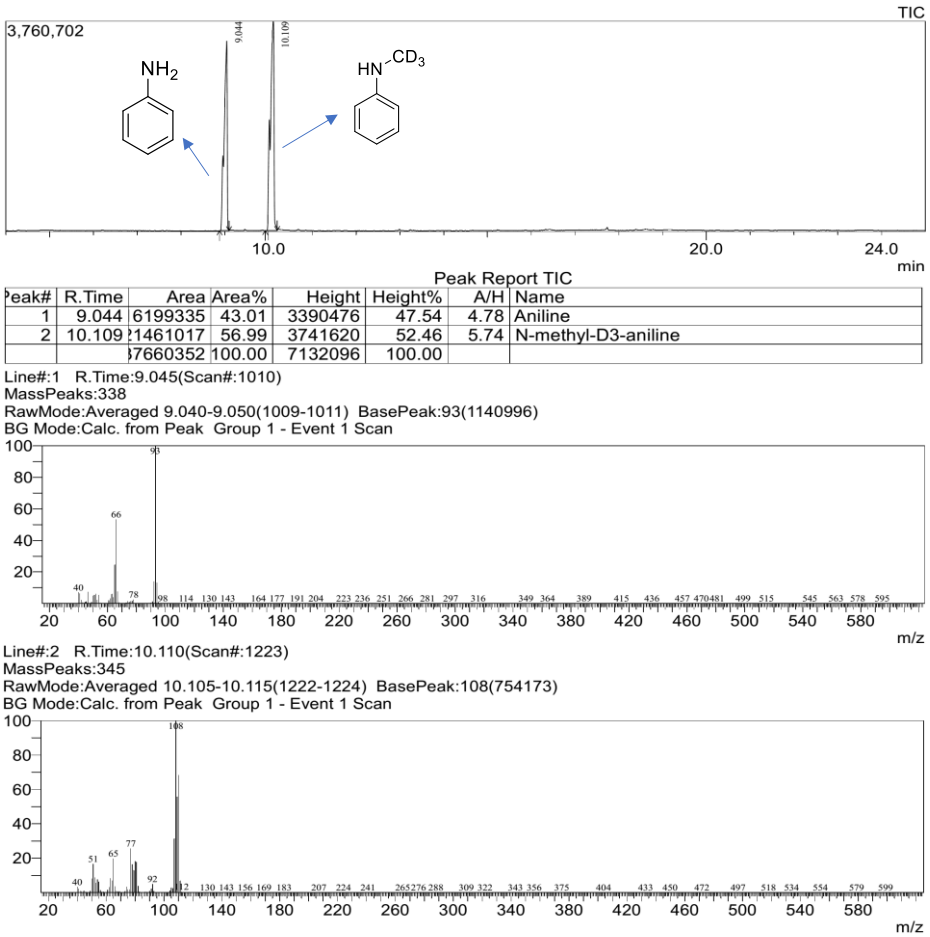

Peak Report TIC

Peak#	R.Time	Area	Area%	Height	Height%	A/H	Name
1	9.044	6199335	43.01	3390476	47.54	4.78	Aniline
2	10.109	21461017	56.99	3741620	52.46	5.74	N-methyl-D3-aniline
		27660352	100.00	7132096	100.00		

Line#:1 R.Time:9.045(Scan#:1010)
MassPeaks:338
RawMode:Averaged 9.040-9.050(1009-1011) BasePeak:93(1140996)
BG Mode:Calc. from Peak Group 1 - Event 1 Scan

Line#:2 R.Time:10.110(Scan#:1223)
MassPeaks:345
RawMode:Averaged 10.105-10.115(1222-1224) BasePeak:108(754173)
BG Mode:Calc. from Peak Group 1 - Event 1 Scan

Figure 3.15 GC-MS of the reaction mixture using deuterated methanol (CD_3OD).

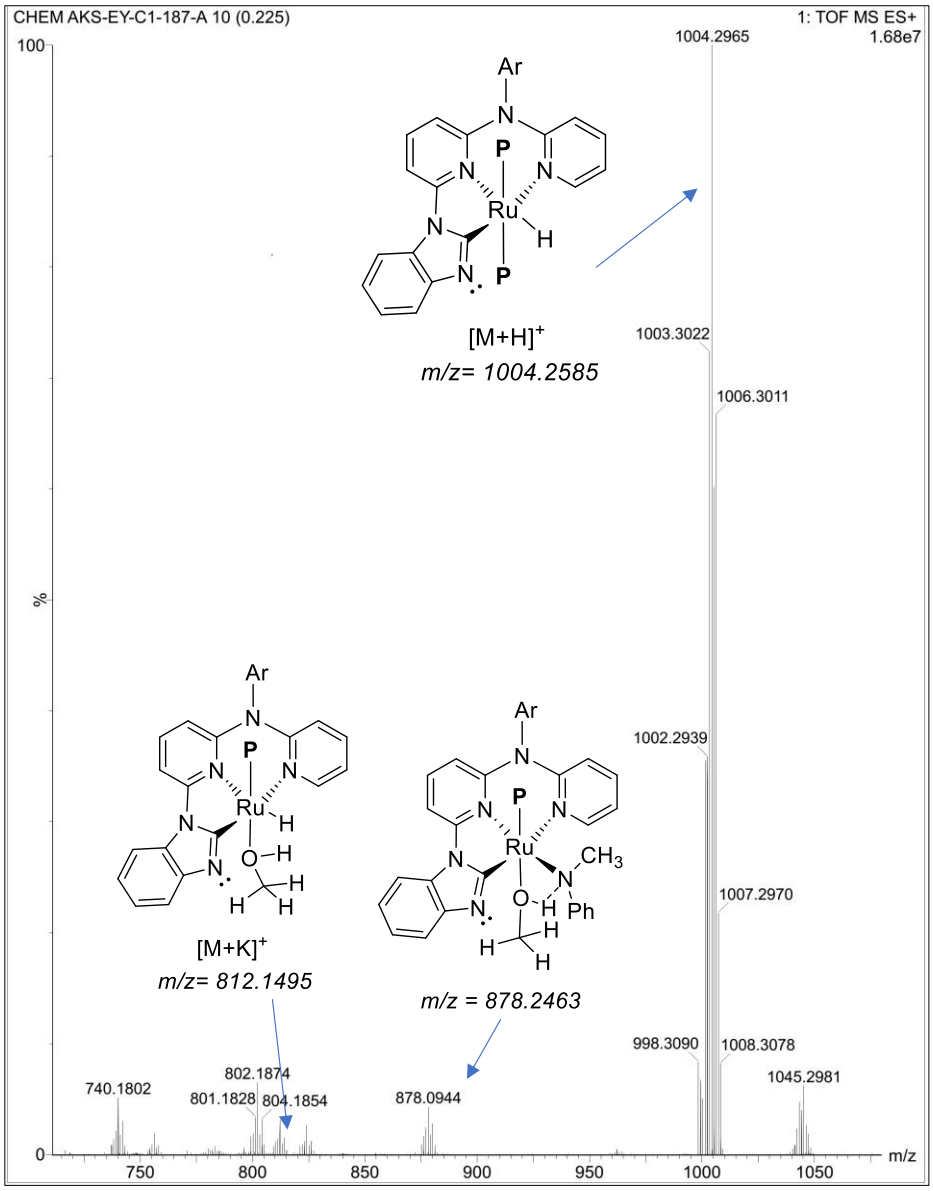

Figure 3.16 LC-MS of [**Ru-A]** under standard conditions after two minutes.

3.5 References

[1] Barreiro, E.J., Kümmerle, A.E., and Fraga, C.A.M. (2011). The Methylation Effect in Medicinal Chemistry. Chem. Rev., *111*, 5215–5246. (https://doi.org/10.1021/cr200060g)

[2] Guedes, J.D.S., Carneiro, T.R., Pinheiro, P.D.S.M., Fraga, C.A.M., Sant′Anna, C.M.R., Barreiro, E.J., and Lima, L.M. (2022). Methyl Effect on the Metabolism, Chemical Stability, and Permeability

Profile of Bioactive *N* -Sulfonylhydrazones. ACS Omega, *7*, 38752–38765. (https://doi.org/10.1021/acsomega.2c04368)

[3] Pinheiro, P.D.S.M., Franco, L.S., and Fraga, C.A.M. (2023). The Magic Methyl and Its Tricks in Drug Discovery and Development. Pharmaceuticals, *16*, 1157. (https://doi.org/10.3390/ph16081157)

[4] Schönherr, H., and Cernak, T. (2013). Profound Methyl Effects in Drug Discovery and a Call for New C-H Methylation Reactions. Angew Chem Int Ed, *52*, 12256–12267. (https://doi.org/10.1002/anie.201303207)

[5] Bayguzina, A.R., and Khusnutdinov, R.I. (2021). Catalytic *N*-Alkylation of Anilines. Russ J Gen Chem, *91*, 305–347. (https://doi.org/10.1134/S1070363221030014)

[6] Yan, W., Tian, T., and Nishihara, Y. (2025). From carboxylic acids or their derivatives to amines and ethers: modern decarboxylative approaches for sustainable C–N and C–O bond formation. Org. Biomol. Chem., *23*, 7367–7382. (https://doi.org/10.1039/D5OB00748H)

[7] Md. Abdur Rauf, S., Arvidsson, P.I., Albericio, F., Govender, T., Maguire, G.E.M., Kruger, H.G., and Honarparvar, B. (2015). The effect of *N*-methylation of amino acids (Ac-X-OMe) on solubility and conformation: a DFT study. Org. Biomol. Chem., *13*, 9993–10006. (https://doi.org/10.1039/C5OB01565K)

[8] Chatterjee, J., Rechenmacher, F., and Kessler, H. (2013). *N* -Methylation of Peptides and Proteins: An Important Element for Modulating Biological Functions. Angew Chem Int Ed, *52*, 254–269. (https://doi.org/10.1002/anie.201205674)

[9] Sun, S., and Fu, J. (2018). Methyl-containing pharmaceuticals: Methylation in drug design. Bioorg. Med. Chem. Lett., *28*, 3283–3289. (https://doi.org/10.1016/j.bmcl.2018.09.016)

[10] Mindt, M., Risse, J.M., Gruß, H., Sewald, N., Eikmanns, B.J., and Wendisch, V.F. (2018). One-step process for production of *N*-methylated amino acids from sugars and methylamine using recombinant Corynebacterium glutamicum as biocatalyst. Sci Rep, *8*, 12895. (https://doi.org/10.1038/s41598-018-31309-5)

[11] Luisa Di Gioia, M., Leggio, A., Malagrinò, F., Romio, E., Siciliano, C., and Liguori, A. (2016). *N*-Methylated α-Amino Acids And Peptides: Synthesis And Biological Activity. MRMC, *16*, 683–690. (https://doi.org/10.2174/1389557516666160322152457)

[12] Linde, Y., Ovadia, O., Safrai, E., Xiang, Z., Portillo, F.P., Shalev, D.E., Haskell-Luevano, C., Hoffman, A., and Gilon, C. (2008). Structure-activity relationship and metabolic stability studies of backbone cyclization and N-methylation of melanocortin peptides. Biopolymers, *90*, 671–682. (https://doi.org/10.1002/bip.21057)

[13] Hemming, E.B., Masters, A.F., Perosa, A., Selva, M., and Maschmeyer, T. (2019). Single-Step Methylation of Chitosan Using Dimethyl Carbonate as a Green Methylating Agent. Molecules, *24*, 3986. (https://doi.org/10.3390/molecules24213986)

[14] Moulay, S. (2019). *N*-Methylation of Nitrogen-Containing Organic Substrates: A Comprehensive Overview. COC, *23*, 1695–1737. (https://doi.org/10.2174/1385272823666190823114547)

[15] Selva, M., and Perosa, A. (2008). Green chemistry metrics: a comparative evaluation of dimethyl carbonate, methyl iodide, dimethyl sulfate and methanol as methylating agents. Green Chem., *10*, 457. (https://doi.org/10.1039/b713985c)

[16] Bobbink, F.D., Das, S., and Dyson, P.J. (2017). *N*-formylation and *N*-methylation of amines using metal-free *N*-heterocyclic carbene catalysts and CO2 as carbon source. Nat Protoc, *12*, 417–428. (https://doi.org/10.1038/nprot.2016.175)

[17] Wang, D., Lang, W., Wang, W., Zou, Q., Yang, C., Liu, F., and Zhao, T. (2023). CuH-Catalyzed Selective *N*-Methylation of Amines Using Paraformaldehyde as a C1 Source. ACS Omega, *8*, 30640–30645. (https://doi.org/10.1021/acsomega.3c04332)

[18] Paul, B., and Kundu, S. (2024). The use of methanol as a C1 building block. Nat Protoc, *19*, 2358–2385. (https://doi.org/10.1038/s41596-024-00978-0)

[19] Choi, G., and Hong, S.H. (2019). Selective *N*-Formylation and *N*-Methylation of Amines Using Methanol as a Sustainable C1 Source. ACS Sustainable Chem. Eng., *7*, 716–723. (https://doi.org/10.1021/acssuschemeng.8b04286)

[20] Choi, G., and Hong, S.H. (2018). Selective Monomethylation of Amines with Methanol as the C_1 Source. Angew Chem Int Ed, *57*, 6166–6170. (https://doi.org/10.1002/anie.201801524)

[21] Sheetal, Mehara, P., and Das, P. (2023). Methanol as a greener C1 synthon under non-noble transition metal-catalyzed conditions. Coord Chem Rev, *475*, 214851. (https://doi.org/10.1016/j.ccr.2022.214851)

[22] Natte, K., Neumann, H., Beller, M., and Jagadeesh, R.V. (2017). Transition-Metal-Catalyzed Utilization of Methanol as a C_1 Source in Organic Synthesis. Angew Chem Int Ed, *56*, 6384–6394. (https://doi.org/10.1002/anie.201612520)

[23] González-Lainez, M., Jiménez, M.V., Azpiroz, R., Passarelli, V., Modrego, F.J., and Pérez-Torrente, J.J. (2022). *N* -Methylation of Amines with Methanol Catalyzed by Iridium(I) Complexes Bearing an N,O-Functionalized NHC Ligand. Organometallics, *41*, 1364–1380. (https://doi.org/10.1021/acs.organomet.2c00125)

[24] González-Lainez, M., Jiménez, M.V., Passarelli, V., and Pérez-Torrente, J.J. (2020). Effective *N* -methylation of nitroarenes with

methanol catalyzed by a functionalized NHC-based iridium catalyst: a green approach to *N* -methyl amines. Catal. Sci. Technol., *10*, 3458–3467. (https://doi.org/10.1039/D0CY00707B)

[25] Goyal, V., Gahtori, J., Narani, A., Gupta, P., Bordoloi, A., and Natte, K. (2019). Commercial Pd/C-Catalyzed *N* -Methylation of Nitroarenes and Amines Using Methanol as Both C1 and H_2 Source. J. Org. Chem., *84*, 15389–15398. (https://doi.org/10.1021/acs.joc.9b02141)

[26] Zhang, F., Chen, K., Min, X., Yang, W., Su, M., and Cao, Z. (2024). Catalysis-Controlled Selective *N* -mono or *N* -di-methylation of Anilines: A Review on Synthesis of *N* -methyl or *N* , *N* -dimethyl anilines. ChemistrySelect, *9*, e202304621. (https://doi.org/10.1002/slct.202304621)

[27] Guin, A.K., Pal, S., Chakraborty, S., Chakraborty, S., and Paul, N.D. (2023). *N* -Alkylation of Amines by C1–C10 Aliphatic Alcohols Using A Well-Defined Ru(II)-Catalyst. A Metal–Ligand Cooperative Approach. J. Org. Chem., *88*, 5944–5961. (https://doi.org/10.1021/acs.joc.3c00313)

[28] Piehl, P., Amuso, R., Spannenberg, A., Gabriele, B., Neumann, H., and Beller, M. (2021). Efficient methylation of anilines with methanol catalysed by cyclometalated ruthenium complexes. Catal. Sci. Technol., *11*, 2512–2517. (https://doi.org/10.1039/D0CY02210A)

[29] Wang, X., Zhao, K., Wang, H., and Shi, F. (2021). Selective synthesis of *N* -monomethyl amines with primary amines and nitro compounds. Catal. Sci. Technol., *11*, 7239–7254. (https://doi.org/10.1039/D1CY01177D)

[30] Elangovan, S., Neumann, J., Sortais, J.-B., Junge, K., Darcel, C., and Beller, M. (2016). Efficient and selective *N*-alkylation of

amines with alcohols catalysed by manganese pincer complexes. Nat Commun, *7*, 12641. (https://doi.org/10.1038/ncomms12641)

[31] Liu, P., Tung, N.T., Xu, X., Yang, J., and Li, F. (2021). *N* -Methylation of Amines with Methanol in the Presence of Carbonate Salt Catalyzed by a Metal–Ligand Bifunctional Ruthenium Catalyst [(*p* -cymene)Ru(2,2′-bpyO)(H_2 O)]. J. Org. Chem., *86*, 2621–2631. (https://doi.org/10.1021/acs.joc.0c02685)

[32] Meng, C., Liu, P., Tung, N.T., Han, X., and Li, F. (2020). *N*-Methylation of Amines with Methanol in Aqueous Solution Catalyzed by a Water-Soluble Metal–Ligand Bifunctional Dinuclear Iridium Catalyst. J. Org. Chem., *85*, 5815–5824. (https://doi.org/10.1021/acs.joc.9b03411)

[33] Rong, M.K., Chirila, A., Franciolus, D., Lutz, M., Nieger, M., Ehlers, A.W., Slootweg, J.C., and Lammertsma, K. (2019). Protic NHC Iridium Complexes with β-H Reactivity–Synthesis, Acetonitrile Insertion, and Oxidative Self-Activation. Organometallics, *38*, 4543–4553. (https://doi.org/10.1021/acs.organomet.9b00584)

[34] Yadav, E., Nath, S., Shahid, N., Saha, A., Das, B., and Singh, A.K. (2025). Enhanced Activity of Proton-Responsive Protic-NHC-Ru(II) Bis(pincer) Complexes for Electrochemical Water Oxidation. ChemCatChem, e01003. (https://doi.org/10.1002/cctc.202501003)

[35] Reed-Berendt, B.G., Latham, D.E., Dambatta, M.B., and Morrill, L.C. (2021). Borrowing Hydrogen for Organic Synthesis. ACS Cent. Sci., *7*, 570–585. (https://doi.org/10.1021/acscentsci.1c00125)

[36] Illam, P.M., and Rit, A. (2022). Electronically tuneable orthometalated Ru^{II} –NHC complexes as efficient catalysts for C–C and C–N bond formations *via* borrowing hydrogen strategy.

Catal. Sci. Technol., *12*, 67–74. (https://doi.org/10.1039/D1CY01767E)

[37] Kuwata, S., and Ikariya, T. (2011). β-Protic Pyrazole and *N*-Heterocyclic Carbene Complexes: Synthesis, Properties, and Metal–Ligand Cooperative Bifunctional Catalysis. Chem Eur J, *17*, 3542–3556. (https://doi.org/10.1002/chem.201003296)

[38] Hahn, F.E. (2013). Substrate Recognition and Regioselective Catalysis with Complexes Bearing NR,NH-NHC Ligands. ChemCatChem, *5*, 419–430. (https://doi.org/10.1002/cctc.201200567)

[39] Chernyshev, V.M., Denisova, E.A., Eremin, D.B., and Ananikov, V.P. (2020). The key role of R–NHC coupling (R = C, H, heteroatom) and M–NHC bond cleavage in the evolution of M/NHC complexes and formation of catalytically active species. Chem. Sci., *11*, 6957–6977. (https://doi.org/10.1039/D0SC02629H)

[40] Garg, N.K., Goriya, Y., Manojveer, S., Wendt, O.F., and Johnson, M.T. (2024). Ruthenium NNN-Based Pincer Complexes with Metal Ligand Cooperation as Catalysts for N-Methylation of Anilines and Nitroarenes with Methanol as a C1 Source. ChemCatChem, *16*, e202301601. (https://doi.org/10.1002/cctc.202301601)

[41] Bai, M., Zhang, S., Lin, Z., Hao, Z., Han, Z., Lu, G.-L., and Lin, J. (2024). Ruthenium Complexes with NNN-Pincer Ligands for *N*-Methylation of Amines Using Methanol. Inorg. Chem., *63*, 11821–11831. (https://doi.org/10.1021/acs.inorgchem.4c01561)

[42] Pirani, F., and Eshghi, H. (2025). Eco-friendly *N*-mono-methylation of anilines with methanol as a sustainable C1 source via hydrogen borrowing: using new caffeine-derived ruthenium–NHC complex as high-efficiency and green catalyst. Inorg. Chem.

Commun., *181*, 115297. (https://doi.org/10.1016/j.inoche.2025.115297)

[43] Biswas, N., and Srimani, D. (2021). Ru-Catalyzed Selective Catalytic Methylation and Methylenation Reaction Employing Methanol as the C1 Source. J. Org. Chem., *86*, 10544–10554. (https://doi.org/10.1021/acs.joc.1c01185)

[44] Maji, M., Chakrabarti, K., Paul, B., Roy, B.C., and Kundu, S. (2018). Ruthenium(II)-NNN-Pincer-Complex-Catalyzed Reactions Between Various Alcohols and Amines for Sustainable C−N and C−C Bond Formation. Adv Synth Catal, *360*, 722–729. (https://doi.org/10.1002/adsc.201701117)

[45] Paul, B., Shee, S., Chakrabarti, K., and Kundu, S. (2017). Tandem Transformation of Nitro Compounds into *N* -Methylated Amines: Greener Strategy for the Utilization of Methanol as a Methylating Agent. ChemSusChem, *10*, 2370–2374. (https://doi.org/10.1002/cssc.201700503)

[46] Zhang, S., Ibrahim, J.J., and Yang, Y. (2019). A pincer ligand enabled ruthenium catalyzed highly selective *N* -monomethylation of nitroarenes with methanol as the C1 source. Org. Chem. Front., *6*, 2726–2731. (https://doi.org/10.1039/C9QO00544G)

[47] Kappe, C.O. (2004). Controlled Microwave Heating in Modern Organic Synthesis. Angew Chem Int Ed, *43*, 6250–6284. (https://doi.org/10.1002/anie.200400655)

[48] Oliver Kappe, C. (2008). Microwave dielectric heating in synthetic organic chemistry. Chem. Soc. Rev., *37*, 1127. (https://doi.org/10.1039/b803001b)

[49] Ju, Y., and Varma, R.S. (2005). An Efficient and Simple Aqueous *N*-Heterocyclization of Aniline Derivatives: Microwave-Assisted

Synthesis of *N* -Aryl Azacycloalkanes. Org. Lett., *7*, 2409–2411. (https://doi.org/10.1021/ol050683t)

[50] Ghosh, S., and Mukhopadhyay, C. (2018). Microwave Syntheses: A Modern Day Approach Towards Sustainable Chemistry. CMIC, *4*. (https://doi.org/10.2174/2213335604666170830122722)

[51] Jaiswal, V., Singh, A., Kumar, N., Misra, S., and Singh, A.K. (2025). Microwave-Assisted Metal-Free C─N Coupling for The Synthesis of Common Ligand Precursors of Organometallic Complexes. ChemistrySelect, *10*, e202500724. (https://doi.org/10.1002/slct.202500724)

[52] Mondal, A., and Mukhopadhyay, C. (2024). Solvent-free microwave reactions towards significant organic transformations: A green approach. Tetrahedron Green Chem, *4*, 100054. (https://doi.org/10.1016/j.tgchem.2024.100054)

[53] Xu, G., and Wang, Y.-G. (2004). Microwave-Assisted Amination from Aryl Triflates without Base and Catalyst. Org. Lett., *6*, 985–987. (https://doi.org/10.1021/ol049963j)

[54] Gour, J., Gatadi, S., Malasala, S., Yaddanpudi, M.V., and Nanduri, S. (2019). A Microwave-Assisted SmI_2 -Catalyzed Direct *N* -Alkylation of Anilines with Alcohols. J. Org. Chem., *84*, 7488–7494. (https://doi.org/10.1021/acs.joc.9b00717)

[55] Kumar, K.Y., Kumar, C.B.P., Prasad, K.N.N., Jeon, B., Alsalme, A., and Prashanth, M.K. (2022). Microwave-assisted *N* -alkylation of amines with alcohols catalyzed by $MnCl_2$: Anticancer, docking, and DFT studies. Archiv der Pharmazie, *355*, 2100443. (https://doi.org/10.1002/ardp.202100443)

[56] Shmidt, M.S., Reverdito, A.M., Kremenchuzky, L., Perillo, I.A., and Blanco, M.M. (2008). Simple and Efficient Microwave

Assisted *N*-Alkylation of Isatin. Molecules, *13*, 831–840. (https://doi.org/10.3390/molecules13040831)

[57] Bhatkar, A., Mane, S., Mekala, S.P., Gogoi, P., Mohapatra, G., Ramakrishnan, A., Marimuthu, P., and Thirumalaiswamy, R. (2022). Microwave-assisted selective *N*-alkylation of aniline over molybdenum supported catalyst. Cat Commun, *168*, 106464. (https://doi.org/10.1016/j.catcom.2022.106464)

[58] Gabano, E., and Ravera, M. (2022). Microwave-Assisted Synthesis: Can Transition Metal Complexes Take Advantage of This "Green" Method? Molecules, *27*, 4249. (https://doi.org/10.3390/molecules27134249)

[59] Priecel, P., and Lopez-Sanchez, J.A. (2019). Advantages and Limitations of Microwave Reactors: From Chemical Synthesis to the Catalytic Valorization of Biobased Chemicals. ACS Sustain. Chem. Eng., *7*, 3–21. (https://doi.org/10.1021/acssuschemeng.8b03286)

[60] Campos, J., Sharninghausen, L.S., Manas, M.G., and Crabtree, R.H. (2015). Methanol Dehydrogenation by Iridium *N*-Heterocyclic Carbene Complexes. Inorg. Chem., *54*, 5079–5084. (https://doi.org/10.1021/ic502521c)

[61] Henary, M., Kananda, C., Rotolo, L., Savino, B., Owens, E.A., and Cravotto, G. (2020). Benefits and applications of microwave-assisted synthesis of nitrogen containing heterocycles in medicinal chemistry. RSC Adv., *10*, 14170–14197. (https://doi.org/10.1039/D0RA01378A)

[62] Tiwari, G., Khanna, A., Mishra, V.K., and Sagar, R. (2023). Recent developments on microwave-assisted organic synthesis of nitrogen- and oxygen-containing preferred heterocyclic scaffolds. RSC Adv., *13*, 32858–32892. (https://doi.org/10.1039/D3RA05986C)

[63] Campos, J., Sharninghausen, L.S., Manas, M.G., and Crabtree, R.H. (2015). Methanol Dehydrogenation by Iridium *N*-Heterocyclic Carbene Complexes. Inorg. Chem., *54*, 5079–5084. (https://doi.org/10.1021/ic502521c)

[64] Nath, S., Yadav, E., Raghuvanshi, A., and Singh, A.K. (2023). Ru(II) Complexes with Protic- and Anionic-Naked-NHC Ligands for Cooperative Activation of Small Molecules**. Chem Eur J, *29*, e202301971. (https://doi.org/10.1002/chem.202301971)

[65] Nath, S., Yadav, E., Raghuvanshi, A., and Singh, A.K. (2023). Mechanistic insights and comparative analysis of Ru(II)–NNC pincer complexes with anionic-, protic-, and classical-NHCs for transfer hydrogenation of ketones. Catal. Sci. Technol., *13*, 7085–7099. (https://doi.org/10.1039/D3CY01383A)

[66] Nath, S., and Singh, A.K. (2025). Substrate-assisted product release in hydrogenation of LOHCs facilitated by hemilabile pyridine in Ru(II)–NNC pincer complexes and enhanced activity of proton-responsive protic-NHC ligands. Catal. Sci. Technol., *15*, 2999–3008. (https://doi.org/10.1039/D5CY00209E)

[67] Yu, X., Cui, X., Jing, H., Qian, B., Yuan, H., and Shi, F. (2024). Recent Development in Synthesis of N-Methylamines with Amines and Methanol. ChemCatChem, *16*, e202400291. (https://doi.org/10.1002/cctc.202400291)

[68] Saha, A., Nath, S., Yadav, E., and Singh, A.K. (2025). Ru(II)-Protic-NHC Complex Catalyzed Selective *N*-alkylation of Anilines with Primary Alcohols: Mechanistic Insights and Role of Salt Additives. ChemCatChem, *17*. (https://doi.org/10.1002/cctc.202500184)

[69] Teng, Q., and Huynh, H.V. (2014). Determining the Electron-Donating Properties of Bidentate Ligands by ^{13}C NMR Spectroscopy. Inorg. Chem., *53*, 10964–10973. (https://doi.org/10.1021/ic501325j)

CHAPTER 4

Structure-Activity Relationships and β- vs γ-Substituent Effects on Formic Acid Dehydrogenation

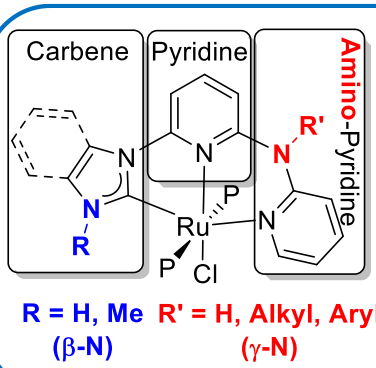

This chapter combines the understanding of the influence of β-Nitrogen and γ-substitution in the CPAP ligand framework on catalytic performance. The catalytic behaviour of the resulting ruthenium complexes was evaluated through formic acid dehydrogenation reactions under base-assisted and ionic solvent conditions. The study demonstrates that subtle electronic and steric modifications at the β- and γ-positions significantly affect catalytic activity and stability, providing deeper insight into the structure-activity relationships within the ligand system.

4.1 Introduction

Growing global energy challenges, including fossil fuel depletion, greenhouse gas emissions, and rising demand, have intensified the shift toward renewable energy sources, necessitating the development of efficient catalysts for clean, economical, and sustainable energy production, storage, and use.[1–10] Extensive global research initiatives are currently focused on the sustainable production and storage of energy, as evidenced by numerous recent reviews covering a wide spectrum of catalytic systems, including homogeneous [11–14] and heterogeneous catalysts,[15–17] photocatalysts,[18,19] and electrocatalysts. [20] Among these, homogeneous catalysis offers distinct advantages, such as operation under relatively mild conditions and the ability to elucidate reaction mechanisms at the molecular level, thereby providing valuable insights for the rational design and optimization of more efficient catalytic processes.[21–26] Among various hydrogen storage candidates, formic acid (FA) has stood out as a benchmark due to its favorable properties: it is a stable liquid, contains 4.4 wt% hydrogen, can be readily synthesized from carbon dioxide or biomass,[27–31] and, under optimal catalytic conditions, can release hydrogen without generating carbon monoxide, thereby avoiding catalyst poisoning.[32–36] Recent advances in Ru- and Fe-based catalysts have enabled stable, additive-free formic acid dehydrogenation (FADH), exemplified by Milstein's acridine-based Ru pincer catalyst achieving a TON of ~1.7×10^6 over a month.[27] These

developments underscore the potential of homogeneous transition-metal catalysts in decarbonizing industry [37] and supporting a renewable hydrogen economy.[38,39]

Comparative studies of ruthenium complexes, such as those by Milstein,[27] Huang,[40] Nielsen,[41] Swarts,[42] and Plietker,[43] revealed substantial variations in catalytic performance, as quantified by the turnover number (TON) and turnover frequency (TOF). For example, Milstein's acridine-based pincer complex exhibits exceptional stability and longevity, achieving TON values exceeding 1.7 million and TOF up to 3,067 h^{-1} under additive-free conditions with neat formic acid, attributed to its robust ligand framework and cooperative activation mechanisms.[27] In contrast, the pyridyl-formamidine half-sandwich complexes of Swarts, when combined with alkali formates, reach TONs of approximately 7,892 and TOFs near 300 h^{-1} at elevated temperatures, highlighting the influence of additives and temperature on catalytic efficiency.[42] Nielsen's POP-pincer systems, operating in ionic liquids without additives, achieve rapid conversions with TOFs up to 4,525 h^{-1} and TONs approaching 1,000, demonstrating the role of solvent and ligand environment in modulating activity.[41] PNNP-Ru catalyst of Plietker, capable of reversible hydrogenation and dehydrogenation, exhibits moderate TONs (~ 4,133) and pronounced sensitivity to additives, such as toluene, which can accelerate reaction rates.[43] Huang's PN_3-pincer complex stands out for its long-term activity and selectivity under base-free, aqueous-tolerant conditions, with TONs exceeding 1 million and TOFs above 7,000 h^{-1}, alongside excellent CO-free H_2 production and air/moisture stability [40] (Figure 4.1).

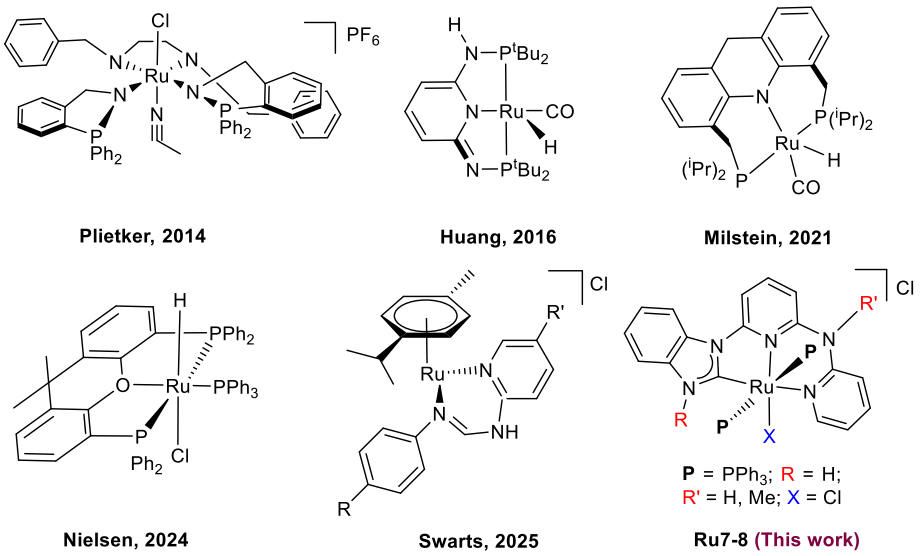

Figure 4.1 Some representative homogeneous Ru-catalysts for formic acid dehydrogenation (FADH).

Within this framework, the strategic incorporation of "non-innocent" or proton-responsive ligands has emerged as a powerful design paradigm.[44–47] Such ligands actively participate in catalytic cycles, shuttling protons and stabilizing reactive intermediates, thereby unlocking new reactivity modes.[48–50] Recent studies have demonstrated that NHCs bearing NH moieties can promote cooperative pathways in challenging transformations such as water splitting, [51–55] CO_2 reduction to methanol,[56–59] nitrogen fixation,[60–62] and hydrogen release from liquid organic hydrogen carriers.[63–67] Building on these advances, our group has developed unsymmetrical CNN-type pincer ligands, enabling access to Ru(II) complexes bearing both protic and classical NHC ligands featuring benzimidazolylidene[68–70] and triazolylidene[71] ligands (Figure 4.2). Herein, we present the first systematic study of Ru(II)-protic-NHC complexes in formic acid dehydrogenation. Specifically, we probed the influence of β- versus γ-substitution (*N*-H vs. *N*-Me) on the catalytic activity by comparing newly synthesized complexes (**Ru7** and **Ru8**) with previously reported analogues [**Ru-A**]-[**Ru-d**]. This comparative approach establishes the structure-activity relationships governing Ru(II)-protic-NHC reactivity, elucidates the mechanistic pathways under both base-assisted and ionic-liquid-mediated conditions,

and highlights the role of substituent effects in enabling efficient and sustainable hydrogen generation.

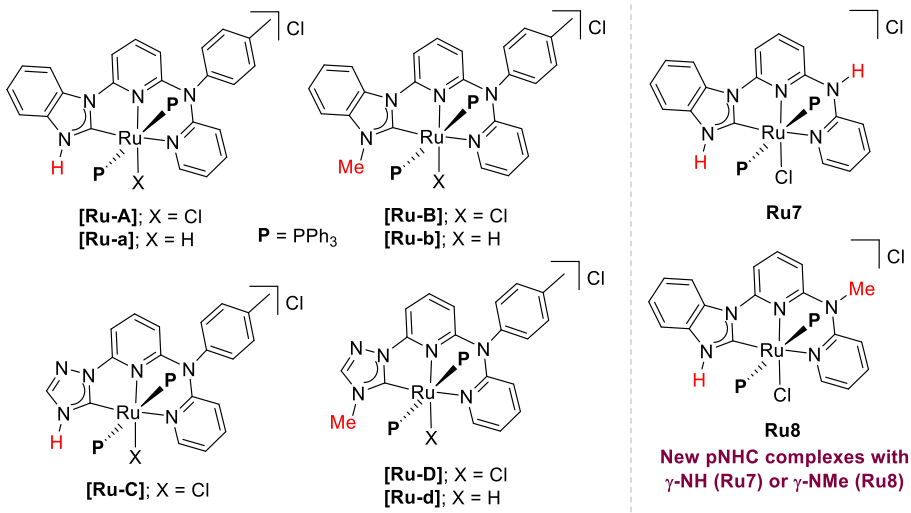

Figure 4.2 Complexes [**Ru-A]-[Ru-d**] and **Ru7-Ru8** were used in this study for formic acid dehydrogenation (FADH).

4.2 Results and discussion

4.2.1 CPAP series of ligands. The structural flexibility of our unsymmetrical, CNN pincer ligand platform has allowed us to extend this series of ligands, now described as **CPAP** (**C**arbene **P**yridine **A**mino-**P**yridine) ligands (Figure 4.3). Different azoles can be used to obtain, for example, benzimidazolylidene,[69] imidazolylidene,[70] or triazolylidene[71] based protic- or classical-NHC containing ligands. Numerous studies have shown that C-H and *N*-H linkers play a crucial role in metal-ligand cooperation, either through aromatization-dearomatization or direct substrate interaction.[72] In pyridine-based pincer ligands (e.g., Milstein's PNP and PNN), C-H arms enable reversible deprotonation and ligand dearomatization, enhancing reactivity.[73] Replacing C-H with more acidic and stronger *N*-H linkers, as in Huang's $PN_3(P)$ platform, alters acidity, bond strength, and aromaticity, leading to distinct reactivity.[74,75]

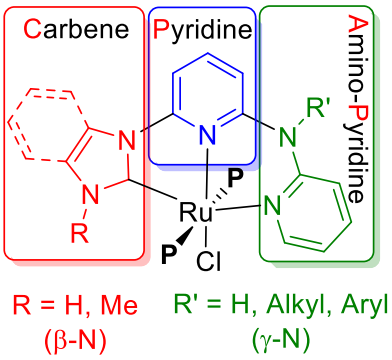

Figure 4.3 Demonstration of the CPAP series of ligands

4.2.2 Synthesis and Characterization of Ligands. Drawing inspiration from these concepts, we strategically modified the bridging nitrogen between the two pyridine units in the CPAP framework by introducing either *N*-H or *N*-Me substituents in place of the previously reported *N*-tolyl group. This modification afforded two new ligands: 6-(1*H*-benzo[*d*]imidazol-1-yl)-*N*-(pyridin-2-yl)pyridin-2-amine (**L5**) and 6-(1*H*-benzo[*d*]imidazol-1-yl)-*N*-methyl-*N*-(pyridin-2-yl)pyridin-2-amine (**L6**). These structural variations provide a platform for probing the effect of bridging nitrogen substitution on the coordination behavior and catalytic reactivity. The ligands were synthesized using a procedure analogous to that employed for the *N*-tolyl variant (Scheme 1).[69]

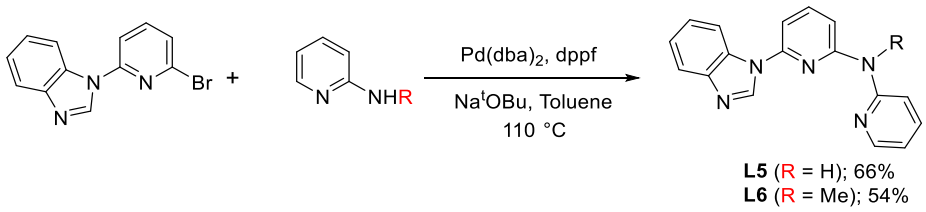

Scheme 4.1 Synthetic route for the preparation of ligands **L5** and **L6**.

The formation of **L5** and **L6** was confirmed by NMR and HRMS characterization. For **L5**, the ^{1}H NMR spectrum displayed a downfield resonance at δ 8.58 ppm, corresponding to the benzimidazole proton, while aromatic signals appeared between δ 8.32-6.91 ppm (Figure 4.4). In **L6**, a distinctive signal at δ 3.70 ppm corresponds to the *N*-methyl group, while the remaining resonances resemble those of **L5** (Figure 4.6). The ^{13}C NMR spectrum of **L6** further showed a methyl resonance at δ

36.5 ppm (Figure 4.7). The HRMS (ESI$^+$) spectrum of **L5** exhibited a peak at m/z 288.1248, corresponding to $[M+H]^+$ (calcd. for $C_{17}H_{13}N_5$:288.1249), confirming the formation of ligand **L5**. Similarly, **L6** displayed a peak at m/z 302.1406 for $[M+H]^+$ (calcd. for $C_{18}H_{15}N_5$: 302.1406).

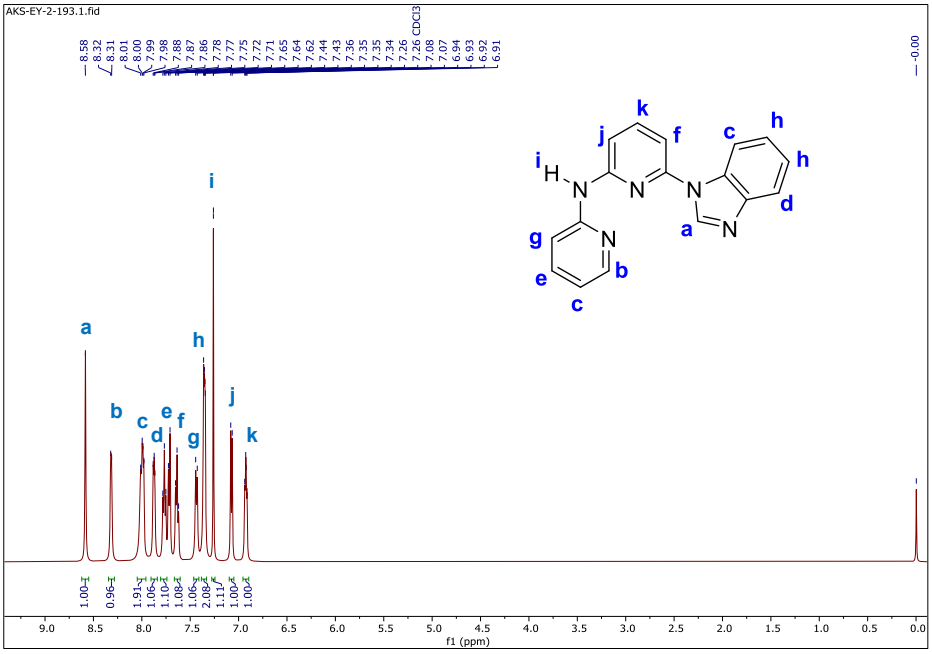

Figure 4.4 ^{1}H NMR of **L5** in $CDCl_3$

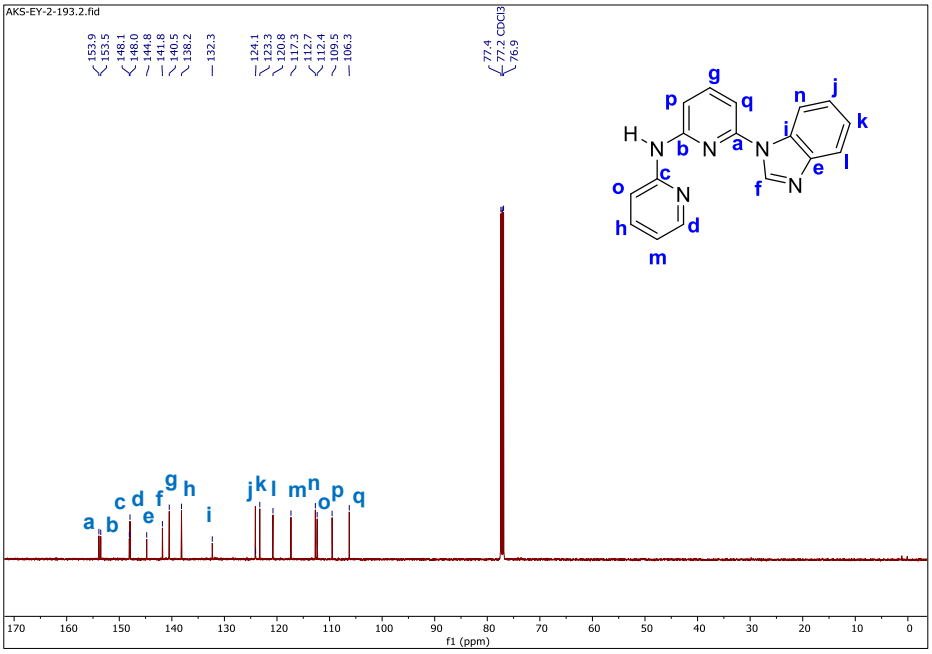

Figure 4.5 ^{13}C NMR of **L5** in $CDCl_3$

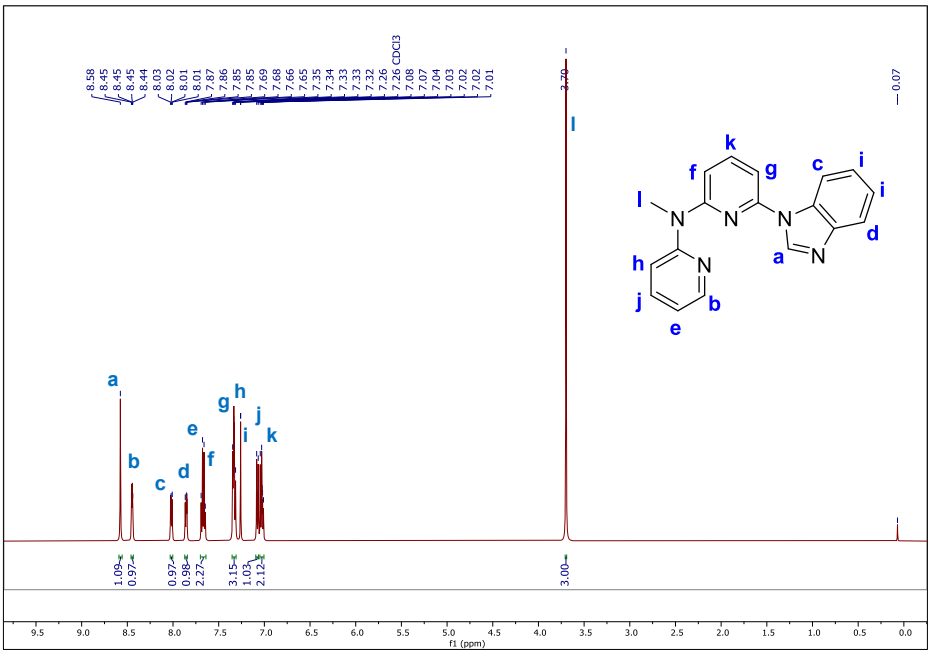

Figure 4.6 ^{1}H NMR of **L6** in $CDCl_3$

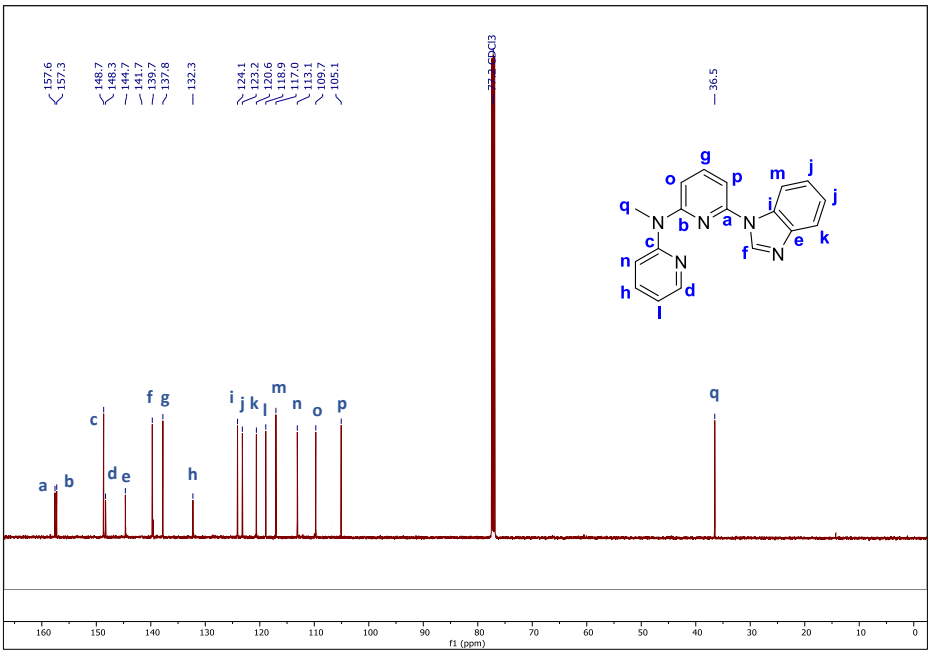

Figure 4.7 ^{13}C NMR of **L6** in $CDCl_3$

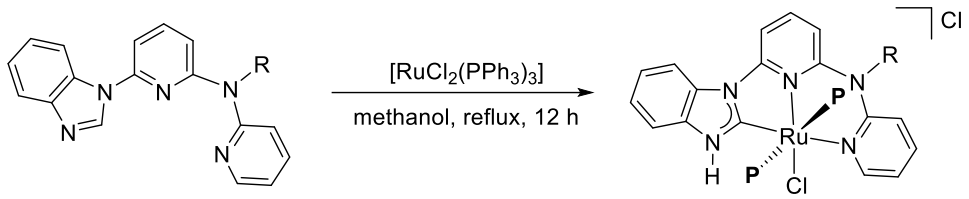

L5 (R = H)
L6 (R = Me)

Ru7; R = H
Ru8; R = Me

Scheme 4.2 Synthetic route for the preparation of **Ru7** and **Ru8** complexes.

4.2.3 Synthesis and Characterization of the Complexes. The Ru(II) protic NHC complexes **Ru7** and **Ru8** were synthesized in good yields through equimolar reactions of $RuCl_2(PPh_3)_3$ with ligands **L5** and **L6**, respectively, under reflux in methanol for 12 h (Scheme 4.2). The identities of the resulting complexes were confirmed by multinuclear NMR spectroscopy. In the ^1H NMR spectrum of **Ru7**, diagnostic downfield resonances at δ 14.10 and 13.87 ppm were assigned to the protic β-NH protons of the monophosphine and bisphosphine species, respectively (Figure 4.8). The bridging γ-NH protons appeared at δ 11.70 (monophosphine form) and δ 11.07 ppm (bisphosphine form), whereas the ortho-pyridyl protons appeared at δ 9.18 and 9.16 ppm for the respective species. The $^{13}C\{^1H\}$ NMR spectrum of **Ru7** exhibited characteristic carbene resonances as a doublet at δ 202.5 ppm and a triplet at δ 204.8 ppm, corresponding to the mono- and bisphosphine species, respectively (Figure 4.9). The $^{31}P\{^1H\}$ NMR spectrum displayed signals at δ 33.6 ppm and 24.6 ppm, attributable to the mono- and bisphosphine species, along with a resonance for free PPh_3 at δ -6.0 ppm (Figure 4.10). The existence of mono-and bisphosphine forms in DMSO-d_6 is a characteristic property of our set of complexes, which has already been discussed in our previous reports.[69] Due to the better solubility of these complexes in DMSO-d_6 compared to other deuterated solvents, the NMR spectra were recorded in this solvent. HRMS (ESI^+) provided additional confirmation, showing a peak at m/z 686.0840, assigned to $[M\text{-}Cl\text{-}PPh_3]^+$ (calcd. for $C_{35}H_{28}ClN_5PRu$: 686.0820), and a peak at m/z

948.1798, corresponding to $[M\text{-}Cl]^+$ (calcd. for $C_{53}H_{43}ClN_5P_2Ru$: 948.1736).

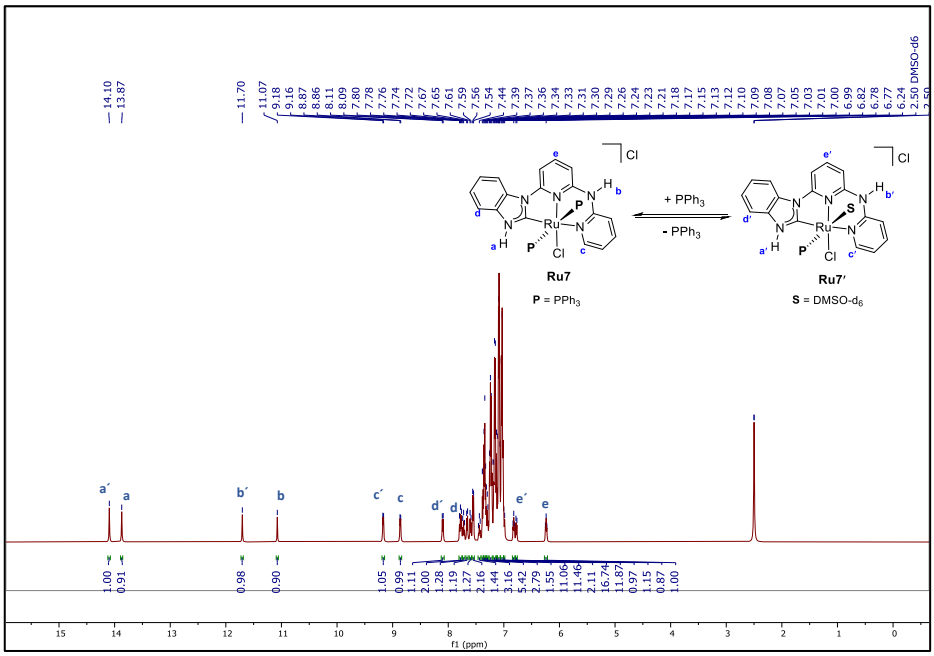

Figure 4.8 ^{1}H NMR of **Ru7** in $DMSO_6$

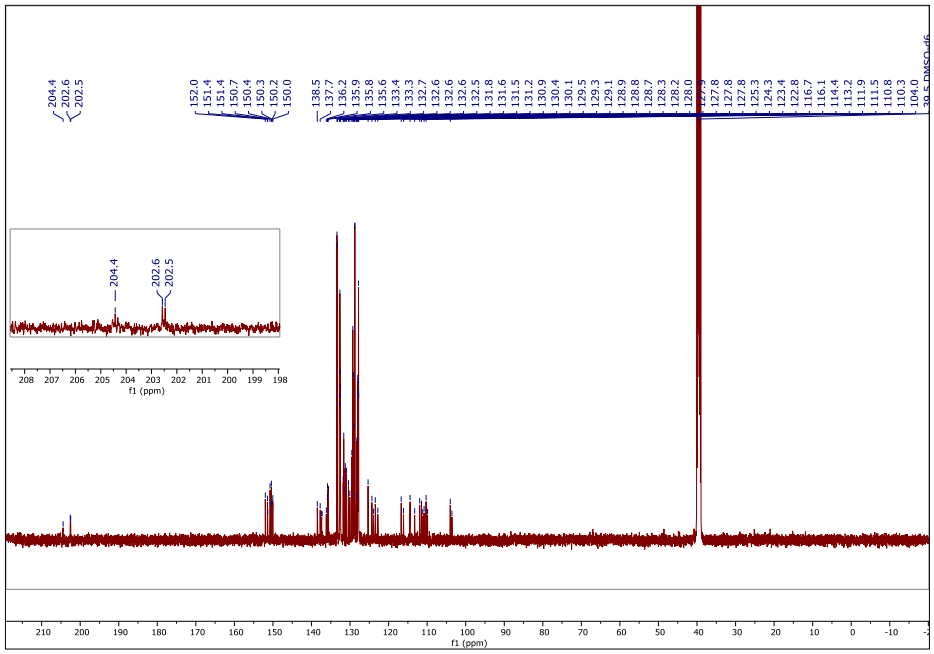

Figure 4.9 ^{13}C NMR of **Ru7** in $DMSO_6$

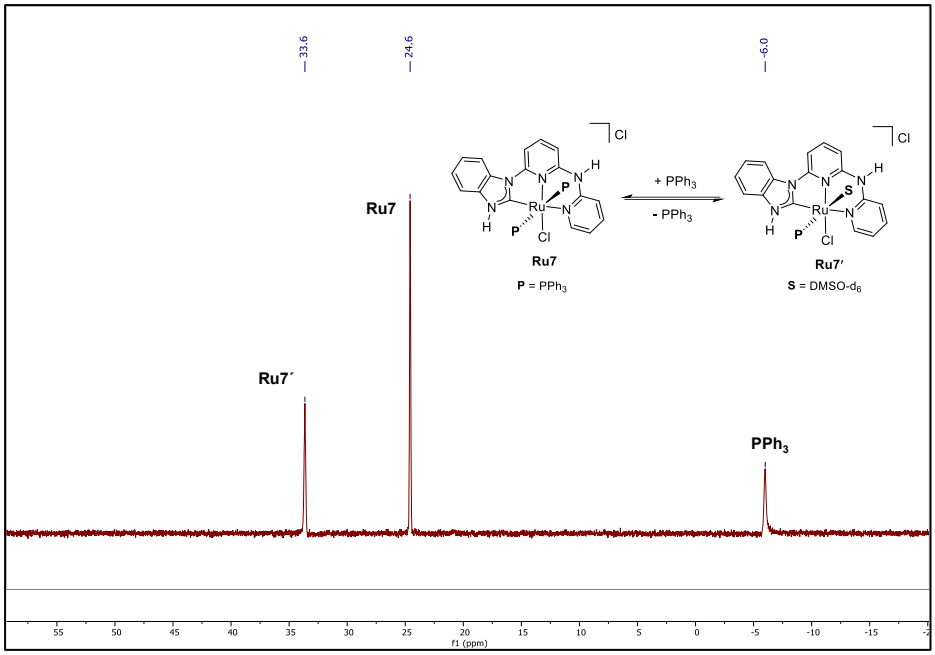

Figure 4.10 ^{31}P NMR of **Ru7** in $DMSO_6$

Similarly, the ^{1}H NMR spectrum of **Ru8** displayed downfield signals at δ 14.13 and 13.92 ppm for the β-NH protons of the mono- and bisphosphine species, respectively. Two distinct sets of ortho-pyridyl protons were observed at δ 9.33 and 8.81 ppm, whereas the methyl protons appeared at δ 3.18 and 2.97 ppm for both species (Figure 4.11). The ^{13}C{^{1}H} NMR spectrum displayed the characteristic carbene signals at δ 203.2 ppm (doublet, monophosphine) and δ 205.1 ppm (triplet, bisphosphine), along with methyl carbon resonances at δ 44.0 and 65.0 ppm (Figure 4.12). The ^{31}P{^{1}H} NMR spectrum showed signals at δ 30.2 and 19.5 ppm corresponding to the mono- and bisphosphine complexes, together with free PPh_3 at δ -6.0 ppm (Figure 4.13). HRMS (ESI^+) analysis of **Ru8** revealed a peak at m/z 700.0999, consistent with $[M\text{-}Cl\text{-}PPh_3]^+$ (calcd. 700.0977 for $C_{36}H_{30}ClN_5PRu$).

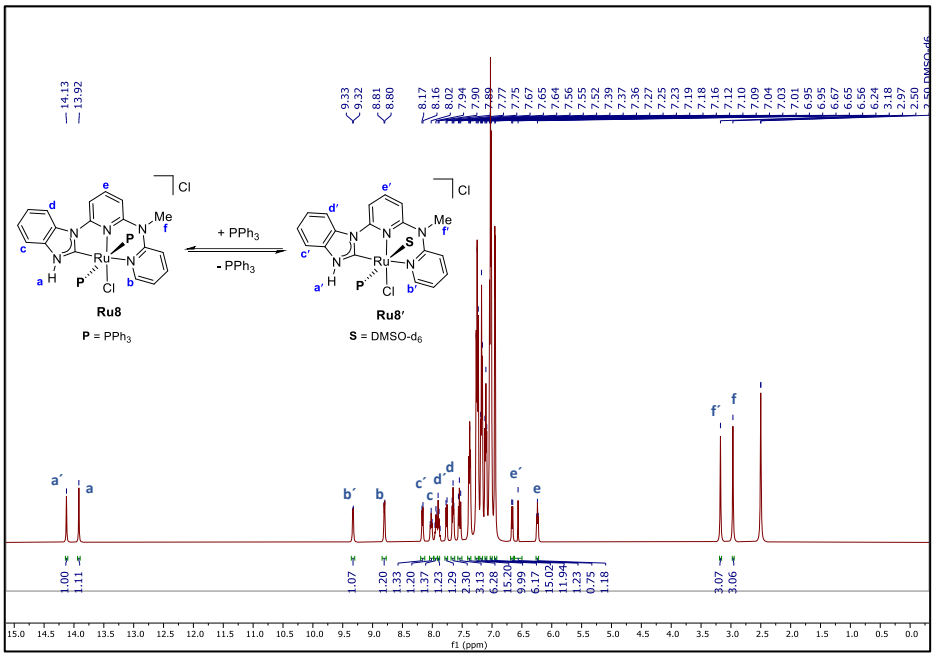

Figure 4.11 ^{1}H NMR of **Ru8** in $DMSO_6$

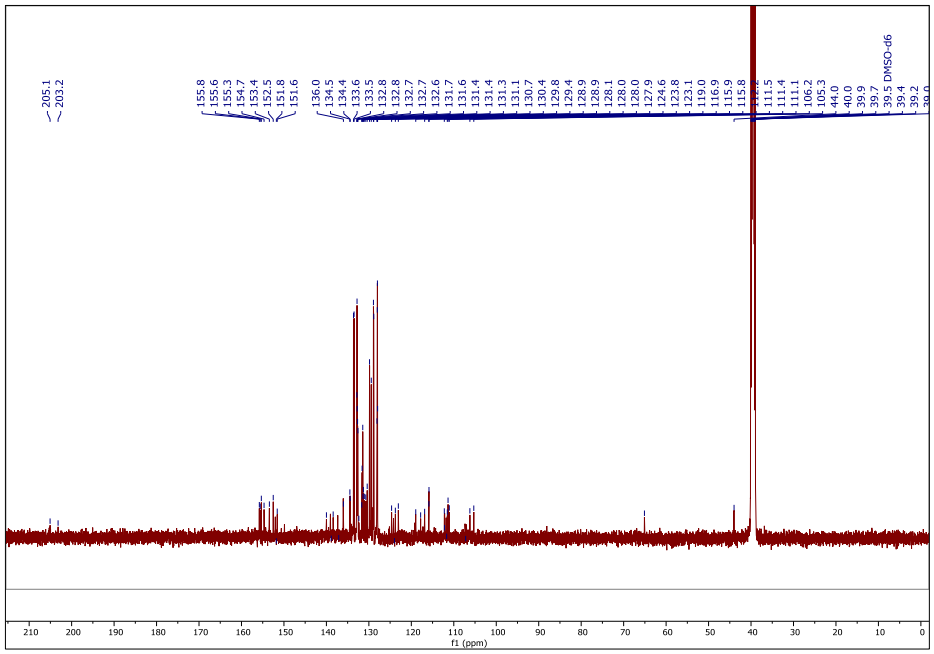

Figure 4.12 $^{13}C\{^{1}H\}$ NMR of **Ru8** in $DMSO_6$

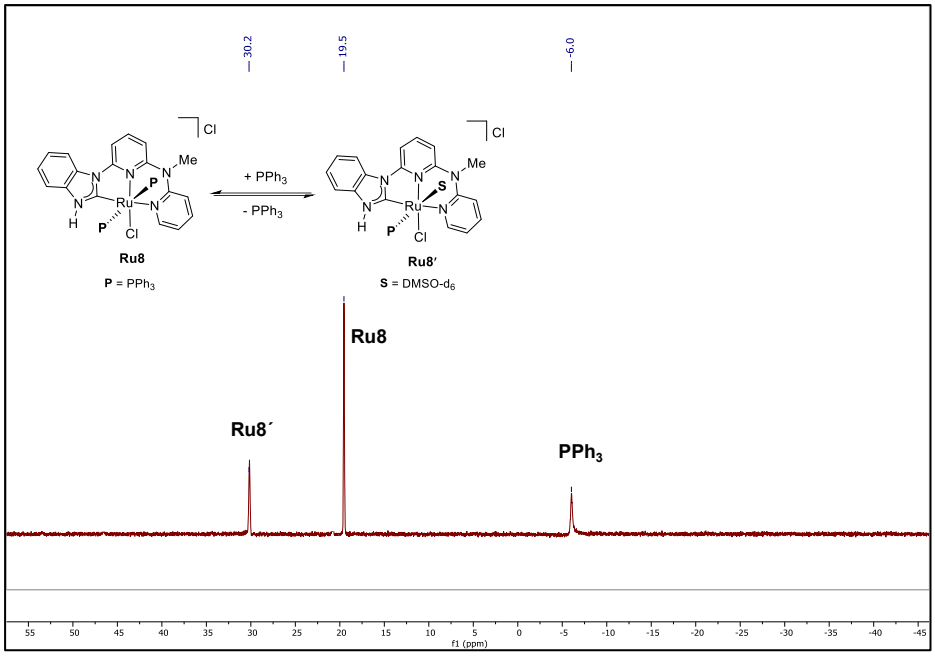

Figure 4.13 $^{31}P\{^{1}H\}$ NMR of **Ru8** in $DMSO_6$

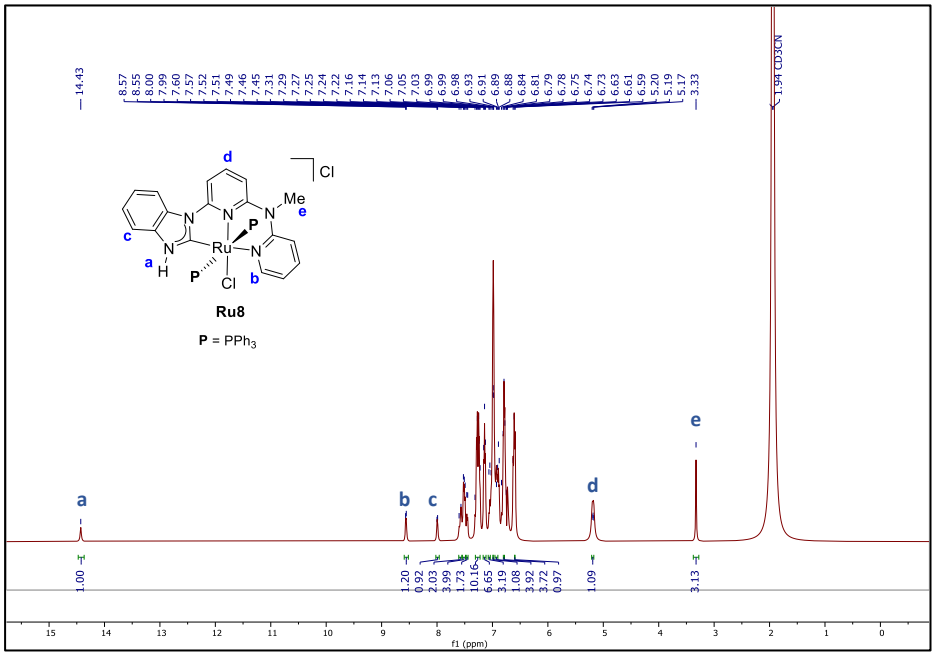

Figure 4.14 ^{1}H NMR of **Ru8** in CD_3CN

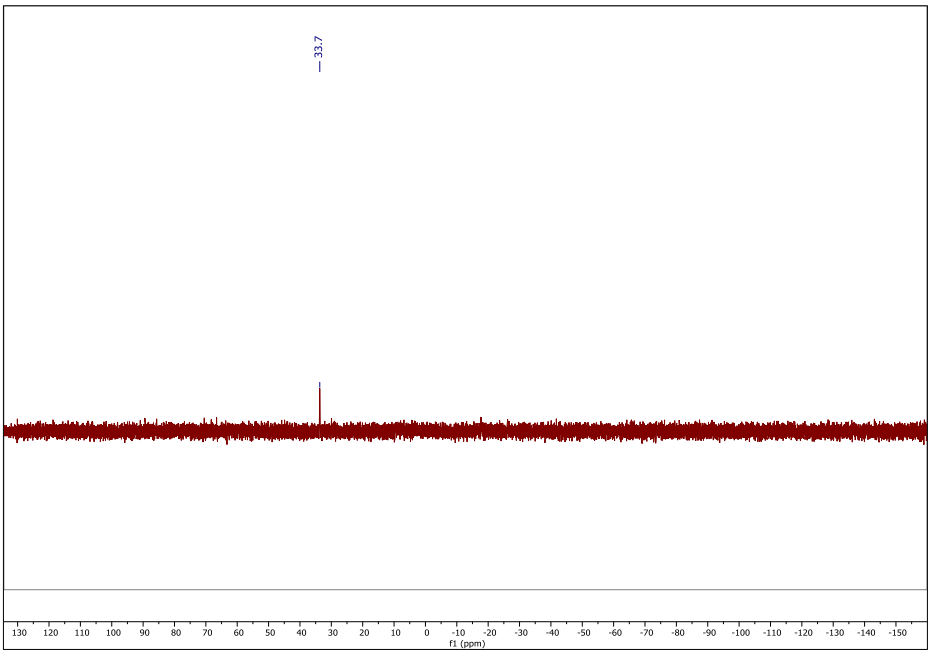

Figure 4.15 ^{31}P NMR of **Ru8** in CD_3CN

The existence of mono- and bisphosphine forms in DMSO-d_6 is well documented for these types of complexes and has been investigated in our previous report.[69] Due to the poor solubility of these complexes in other deuterated solvents, the NMR spectra were recorded in DMSO-d_6. To further confirm the existence of mono- and bisphosphine forms due to phosphine substitution by DMSO-d_6, we examined the NMR spectrum of **Ru8** in acetonitrile-d_3, despite its poor solubility. Although the ^{13}C NMR could not be obtained due to solubility issues, and **Ru7** could not be analyzed because of its very poor solubility in acetonitrile-d_3, the ^{1}H and ^{31}P NMR spectra of **Ru8** in acetonitrile-d_3 show no phosphine substitution and give a single set of signals (Figure 4.14-4.15).

4.2.4 Comparative study of Ru(II) complexes in formic acid dehydrogenation (FADH).

4.2.4.1 Base-assisted FADH. Formic acid dehydrogenation was chosen as a benchmark reaction owing to the previously observed exceptional catalytic efficiency of [**Ru-A]-[Ru-d**] complexes in sustainable transformation reactions. Complexes [**Ru-A]-[Ru-b**], which incorporate benzimidazolylidene-derived protic and classical *N*-heterocyclic carbene (NHC) ligands, exhibited significant activity in small molecule

activation and transfer hydrogenation reactions.[68,69] In comparison, the triazolylidene-based analogues, [**Ru-C**]-[**Ru-d**], were recently investigated in our studies on the hydrogenation of liquid organic hydrogen carriers (LOHCs).[71] Here, all complexes [**Ru-A**]-[**Ru-d**] and **Ru7**-**Ru8** were systematically evaluated to compare their catalytic efficiency.

Under optimized standard conditions, [**Ru-A**] catalyzed formic acid dehydrogenation (FADH) with remarkable efficiency, generating 1985 mL of gas within 6 hours. Prolonging the reaction to 24 h resulted in no significant additional gas evolution, thereby establishing 6 h as the optimal reaction time (Table 4.1, entry 1). The hydride-containing complex analogous to [**Ru-A**], designated [**Ru-a**], produced only 1120 mL of gas under the experimental conditions, indicating a comparatively lower hydrogen release efficiency (Table 4.1, entry 2). The lower reactivity of [**Ru-a**] is attributed to its reduced ability to dissociate PPh_3 ligands, a behavior that has been documented for this complex.[68] The classical-NHC complex, [**Ru-B**], afforded only 1660 mL of gas in 6 h (Table 4.1, entry 3), while its hydride-containing counterpart, [**Ru-b**], released 980 mL of gas within 6 h, and no further release of gas was observed after continuing for 24 h. A comparable trend was observed for the triazolylidene derivatives, [**Ru-C**] (protic NHC) and [**Ru-d**], where [**Ru-C**] exhibited superior catalytic activity relative to [**Ru-D**] (Table 4.1, entries 5-6). Notably, [**Ru-d**] displayed the poorest performance in the series, affording only 650 mL of gas after correcting for thermal expansion (Table 4.1, entry 7).

Although **Ru7** and **Ru8** were newly synthesized for this study, both complexes exhibited moderate catalytic performance. After 1 h, **Ru7** generated 1030 mL of gas mixture (Table 4.1, entry 8), whereas **Ru8** produced 1180 mL (Table 4.1, entry 9). These results suggest that the nature of the *N*-linker substitution plays a significant role in influencing reactivity, as this substitution constitutes a significant structural difference between [**Ru-A**], **Ru7**, and **Ru8**. Variations in the β-nitrogen substituent, namely between hydrogen and methyl groups, did

not provide conclusive insights into metal-ligand cooperativity. Notably, the presence of a protic *N*-H proton can enhance the activity owing to the potential for deprotonation. Such deprotonation increases the electron density at the metal center, which may affect the catalytic behavior. To rigorously assess the effect of *N*-linker substitution, experiments were designed to maintain a constant β-nitrogen environment while varying the linker. Under these controlled conditions, differential activity was observed, where [**Ru-A]**, with an *N*-tolyl group, and **Ru8**, with an *N*-Me group, exhibited better activity than **Ru7**, with an *N*-H group, ruling out the possibility of metal-ligand cooperation via the γ-*N*-H bond. Our previous report on the hydrogenation of nitriles highlights the participation of hemilability in the pyridine, which may be the case for the aforementioned trend.[71] The comparative evaluation of catalytic activity among β-*N*-substituted complexes revealed enhanced performance in the presence of an *N*-H moiety compared to its *N*-methyl analogue. In contrast, the γ-*N*-substituted complexes ([**Ru-A]**, **Ru7**, and **Ru8**) exhibited reduced catalytic activity in the presence of the *N*-H group, indicating that substitution with alkyl or aryl groups at the γ-position is more favorable for catalysis.

Table 4.1 Dehydrogenation of formic acid with ruthenium complexes[a]

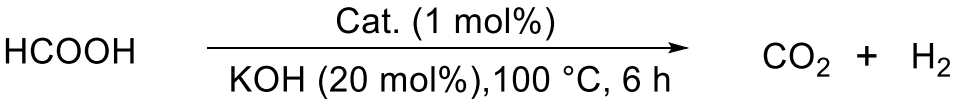

#	Cat.	Base (mol %)	Temp (°C)	Time (h)	Total Volume (mL)	TON	TOF(h^{-1})
1.	**[Ru-A]**	20	100	6	1985	72	12
2.	**[Ru-a]**	20	100	6	1120	40	7
3.	**[Ru-B]**	20	100	6	1660	60	10
4.	**[Ru-b]**	20	100	6	980	35	6
5.	**[Ru-C]**	20	100	6	1600	58	10
6.	**[Ru-D]**	20	100	6	1290	47	8
7.	**[Ru-d]**	20	100	6	650	23	4
8.	**Ru7**	20	100	6	1030	37	6
9.	**Ru8**	20	100	6	1180	43	7
10.[b]	**[Ru-A]**	20	100	6	1200	43	7

11.	**[Ru-A]**	20	90	6	1790	65	11
12.	**[Ru-A]**	20	80	6	1240	45	7
13.	**[Ru-A]**	20	70	6	850	31	5
14.[c]	**[Ru-A]**	10	100	6	1900	69	11
15.[d]	**[Ru-A]**	**20**	**100**	**6**	**1920**	**140**	**23**
16.[e]	**[Ru-A]**	20	100	6	150	22	4
17.[f]	**[Ru-A]**	10	100	6	1500	110	18
18.[g]	**[Ru-A]**	10	80	6	1020	74	12
19.	**[Ru-A]**	-	100	6	150	5	1
20.	**$RuCl_2(PPh_3)_3$**	20	100	6	700	25	4

[a]Reaction conditions: Formic acid (2.33 mL, 0.0617 mol), cat. (1 mol%), and KOH (20 mol%) at 100 °C for 6 h. [b]NaOH as a base. [c]10 mol% KOH. [d]0.5 mol% catalyst loading. [e]0.25 mol%. [f]0.5 mol% catalyst loading and 10 mol% KOH. [g]0.5 mol% catalyst loading and 10 mol% KOH with 80 °C.

Further screening of inorganic bases using [**Ru-A]** revealed that KOH was the most effective, producing the highest gas volume among KOH, NaOH, and NaOMe. Lowering the base loading from 20 mol% to 10 mol% resulted in only a slight decline in the catalytic activity (Table 4.1, entry 14), whereas further reduction led to a complete loss of activity. A decrease in temperature also negatively impacted gas evolution, with a significantly reduced output at 70 °C (Table 4.1, entries 11-13). Notably, efficient FADH was maintained with 0.5 mol% [**Ru-A]** and 20 mol% KOH, establishing these as optimal conditions (Table 4.1, entry 15). Further reduction of the catalyst to 0.25 mol% decreased the activity (entry 16). Reducing the base loading to 10 mol% KOH with 0.5 mol% [**Ru-A]** again reduced the performance (entry 17). A similar temperature dependence was observed under the optimized conditions (entry 18). Without a base, almost no reactivity was observed (entry 19), whereas with the metal precursor $RuCl_2(PPh_3)_3$, under the optimized reaction conditions, approximately 700 mL of gas mixture was obtained (entry 20).

4.2.4.2 Ionic liquid-mediated FADH. To avoid the requirement of an external base, ionic liquids have emerged as versatile reaction media owing to their intrinsic basicity.[76–78] In this study, we adopted the

strategy reported by Nielsen et al., who demonstrated impressive catalytic performance under these conditions.[41,79,80] Specifically, we utilized 1-butyl-3-methylimidazolium acetate (BMIMOAc), in which the acetate anion efficiently deprotonates formic acid to form formate. The generated formate subsequently coordinates with Ru, affording a Ru-formate intermediate that decomposes to release H_2 and CO_2.

BMIMOAc was employed in 0.4 equiv. relative to formic acid, which afforded excellent catalytic performance. Even at a reduced catalyst loading of 0.016 mol%, high activity was observed at 100 °C with an optimized reaction time of 1 h. Under these conditions, [**Ru-A]** displayed better catalytic activity than the other complexes investigated. Although all the complexes exhibited improved activity in the presence of BMIMOAc compared to base-assisted conditions, [**Ru-A]** consistently outperformed the others and was therefore selected for further studies. Within one hour, [**Ru-A]** produced 2675 ml of gas, which exceeded the amount generated under base-assisted conditions (Table 4.2, entry 1). Complexes [**Ru-a]-**[**Ru-d]** were evaluated under identical reaction conditions. Complexes [**Ru-B]** to [**Ru-D]** required a longer duration than one hour (Table 4.2, entries 3-6); nevertheless, their reactivity towards FADH was slightly lower than that of [**Ru-A]**. The newly synthesized complexes **Ru7** and **Ru8** exhibited moderate behavior, with **Ru7** demonstrating superior performance compared to [**Ru-B]-**[**Ru-d]**(Table 4.2, entry 8). In contrast, **Ru8** displayed an activity similar to that of the [**Ru-a]** complex (Table 4.2, entry 9). The correlation between temperature and catalytic efficiency again showed a similar trend (Table 4.2, entries 10-12).

Table 4.2 Optimization of reaction conditions using [Ru-A] in the presence of ionic liquid as solvent.

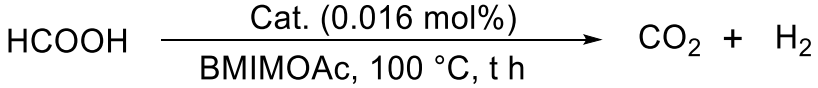

#	Cat.	Temp (°C)	Time (h)	Total volume (mL)	TON	TOF(h^{-1})
1.	**[Ru-A]**	100	1	2675	6100	6100
2.	**[Ru-a]**	100	1	1990	4500	4500

3.	**[Ru-B]**	100	1.16	2100	4800	4100
4.	**[Ru-b]**	100	2	1720	3900	1900
5.	**[Ru-C]**	100	1.75	1970	4500	2500
6.	**[Ru-D]**	100	1.75	1880	4300	2400
7.	**[Ru-d]**	100	1	1100	2500	2500
8.	**Ru7**	100	1	1870	4200	4200
9.	**Ru8**	100	1	1980	4500	4500
10.	**[Ru-A]**	90	1	2250	5100	5100
11.	**[Ru-A]**	80	1	1990	4500	4500
12.	**[Ru-A]**	70	1	1020	2300	2300

[a]Reaction conditions: formic acid (2.33 mL, 0.0617 mol), catalyst (0.016 mol%), and BMIMOAc (0.4 equiv. w.r.t substrate, 0.02468 mol, 4.66 mL), at 100 °C in 1 h. (TONs and TOFs are rounded off to two significant numbers.)

4.2.5 Kinetics of formic acid dehydrogenation: temperature, turnover number (TON) evolution, and reaction order. The gas volume-temperature plot (Figure 4.16a) clearly reveals a progressive decrease in gas release with a declining temperature, underscoring the temperature-dependent nature of gaseous product formation under the applied reaction conditions. In parallel, the TON-time profile (Figure 4.16b), monitored at 10-minute intervals, displayed a distinctly non-linear growth. A pronounced catalytic activity was evident within the first 10 min, followed by a more gradual increase thereafter. The TON continued to rise steadily over 60 min, implying the sustained efficiency and stability of the catalyst throughout the monitored timeframe.

4.2.6 Time-resolved kinetic analysis of formic acid dehydrogenation was performed by monitoring the TON as a function of time (Figure 4.17). A linear regression of the complete dataset afforded an average slope of 93 TOF·min^{-1} (corresponding to 5600 TOF·h^{-1}). However, interval-specific TOF calculations revealed a pronounced time dependence of the catalytic rate. The maximum TOF (~ 13,000 h^{-1}) is attained within the first 10 min, followed by a gradual decline to ~ 3700 h^{-1} in the final interval. This non-linear trend excludes the possibility of zero-order kinetics and instead points to pseudo-first-order kinetics in the early stages, likely governed by substrate availability or catalyst

transformation at later time points. Importantly, TON-time plots alone are insufficient to establish the reaction order unambiguously; a rigorous determination requires analysis of substrate concentration versus time data.

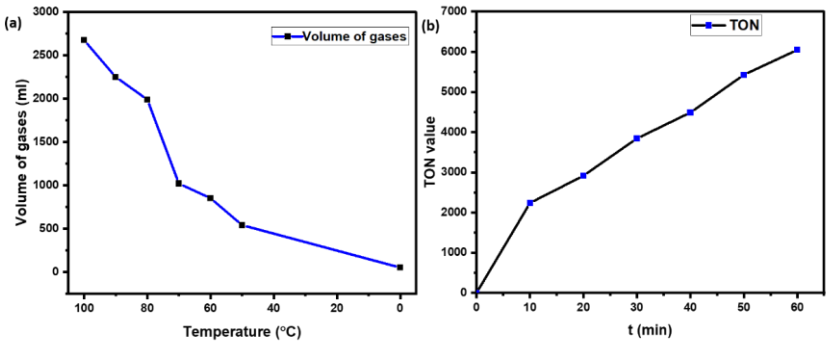

Figure 4.16 (**a**) Temperature-dependent gas evolution of [**Ru-A**]. (**b**) Time-resolved TON profile of [**Ru-A**] under the optimized reaction conditions. Reaction conditions: formic acid (0.0617 mol), Ru1 (0.016 mol%), BMIM(OAc) (0.02468 mol, 4.66 mL; 0.4 equiv. w.r.t to substrate), 100 °C.

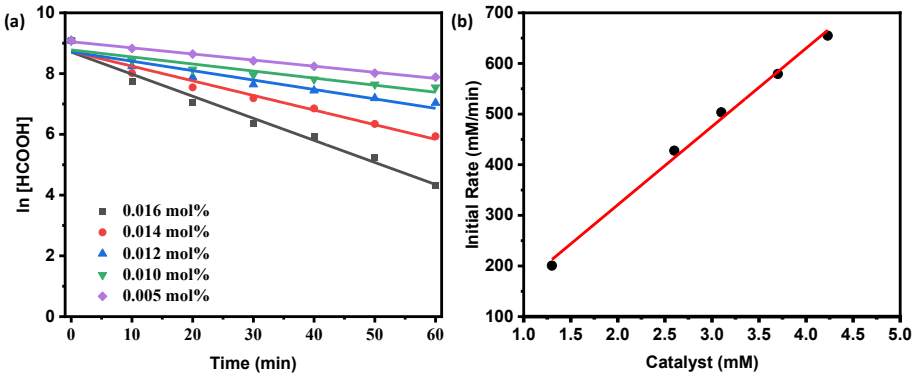

Figure 4.17 (**a**) Reaction time versus substrate concentration plots used to extract the initial rates of formic acid dehydrogenation at varying concentrations of the [**Ru-A**] complex. (**b**) Dependence of the initial dehydrogenation rate on the [**Ru-A**] catalyst concentration. The linear correlation confirmed a first-order relationship with respect to [**Ru-A**] under the examined conditions.

To establish the reaction order with respect to the catalyst, kinetic studies were conducted under ionic liquid conditions by varying the

catalyst concentration. The initial rates were extracted from the linear region of substrate consumption during the first 10 min, with each concentration examined in triplicate to ensure reproducibility. For a more rigorous evaluation of the kinetic order, the concentration of formic acid (A) was monitored as a function of time at different catalyst loadings, and ln[A] was plotted against time (Figure 4.17). The resulting linear correlations, particularly at early time intervals, unambiguously confirmed a first-order dependence on formic acid under the studied conditions.

4.2.7 Effect of sequential base addition on catalytic performance and gas evolution.

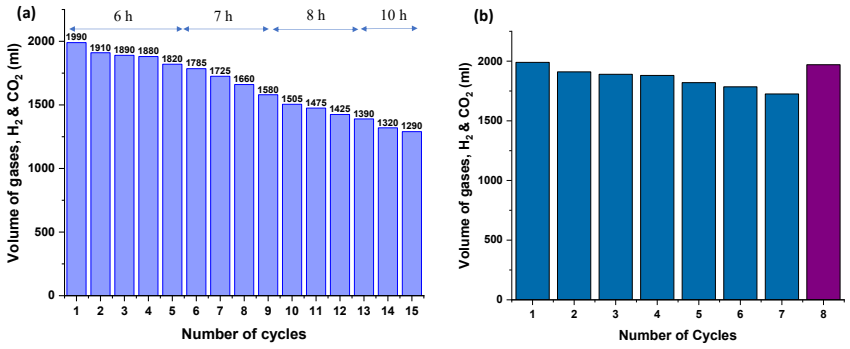

Figure 4.18 Plot of gas volume versus number of cycles for formic acid dehydrogenation at standard conditions (Formic acid (2.33 mL, 0.0617 mol), cat. (0.5 mol%), and KOH (20 mol%) at 100 °C for 6 h.), using a single catalyst addition: (**a**) 15 consecutive cycles after addition of base only for first cycle, and (**b**) addition of base after 7th cycle.

To evaluate the catalytic performance under gram-scale conditions, 15 consecutive cycles of formic acid dehydrogenation were performed with the sequential addition of the substrate to the reaction medium. In this control experiment, the catalyst and base were added only once at the outset, followed by successive substrate additions, which exhibited a progressive decline in gas production and extended time to reach peak gas evolution over successive cycles (Figure 4.18a). These observations

underscore the pivotal role of the base in sustaining the catalytic activity and facilitating rapid substrate conversion during formic acid dehydrogenation. Furthermore, the catalytic activity could be effectively restored by reintroducing the base after the observed decline in the seventh cycle. The addition of base at this stage resulted in a substantial enhancement of catalytic performance, reflected by an increase of ~245 mL in gas evolution relative to the preceding cycle (Figure 4.18b). Collectively, these results highlight the crucial role of the base in maintaining the catalyst activity across multiple consecutive cycles.

Additionally, in another set of experiments, KOH was added to each catalytic cycle, following the observation of enhanced gas evolution and shorter reaction times. In a complementary experiment, successive batches of formic acid were introduced at approximately 80% conversion of the preceding cycle without allowing the reaction mixture to dry. This modification resulted in a modest improvement in the cumulative gas evolution, with an increase of ~360 mL over seven cycles.

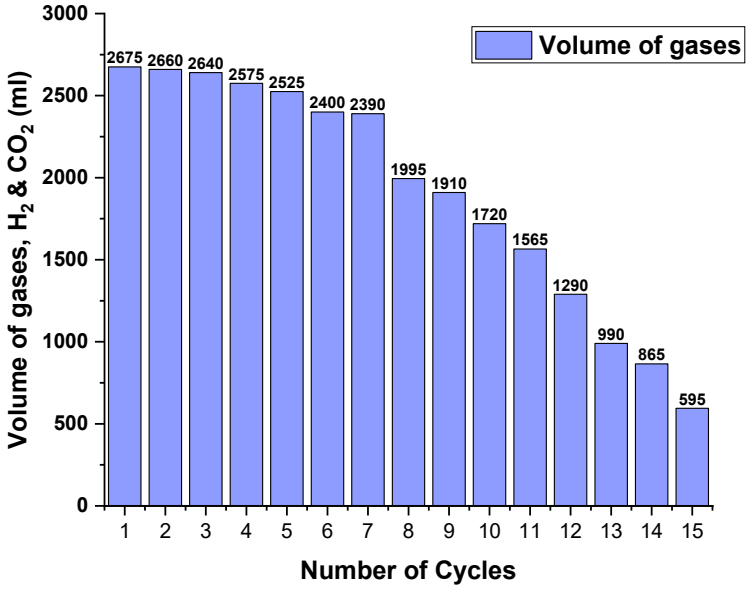

Figure 4.19 Graph between the number of cycles and the volume of gas collected using a single addition of catalyst [**Ru-A]** with BMIMOAc under standard conditions (formic acid, 0.0617 mol), cat. (0.016 mol%) and ionic solvent, that is, BMIMOAc (0.4 equiv.) at 100 °C in 1 h).

In the presence of an ionic solvent, successive additions of formic acid to a reaction mixture containing 0.016 mol% catalyst and 0.4 equivalents of ionic liquid solvent maintained nearly constant gas evolution over the first five cycles, with a gradual decline observed from the sixth cycle onward. By the fifteenth cycle, the gas output decreased to ~50% of its initial value (Figure 4.19). The cumulative gas evolution across all 15 cycles corresponded to an overall TON of 65,000 and TOF of 4300 h^{-1}. To evaluate the potential deactivation from air exposure during intermittent openings, a continuous single-cycle experiment with dropwise addition of formic acid was performed, resulting in slightly enhanced efficiency (TON = 72,000; TOF = 4,800 h^{-1}). These results demonstrate that the catalyst retains substantial activity under extended multi-cycle operation, and continuous addition can further optimize its performance.

The modest decline in gas evolution after seven cycles is likely attributable to the formation of a Ru-H complex bearing two phosphine ligands, as confirmed by LC-MS (m/z = 1004.2543 for $C_{60}H_{50}N_5P_2Ru$). Reactions initiated with the Ru-H complex exhibit lower activity than Ru-Cl species, reflecting the reduced phosphine dissociation tendency in the former (Table 4.1).[68] No specific catalyst regeneration protocol was employed, as the focus was on evaluating intrinsic stability over multiple cycles. Notably, the Ru-H complex can be converted back to the active Ru-Cl species ([**Ru-A]**) via treatment with aqueous HCl in methanol, as previously demonstrated, allowing for subsequent catalytic cycles.[69]

4.2.8 TON/TOF Calculation details

General Calculation

Gas evolved (H_2 + CO_2) = 2675 ml

Catalyst loading = 0.016 mol %

At STP, 1 mol gas = 22.4 L

Number of moles = (gas volume (ml))/22.4L = (2675 ml)/(22400 ml) = 0.1194 mol of gas

Since formic acid dehydrogenation releases 1 mol H_2 + 1 mol CO_2 = 2 mol gas/mol HCOOH

Mol of formic acid converted = 0.1194/2 = 0.0597 mol

Moles of catalyst = 0.0617 X 0.016/100 = 0.00000987 mol

TON = 0.0597/0.00000987 = 6050

~6100 (rounded off to two significant numbers)

Calculation for the overall TON after 15 cycles-

Gas evolved after 15 h (H_2 + CO_2) = 31780 ml

Catalyst loading = 0.016 mol %

At STP, 1 mol gas = 22.4 L

Number of moles = (gas volume (ml))/22.4L = (31780 ml)/(22400 ml) = 1.41875 mol of gas

Since formic acid dehydrogenation releases 1 mol H_2 + 1 mol CO_2 = 2 mol gas/mol HCOOH

Mol of formic acid converted = 1.41872/2 = 0.709 mol

Moles of catalyst = 0.0617 X 0.016/100 = 0.00000987 mol

TON = 0.709/0.00000987 = 71872

~72000 (rounded off to two significant numbers)

4.2.9 Controlled Experiments

4.2.9.1 Effect of CuI as a phosphine scavenger. Under base-assisted conditions (0.5 mol% catalyst, 20 mol% KOH, 0.0617 mol formic acid), the addition of CuI (2.5 mol%) enhanced gas evolution (~1900 mL) and

reduced the reaction time from 6 h to 4 h, indicating that CuI facilitates phosphine dissociation and accelerates catalysis. In contrast, under ionic liquid conditions, CuI suppressed gas evolution (1670 mL vs. 2675 mL without CuI in 1 h), consistent with catalyst poisoning by coordination to anionic NHC species. Previous studies have demonstrated that CuI binds to the deprotonated NHC ligand of [**Ru-A]**, thereby inhibiting its catalytic activity.[68] These observations confirm the dual role of CuI: promoting phosphine dissociation and turnover in base-assisted systems while suppressing activity in ionic liquid pathways by stabilizing anionic NHC intermediates (Figure 4.20c-d).

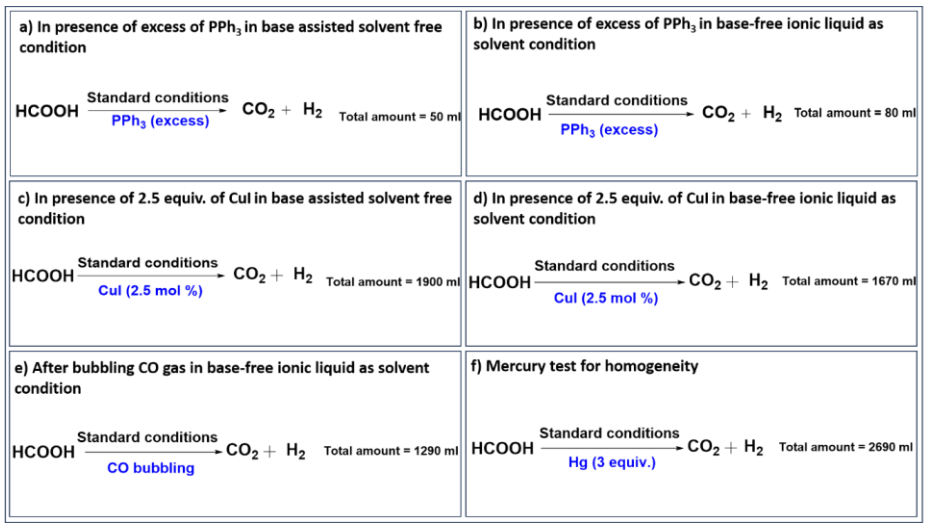

Figure 4.20 Controlled experiments were conducted under both conditions: base-assisted solvent-free and ionic liquid as solvent.

4.2.9.2 Effect of excess PPh_3. The crucial role of phosphine dissociation was further validated by adding excess PPh_3 to both the base-assisted and ionic liquid solvent systems. In both cases, gas evolution was markedly suppressed (50 mL and 80 mL, respectively), thereby unequivocally establishing phosphine dissociation as a prerequisite step in both catalytic pathways (Figure 4.20a-b).[68]

4.2.9.3 Hg test for homogeneity. To ascertain the homogeneity of the formic acid dehydrogenation (FADH) reaction, a mercury drop test was performed by introducing three equivalents of Hg into the reaction mixture. The absence of any measurable change in the total gas volume

clearly indicates that catalysis proceeds through a homogeneous pathway under the investigated conditions (Figure 4.20f).

4.2.9.4 Effect of CO bubbling. To investigate the role of CO in the reaction, a controlled experiment was conducted by introducing CO into the system (Figure 4.20e). Consistent with our earlier findings that CO poisons protic-NHC catalysts via pyridine displacement,[71] CO bubbling led to a marked reduction in gas evolution, yielding only ~ 50% of the standard output. LC-MS (ESI^+) analysis displayed a peak at m/z 542.0322, assigned to the $[M\text{-}Cl\text{-}PPh_3+CO]^+$ fragment (calcd. 542.0332 for $C_{25}H_{19}ClN_5ORu$), indicating phosphine substitution by CO at the active coordination site. Prolonged CO bubbling (1 h) further generated species bearing multiple CO ligands together with a hydride, corroborating CO coordination and irreversible catalyst deactivation. These results confirm that CO suppresses the catalytic activity by poisoning the active site.

4.2.10 Formic acid dehydrogenation (FADH) reaction setup

The evolution of gaseous products during formic acid dehydrogenation was quantified using a gas collection apparatus designed according to established protocols reported in the literature. The experimental setup employed a three-neck round-bottom flask (RB flask) equipped with a water-cooled condenser to suppress solvent loss and maintain thermal stability under the reaction conditions. The flask was configured with one neck connected to the condenser, a second neck connected to a nitrogen inlet (Schlenk line) for system purging, and a third neck sealed with a stopcock.

The outlet of the condenser was connected via silicon rubber tubing to an inverted water-filled graduated cylinder, which enabled the direct measurement of the evolved gas volume (mL). To qualitatively monitor the CO_2 evolution, a gas bubbler containing an alkaline solution was intermittently interposed between the condenser outlet and measuring cylinder. Prior to initiating the reaction, the oil bath was preheated to the desired temperature, and the condenser was precooled to minimize errors arising from the thermal expansion of gases or solvents. For the catalytic runs, the RB flask was charged with the catalyst, ionic liquid (or base for

base-assisted dehydrogenation), and formic acid, followed by sealing and thorough purging with nitrogen to exclude atmospheric contaminants. The system was then rendered airtight to ensure precise gas collection. Gas volumes were determined using the water-displacement (inverted cylinder) method, with an estimated manual measurement uncertainty of ±50 mL.

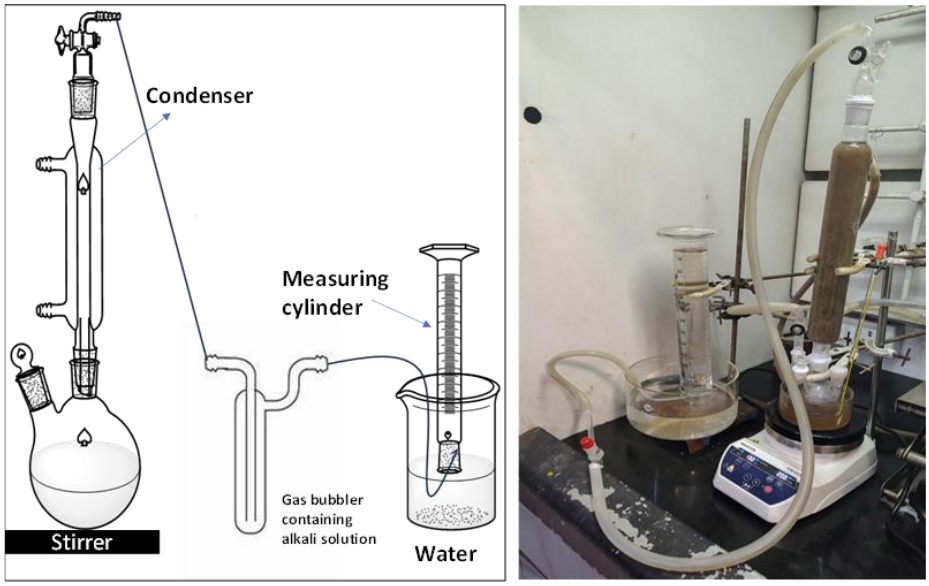

Figure 4.21 Experimental setup employed for formic acid dehydrogenation studies.

4.2.11 Systematic utilization and characterization of H_2/CO_2 evolved from FADH.

a) Alkene hydrogenation. The H_2/CO_2 mixture generated from FADH was employed for the hydrogenation of styrene to ethylbenzene, which served as a model reaction. Notably, [**Ru-A]**, in the presence of 20 mol% base, effectively utilized the mixed gas feed, affording a 38% yield of ethylbenzene, as confirmed by the GC-MS analysis.

b) CO_2 detection and activation. Following H_2 consumption during styrene hydrogenation, the residual gas was introduced into a DMSO-d_6 solution of the anionic NHC complex [**Ru-A]′** in a J-Young NMR tube. Consistent with our previous methodology,[69] this led to the formation of a CO_2-bound ruthenium complex. The ^{13}C NMR spectrum displayed a signal at δ 155 ppm, characteristic of CO_2 coordination to the metal center via phosphine dissociation, alongside a carbene resonance at δ 193

ppm. The ^{1}H NMR spectrum indicated two species, although the carbene signal was weak due to low concentration (**Ru10**). The $^{31}P\{^{1}H\}$ NMR spectrum exhibited resonances at δ -6.00 ppm (free phosphine) and δ 26.62 ppm (new complex), confirming CO_2 binding to the ruthenium center.[69]

c) CO_2 Removal. To enable the selective separation of CO_2 from the evolved gas mixture, the reaction setup was modified by introducing a downstream bubbler containing an alkaline solution (KOH or NaOH). The passage of the gas stream through this trap efficiently captured CO_2 via the reaction $CO_2 + 2OH^- \rightarrow CO_3^{2-} + H_2O$. The formation of carbonate was confirmed by ^{13}C NMR spectroscopy, which displayed a characteristic resonance at δ 168 ppm. This approach provided both qualitative and quantitative validation of CO_2 evolution while ensuring accurate measurement of H_2 yield.

d) H_2 activation after CO_2 removal. To investigate H_2 activation, the anionic NHC complex [**Ru-A]′** in DMSO-d_6 was exposed to H_2 purified by passage through two consecutive NaOH solutions to remove residual CO_2 from the gas. ^{1}H NMR analysis revealed the reappearance of the protic NH signal, with a characteristic peak at δ 12.3 ppm and a hydride triplet at δ -10.6 ppm, confirming the formation of the protic-NHC Ru-H species ([**Ru-a]**. $^{31}P\{^{1}H\}$ NMR further corroborated complex formation with a signal at δ 51.1 ppm.

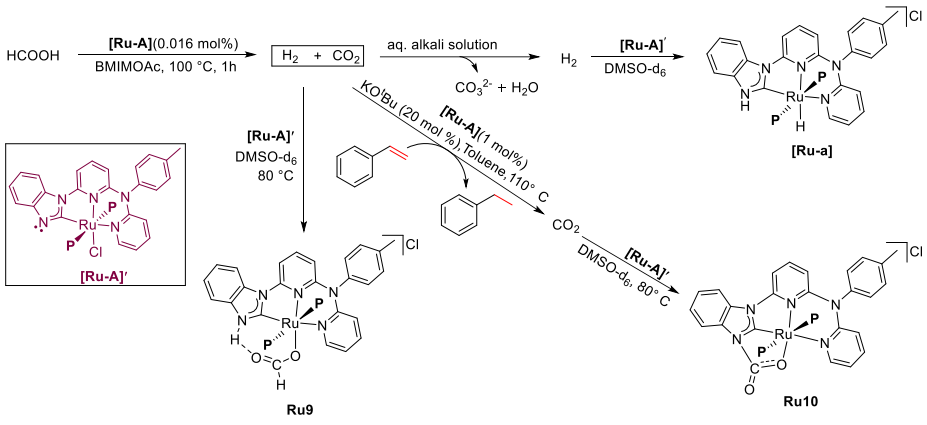

Figure 4.22 Schematic representation of the controlled experiments designed to evaluate the utilization of the evolved gases.

e) Formation of ruthenium-formate complex. The generation of a ruthenium-formate species was probed by bubbling the gas mixture into a DMSO-d_6 solution of [**Ru-A]′** under ambient conditions. While ^{1}H NMR initially showed no formate signals, heating to 60-80 °C led to the appearance of a singlet at δ 8.9 ppm, indicative of Ru-formate complex formation (**Ru9**). Concurrently, $^{31}P\{^1H\}$ NMR revealed a new resonance at δ 45.6 ppm, confirming the phosphine-ligated ruthenium-formate species (Figure 4.22).

4.2.12 Comparative mechanistic insights into base- and ionic liquid-mediated FADH by [Ru-A]

Mechanistic investigations revealed distinct yet converging pathways for formic acid dehydrogenation catalyzed by [**Ru-A]** under basic and ionic liquid conditions.

4.2.12.1 Probing catalytic intermediates via NMR spectroscopy. To gain insight into the base-assisted pathway, mechanistic NMR studies were performed on [**Ru-A]** in DMSO-d_6 using a J-Young NMR tube. The characteristic protic signal of [**Ru-A]** disappeared after treatment with 1 equiv. KOH. The subsequent addition of formic acid restored the protic signal, in contrast to the ionic liquid case, and new resonances emerged, including a carbene carbon at δ 211 ppm, consistent with the formation of a Ru-formato intermediate. No hydride species were detected at ambient temperature; however, heating to 60 °C for 1 h yielded two Ru-H signals: a triplet at -10.61 ppm attributable to a protic-NHC-Ru-H complex (**[Ru-a]**) and a doublet at -11.34 ppm assignable to a Ru-formato species (species 1, Scheme 4.3). Distinct protic signals at δ 12.3 ([**Ru-a]**) and δ 13.88 (Ru-Cl bisphosphine) were observed in the spectra. The disappearance of the δ 211 ppm resonance upon heating supports the thermal decomposition of the formato intermediate into H_2 and CO_2. Complementary $^{31}P\{^1H\}$ NMR (δ 45.6 ppm) and LC-MS (m/z 786.1675; $[M\text{-}Cl]^+$, calcd. 786.1572; Fig. S53) confirmed the assignment of species 1 as a formate-bound Ru-monophosphine complex.

To probe mechanistic insight into the catalytic pathway under ionic liquid conditions, NMR studies were performed in a J-Young tube.

The parent complex [**Ru-A]** in DMSO-d_6 exhibited the expected diagnostic resonance (Figure 4.23a). Upon the addition of BMIMOAc, the protic NH signal vanished (Figure 4.23b), consistent with acetate-induced deprotonation, and new resonances emerged, including a characteristic doublet at δ 10.33 ppm, assigned to species **A** (Scheme 4.4). The corresponding $^{31}P\{^{1}H\}$ NMR spectrum showed a new resonance at δ 47.68, confirming the formation of this intermediate. Subsequent treatment with 1 equiv. formic acid afforded three Ru-H resonances in the ^{1}H NMR spectrum (Figure 4.23c). The triplet at δ -12.46 corresponds to the anionic NHC species **5′**, in agreement with prior reports, while the doublet at δ -11.48 and triplet at δ -13.15 are assigned to species **3′** and **6′**, respectively.

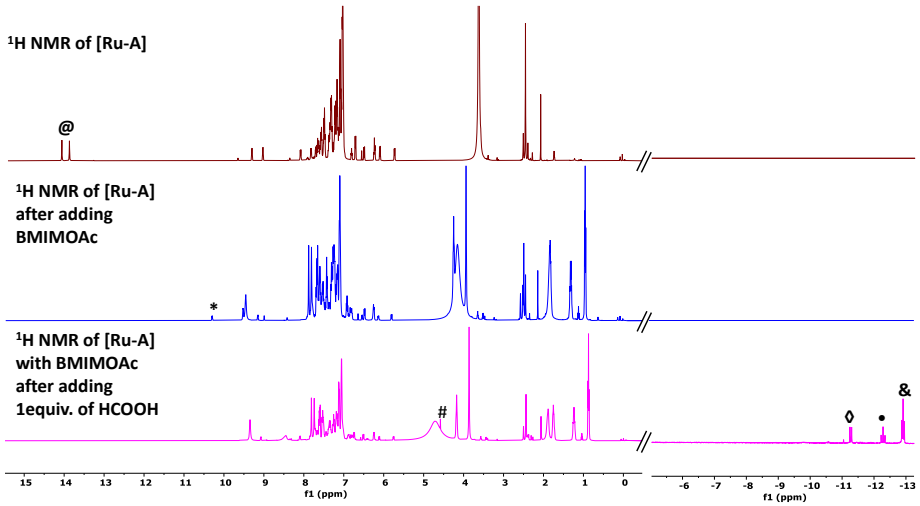

Figure 4.23 Stepwise ^{1}H NMR spectra illustrating the sequential transformations of [**Ru-A]** upon successive additions of the ionic liquid (as solvent) and formic acid. The annotations denote: @, protic NH resonance of [**Ru-A]**; *, ortho-pyridyl proton of intermediate species **A**; #, dissolved H_2; ◊, Ru-H resonance of species **3′**; •, Ru–H resonance of species **5′**; and &, Ru-H resonance of species **6′**.

Notably, the repeated regeneration of the [**Ru-A]** protic signal upon formic acid addition in the base-assisted system, in contrast to the ionic liquid pathway, highlights a more facile protonation process. Taken together, these observations suggest that the base-assisted pathway

operates through a protic NHC species, whereas the ionic liquid-mediated system proceeds via an anionic NHC intermediate.

4.2.13 Proposed mechanistic pathways for FADH under basic and ionic liquid conditions

Based on prior reports,[27,41,81–84] and our experimental evidence, we propose a mechanistic pathway for [**Ru-A]** under both basic and ionic liquid conditions (Schemes 4.3 and 4.4). In the base-assisted pathway, solvated [**Ru-A]** undergoes phosphine dissociation, yielding the catalytically active monophosphine species, **Ru1a**. This species enters the cycle through chloride substitution by formate, releasing potassium chloride (KCl) and water. The vacant site is stabilized via an agostic interaction with the formate proton, enabling the formation of a Ru-H bond along with a Ru-CO_2 fragment. Subsequent reaction with formic acid liberates CO_2 and affords species **3**, whereas coordination with PPh_3 generates [**Ru-a]**. Both species coexist, with **3** advancing catalysis and [**Ru-a]** serving as the resting state. Species **3** promotes H_2 evolution via heterolytic cleavage involving the Ru-H moiety and a proton from formic acid. The final H_2 release from intermediate **4** regenerates [**Ru-A]**, thereby completing the catalytic cycle (Scheme 4.3).

An alternative pathway operates in the presence of the ionic liquid BMIMOAc, wherein the acetate anion acts as a Brønsted base to deprotonate [**Ru-A]**, generating the anionic NHC complex [**Ru-A]′** bearing two phosphines and a deprotonated β-N atom. This transformation, involving two equivalents of BMIMOAc, affords [**Ru-A]′** along with BMIMCl and acetic acid. Subsequent ligand exchange with acetate replaces the chloride ligand, yielding ruthenium-acetate species **A**. Insertion of formic acid promotes phosphine dissociation, and protonation of acetate facilitates the release of acetic acid while coordinating formate to the metal center, yielding formato complex **1′**. Progression through Ru-H and Ru-CO_2 bond formation produces species **2′**, which, upon CO_2 elimination, generates the key Ru-hydride **3′**.

Protonation by formic acid then affords intermediate **4′**, ultimately leading to H_2 evolution and the regeneration of active species **1′**.' Alternatively, if phosphine re-enters the cycle after **2′**, CO_2 elimination affords Ru-hydride **5′**. Our earlier work demonstrated that such anionic Ru-H species promote ligand hemilability, supporting this pathway.[71] Subsequent formic acid coordination, accompanied by pyridine dissociation, yields intermediate **6′**, from which H_2 release regenerates **1′** via intermediates **3′** and **4′**.

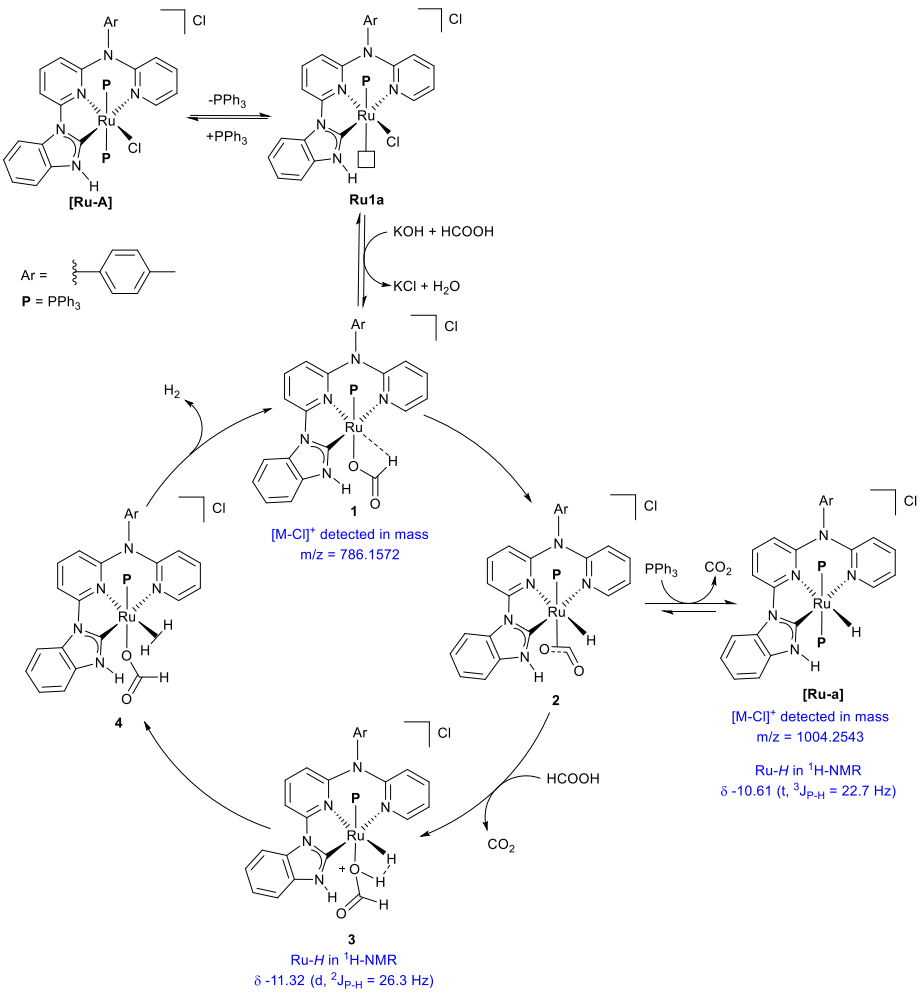

Scheme 4.3 Proposed catalytic cycle for base-assisted dehydrogenation of formic acid by [**Ru-A**].

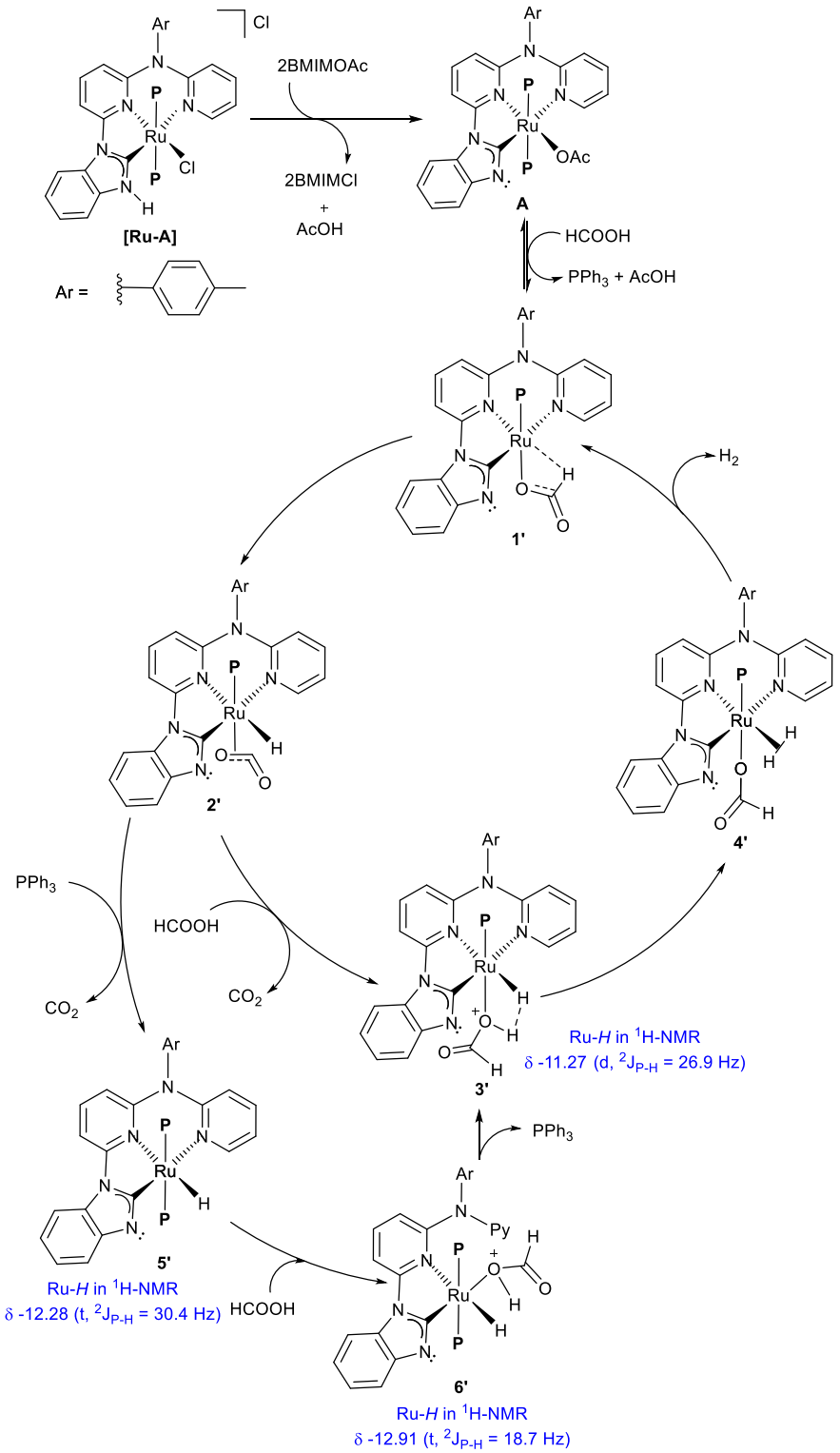

Scheme 4.4 Proposed catalytic cycle for formic acid dehydrogenation by **[Ru-A]** in an ionic liquid medium.

4.3 Conclusions

In summary, we systematically investigated the influence of β- and γ-substituents in Ru(II)-protic-NHC complexes on catalytic formic acid dehydrogenation (FADH) using base-assisted and ionic liquid-mediated pathways. The study demonstrates that all complexes ([**Ru-A]**-**Ru8**) exhibit appreciable catalytic activity, with [**Ru-A]** consistently outperforming the other analogues under optimized conditions, achieving an exceptional TON (65,000) and TOF (4,300 h^{-1}) over multiple consecutive cycles in an ionic liquid. The catalytic performance of β-*N*-substituted complexes was superior when the *N*-H functionality was retained, as opposed to methyl substitution. In contrast, γ-*N*-substituted complexes ([**Ru-A]**, **Ru7**, **Ru8**) exhibited an observed decrease in activity upon introduction of an *N*-H group, highlighting its detrimental influence relative to alkyl or aryl analogues. Mechanistic investigations reveal distinct pathways: the base-assisted system proceeds via protic NHC intermediates, whereas the ionic liquid system generates anionic NHC species, highlighting the pivotal roles of ligand deprotonation and phosphine dissociation in facilitating H_2 evolution. Controlled experiments further underscore the necessity of phosphine dissociation and the homogeneous nature of catalysis, whereas CO inhibits activity through active-site poisoning. Additionally, the evolved H_2/CO_2 mixture was successfully harnessed for downstream hydrogenation reactions, and CO_2 capture and activation studies confirmed the reversibility of substrate coordination, further demonstrating the versatility of these Ru(II)-pNHC complexes in sustainable hydrogen production. Collectively, this work establishes the structural and mechanistic principles governing Ru(II)-protic-NHC-catalyzed FADH, providing a robust framework for the rational design of next-generation, high-performance, earth-abundant metal catalysts for hydrogen evolution and small-molecule activation.

4.4 Experimental Section

General experimental Information

All ligand and complex syntheses were performed under a nitrogen atmosphere using standard Schlenk line techniques. The solvents were purified according to established procedures under nitrogen and subsequently stored over 4 Å molecular sieves inside an N_2-filled glovebox. Reagents and solvents, such as HCOOH, BMIMOAc, KOH, NaOH, and NaOAc, were obtained from commercial suppliers and used as received unless otherwise noted. In several cases, additional purification was performed following standard protocols. The ruthenium precursor complex $RuCl_2(PPh_3)_3$ was synthesized according to a previously reported method.[85] NMR spectra were recorded at ambient temperature and pressure using Bruker Avance 400 MHz (^{1}H: 400 MHz; ^{13}C: 100 MHz; ^{31}P: 162 MHz) and 500 MHz (^{1}H: 500 MHz; ^{13}C: 125 MHz; ^{31}P: 202 MHz) spectrometers. Deuterated solvents, such as dimethyl sulfoxide (DMSO-d_6) and chloroform ($CDCl_3$), were used for NMR analyses. Chemical shifts (δ) are reported in parts per million (ppm) relative to the residual solvent peaks: δ = 7.26 ppm for ^{1}H and δ = 77.0 ppm for ^{13}C in $CDCl_3$; δ = 2.50 ppm for ^{1}H and δ = 40.45 ppm for ^{13}C in DMSO-d_6. Electrospray ionization (ESI) and high-resolution mass spectra (HRMS) measurements were performed on a Bruker-Doltonics-micro TOF-QII spectrometer at 22 °C. The Sample was diluted to a total volume of approximately 1.5 mL using toluene before GC-MS analysis. GC-MS was carried out on a Shimadzu QP2010 Ultra. LCMS for a few samples was performed on an Xevo G3 QTOF mass spectrometer coupled with Acquity H-class plus UPLC with a mass range of 20 to 1500 daltons in ESI+ ionization mode.

4.4.1 Synthesis of Ligand L5: A two-neck round-bottom flask (100 mL) was oven-dried, fitted with a reflux condenser, and charged with 6-bromo-2-benzimidazole (2.740 g, 10 mmol), 2-aminopyridine (1.223 g, 13 mmol), bis(dibenzylideneacetone)palladium(0) [$Pd(dba)_2$] (0.218 g, 0.38 mmol), 1,1'-bis(diphenylphosphino)ferrocene (dppf) (0.211 g, 0.38 mmol), sodium tert-butoxide (1.153 g, 12 mmol), and anhydrous toluene

(20 ml) under an inert atmosphere. The reaction mixture was heated to reflux in an oil bath for 24 h. The mixture was cooled to ambient temperature, ethyl acetate (20 ml) was added, and the mixture was stirred for 30 min, resulting in the formation of a red precipitate. The reaction mixture was subsequently filtered through Celite, and the filtrate was concentrated in vacuo to yield a light-brown solid. Purification via column chromatography (silica gel, ethyl acetate/hexane, 70:30) yielded the desired product as a brown solid (1.90 g, 66% yield). **^{1}H NMR** (500 MHz, $CDCl_3$, 25 °C) δ 8.58 (s, 1H), 8.32 (d, *J* = 5.0 Hz, 1H), 7.99 (dd, *J* = 10.3, 6.3 Hz, 2H), 7.90 – 7.85 (m, 1H), 7.77 (t, *J* = 7.8 Hz, 1H), 7.72 (d, *J* = 8.3 Hz, 1H), 7.64 (t, *J* = 7.8 Hz, 1H), 7.44 (d, *J* = 8.1 Hz, 1H), 7.38 – 7.32 (m, 2H), 7.07 (d, *J* = 7.6 Hz, 1H), 6.92 (dd, *J* = 7.2, 4.7 Hz, 1H).**^{13}C NMR** (126 MHz, $CDCl_3$, 25 °C) δ 153.9, 153.5, 148.1, 148.0, 144.8, 141.8, 140.5, 138.2, 132.3, 124.1, 123.3, 120.8, 117.3, 112.7, 112.4, 109.5, 106.3.

4.4.2 Synthesis of complex Ru7. An oven-dried Schlenk tube was charged with **L1** (0.057 g, 0.2 mmol) in methanol (10 ml), followed by the addition of $RuCl_2(PPh_3)_3$ (0.191 g, 0.2 mmol). The resulting mixture was stirred at reflux temperature for 12 h. After the reaction was complete, the mother liquor was filtered through a short Celite pad and reduced to 1-2 mL under reduced pressure. Diethyl ether was then added, and a yellow precipitate was obtained. Finally, after drying in a high vacuum, the compound was obtained as a yellow powder. Yield 0.110 g (55.9%).**^{1}H NMR** (500 MHz, DMSO-d_6, 25 °C) δ 14.10 (s, 1H), 13.87 (s, 1H), 11.70 (s, 1H), 11.07 (s, 1H), 9.17 (d, *J* = 6.3 Hz, 1H), 8.86 (d, *J* = 6.1 Hz, 1H), 8.10 (d, *J* = 8.1 Hz, 1H), 7.81 – 7.75 (m, 2H), 7.72 (t, *J* = 8.2 Hz, 2H), 7.66 (d, *J* = 7.9 Hz, 4H), 7.60 (d, *J* = 8.5 Hz, 2H), 7.55 (d, *J* = 7.9 Hz, 4H), 7.43 (d, *J* = 7.2 Hz, 2H), 7.34 (ddt, *J* = 20.4, 13.9, 6.5 Hz, 12H), 7.23 (q, *J* = 7.5, 6.9 Hz, 10H), 7.16 (q, *J* = 10.4, 9.1 Hz, 12H), 7.12 – 7.06 (m, 14H), 7.03 (t, *J* = 7.6 Hz, 13H), 6.82 (t, *J* = 6.6 Hz, 1H), 6.24 (t, *J* = 6.6 Hz, 1H). **^{31}P NMR** (202 MHz, DMSO-d_6, 25 °C) δ 33.6(s), 24.6(s), -6.0(s, PPh_3).**^{13}C NMR** (126 MHz, DMSO-d_6, 25 °C) δ 204.4, 202.5, 152.0, 151.4, 151.3, 150.7, 150.4, 150.3, 150.2, 150.0,

138.5, 137.7, 136.2, 135.8, 135.6, 133.4, 133.2, 132.7, 132.6, 132.6, 132.5, 131.8, 131.6, 131.5, 131.2, 130.9, 130.4, 130.1, 129.5, 129.3, 129.1, 128.9, 128.8, 128.7, 128.3, 128.2, 128.0, 127.9, 127.8, 127.8, 127.7, 125.3, 123.9, 123.4, 122.8, 116.7, 116.1, 114.4, 113.2, 111.9, 111.5, 111.1, 110.8, 110.3, 109.9, 104.0, 103.6. Anal. Calcd for $C_{53}H_{43}Cl_2N_5P_2Ru$: C, 64.70; H, 4.41; N, 7.12. Found: C, 64.27; H, 4.13; N, 6.88.

4.4.3 Synthesis of Ligand L6: A two-neck round-bottom flask (100 mL) was oven-dried, fitted with a reflux condenser, and charged with 6-bromo-2-benzimidazole (2.740 g, 10 mmol), *N*-methylpyridin-2-amine (1.405 g, 13 mmol), bis(dibenzylideneacetone)palladium(0) [$Pd(dba)_2$] (0.218 g, 0.38 mmol), 1,1'-bis(diphenylphosphino)ferrocene (dppf) (0.211 g, 0.38 mmol), sodium tert-butoxide (1.153 g, 12 mmol), and anhydrous toluene (20 ml) under an inert atmosphere. The reaction mixture was heated to reflux in an oil bath for 24 h. The mixture was cooled to ambient temperature, ethyl acetate (20 ml) was added, and the mixture was stirred for 30 min, resulting in the formation of a red precipitate. The reaction mixture was subsequently filtered through Celite, and the filtrate was concentrated in vacuo to yield a yellowish brown solid. Purification via column chromatography (silica gel, ethyl acetate/hexane, 80:20) yielded the desired product as a brown solid (1.63 g, 54% yield). **^{1}H NMR** (500 MHz, $CDCl_3$, 25 °C) δ 8.58 (s, 1H), 8.45 (dd, *J* = 5.0, 2.2 Hz, 1H), 8.02 (dd, *J* = 6.5, 2.8 Hz, 1H), 7.86 (dd, *J* = 5.7, 3.6 Hz, 2H), 7.39 - 7.30 (m, 3H), 7.08 (d, *J* = 8.4 Hz, 2H), 7.06 - 6.99 (m, 2H), 3.70 (s, 3H). **^{13}C NMR** (126 MHz, $CDCl_3$, 25 °C) δ 157.6, 157.3, 148.7, 148.3, 144.7, 141.7, 139.7, 137.8, 132.3, 124.1, 123.2, 120.6, 118.9, 117.0, 113.1, 109.7, 105.1, 36.5.

4.4.4 Synthesis of complex Ru8. An oven-dried Schlenk tube was charged with **L2** (0.060 g, 0.2 mmol) in methanol (10 ml), followed by the addition of $RuCl_2(PPh_3)_3$ (0.191 g, 0.2 mmol). The resulting mixture was stirred at reflux temperature for 12 h. After the completion of the reaction, the mother liquor was filtered through a short celite pad and reduced to 1-2 ml at reduced pressure. Diethyl ether was then added, and

a yellow precipitate was obtained. Finally, after drying in a high vacuum, the compound was obtained as a yellow powder. Yield 0.085 g (43%).**^{1}H NMR** (500 MHz, DMSO-d_6, 25 °C) δ 14.13 (s, 1H), 13.92 (s, 1H), 9.33 (d, *J* = 5.8 Hz, 1H), 8.80 (d, *J* = 5.6 Hz, 1H), 8.16 (d, *J* = 8.1 Hz, 1H), 8.02 (t, *J* = 7.8 Hz, 1H), 7.91 (dq, *J* = 16.8, 8.4 Hz, 2H), 7.76 (d, *J* = 8.2 Hz, 1H), 7.65 (t, *J* = 7.0 Hz, 2H), 7.58 – 7.48 (m, 2H), 7.39 - 7.33 (m, 6H), 7.28 - 7.22 (m, 15H), 7.18 (t, *J* = 7.5 Hz, 10H), 7.10 (t, *J* = 7.6 Hz, 7H), 7.03 (t, *J* = 7.6 Hz, 22H), 6.95 (d, *J* = 4.3 Hz, 9H), 6.66 (d, *J* = 8.4 Hz, 1H), 6.56 (s, 1H), 6.24 (t, *J* = 6.5 Hz, 1H), 3.18 (s, 3H), 2.97 (s, 3H). **^{31}P NMR** (202 MHz, DMSO-d_6, 25 °C) δ 30.20, 19.54, -6.03. **^{13}C NMR** (126 MHz, DMSO-d_6, 25 °C) δ 205.1, 203.2, 155.8, 155.6, 155.3, 154.7, 153.4, 152.5, 151.6, 140.0, 138.4, 136.0, 134.5, 134.4, 133.6, 133.5, 132.8, 132.8, 132.7, 132.7, 132.6, 131.7, 131.6, 131.4, 131.4, 131.3, 131.1, 130.7, 130.4, 129.8, 129.4, 128.9, 128.8, 128.1, 128.1, 128.0, 127.9, 124.6, 123.8, 123.1, 119.0, 117.8, 116.9, 115.9, 115.8, 112.2, 111.5, 111.3, 111.1, 106.2, 65.1, 44.0. Anal. Calcd for $C_{54}H_{45}Cl_2N_5P_2Ru$: C, 65.00; H, 4.55;N, 7.02. Found: C, 65.19; H, 4.31; N, 6.67.

4.4.5 H_2 capture by using [Ru-A]′. After passing the obtained gas mixture via a bubbler containing an alkali solution, an outlet was set to the J-Young NMR tube containing [**Ru-A]′** in DMSO-d_6, and the J-Young NMR was heated slightly. **^{1}H NMR** (400 MHz, DMSO- d_6, 25 °C) δ 12.26 (s, 1H), 8.26 (d, *J* = 6.1 Hz, 2H), 7.67 (t, *J* = 8.4 Hz, 2H), 7.56 (d, *J* = 8.4 Hz, 2H), 7.44 (d, *J* = 8.1 Hz, 4H), 7.39 (d, *J* = 8.1 Hz, 2H), 7.15 (t, *J* = 7.2 Hz, 8H), 7.10 (d, *J* = 4.4 Hz, 16H), 7.08 - 7.02 (m, 20H), 6.99 (d, *J* = 8.2 Hz, 1H), 6.69 (d, *J* = 8.1 Hz, 4H), 6.29 (d, *J* = 8.7 Hz, 2H), 6.02 (t, *J* = 6.5 Hz, 2H), 5.82 (d, *J* = 8.9 Hz, 2H), 2.43 (s, 6H), -10.57 (t, *J* = 22.9 Hz, 2H). **^{13}C NMR** (101 MHz, DMSO- d_6, 25 °C) δ 159.6, 154.2, 152.4, 150.2, 140.3, 139.3, 136.6, 136.2, 136.1, 134.0, 133.8, 133.6, 133.4, 132.4,132.2, 130.7, 129.9, 129.0, 128.8, 127.9, 124.2, 123.0, 121.7, 116.9, 116.3, 111.3, 110.5, 109.9, 105.5, 20.8.**^{31}P NMR** (162 MHz, DMSO-d_6, 25 °C) δ 51.1.

4.4.6 CO_2 capture by using [Ru-A]′. For the detection of CO_2, an additional experimental setup was connected. The gas mixture was

passed through a Schlenk tube containing a magnetic stirrer bar, styrene (114.58 ml, 1 mmol), KO^{t}Bu (22.4 mg, 0.2 mmol), [Ru-A] (10.73 mg, 0.01 mmol), and toluene. The reaction mixture was heated under reflux in an oil bath to obtain a yellow solution. One outlet was attached to a J-young NMR tube containing the DMSO-d_6 solution of [**Ru-A]′**. After bubbling the gas into the J-Young NMR tube, NMR spectra were recorded. **^{1}H NMR** (500 MHz, DMSO- d_6, 25 °C) δ 9.72 – 9.68 (m, 1H), 9.09 (d, *J* = 5.8 Hz, 0H), 7.96 (d, *J* = 8.0 Hz, 0H), 7.87 (t, *J* = 8.2 Hz, 0H), 7.81 (d, *J* = 8.1 Hz, 0H), 7.74 (t, *J* = 8.0 Hz, 1H), 7.62 (d, *J* = 7.6 Hz, 17H), 7.60 – 7.58 (m, 26H), 7.52 (td, *J* = 7.8, 2.9 Hz, 31H), 7.35 (d, *J* = 5.9 Hz, 10H), 7.21 (t, *J* = 7.9 Hz, 7H), 7.16 (d, *J* = 7.7 Hz, 3H), 7.05 (p, *J* = 7.8, 6.5 Hz, 10H), 2.42 (s, 1H), 2.39 (s, 1H).**^{13}C NMR** (126 MHz, DMSO- d_6, 25 °C) δ 193.4, 155.7, 154.3, 153.8, 153.1, 152.0, 148.2, 141.9, 140.1, 139.9, 139.8, 139.2, 138.7, 136.5, 133.5, 133.4, 133.0, 132.3, 132.2, 131.7, 131.6, 129.3, 129.0, 129.0, 128.1, 124.4, 122.5, 120.4, 118.1, 117.4, 116.8, 116.5, 116.0, 112.0, 110.7, 103.2, 21.0**. ^{31}P NMR** (202 MHz, DMSO-d_6, 25 °C) 48.9, 36.3, 26.6, 25.2, -6.0

4.4.7 Formate formation by using [Ru-A]′. The gas mixture passed through a J-Young NMR tube containing the DMSO-d_6 solution of [**Ru-A]′** and was heated at 80 °C for 2-4 hours. Subsequently, multinuclear NMR spectra were recorded. **^{1}H NMR** (500 MHz, DMSO-d_6, 25 °C) δ 10.24 (dd, *J* = 5.9, 2.1 Hz, 1H), 9.70 (dd, *J* = 5.8, 2.2 Hz, 6H), 9.58 (dd, *J* = 5.7, 2.3 Hz, 1H), 9.48 (s, 1H), 8.92 (s, 0.13H), 8.03 (d, *J* = 8.0 Hz, 0.15H), 7.98 (d, *J* = 8.0 Hz, 5H), 7.89 (t, *J* = 8.2 Hz, 5H), 7.84 (d, *J* = 8.0 Hz, 5H), 7.78 (ddd, *J* = 9.0, 6.9, 2.1 Hz, 6H), 7.74 (s, 0.17 H), 7.65 (s, 2H), 7.63 (d, *J* = 3.8 Hz, 9H), 7.62 (s, 13H), 7.61 (s, 3H), 7.60 (d, *J* = 2.5 Hz, 9H), 7.56 (d, *J* = 3.1 Hz, 11H), 7.54 (t, *J* = 3.2 Hz, 15H), 7.52 (d, *J* = 3.2 Hz, 3H), 7.49 (d, *J* = 8.4 Hz, 10H), 7.18 (t, *J* = 7.6 Hz, 6H), 6.92 (d, *J* = 8.8 Hz, 5H), 6.88 – 6.84 (m, 3H), 6.65 (d, *J* = 8.2 Hz, 5H), 6.48 (d, *J* = 8.8 Hz, 1H), 6.43 (d, *J* = 8.4 Hz, 0H), 6.19 (d, *J* = 8.6 Hz, 1H), 5.76 (s, 2H), 4.02 (q, *J* = 7.1 Hz, 1H), 3.77 (p, *J* = 6.1 Hz, 1H), 3.61 – 3.57 (m, 3H), 2.43 (s, 19H), 2.39 (s, 3H), 2.29 (s, 2H), 2.08 (d, *J* = 4.4

Hz, 1H), 1.98 (s, 1H), 1.04 (d, J = 6.1 Hz, 7H). **^{31}P NMR** (202 MHz, DMSO-d_6, 25 °C) δ 45.6, 22.4, -6.0

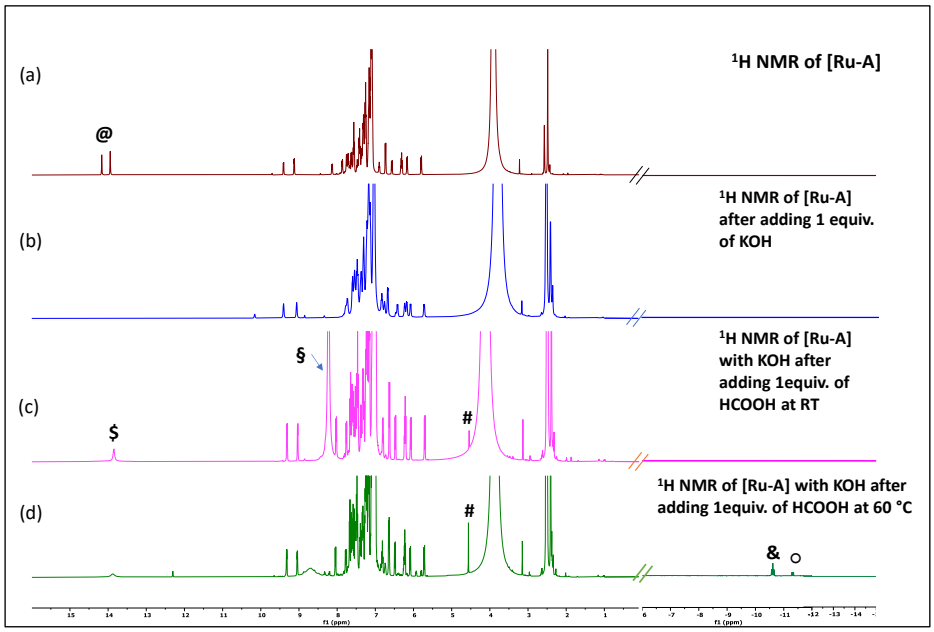

Figure 4.24 NMR stacking for the base-assisted FADH reaction

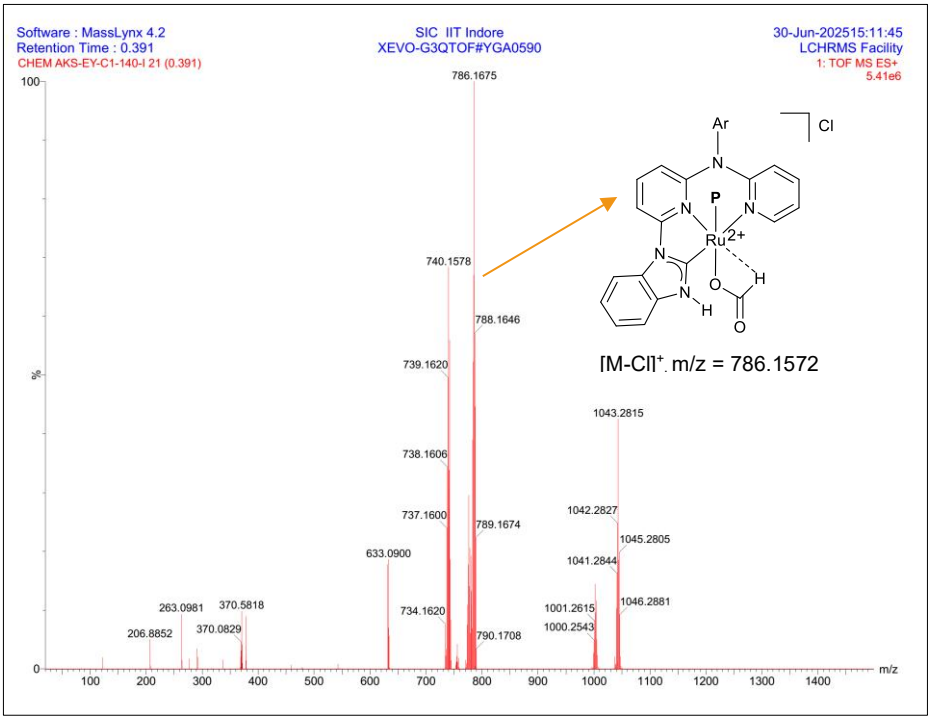

Figure 4.25 LC-MS of the reaction mixture of the base-assisted FADH reaction

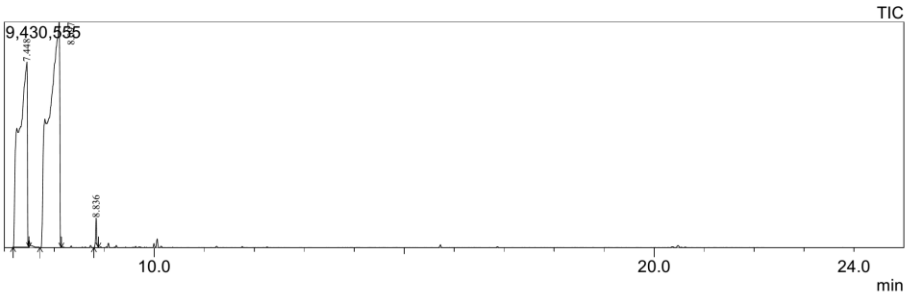

Peak Report TIC

Peak#	R.Time	Area	Area%	Height	Height%	A/H	Name
1	7.448	7751906	38.68	7732803	42.10	11.35	Ethylbenzene
2	8.097	7171494	60.47	9402731	51.20	14.59	Styrene
3	8.836	1925834	0.85	1230120	6.70	1.57	
		6849234	100.00	18365654	100.00		

Spectrum

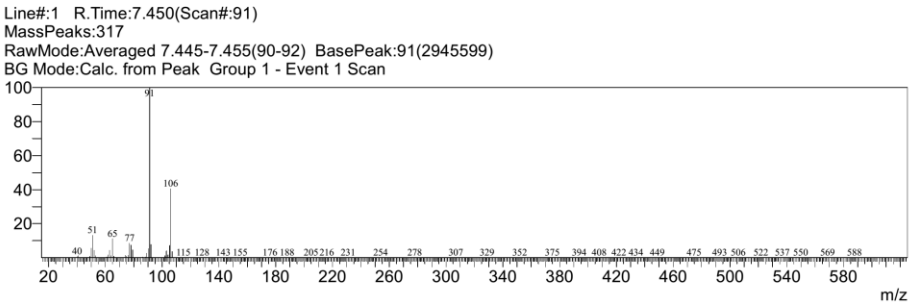

Figure 4.26 GC-MS of the reaction mixture containing [**Ru-A]** (1 mol%), 20 mol% of KO^{t}Bu, and 1mmol of styrene in dry toluene solvent

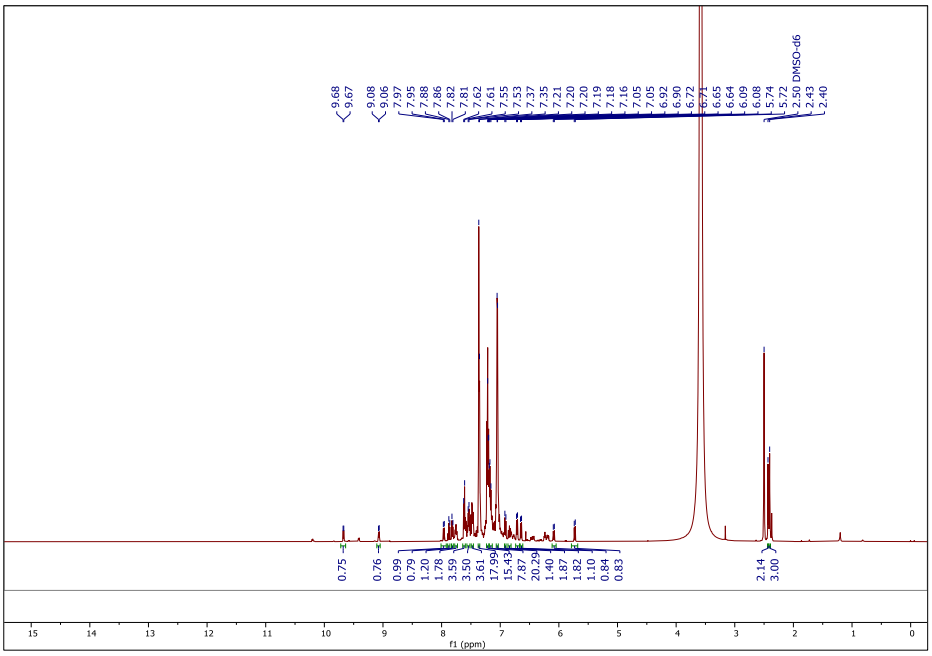

Figure 4.27 ^{1}H NMR of anionic NHC complex after bubbling the gas and after passing through the reaction setup containing styrene

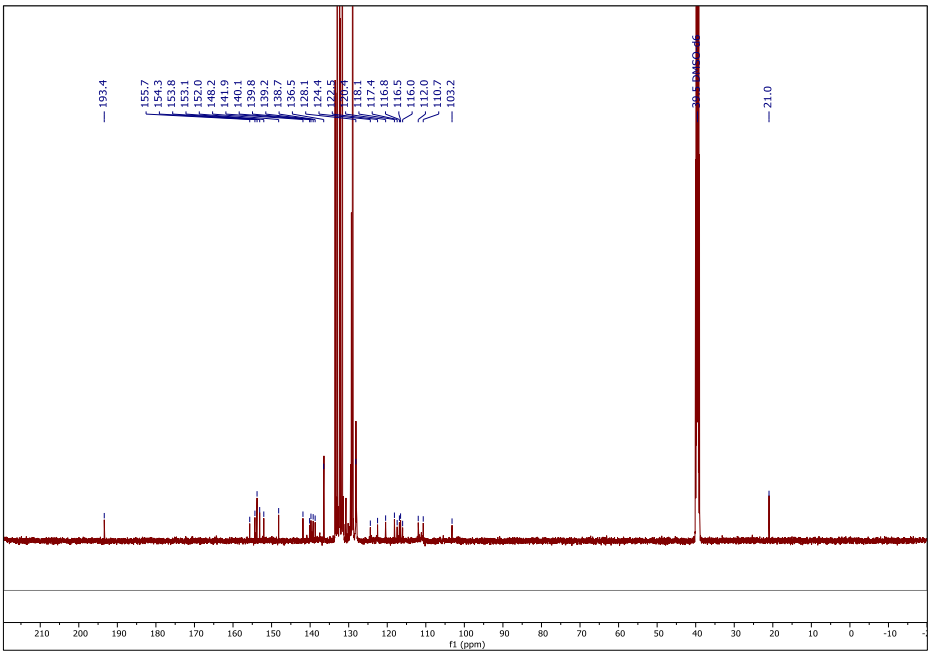

Figure 4.28 $^{13}C\{^{1}H\}$ NMR of anionic NHC complex after bubbling the gas and after passing through the reaction setup containing styrene

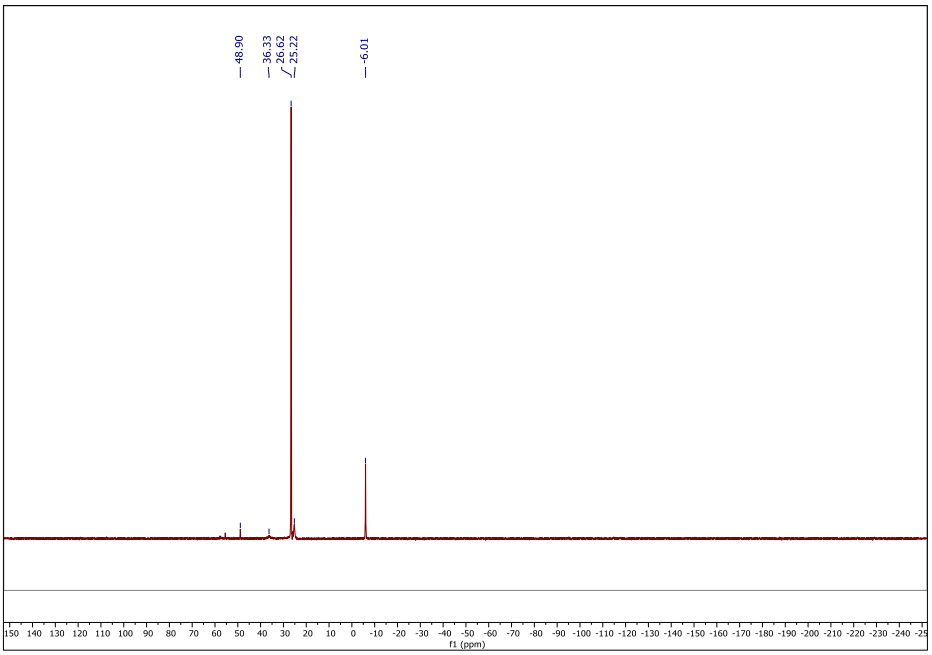

Figure 4.29 $^{31}P\{^{1}H\}$ NMR of anionic NHC complex after bubbling the gas after passing with reaction setup containing styrene

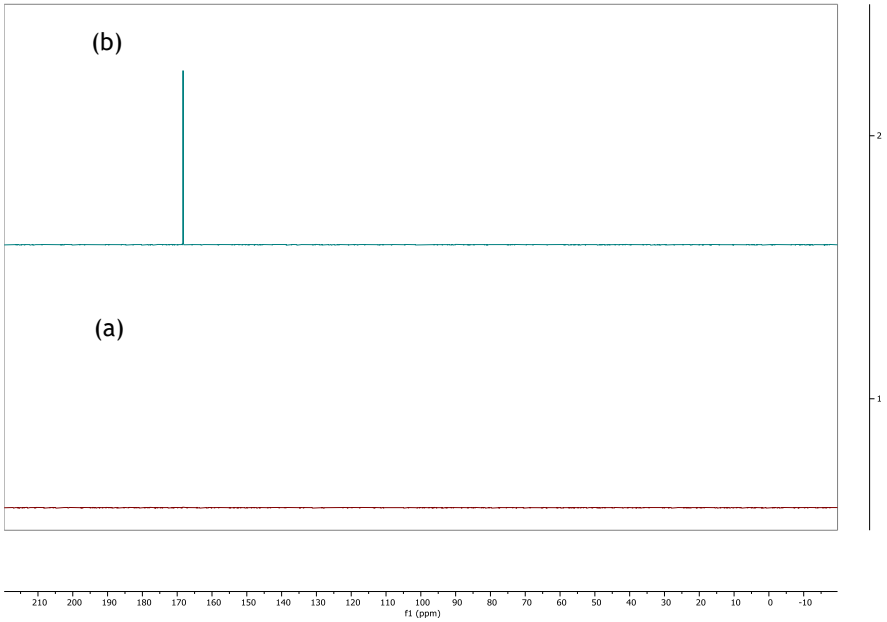

Figure 4.30 $^{13}C\{^{1}H\}$ NMR of alkali solution (NaOH) in D_2O (a) before CO_2 bubbling (b) after CO_2 bubbling

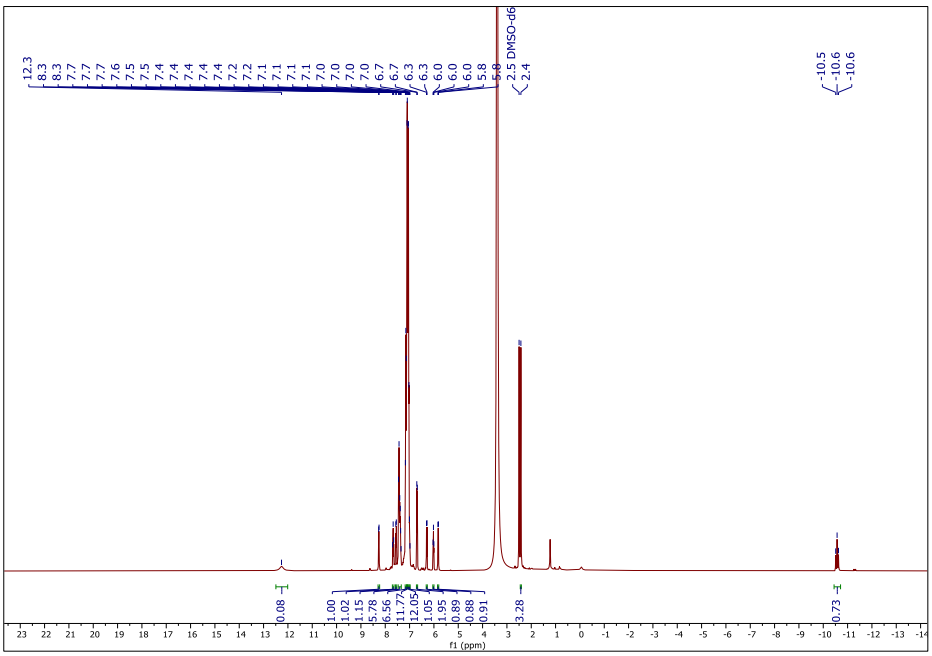

Figure 4.31 ^{1}H NMR of anionic NHC complex after bubbling the gas after passing with an alkali solution

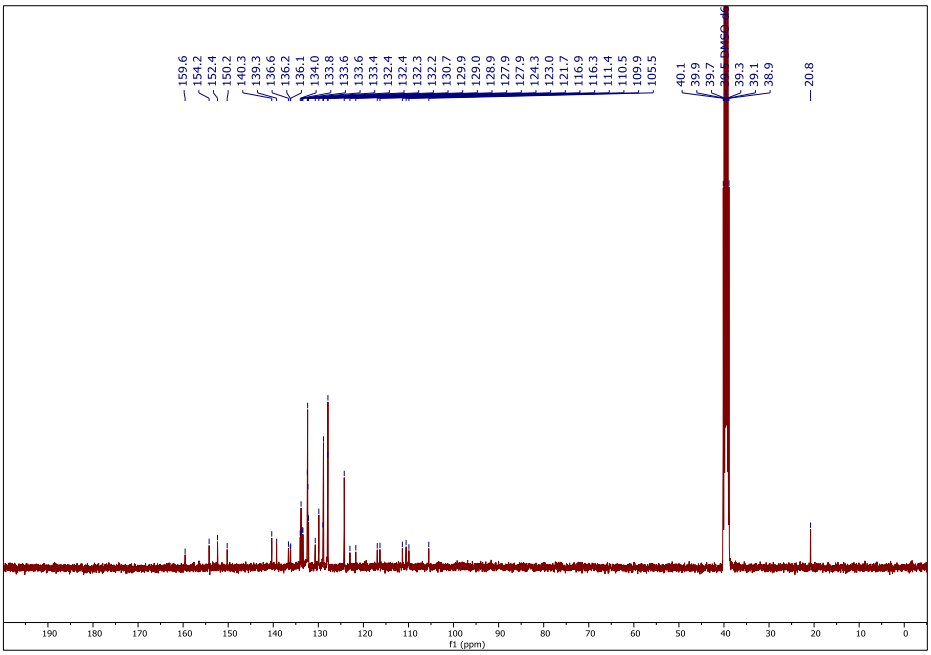

Figure 4.32 $^{13}C\{^{1}H\}$ NMR of anionic NHC complex after bubbling the gas after passing with alkali solution

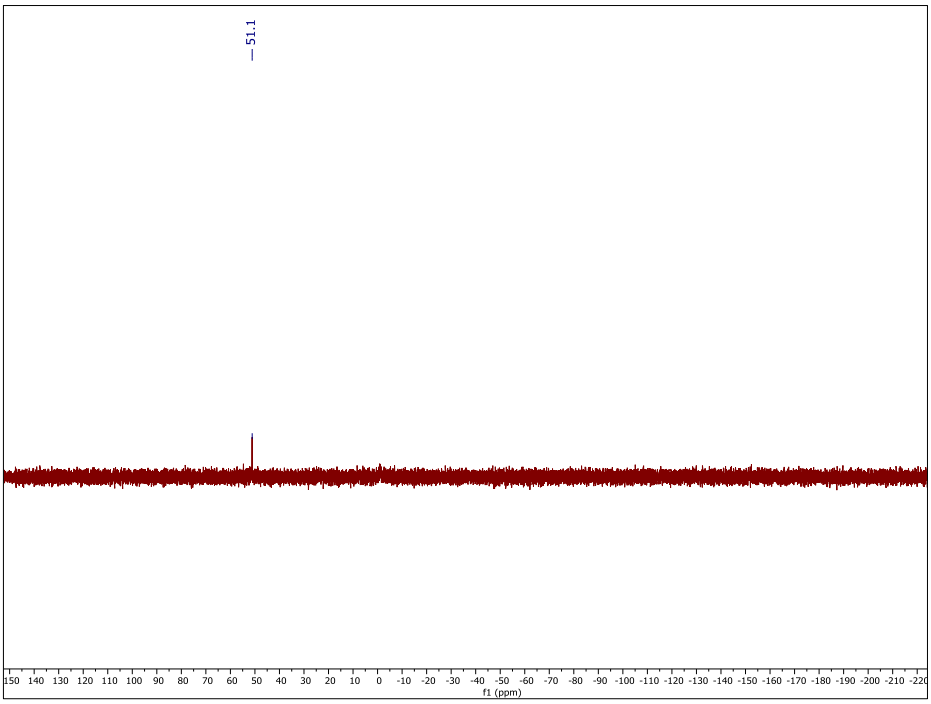

Figure 4.33 $^{31}P\{^{1}H\}$ NMR of anionic NHC complex after bubbling the gas after passing with alkali solution

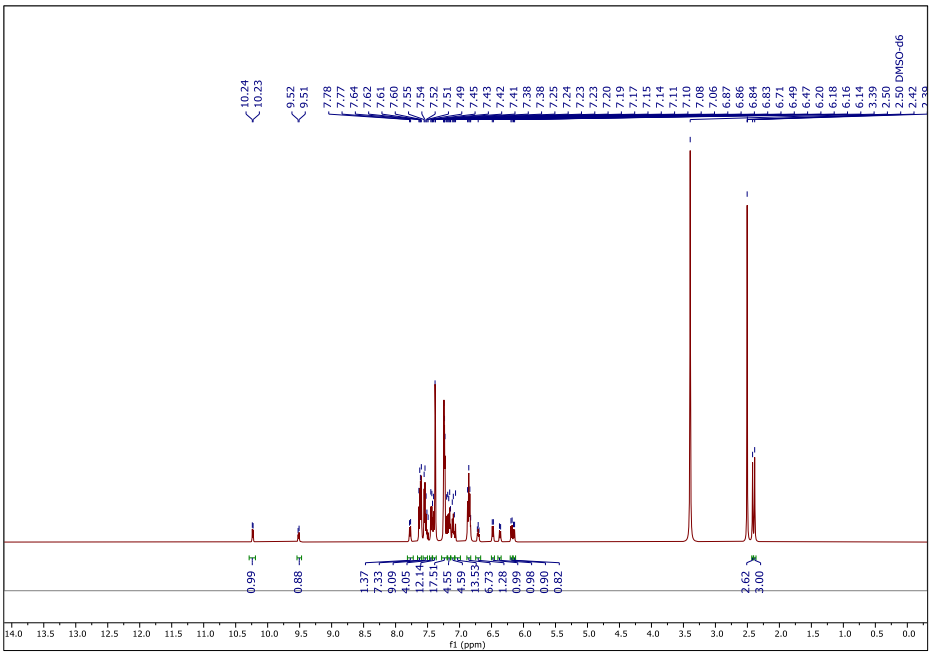

Figure 4.34 ^{1}H NMR of anionic NHC complex before bubbling the mixture gas

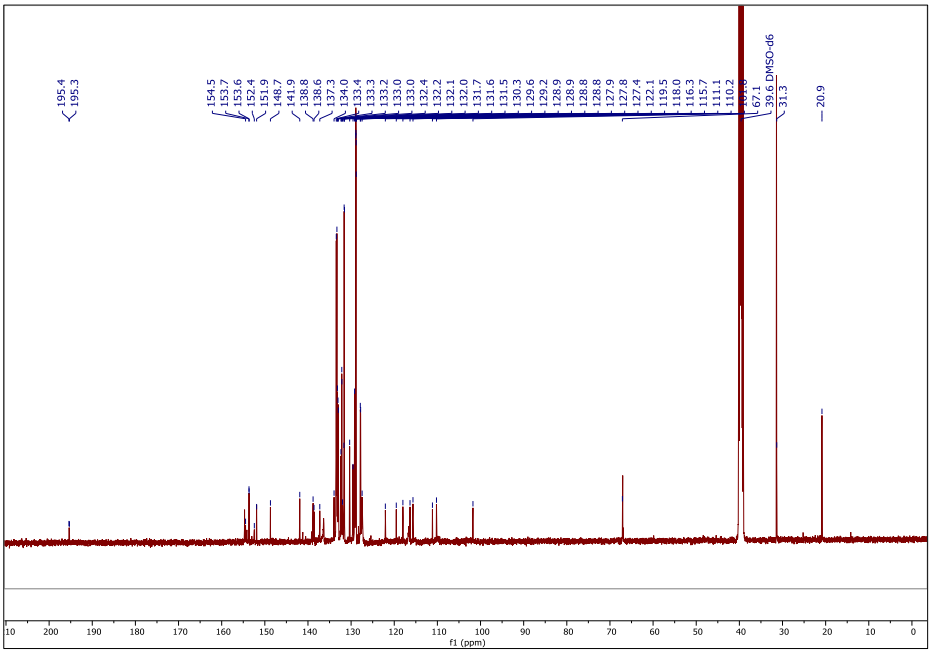

Figure 4.35 ^{13}C{^{1}H} NMR of anionic NHC complex before bubbling the mixture gas

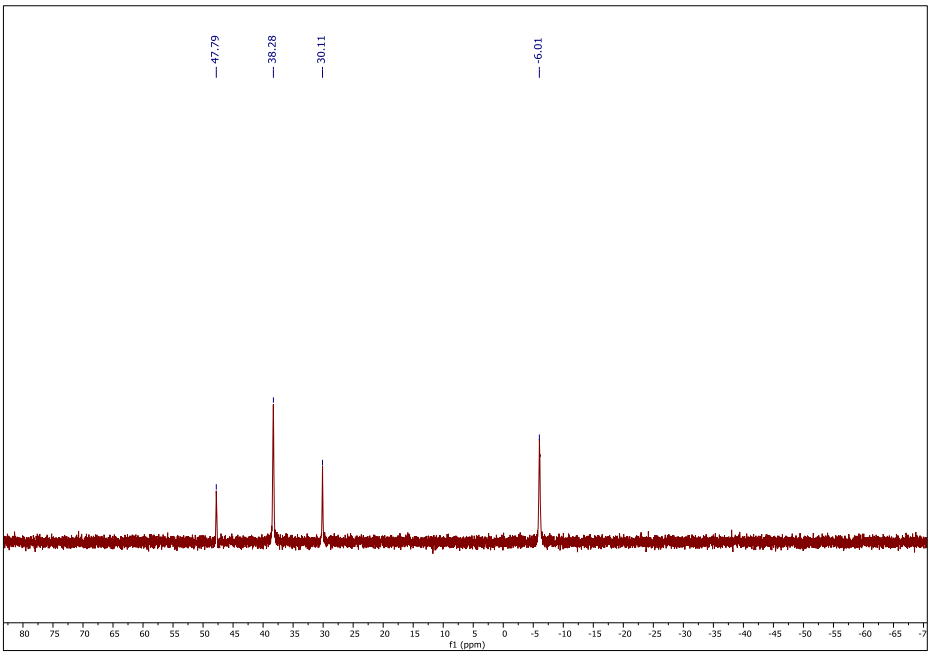

Figure 4.36 $^{31}P\{^{1}H\}$ NMR of anionic NHC complex before bubbling the mixture gas

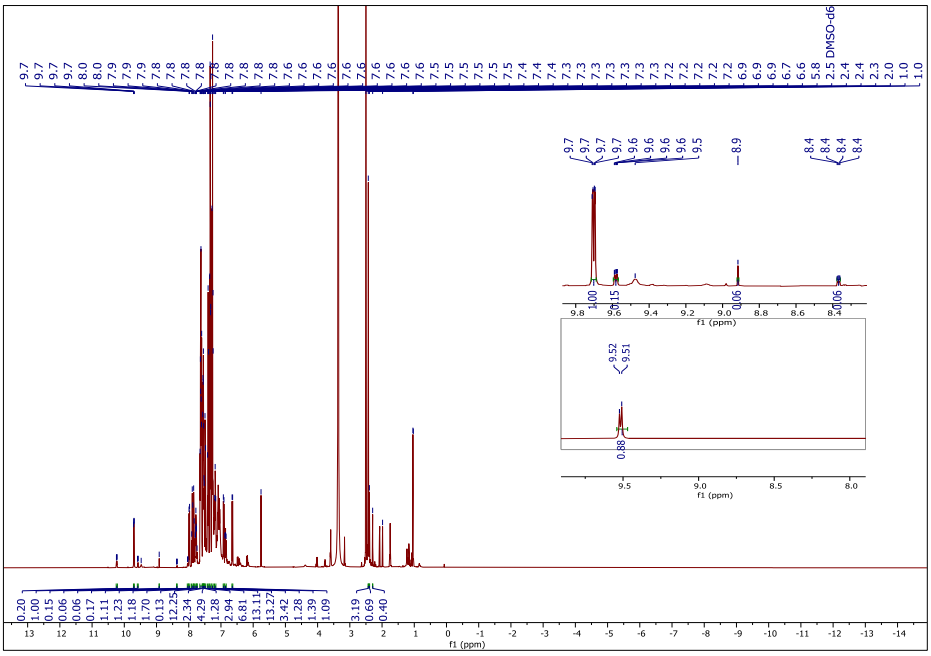

Figure 4.37 ^{1}H NMR of anionic NHC complex after bubbling the mixture gas

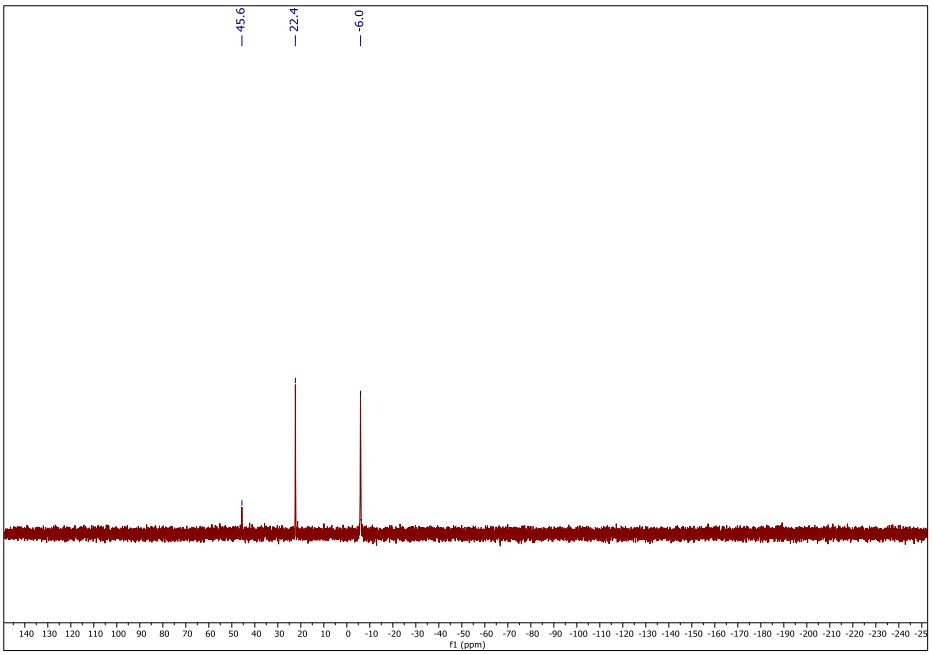

Figure 4.38 $^{31}P\{^{1}H\}$ NMR of anionic NHC complex after bubbling the mixture gas

4.5 References

[1] Zhang, J. (2024). Energy access challenge and the role of fossil fuels in meeting electricity demand: Promoting renewable energy capacity for sustainable development. GSF, *15*, 101873. (https://doi.org/10.1016/j.gsf.2024.101873)

[2] Alagoz, E., and Alghawi, Y. (2023). The Future of Fossil Fuels: Challenges and Opportunities in a Low- Carbon World. IJESKA, 5(3). (https://orcid.org/0000-0002-2622-0453)

[3] Capellán-Pérez, I., Mediavilla, M., De Castro, C., Carpintero, Ó., and Miguel, L.J. (2014). Fossil fuel depletion and socio-economic scenarios: An integrated approach. Energy, *77*, 641–666. (https://doi.org/10.1016/j.energy.2014.09.063)

[4] Omer, A.M. (2008). Energy, environment and sustainable development. Renew. Sustain. Energy Rev., *12*, 2265–2300. (https://doi.org/10.1016/j.rser.2007.05.001)

[5] Achakulwisut, P., Erickson, P., Guivarch, C., Schaeffer, R., Brutschin, E., and Pye, S. (2023). Global fossil fuel reduction pathways under different climate mitigation strategies and ambitions. Nat Commun, *14*, 5425. (https://doi.org/10.1038/s41467-023-41105-z)

[6] Huo, J., and Peng, C. (2023). Depletion of natural resources and environmental quality: Prospects of energy use, energy imports, and economic growth hindrances. Resour. Policy, *86*, 104049. (https://doi.org/10.1016/j.resourpol.2023.104049)

[7] Zou, C., Zhao, Q., Zhang, G., and Xiong, B. (2016). Energy revolution: From a fossil energy era to a new energy era. Natural Gas Industry B, *3*, 1–11. (https://doi.org/10.1016/j.ngib.2016.02.001)

[8] Sheldon, R.A. (2007). The E Factor: fifteen years on. Green Chem. *9*, 1273. (https://doi.org/10.1039/b713736m)

[9] Armaroli, N., and Balzani, V. (2007). The Future of Energy Supply: Challenges and Opportunities. Angew Chem Int Ed, *46*, 52–66. (https://doi.org/10.1002/anie.200602373)

[10] Wang, X., Sun, X., Ahmad, M., and Chen, J. (2024). Energy transition, ecological governance, globalization, and environmental sustainability: Insights from the top ten emitting countries. Energy, *292*, 130551. (https://doi.org/10.1016/j.energy.2024.130551)

[11] Kasera, A., Biswas, J.P., Ali Alshehri, A., Ahmed Al-Thabaiti, S., Mokhtar, M., and Maiti, D. (2023). Transition metal pincer complexes: A series of potential catalysts in C H activation reactions. Coord Chem Rev., *475*, 214915. (https://doi.org/10.1016/j.ccr.2022.214915)

[12] Komuro, T., Nakajima, Y., Takaya, J., and Hashimoto, H. (2022). Recent progress in transition metal complexes supported by

multidentate ligands featuring group 13 and 14 elements as coordinating atoms. Coord Chem Rev., *473*, 214837. (https://doi.org/10.1016/j.ccr.2022.214837)

[13] Yin, X., and Moss, J.R. (1999). Recent developments in the activation of carbon dioxide by metal complexes. Coord Chem Rev., *181*, 27–59. (https://doi.org/10.1016/S0010-8545(98)00171-4)

[14] Ganley, J.M., Joe, C.L., and Simmons, E.M. (2025). Development of Robust, Efficient and Scalable Transition Metal Catalyzed Transformations: Translation of Reactions from Micromole to Multi-Kilogram Scale Processes. ACS Catal., *15*, 8317–8336. (https://doi.org/10.1021/acscatal.5c00836)

[15] Abdinejad, M., Hossain, M.N., and Kraatz, H.-B. (2020). Homogeneous and heterogeneous molecular catalysts for electrochemical reduction of carbon dioxide. RSC Adv., *10*, 38013–38023. (https://doi.org/10.1039/D0RA07973A)

[16] Mak, C.H., Han, X., Du, M., Kai, J.-J., Tsang, K.F., Jia, G., Cheng, K.-C., Shen, H.-H., and Hsu, H.-Y. (2021). Heterogenization of homogeneous photocatalysts utilizing synthetic and natural support materials. J. Mater. Chem. A, *9*, 4454–4504. (https://doi.org/10.1039/D0TA08334H)

[17] Cui, X., Huang, R., and Deng, D. (2021). Catalytic conversion of C1 molecules under mild conditions. EnergyChem, *3*, 100050. (https://doi.org/10.1016/j.enchem.2020.100050)

[18] Mohamadpour, F., and Amani, A.M. (2024). Photocatalytic systems: reactions, mechanism, and applications. RSC Adv., *14*, 20609–20645. (https://doi.org/10.1039/D4RA03259D)

[19] Chakravorty, A., and Roy, S. (2024). A review of photocatalysis, basic principles, processes, and materials. Sustain. Chem. Environ., *8*, 100155. (https://doi.org/10.1016/j.scenv.2024.100155)

[20] Zhou, C., Tao, L., Yang, F., Wang, B., Wan, X., Jin, Y., Yu, H., and Yang, Y. (2019). Application of electrochemical methods in heterogeneous catalysis. Curr. Opin. Chem. Eng., *26*, 88–95. (https://doi.org/10.1016/j.coche.2019.09.007)

[21] Rana, J., Sahoo, S.T., and Daw, P. (2021). Homogeneous first-row transition metal catalyst for sustainable hydrogen production and organic transformation from methanol, formic acid, and bio-alcohols. Tetrahedron, *99*, 132473. (https://doi.org/10.1016/j.tet.2021.132473)

[22] Piccirilli, L., Lobo Justo Pinheiro, D., and Nielsen, M. (2020). Recent Progress with Pincer Transition Metal Catalysts for Sustainability. Catalysts, *10*, 773. (https://doi.org/10.3390/catal10070773)

[23] Lal Verma, N., Kumar, M., Sharma, D., Jaipal, Kumar, S., Rathore, N., and Jaiswar, G. (2023). Transition-metal-mediated C-C bond activation: Recent advances and its applications in organic synthesis. Results Chem., *6*, 101130. (https://doi.org/10.1016/j.rechem.2023.101130)

[24] Renfrew, A.K. (2014). Transition metal complexes with bioactive ligands: mechanisms for selective ligand release and applications for drug delivery. Metallomics, *6*, 1324–1335. (https://doi.org/10.1039/C4MT00069B)

[25] Feng, Y., Yang, H., Wang, X., Hu, C., Jing, H., and Cheng, J. (2022). Role of transition metals in catalyst designs for oxygen evolution reaction: A comprehensive review. Int. J. Hydrogen Energy, *47*, 17946–17970. (https://doi.org/10.1016/j.ijhydene.2022.03.270)

[26] Saha, A., Nath, S., Yadav, E., and Singh, A.K. (2025). Ru(II)-Protic-NHC Complex Catalyzed Selective *N*-alkylation of Anilines with Primary Alcohols: Mechanistic Insights and Role of Salt Additives. ChemCatChem, *17*. (https://doi.org/10.1002/cctc.202500184)

[27] Kar, S., Rauch, M., Leitus, G., Ben-David, Y., and Milstein, D. (2021). Highly efficient additive-free dehydrogenation of neat formic acid. Nat Catal, *4*, 193–201. (https://doi.org/10.1038/s41929-021-00575-4)

[28] Eppinger, J., and Huang, K.-W. (2017). Formic Acid as a Hydrogen Energy Carrier. ACS Energy Lett., *2*, 188–195. (https://doi.org/10.1021/acsenergylett.6b00574)

[29] Al-Nayili, A., Majdi, H.Sh., Albayati, T.M., and Saady, N.M.C. (2022). Formic Acid Dehydrogenation Using Noble-Metal Nanoheterogeneous Catalysts: Towards Sustainable Hydrogen-Based Energy. Catalysts, *12*, 324. (https://doi.org/10.3390/catal12030324)

[30] Liu, X., Li, S., Liu, Y., and Cao, Y. (2015). Formic acid: A versatile renewable reagent for green and sustainable chemical synthesis. Chin. J. Catal., *36*, 1461–1475. (https://doi.org/10.1016/S1872-2067(15)60861-0)

[31] Arora, V., Yasmin, E., Tanwar, N., Hathwar, V.R., Wagh, T., Dhole, S., and Kumar, A. (2023). Pincer–Ruthenium-Catalyzed Reforming of Methanol─Selective High-Yield Production of Formic Acid and Hydrogen. ACS Catal., *13*, 3605–3617. (https://doi.org/10.1021/acscatal.2c05587)

[32] Vatsa, A., Mishra, A., and Padhi, S.K. (2022). Monitoring of catalytic dehydrogenation of formic acid by a ruthenium (II) complex through manometry. Inorg. Chem. Commun., *144*, 109898. (https://doi.org/10.1016/j.inoche.2022.109898)

[33] Vatsa, A., and Padhi, S.K. (2021). Dehydrogenation of Formic Acid by a Ru^{II} Half Sandwich Catalyst. ChemistrySelect, *6*, 9447–9452. (https://doi.org/10.1002/slct.202102735)

[34] Vatsa, A., and Padhi, S.K. (2022). Formic acid dehydrogenation by [Ru(η^6 -benzene)(L)Cl] catalysts: L = 2-methylquinolin-8-olate and quinolin-8-olate. New J. Chem., *46*, 15723–15731. (https://doi.org/10.1039/D2NJ03121C)

[35] Wang, X., Meng, Q., Gao, L., Jin, Z., Ge, J., Liu, C., and Xing, W. (2018). Recent progress in hydrogen production from formic acid decomposition. Int. J. Hydrogen Energy, *43*, 7055–7071. (https://doi.org/10.1016/j.ijhydene.2018.02.146)

[36] Mardini, N., and Bicer, Y. (2021). Direct synthesis of formic acid as hydrogen carrier from CO2 for cleaner power generation through direct formic acid fuel cell. Int. J. Hydrogen Energy, *46*, 13050–13060. (https://doi.org/10.1016/j.ijhydene.2021.01.124)

[37] Chung, C., Kim, J., Sovacool, B.K., Griffiths, S., Bazilian, M., and Yang, M. (2023). Decarbonizing the chemical industry: A systematic review of sociotechnical systems, technological innovations, and policy options. Energy Res. Soc. Sci., *96*, 102955. (https://doi.org/10.1016/j.erss.2023.102955)

[38] Gao, X., Yang, Y., Yang, S., Wang, T., Liu, Z., and Yu, Z. (2024). Production of CO-free H2 through aqueous formic acid dehydrogenation over the α-Mo2C/NC catalyst. Chem. Eng. J., *500*, 156933. (https://doi.org/10.1016/j.cej.2024.156933)

[39] Megía, P.J., Vizcaíno, A.J., Calles, J.A., and Carrero, A. (2021). Hydrogen Production Technologies: From Fossil Fuels toward Renewable Sources. A Mini Review. Energy Fuels *35*, 16403–16415. (https://doi.org/10.1021/acs.energyfuels.1c02501)

[40] Pan, Y., Pan, C., Zhang, Y., Li, H., Min, S., Guo, X., Zheng, B., Chen, H., Anders, A., Lai, Z., et al. (2016). Selective Hydrogen Generation from Formic Acid with Well-Defined Complexes of Ruthenium and Phosphorus–Nitrogen PN^3 -Pincer Ligand. Chem. Asian J., *11*, 1357–1360. (https://doi.org/10.1002/asia.201600169)

[41] Nikol, A.T., Rabell, B., Jørgensen, M.S.B., Larsen, R.W., and Nielsen, M. (2024). Formic acid dehydrogenation using Ruthenium-POP pincer complexes in ionic liquids. Sci Rep, *14*, 26209. (https://doi.org/10.1038/s41598-024-76782-3)

[42] Edor, J.M., Joseph, M.C., Jordaan, J.H.L., Vosloo, H.C.M., and Swarts, A.J. (2025). Formic Acid Dehydrogenation Catalysis Using Novel Pyridyl-Formamidine Half-Sandwich Ruthenium(II) Complexes. Applied Organom Chemis, *39*, e70016. (https://doi.org/10.1002/aoc.70016)

[43] Hsu, S., Rommel, S., Eversfield, P., Muller, K., Klemm, E., Thiel, W.R., and Plietker, B. (2014). A Rechargeable Hydrogen Battery Based on Ru Catalysis. Angew Chem Int Ed, *53*, 7074–7078. (https://doi.org/10.1002/anie.201310972)

[44] Matsuoka, W., Harabuchi, Y., and Maeda, S. (2023). Virtual Ligand Strategy in Transition Metal Catalysis Toward Highly Efficient Elucidation of Reaction Mechanisms and Computational Catalyst Design. ACS Catal., *13*, 5697–5711. (https://doi.org/10.1021/acscatal.3c00576)

[45] Lundgren, R.J., and Stradiotto, M. (2016). Key Concepts in Ligand Design: An Introduction. In Ligand Design in Metal Chemistry, M. Stradiotto and R. J. Lundgren, eds. (Wiley), pp. 1–14. (https://doi.org/10.1002/9781118839621.ch1)

[46] Wang, W., Hammond, G.B., and Xu, B. (2012). Ligand Effects and Ligand Design in Homogeneous Gold(I) Catalysis. J. Am. Chem. Soc., *134*, 5697–5705. (https://doi.org/10.1021/ja3011397)

[47] Nahra, F., Nelson, D.J., and Nolan, S.P. (2020). Design Concepts for *N*-Heterocyclic Carbene Ligands. Trends Chem., *2*, 1096–1113. (https://doi.org/10.1016/j.trechm.2020.10.003)

[48] Lyaskovskyy, V., and De Bruin, B. (2012). Redox Non-Innocent Ligands: Versatile New Tools to Control Catalytic Reactions. ACS Catal., *2*, 270–279. (https://doi.org/10.1021/cs200660v)

[49] Berben, L.A., De Bruin, B., and Heyduk, A.F. (2015). Non-innocent ligands. Chem. Commun., *51*, 1553–1554. (https://doi.org/10.1039/C4CC90480J)

[50] De Bruin, B., Gualco, P., and Paul, N.D. (2016). Redox Non-innocent Ligands: Reactivity and Catalysis. In Ligand Design in Metal Chemistry, M. Stradiotto and R. J. Lundgren, eds. (Wiley), pp. 176–204. (https://doi.org/10.1002/9781118839621.ch7)

[51] Li, X., Zhao, L., Yu, J., Liu, X., Zhang, X., Liu, H., and Zhou, W. (2020). Water Splitting: From Electrode to Green Energy System. Nano-Micro Lett. *12*, 131. (https://doi.org/10.1007/s40820-020-00469-3)

[52] Shi, J., Bao, Y., Ye, R., Zhong, J., Zhou, L., Zhao, Z., Kang, W., and Aidarova, S.B. (2025). Recent progress and perspective of electrocatalysts for the hydrogen evolution reaction. Catal. Sci. Technol., *15*, 2104–2131. (https://doi.org/10.1039/D4CY01449A)

[53] Choudhury, D., Das, R., Tripathi, A.K., Priyadarshani, D., and Neergat, M. (2022). Kinetics of Hydrogen Evolution Reactions in Acidic Media on Pt, Pd, and MoS_2. Langmuir, *38*, 4341–4350. (https://doi.org/10.1021/acs.langmuir.2c00090)

[54] González-Poggini, S. (2024). Hydrogen evolution descriptors: A review for electrocatalyst development and optimization. Int. J. Hydrogen Energy, *59*, 30–42. (https://doi.org/10.1016/j.ijhydene.2024.01.362)

[55] Lasia, A. (2019). Mechanism and kinetics of the hydrogen evolution reaction. Int. J. Hydrogen Energy, *44*, 19484–19518. (https://doi.org/10.1016/j.ijhydene.2019.05.183)

[56] Biswal, T., Shadangi, K.P., Sarangi, P.K., and Srivastava, R.K. (2022). Conversion of carbon dioxide to methanol: A comprehensive review. Chemosphere *298*, 134299. (https://doi.org/10.1016/j.chemosphere.2022.134299)

[57] Azhari, N.J., Erika, D., Mardiana, S., Ilmi, T., Gunawan, M.L., Makertihartha, I.G.B.N., and Kadja, G.T.M. (2022). Methanol synthesis from CO2: A mechanistic overview. Results in Engineering, *16*, 100711. (https://doi.org/10.1016/j.rineng.2022.100711)

[58] Xie, S., Zhang, W., Lan, X., and Lin, H. (2020). CO_2 Reduction to Methanol in the Liquid Phase: A Review. ChemSusChem, *13*, 6141–6159. (https://doi.org/10.1002/cssc.202002087)

[59] Yao, L., Rivera-Cruz, K.E., Zimmerman, P.M., Singh, N., and McCrory, C.C.L. (2024). Electrochemical CO_2 Reduction to Methanol by Cobalt Phthalocyanine: Quantifying CO_2 and CO Binding Strengths and Their Influence on Methanol Production. ACS Catal., *14*, 366–372. (https://doi.org/10.1021/acscatal.3c04957)

[60] Tanabe, Y., and Nishibayashi, Y. (2022). Recent advances in catalytic nitrogen fixation using transition metal–dinitrogen complexes under mild reaction conditions. Coord Chem Rev, *472*, 214783. (https://doi.org/10.1016/j.ccr.2022.214783)

[61] Ashida, Y., and Nishibayashi, Y. (2021). Catalytic conversion of nitrogen molecule into ammonia using molybdenum complexes under ambient reaction conditions. Chem. Commun., *57*, 1176–1189. (https://doi.org/10.1039/D0CC07146C)

[62] Roux, Y., Duboc, C., and Gennari, M. (2017). Molecular Catalysts for N_2 Reduction: State of the Art, Mechanism, and Challenges. ChemPhysChem, *18*, 2606–2617. (https://doi.org/10.1002/cphc.201700665)

[63] Cabrera, G., Mora, M., Gil-Burgos, J.P., Visbal, R., Machuca-Martínez, F., and Mosquera-Vargas, E. (2024). Liquid Organic Hydrogen Carrier Concepts and Catalysts for Hydrogenation and Dehydrogenation Reactions. Molecules, *29*, 4938. (https://doi.org/10.3390/molecules29204938)

[64] Le, T.-H., Tran, N., and Lee, H.-J. (2024). Development of Liquid Organic Hydrogen Carriers for Hydrogen Storage and Transport. IJMS, *25*, 1359. (https://doi.org/10.3390/ijms25021359)

[65] Ramadhani, S., Dao, Q.N., Imanuel, Y., Ridwan, M., Sohn, H., Jeong, H., Kim, K., Yoon, C.W., Song, K.H., and Kim, Y. (2024). Advances in Catalytic Hydrogenation of Liquid Organic Hydrogen Carriers (LOHCs) Using High-Purity and Low-Purity Hydrogen. ChemCatChem, *16*, e202401278. (https://doi.org/10.1002/cctc.202401278)

[66] Zhou, M., Miao, Y., Gu, Y., and Xie, Y. (2024). Recent Advances in Reversible Liquid Organic Hydrogen Carrier Systems: From Hydrogen Carriers to Catalysts. Adv. Mater., *36*, 2311355. (https://doi.org/10.1002/adma.202311355)

[67] Chu, C., Wu, K., Luo, B., Cao, Q., and Zhang, H. (2023). Hydrogen storage by liquid organic hydrogen carriers: Catalyst, renewable carrier, and technology – A review. Carbon Resources Conversion *6*, 334–351. (https://doi.org/10.1016/j.crcon.2023.03.007)

[68] Nath, S., Yadav, E., Raghuvanshi, A., and Singh, A.K. (2023). Mechanistic insights and comparative analysis of Ru(II)–NNC pincer complexes with anionic-, protic-, and classical-NHCs for

transfer hydrogenation of ketones. Catal. Sci. Technol., *13*, 7085–7099. (https://doi.org/10.1039/D3CY01383A)

[69] Nath, S., Yadav, E., Raghuvanshi, A., and Singh, A.K. (2023). Ru(II) Complexes with Protic- and Anionic-Naked-NHC Ligands for Cooperative Activation of Small Molecules**. Chem Eur J, *29*, e202301971. (https://doi.org/10.1002/chem.202301971)

[70] Yadav, E., Nath, S., Shahid, N., Saha, A., Das, B., and Singh, A.K. (2025). Enhanced Activity of Proton-Responsive Protic-NHC-Ru(II) Bis(pincer) Complexes for Electrochemical Water Oxidation. ChemCatChem, e01003. (https://doi.org/10.1002/cctc.202501003)

[71] Nath, S., and Singh, A.K. (2025). Substrate-assisted product release in hydrogenation of LOHCs facilitated by hemilabile pyridine in Ru(II)–NNC pincer complexes and enhanced activity of proton-responsive protic-NHC ligands. Catal. Sci. Technol., *15*, 2999–3008. (https://doi.org/10.1039/D5CY00209E)

[72] Shimbayashi, T., and Fujita, K. (2020). Recent Advances in Homogeneous Catalysis via Metal–Ligand Cooperation Involving Aromatization and Dearomatization. Catalysts, *10*, 635. (https://doi.org/10.3390/catal10060635)

[73] Gunanathan, C., and Milstein, D. (2011). Metal–Ligand Cooperation by Aromatization–Dearomatization: A New Paradigm in Bond Activation and "Green" Catalysis. Acc. Chem. Res., *44*, 588–602. (https://doi.org/10.1021/ar2000265)

[74] He, L.-P., Chen, T., Gong, D., Lai, Z., and Huang, K.-W. (2012). Enhanced Reactivities toward Amines by Introducing an Imine Arm to the Pincer Ligand: Direct Coupling of Two Amines To Form an Imine Without Oxidant. Organometallics, *31*, 5208–5211. (https://doi.org/10.1021/om300422v)

[75] Gonçalves, T.P., Dutta, I., and Huang, K.-W. (2021). Aromaticity in catalysis: metal ligand cooperation *via* ligand dearomatization and rearomatization. Chem. Commun., *57*, 3070–3082. (https://doi.org/10.1039/D1CC00528F)

[76] Ratti, R. (2014). Ionic Liquids: Synthesis and Applications in Catalysis. Adv. Chem., *2014*, 1–16. (https://doi.org/10.1155/2014/729842)

[77] Jhanji, I. (2023). The Role of Ionic Liquids in Green Solvent Chemistry: Properties and Applications. IRJEAS, *11*, 57–67. (https://doi.org/10.55083/irjeas.2023.v11i04009)

[78] Kaur, G., Kumar, H., and Singla, M. (2022). Diverse applications of ionic liquids: A comprehensive review. J. Mol. Liq., *351*, 118556. (https://doi.org/10.1016/j.molliq.2022.118556)

[79] Aufricht, P., Nori, V., Rabell, B., Piccirilli, L., Koranchalil, S., W. Larsen, R., Nielsen, M.T., and Nielsen, M. (2025). Formic acid dehydrogenation catalysed by a novel amino-di(*N*-heterocyclic carbene) based Ru-CNC pincer complex. Chem. Commun., *61*, 3986–3989. (https://doi.org/10.1039/D4CC05164E)

[80] Piccirilli, L., Rabell, B., Padilla, R., Riisager, A., Das, S., and Nielsen, M. (2023). Versatile CO_2 Hydrogenation–Dehydrogenation Catalysis with a Ru–PNP/Ionic Liquid System. J. Am. Chem. Soc., *145*, 5655–5663. (https://doi.org/10.1021/jacs.2c10399)

[81] Kumar, N.S., and Adhikary, A. (2024). Transition metal pincer catalysts for formic acid dehydrogenation: a mechanistic perspective. Front. Chem., *12*, 1452408. (https://doi.org/10.3389/fchem.2024.1452408)

[82] Léval, A., Agapova, A., Steinlechner, C., Alberico, E., Junge, H., and Beller, M. (2020). Hydrogen production from formic acid

catalyzed by a phosphine free manganese complex: investigation and mechanistic insights. Green Chem., *22*, 913–920. (https://doi.org/10.1039/C9GC02453K)

[83] Boddien, A., Mellmann, D., Gärtner, F., Jackstell, R., Junge, H., Dyson, P.J., Laurenczy, G., Ludwig, R., and Beller, M. (2011). Efficient Dehydrogenation of Formic Acid Using an Iron Catalyst. Science, *333*, 1733–1736. (https://doi.org/10.1126/science.1206613)

[84] Johnee Britto, N., and Jaccob, M. (2022). Unveiling the mechanistic landscape of formic acid dehydrogenation catalyzed by Cp∗M(III) catalysts (M = Co or Rh or Ir) with bis(pyrazol-1-yl)methane ligand architecture: A DFT investigation. Int. J. Hydrogen Energy, *47*, 21736–21744. (https://doi.org/10.1016/j.ijhydene.2022.05.021)

[85] Hallman, P.S., Stephenson, T.A., and Wilkinson, G. (1970). Tetrakis(triphenylphosphine)dichlororuthenium(II) and Tris(triphenylphosphine)dichlororuthenium(II). In Inorganic Syntheses, R. W. Parry, ed. (Wiley), pp. 237–240. (https://doi.org/10.1002/9780470132432.ch40)

CHAPTER 5

Structural and Photophysical Correlation in γ-Substituted Metal Complexes: Fluorescence as a Probe for Ligand Hemilability

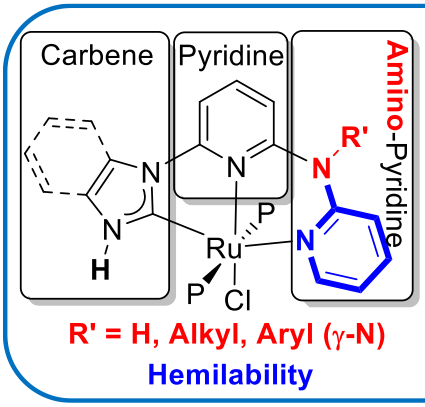

The present study examines the influence of γ-substitution while maintaining a constant β-NH fragment in the ligand framework. This substitution pattern significantly modulates the fluorescence response of the corresponding complexes. Fluorescence study utilized to probe the hemilability of the pyridine ring, revealing varying results with γ-substitution.

5.1 Introduction

Designing metal complexes with tunable fluorescence properties is an emerging approach for developing multifunctional photoactive materials for applications in sensing, catalysis, and optoelectronics.[1,2] The coexistence of ligand-centered emission, metal-influenced states, and charge-transfer processes often results in dual or multiple emissive states.[3,4] However, establishing correlations between these photophysical behaviors and specific structural parameters remains a significant challenge. The strategic design of ligands is essential for the development of advanced transition metal complexes with targeted reactivity and selectivity.[5,6] Among the various approaches employed, hemilability and metal-ligand cooperation (MLC) are two distinct yet complementary strategies for modulating metal-centered reactivity through ligand architecture.[7,8] Hemilabile ligands, characterized by both strong and weak donor groups, can reversibly dissociate and reassociate with the metal center during catalytic processes. This dynamic behavior facilitates the stabilization of reactive intermediates, assists in substrate binding, and enhances catalytic turnover.[9,10] In contrast, ligands exhibiting MLC actively participate in the catalytic process by undergoing reversible changes in their electronic or structural state, such as the transfer of protons, hydrides, or electrons, thereby providing an alternative mechanism for substrate activation and stabilization of high-energy transition states.[11–13]

The choice between hemilability and metal-ligand cooperation (MLC) is primarily contingent upon the specific catalytic transformation desired and the electronic and steric properties of the ligand framework. Hemilabile systems are particularly advantageous in processes necessitating the formation of a temporary vacancy at the metal site.[14] In contrast, MLC-based designs have demonstrated significant efficacy in bond activation reactions, such as hydrogenation, dehydrogenation, and small-molecule activation, by promoting cooperative transformations at the metal-ligand interface. Despite their distinct functionalities, recent research has indicated the potential for integrating both features within a single ligand scaffold to achieve unprecedented catalytic performance.[15–17]

Fluorescence spectroscopy has emerged as a highly sensitive technique for examining the intricate coordination dynamics and electronic interactions within complex systems.[18] The integration of fluorescent reporter groups into the ligand framework enables the detection of metal-ligand interactions through variations in emission, such as quenching, enhancement, or spectral shifts.[19,20] These variations offer direct insights into coordination equilibria and electronic redistribution. By correlating fluorescence responses with structural, spectroscopic, and catalytic data, researchers can differentiate between hemilabile behavior, characterized by reversible donor exchange, and metal-ligand cooperative processes, which involve chemical transformations at the ligand site.[21–23] This integrated approach, combining ligand design with fluorescence-based analysis, provides a robust strategy for elucidating the mechanistic distinctions between hemilability and metal-ligand cooperativity, thereby advancing the understanding of dynamic bonding and reactivity in contemporary coordination chemistry.[24]

The present study examines ligand designs that systematically modulate the hemilability of the ligand through slight structural modifications, thereby elucidating the impact of this fundamental concept on the photophysical properties of the system. By precisely adjusting the electronic and geometric properties of the ligand, this study provides a

more profound understanding of the interaction between hemilability and ligand design, facilitating the development of next-generation catalysts with enhanced functional versatility. To analyze this, we compared the complexes based on the γ-*N*-substitution of the CPAP ligands (Figure 5.1).

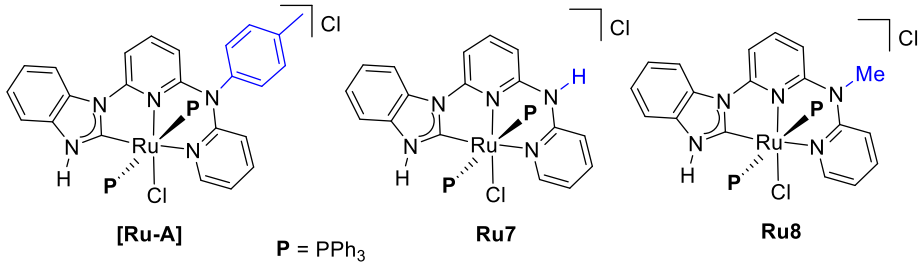

Figure 5.1 Complexes **[Ru-A], Ru7**, and **Ru8** used for the fluorescence study

5.2 Results and discussion

5.2.1 Synthesis and characterization of complex Ru9. A new complex, **Ru9**, based on our previously synthesized unsymmetrical ligand, 6-(1*H*-benzo[d]imidazol-1-yl)-*N*-(pyridin-2-yl)-*N*-(p-tolyl)pyridin-2-amine,[25] was synthesized by substituting one phosphine and one chloride group from the previously reported complex, [**Ru-A]**, by our group.[25] Under reflux conditions, an ethanolic solution of [**Ru-A]** was refluxed after the addition of bipyridine for 24 h. The bipyridine ligand was attached in place of one phosphine and chloride group to form complex **Ru9** (Scheme 5.1).

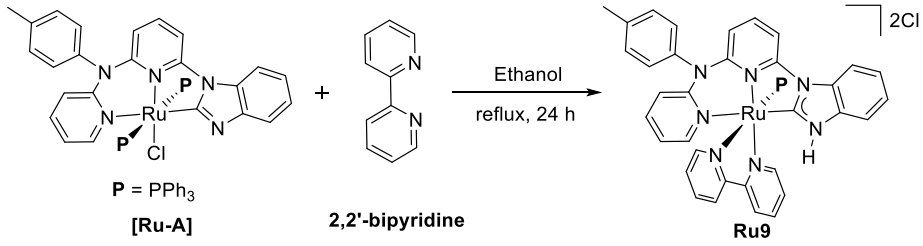

Scheme 5.1 Synthetic representation of the formation of complex **Ru9**.

Characterizations were conducted to confirm the formation of complex **Ru9**. The spectroscopic findings confirmed the formation of **Ru9**. The ^{1}H NMR spectrum showed a peak at δ 14.92 ppm for the protic *N*-H

peak. The aromatic region, from δ 9.02 to 6.46 ppm, confirmed the peaks corresponding to complex **Ru9**. The methyl group protons appeared at 2.54 ppm as a singlet (Figure 5.2). ^{13}C NMR has all the corresponding peaks regarding the formed complex.

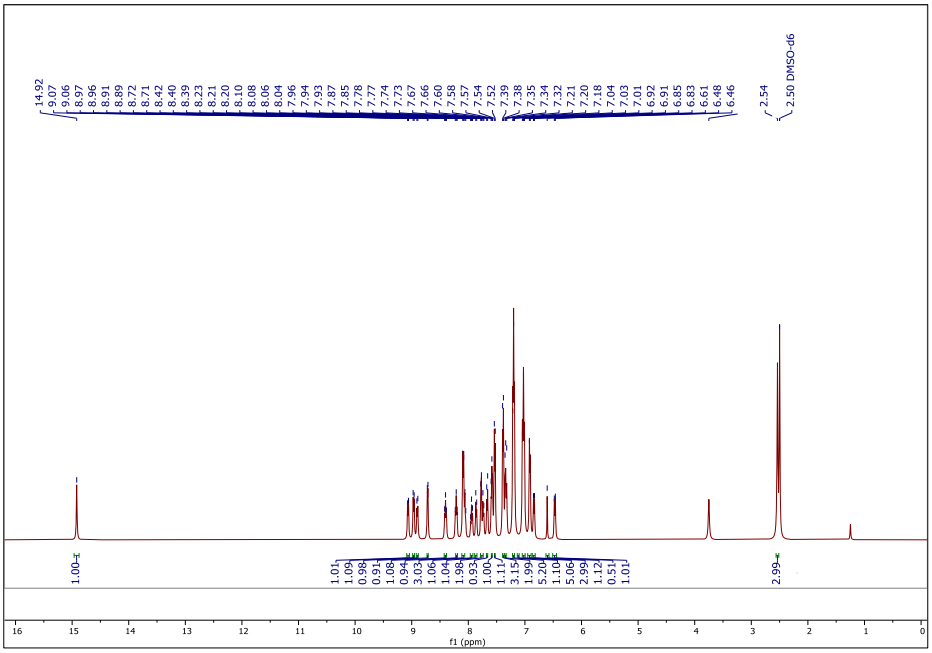

Figure 5.2 ^{1}H NMR of Ru-bpy complex, **Ru9**

The characteristic carbene carbon peak at δ 201.6 ppm was observed as a doublet because of the presence of one phosphine group. The methyl group carbon peak resonated at δ 20.8 ppm, along with other peaks (Figure 5.3). Another confirmation was provided by 31P NMR spectroscopy, where the peak at δ 46.2 ppm indicated that the complex contained one phosphine group in the system (Figure 5.4).

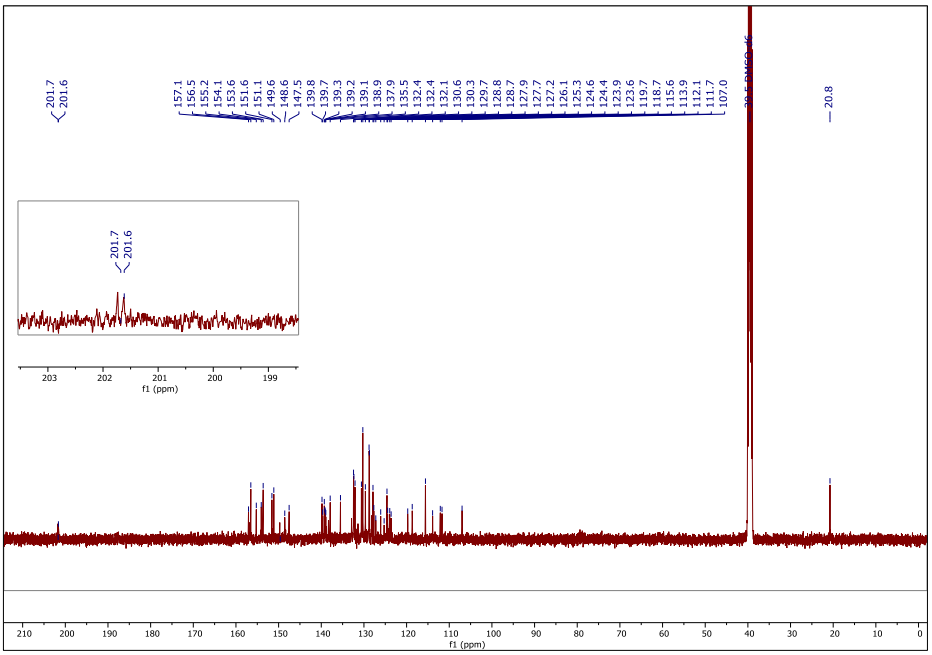

Figure 5.3 ^{13}C NMR of Ru-bpy complex, **Ru9**

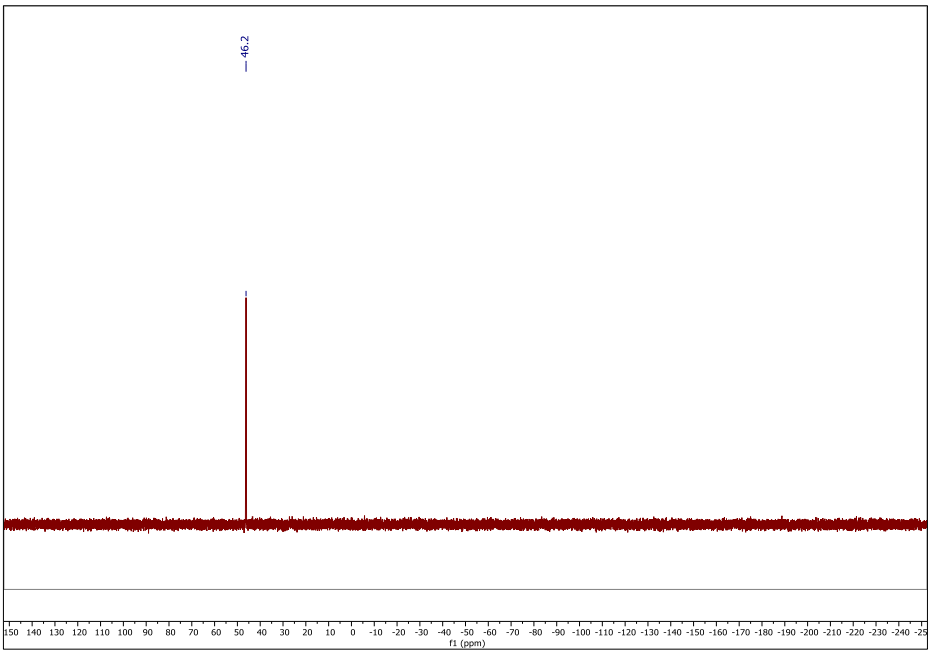

Figure 5.4 ^{31}P NMR of Ru-bpy complex, **Ru9**

LCMS(ESI$^+$) supports the formation of **Ru9** complex with a corresponding peak for $[M\text{-}2Cl]^{2+}$ at m/z = 448.5950 (calculated for $C_{52}H_{42}N_7PRuCl_2$: 448.6143) and an additional peak $[M\text{-}2Cl\text{-}H]^+$ at m/z = 896.1963 (calculated for $C_{52}H_{42}N_7PRuCl_2$: 896.2213). The HRMS shows the peak for $[M\text{-}2Cl]^{2+}$ at m/z = 448.6163 and for $[M\text{-}2Cl\text{-}H]^+$ at m/z = 898.2187.

5.2.2 Molecular structure of complex Ru9

The molecular structure of the ruthenium complex **Ru9** was elucidated using single-crystal X-ray crystallography (Figure 5.5). The complex crystallized in the orthorhombic crystal system and belonged to the Pccn space group. It features a distorted octahedral coordination geometry, which includes a five-membered metallacycle formed by the 2,2′-bipyridine (bpy) ligand, two nearly planar five- and six-membered metallacycles from the asymmetric CNN pincer ligand, and a phosphine ligand occupying the sixth coordination site around the ruthenium center. The bpy bidentate ligand takes up two coordination sites at the core of the ruthenium. One pyridine unit of the bpy ligand is positioned trans to the pyridine unit of the CNN pincer ligand. The sixth coordination site of the ruthenium atom is filled by another pyridine unit of the bipyridine ligand.

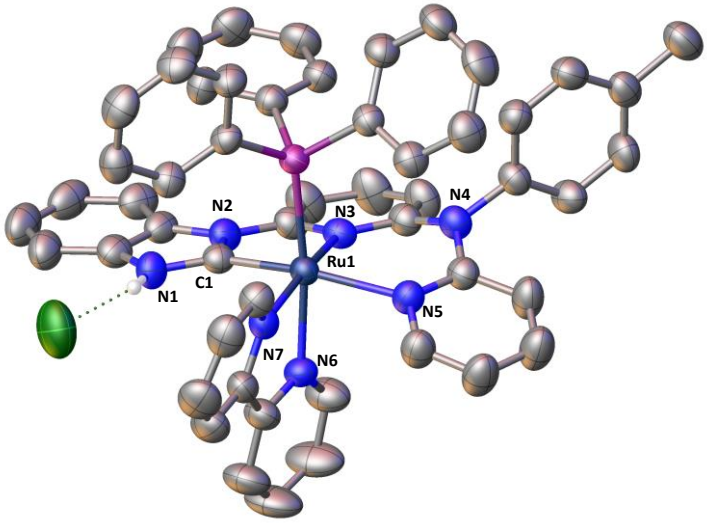

Figure 5.5 Molecular structure of complex **Ru9** obtained from a single-crystal X-ray diffraction study. All hydrogen atoms (except *N*-H) are omitted for clarity. Selected bond distances (Å) and angles (°): Ru1-C1= 1.964(4), Ru1-N3 = 2.062(3), Ru1-N5 = 2.176(3), Ru1-N6 = 2.096(3), Ru1-N7 = 2.121(3), C1-Ru1-N3 = 79.61(13); C1-Ru1-N5 = 163.15(13), C1-Ru1-N6 =96.66(13); C1-Ru1-N7 = 85.62(12).

5.2.3 Photophysical properties

To gain insights into the photophysical properties of complex **Ru9**, fluorescence spectroscopy was chosen. Fluorescence spectroscopy probes metal-ligand interactions and dynamics in coordination chemistry. It enables the detection of changes in the electronic environment and the coordination geometry around metal centers. Fluorescence quenching, enhancement, or shifts provide insights into ligand binding, dissociation, and electronic communication with the metal. By correlating fluorescence responses with structural and catalytic data, the mechanistic details of dynamic bonding and reactivity can be elucidated.

5.2.4 UV-visible and fluorescence study of complex Ru9

To analyze the photophysical activity of complex **Ru9**, we have checked its UV-visible spectrum. The UV spectrum showed two distinct peaks for complex **Ru9** (Figure 5.6). This clearly demonstrates the dual emissive property. In general, dual emission depends on various factors; here, the dual emission is attributed to both the bpy-containing complex and the ligand itself. To confirm this, we have recorded the fluorescence for complex **Ru9**.

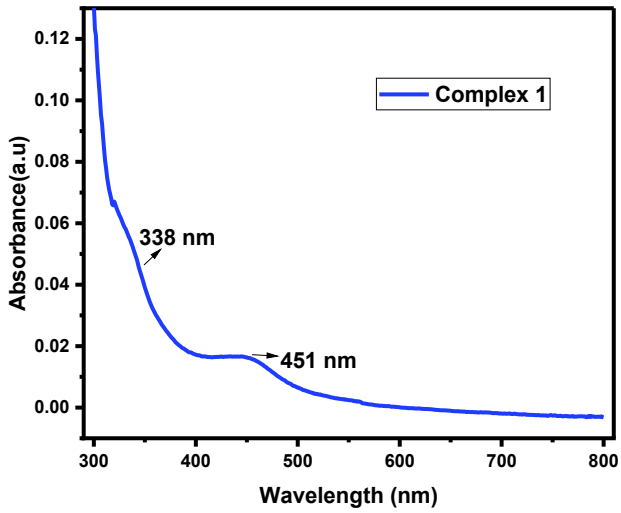

Figure 5.6 Absorbance spectrum of complex **Ru9**

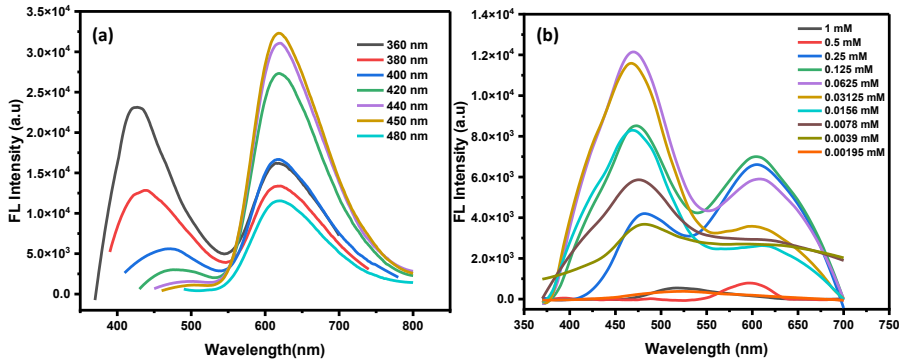

Figure 5.7 Emission spectra for complex **Ru9**; **(a)** Emission at different wavelength ranges, **(b)** Emission at fixed wavelength range on different concentrations

The fluorescence spectrum also confirmed the existence of dual emission. One peak appears at 426 nm, and another at 619 nm (Figure 5.7). Unsubstituted 2,2′-bipyridine does not exhibit intrinsic fluorescence (shows very low fluorescence).[26] However, numerous reports exist on the induced fluorescence of bipyridine ligands in metal complexes.[27] Most of the complexes showed a single peak for fluorescence, whereas our complex showed dual emission. To investigate the reason behind the dual emissive property, we have explored the fluorescence of the parent complex **[Ru-A]**, which could be one of the possibilities for the existence of more than one fluorescence peak.

5.2.5 Photophysical properties of [Ru-A] and ligand L1

The absorption peaks indicate π-conjugated systems and aromatic rings, facilitating ligand transitions and fluorescence potential. Complex [**Ru-A]** exhibited three major absorption bands at 204, 262, and 305 nm. These high-energy absorptions are typical for ligand-centered π-π* transitions (204 nm, 262 nm) and possibly charge transfer transitions (305 nm) involving the metal and conjugated ligand framework. Complex [**Ru-A]** showed fluorescence at 447 nm at various concentrations. Initially, at a 1mM concentration of [**Ru-A]**, the intensity was approximately 1000, which remained the same at 0.5 mM. Upon dilution, the intensity of the peak initially increased up to 4×10^4 at

0.03125 mM, and then decreased significantly with further dilutions. Here, we observed only one peak, which contrasts with that of complex **Ru9**, which shows two peaks. This further confirms that the dual emission fluorescence of complex **Ru9** is mainly due to the ligand bpy (Figure 5.8).

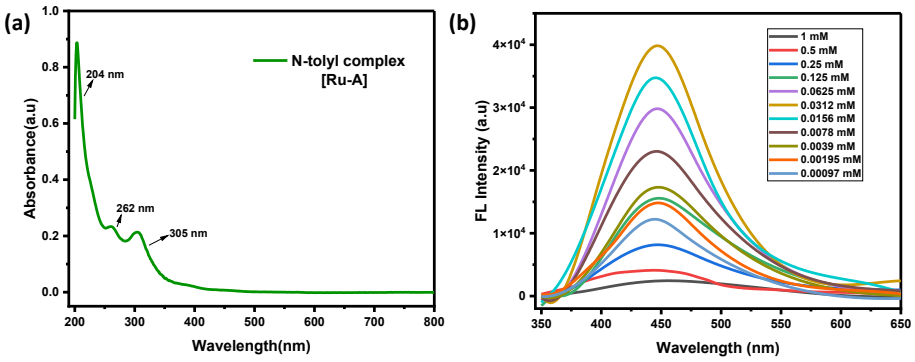

Figure 5.8 (a) Absorption spectrum for complex **[Ru-A]**; **(b)** Emission spectrum of **[Ru-A]** at fixed wavelength range on different concentrations

To gain better insights into the ligand, we further analyzed the photophysical properties of **L1**. The ligand **L1** used in the formation of complex **Ru9** is the most well-known part of the ligand family called CPAP, which has already been reported by our group.[25] As depicted in Figure 5.9, it exhibits notable photophysical properties. The UV-Vis absorbance spectrum exhibits major peaks at 204, 248, 275, 302, and 320 nm, indicating strong π-π* and n-π* transitions characteristic of conjugated aromatic and heteroaromatic systems with electron-rich donors such as pyridine and benzimidazole derivatives. In this case, 204 and 248 nm represent transitions typical of aromatic π-π* systems, whereas the transitions at 275, 302, and 320 nm suggest additional n-π* transitions.

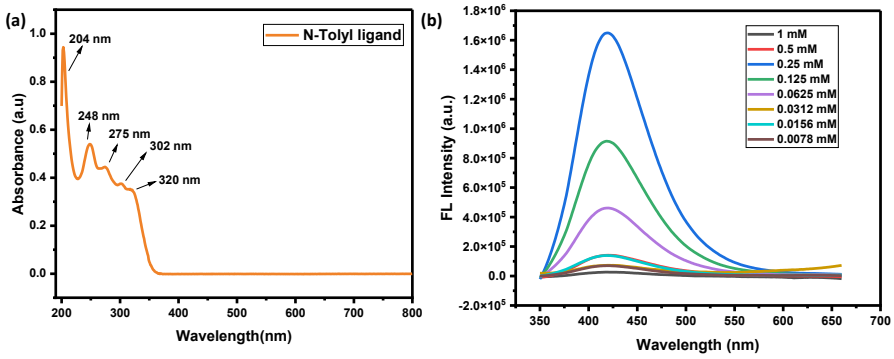

Figure 5.9 (a) Absorption spectrum for ligand **L1**; **(b)** Emission spectrum of **L1** at fixed wavelength range on different concentrations

Initially, the fluorescence of the ligand **L1**, 6-(1*H*-benzo[d]imidazol-1-yl)-*N*-(pyridin-2-yl)-*N*-(p-tolyl)pyridin-2-amine was recorded. The fluorescence peak for **L1** was observed at 419 nm in a methanol solution (Figure 5.9b). The spectrum was recorded at room temperature over a wide range of wavelengths. Better data were recorded at 340 nm. The ligand peak at 419 nm is a characteristic peak for the ligand, which is in close proximity to the fluorescence peak obtained for complex **Ru9**, demonstrating the relationship between the fluorescent peak and the ligand moiety, while the other peak is for the complexation of the bpy group to the ruthenium metal center. In continuation of this, we also checked the fluorescence of the other ligands in the CPAP family, which vary based on *N*-substitution.

5.2.6 UV-Vis absorption and fluorescence for the ligands and metal complexes, illustrating structural effects

The multiple absorption peaks are characteristic of extended π-conjugated systems and aromatic rings, supporting ligand-centered transitions and the potential for high fluorescence in each ligand. The UV-Vis spectrum of **L6** showed transitions similar to those of **L1**, with peaks at 204, 244, 275, and 320 nm attributed to the π-π* and n-π* transitions (Figure 5.10). Similarly, **L5** also possesses transitions at 204, 244, and 320 nm, but a peak at 269 nm differs from the other ligands

containing alkyl groups at γ-N, i.e., tolyl and methyl groups. Here, ligand **L5** has an NH linker, which has a different effect on the absorption.

In another series (**c-d**) in Figure 5.10, the complexes **Ru7** and **Ru8** also undergo UV-Vis studies; the complex **Ru8** displays strong absorption at 204 nm, similar to all the listed ligands and complexes, a secondary intense band at 262 nm, and a different broad, weaker absorption around 296 nm. Compared to the *N*-tolyl congener, the main diagnostic difference is the slight hypsochromic shift from 305 nm (**[Ru-A]**) to 296 nm (**Ru8**), reflecting a slight change in the π-system and charge transfer propensity. Similarly, **Ru7** exhibited peaks at 204 and 262 nm, which were consistent with those of the other complexes. An additional peak at 307 nm was observed for the variation in the complex. All bands were attributed to ligand-centered π-π* transitions.

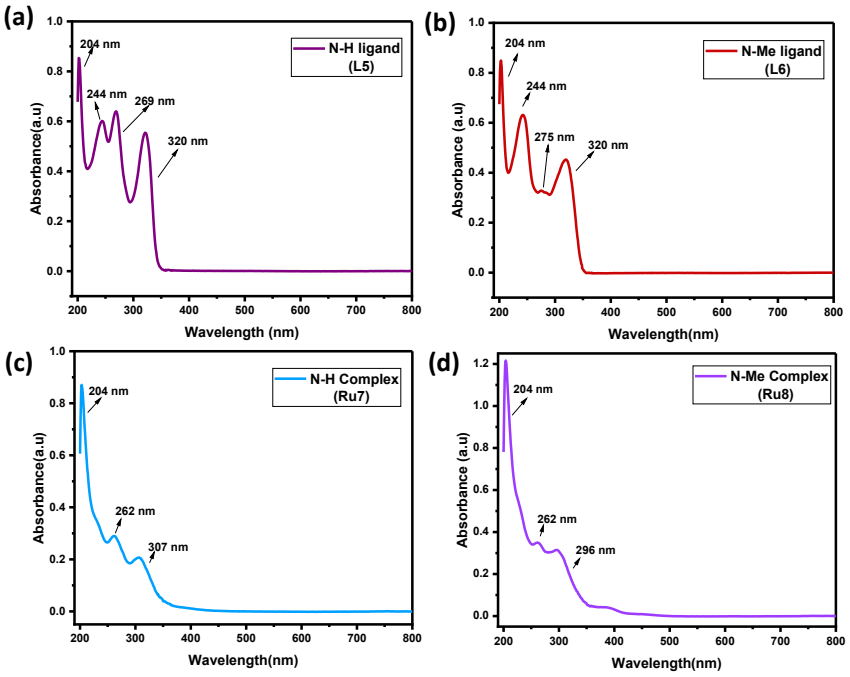

Figure 5.10 Absorption spectra for **(a)** γ-*N*-H ligand (**L5**);**(b)** γ-*N*-Me ligand (**L6**); **(c)** γ-*N*-H complex (**Ru7**); **(d)** γ-*N*-Me complex (**Ru8**)

5.2.6.1 Fluorescence in CPAP ligands

The ligands, **L5** and **L6**, having γ-*N*-H and γ-*N*-Me linkers, respectively, are tested for the photophysical properties. Upon recording fluorescence, **L5** showed a peak at 356 nm, while **L6** showed a peak at 342 nm,

demonstrating the fluorescent behavior of all the ligands. All ligands were highly fluorescent at dilute concentrations. In the case of **L1**, the concentrations were varied from 1mM to 0.00097 mM to study the dilution effect on the ligand. Initially, at 1 mM, the intensity was approximately 8000, which remained constant at 0.5 mM. Upon further dilution to 0.125 mM, the intensity increased. Dilution after 0.125 mM showed a decrease in intensity up to 0.0078 mM. Similarly, for **L6** and **L5**, the fluorescence intensity increased up to 0.125 mM and 0.0625 mM, respectively, and then decreased with further dilution. Concentrations higher than 1 mM do not exhibit fluorescence, indicating that the fluorescence property is quenched due to the aggregation of molecules at higher concentrations (Figure 5.11).

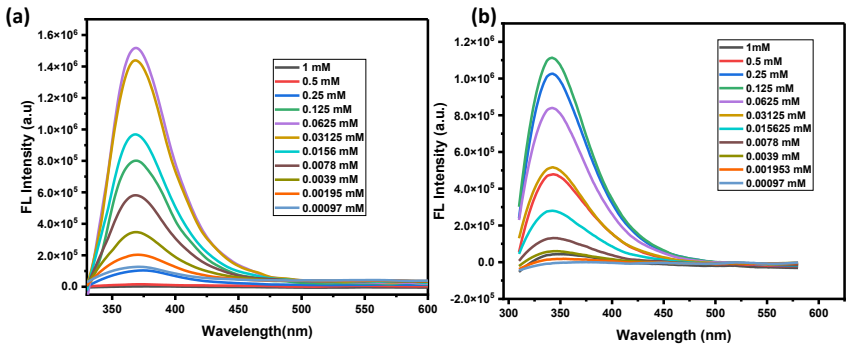

Figure 5.11 Emission spectra of Ligands **L5** and **L6** in methanol at room temperature; **(a)** emission spectrum of **L5** at different concentrations, **(c)** emission spectrum of **L6** at different concentrations.

5.2.6.2 Fluorescence in metal complexes synthesized with the CPAP ligands

To further study the effect of structural modifications in the ligand on the photophysical properties of the system, complexes formed by ligands **L5** and **L6** were used. Complexes **Ru7** and **Ru8** were tested for the fluorescence study, which were synthesized using **L5** and **L6**, respectively. The idea of incorporating metal complex fluorescence is to study the effect of ligand structural variation on the metal center in terms of fluorescence and how it frequently affects the photophysical activity. Among other structural variations, the possibility of hemilability due to the one linker of the ligands can be tested using fluorescence

spectroscopy as the probe. All the complexes were tested for fluorescence under the same external conditions. Complex **Ru8** demonstrated a peak at 420 nm, which suggested the emission intensity increases with concentration but saturates at high concentrations, a typical feature in photoluminescence where self-quenching or aggregation may occur. The excitation responsible for this emission likely originates from the absorption bands near 305 nm, indicating an efficient coupling between the absorption and emission processes. **Ru8** displayed an emission band at 420 nm. The highest intensity was observed at a concentration of 0.0625 mM, corresponding to approximately 4.8×10^4. At high concentrations, self-quenching occurs, whereas after 0.0625 mM, the intensity decreases again. **Ru7** showed the highest intensity among all at 0.03125 mM. It showed the emission band at 415 nm. All the complexes exhibited similar self-quenching properties at high concentrations (Figure 5.12).

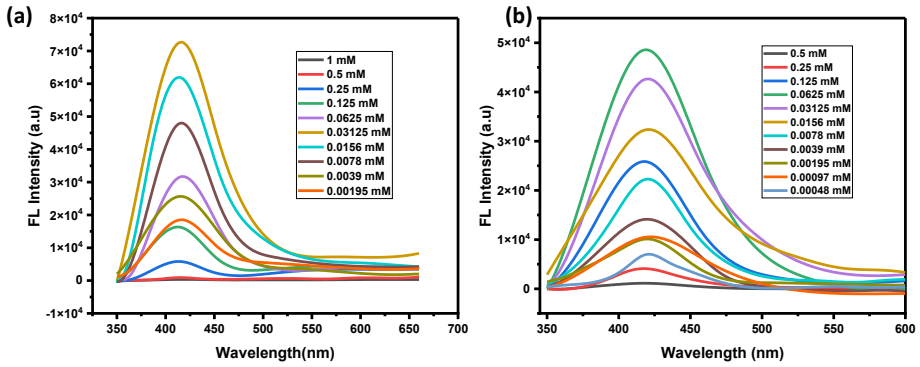

Figure 5.12 Emission spectra of Complexes **Ru7** and **Ru8** in methanol at room temperature: **(a)** emission spectrum of **Ru7** at different concentrations; **(b)** emission spectrum of **Ru8** at different concentrations.

5.2.7 Effect of the addition of 4-aminopyridine on fluorescence

Our previous reports have shown the possibility of hemilability in the **[Ru-A]** complex.[28] It was tested by adding 4-aminopyridine to the methanolic solution of **[Ru-A]**, which was confirmed by the formation of a complex where the 4-aminopyridine attaches to the site where pyridine is detached from the metal center.[28] To ensure the existence of

hemilability in this system and the effect of structural variation resulting from the substitution of the *N*-linker, we performed experiments by adding 4-aminopyridine to each complex in a subsequent step. For this, a 0.5 mM concentration is selected, as the small intensity of the complexes is present at this concentration, which does not hinder the experiment and can be helpful in analyzing the fluorescence spectra.

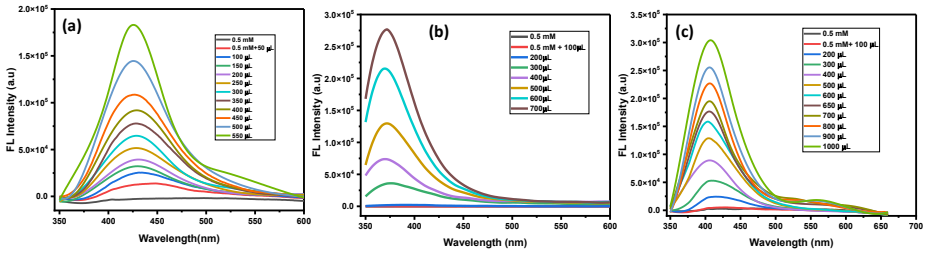

Figure 5.13 Emission spectra for complexes **[Ru-A]**, **Ru7,** and **Ru8** in methanol at room temperature after the sequential addition of 4-aminopyridine.

In **[Ru-A]**, the addition of 50 µL of 4-aminopyridine suddenly showed a peak at 428 nm, which further increased with the addition of 4-aminopyridine (Figure 5.13). Upon the addition of 550 µL, a peak intensity of 1.8×10^5 was observed. The position of the emission band was closer to that of the ligand, indicating the possibility of hemilability. The higher fluorescence may be due to the improved conjugation, and the dissociation suppresses photoinduced electron transfer (PET).[29] When pyridine is coordinated, PET is active, and the fluorescence is quenched. Upon dissociation, PET stops, resulting in an increase in fluorescence.[29,30] In this scenario, another possibility is that the metal-ligand charge transfer (MLCT) becomes less efficient and the intra-ligand charge transfer (ILCT)/π-π- emission dominates.

In the case of **Ru8**, after the addition of 4-aminopyridine at a concentration of 0.5 mM, no such band was initially observed. Even after adding 100 µL, no bands were observed. After the addition of 200 µL, a band at 405 nm appeared, which further increased in intensity with the subsequent addition of 4-aminopyridine. When comparing with **[Ru-A]**, at 500 µL, the intensity is approximately 1.25×10^5. In contrast to

complexes **[Ru-A]** and **Ru8**, **Ru7** has shown that even after the addition of 200 μL of 4-aminopyridine, no band was observed. On increasing the amount of 4-aminopyridine, the intensity of the band at 372 nm increases. The bands of all the complexes were found to be in closer proximity to the ligand than to the metal complex. The ratio of the initial intensity of the ligand to the band observed after the addition of 4-aminopyridine illustrates that the enhancement of intensity after the addition of 4-aminopyridine is more pronounced in the case of **[Ru-A]**, which has an *N*-tolyl group, than in the case of the *N*-methyl and *N*-H linker complexes, **Ru8** and **Ru7**, respectively.

The fluorescence of the ligand was significantly diminished upon metalation, resulting in a reduction in fluorescence intensity and the appearance of peaks at positions distinct from those of the ligand. Upon the addition of 4-aminopyridine, as previously reported for **[Ru-A]**, 4-AP replaces pyridine, and the hemilability of this pyridine results in a different band. This indicates that hemilability induces conjugation of the ligand, which may initially be reduced because of metal-ligand interactions. Similarly, **Ru8** and **Ru7** exhibit similar properties, which, based on the ratio of the initial ligand intensity to the band intensity following the addition of 4-aminopyridine, suggests an enhancement in intensity for **Ru7**, albeit less than that for **Ru8**, which is further lower than **that for [Ru-A]**. This clearly suggests the possibility that the *N*-tolyl group, due to its bulkiness and strong electron-donating properties, detaches more readily compared to the *N*-Me group, which is less bulky than the *N*-tolyl group. In contrast, for *N*-H, dissociation is less feasible because the dissociation of *N*-H may further increase the electron density on the metal center, making dissociation less likely.

We plotted a calibration curve by correlating the fluorescence intensity of all the ligands and complexes with their concentration over a defined range, which showed a clear linear relationship consistent with Beer-Lambert-type behavior in fluorescence measurements. This calibration graph enables the determination of the concentration of an unknown sample by measuring its emission intensity and using the standard curve

to interpolate the corresponding concentration. Fluorescence-based calibration is highly sensitive, enabling precise quantification even at low analyte concentrations, and is particularly useful when sample quantities are limited. In the present study, this approach provides a reliable quantitative tool for estimating unknown concentrations, validating the reproducibility of photophysical measurements, and comparing the emissive behavior of different ligands or complex systems. Overall, the fluorescence calibration method significantly enhances the analytical robustness and interpretability of fluorescence studies.

5.3 Conclusion

A new luminescent complex, **Ru9**, exhibiting dual fluorescence, has been successfully synthesized from a known precursor **[Ru-A]**. All the ligands being fluorescent showed different behaviour after the metalation due to the quenching. Alteration in intensities of the fluorescence of the complexes, turn this study towards the investigation of hemilability of all the ligands in their corresponding complexes. A systematic investigation demonstrated that hemilability and *N*-linker substitution are pivotal in modulating fluorescence behavior. These findings underscore the correlation between ligand dynamics and photophysical response, offering valuable design principles for the development of next-generation responsive luminescent materials. All complexes, **[Ru-A], Ru7**, and **Ru8**, exhibited a trend consistent with the hypothesis regarding the hemilability of the system based on *N*-substitution.

5.4 Experimental Section

5.4.1 General experimental Information

All synthesis experiments for preparing the complexes were conducted under a nitrogen atmosphere using standard Schlenk line techniques. Solvents were purified following established protocols under nitrogen and stored over 4 Å molecular sieves within an N_2 glove box. Reagents were purchased from commercial suppliers and used without additional purification, although many chemicals underwent purification according

to standard methods. NMR spectra were recorded at room temperature and pressure using a Bruker Avance 400 MHz spectrometer (400 MHz for ^{1}H, 100 MHz for ^{13}C, and 162 MHz for ^{31}P) and a 500 MHz spectrometer (500 MHz for ^{1}H, 125 MHz for ^{13}C, and 202 MHz for ^{31}P). Deuterated solvents, including dimethyl sulfoxide and chloroform, were employed for NMR analysis, with chemical shift values (δ) reported in parts per million relative to the residual solvent signals. The resonance peaks for ^{1}H in $CDCl_3$ are at δ 7.26 and in DMSO-d_6 at δ 2.50 ppm; for ^{13}C, $CDCl_3$ appears at δ 77.0 and DMSO-d_6 at δ 40.45 ppm. Varian UV-vis spectrophotometer for UV-visible absorption studies. Fluorescence spectra for all compounds were recorded using a HORIBA Jobin Yvon model FM-100 Fluoromax-4Spectrofluorometer.

5.4.2 Synthesis of complex Ru9. An oven-dried Schlenk tube was charged with [**Ru-A]** (53.65 mg, 0.05 mmol) in ethanol (10 mL), followed by the addition of 2,2′-bipyridine (46.85 mg, 0.30 mmol). The resulting mixture was stirred at reflux temperature for 36 h. After the reaction was completed, the mother liquor was filtered through a short Celite pad and reduced to 1-2 mL under reduced pressure. Then, diethyl ether was added, and an orange precipitate was obtained. Finally, after drying under high vacuum, the compound was obtained as an orange powder. Yield 26 mg (56%).**^{1}H NMR** (500 MHz, DMSO-d_6, 25 °C) ^{1}H NMR (500 MHz, DMSO) δ 14.92 (s, 1H), 9.06 (d, *J* = 8.2 Hz, 1H), 8.97 (d, *J* = 8.5 Hz, 1H), 8.90 (d, *J* = 8.2 Hz, 1H), 8.72 (d, *J* = 5.8 Hz, 1H), 8.40 (t, *J* = 8.0 Hz, 1H), 8.21 (t, *J* = 7.9 Hz, 1H), 8.07 (dd, *J* = 18.8, 8.1 Hz, 3H), 7.94 (t, *J* = 8.5 Hz, 1H), 7.86 (d, *J* = 8.1 Hz, 1H), 7.75 (dd, *J* = 19.9, 6.8 Hz, 2H), 7.67 (d, *J* = 7.9 Hz, 1H), 7.58 (t, *J* = 6.5 Hz, 2H), 7.53 (d, *J* = 7.9 Hz, 3H), 7.39 (d, *J* = 7.5 Hz, 3H), 7.35 – 7.31 (m, 2H), 7.20 (t, *J* = 7.8 Hz, 7H), 7.03 (t, *J* = 9.1 Hz, 6H), 6.91 (d, *J* = 7.6 Hz, 3H), 6.84 (d, *J* = 8.7 Hz, 1H), 6.61 (s, 1H), 6.47 (d, *J* = 9.0 Hz, 1H), 2.54 (s, 4H).**^{31}P NMR** (202 MHz, DMSO-d_6, 25 °C) δ 46.2 **^{13}C NMR** (126 MHz, DMSO-d_6, 25 °C) ^{13}C NMR (126 MHz, DMSO) δ 201.6, 157.1, 156.5, 155.2, 154.1, 153.6, 151.6, 151.1, 148.6, 147.5, 139.8, 139.7, 139.3, 139.2, 139.1, 138.9, 137.9, 135.5, 132.6, 132.1, 130.6, 130.3, 129.7, 128.8,

127.9, 126.1, 125.3, 124.6, 123.9, 119.7, 118.7, 115.6, 113.9, 112.1, 111.7, 107.0, 20.8. ESI-MS calculated accordance to $C_{52}H_{42}N_7PRuCl_2$, obtained value for $[M\text{-}2Cl]^{2+}$ at m/z = 448.6163 and for $[M\text{-}2Cl\text{-}H]^{+}$ at m/z = 898.2187.

5.4.3 X-ray crystallography

Single crystals of complex **Ru9** suitable for X-ray crystallographic analysis were obtained by layering the corresponding solutions in acetonitrile with diethyl ether (1:3, v/v) at -4°C. X-ray diffraction studies were conducted using an Agilent dual-core SuperNova CCD system (Oxford Diffraction) with monochromated Mo-Kα radiation (λ = 0.71073 Å). Unit cell determination, data collection, reduction, and empirical absorption corrections were processed with the CrysAlisPro65 software. The graphical interface Olex 2-1.5 was used for structural visualization.[31] The structures were solved using direct methods via SHELXT,[32] revealing all non-disordered, non-hydrogen atoms, which were refined anisotropically. The structural model was refined by full-matrix least-squares minimization on F^2, utilizing ShelXL [33] within the Olex2 graphical interface. Hydrogen atoms were placed in fixed positions during the final stages of refinement. The crystallographic data corresponding to the Cambridge Crystallographic Data Centre (CCDC) entry 2492139 for **Ru9** are available free of charge through the joint CCDC/Fachinformationszentrum Karlsruhe Access Structures service. These data can also be requested by emailing deposit@ccdc.cam.ac.uk.

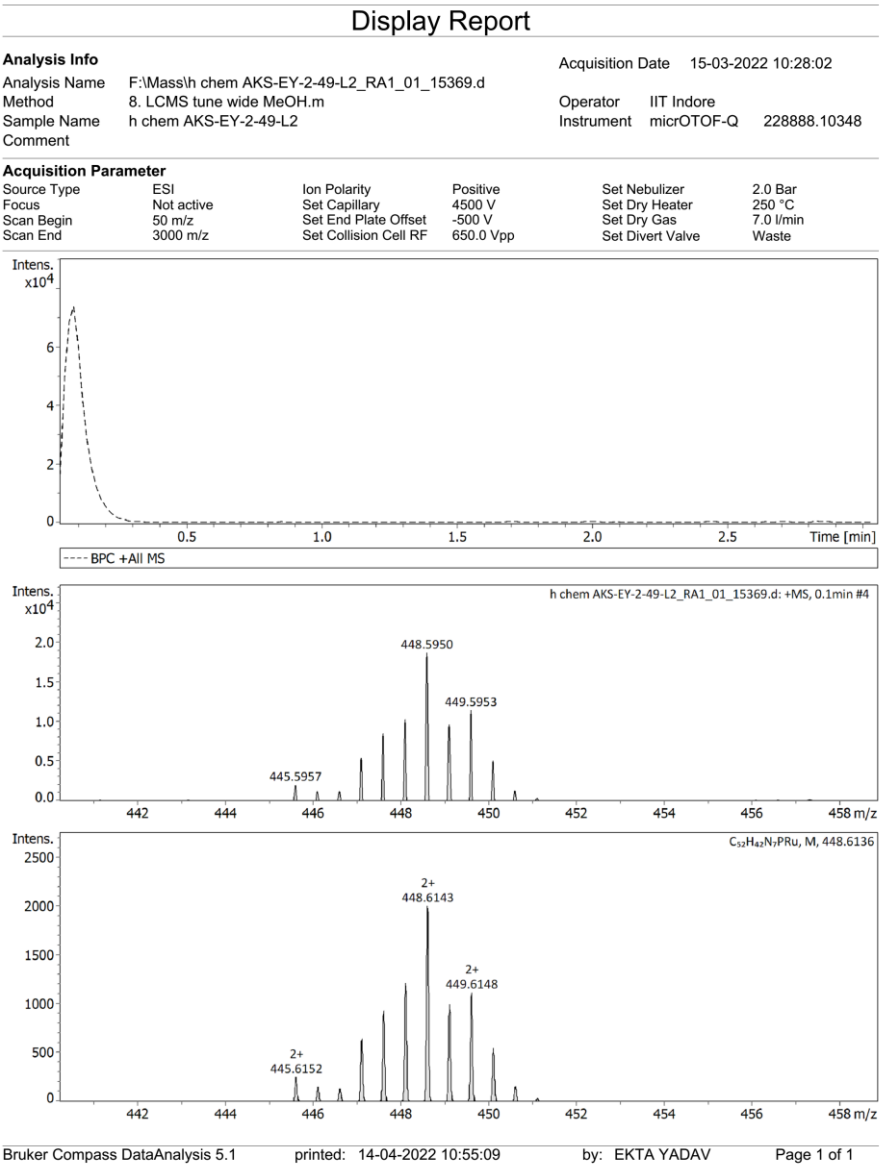

Figure 5.14 LCMS of **Ru9** for $[M\text{-}2Cl]^{2+}$

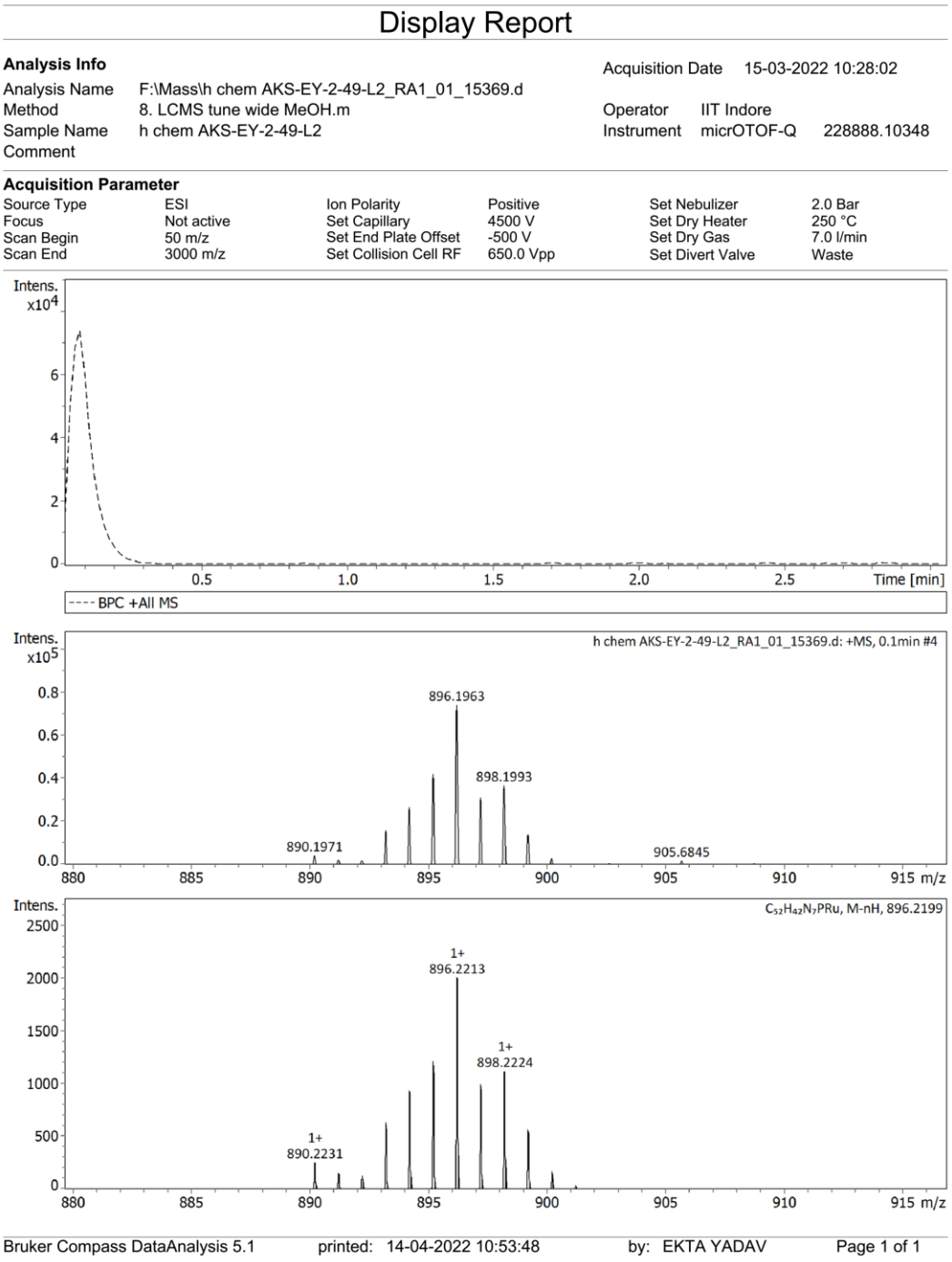

Figure 5.15 LCMS of **Ru9** for $[M\text{-}2Cl\text{-}H]^+$

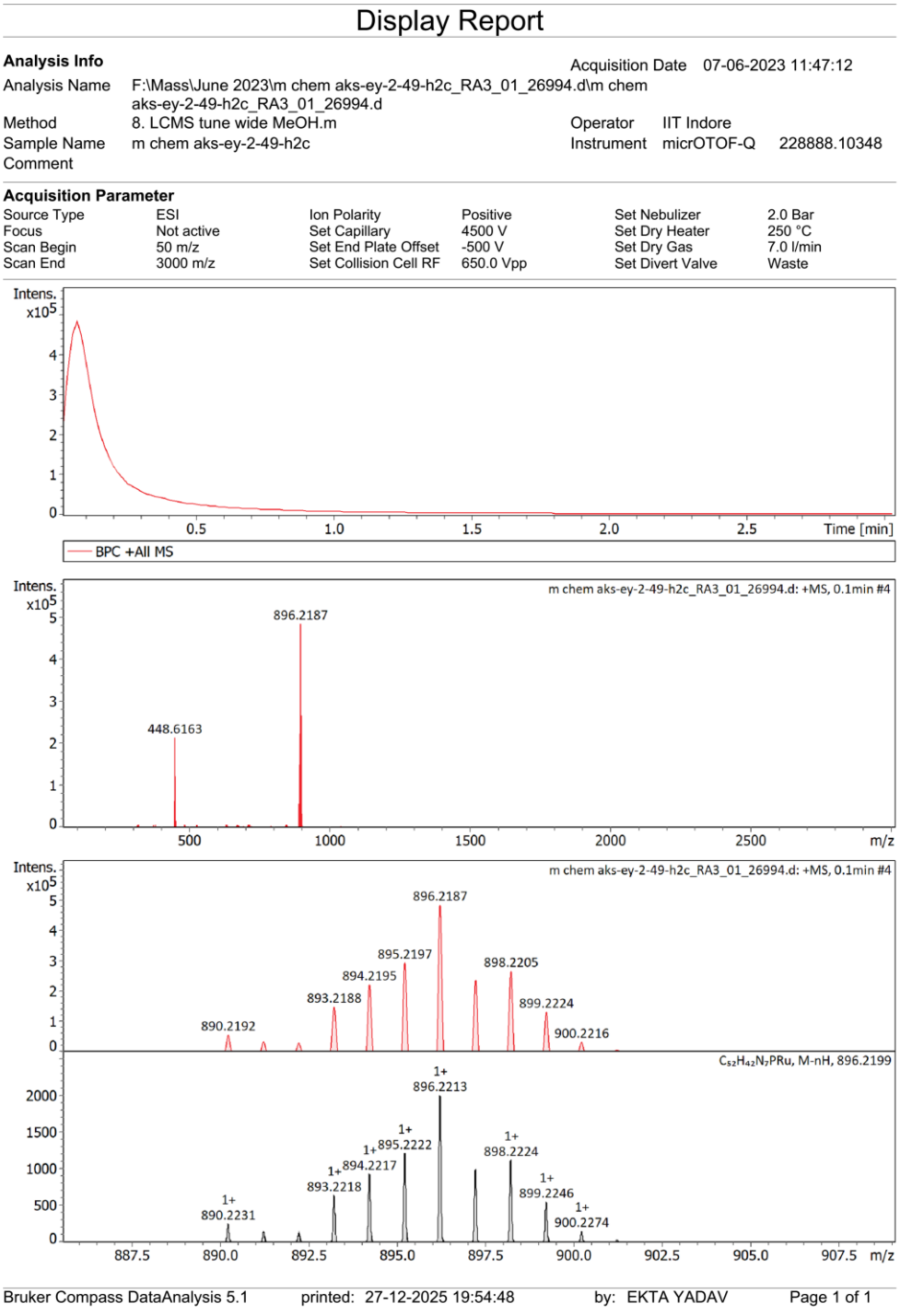

Figure 5.16 HRMS of **Ru9** for $[M\text{-}2Cl\text{-}H]^+$

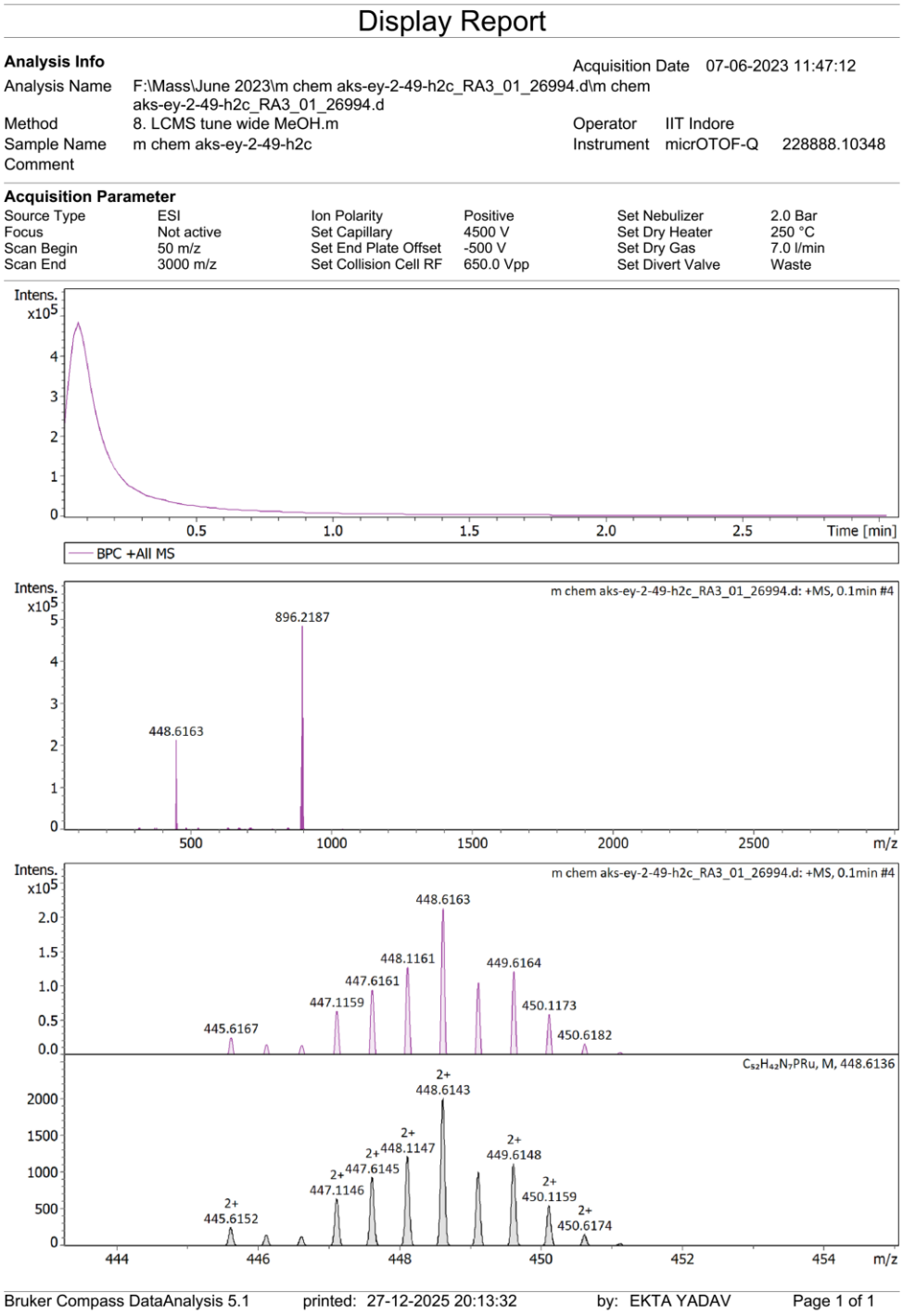

Figure 5.17 HRMS of **Ru9** for $[M\text{-}2Cl]^{2+}$

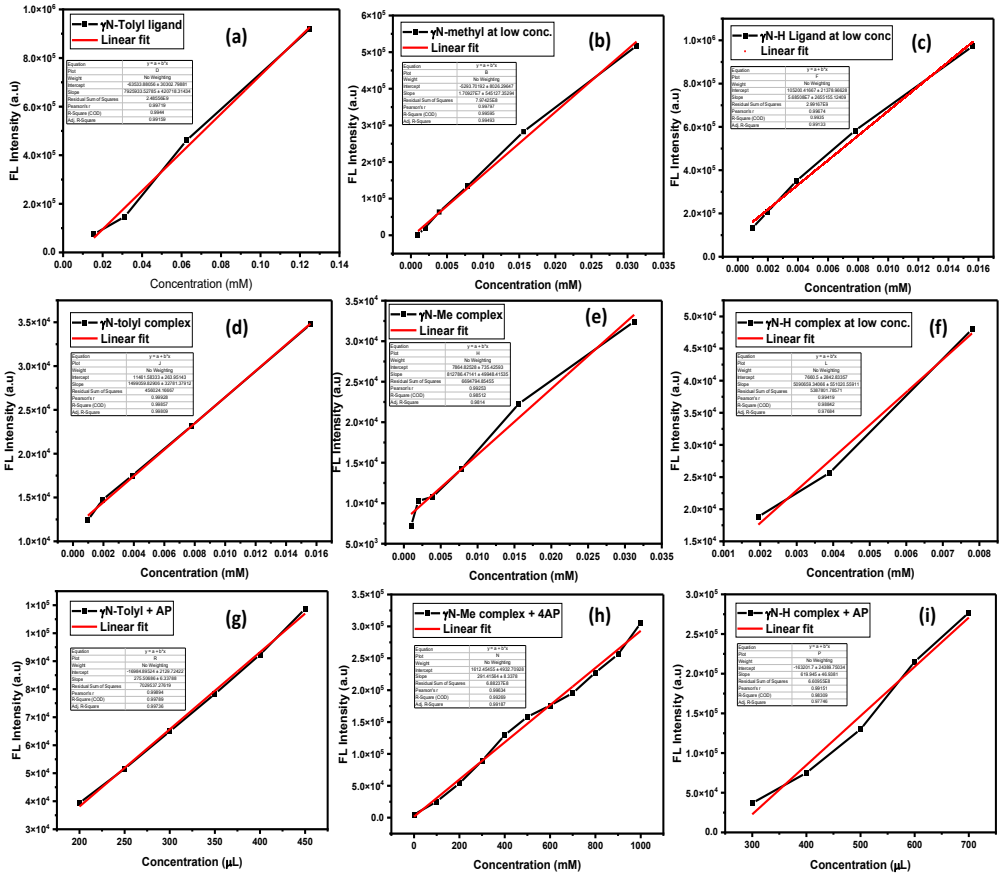

Figure 5.18 Correlation of fluorescence intensity and the concentrations of (a-b) ligands; (c-e) complexes; (f-h) after addition of 4-aminopyridine

5.5 References

[1] Dong, J., Zhang, X.-D., Xie, X.-F., Guo, F., and Sun, W.-Y. (2020). Amino group dependent sensing properties of metal–organic frameworks: selective turn-on fluorescence detection of lysine and arginine. RSC Adv., *10*, 37449–37455. (https://doi.org/10.1039/D0RA06879A)

[2] Xu, J., and Shalom, M. (2019). Conjugated Carbon Nitride as an Emerging Luminescent Material: Quantum Dots, Thin Films and Their Applications in Imaging, Sensing, Optoelectronic Devices

and Photoelectrochemistry. ChemPhotoChem, *3*, 170–179. (https://doi.org/10.1002/cptc.201800256)

[3] Williams, J.A.G. (2007). Photochemistry and Photophysics of Coordination Compounds: Platinum. In Photochemistry and Photophysics of Coordination Compounds II Topics in Current Chemistry., V. Balzani and S. Campagna, eds. (Springer Berlin Heidelberg), pp. 205–268. (https://doi.org/10.1007/128_2007_134)

[4] Saha, M.L., Yan, X., and Stang, P.J. (2016). Photophysical Properties of Organoplatinum(II) Compounds and Derived Self-Assembled Metallacycles and Metallacages: Fluorescence and its Applications. Acc. Chem. Res., *49*, 2527–2539. (https://doi.org/10.1021/acs.accounts.6b00416)

[5] Treacy, S.M., and Rovis, T. (2024). Photoinduced Ligand-to-Metal Charge Transfer in Base-Metal Catalysis. Synthesis *56*, 1967–1978. (https://doi.org/10.1055/s-0042-1751518)

[6] Herr, P., Kerzig, C., Larsen, C.B., Häussinger, D., and Wenger, O.S. (2021). Manganese(i) complexes with metal-to-ligand charge transfer luminescence and photoreactivity. Nat. Chem., *13*, 956–962. (https://doi.org/10.1038/s41557-021-00744-9)

[7] Juliá, F. (2022). Ligand-to-Metal Charge Transfer (LMCT) Photochemistry at 3d-Metal Complexes: An Emerging Tool for Sustainable Organic Synthesis. ChemCatChem, *14*, e202200916. (https://doi.org/10.1002/cctc.202200916)

[8] Bo, C.-B., Bu, Q., Li, X., Ma, G., Wei, D., Guo, C., Dai, B., and Liu, N. (2020). Highly Active and Robust Ruthenium Complexes Based on Hemilability of Hybrid Ligands for C–H Oxidation. J. Org. Chem., *85*, 4324–4334. (https://doi.org/10.1021/acs.joc.0c00025)

[9] Adams, G.M., and Weller, A.S. (2018). POP-type ligands: Variable coordination and hemilabile behaviour. Coord Chem Rev, *355*, 150–172. (https://doi.org/10.1016/j.ccr.2017.08.004)

[10] Verhoeven, D.G.A., and Moret, M.-E. (2016). Metal–ligand cooperation at tethered π-ligands. Dalton Trans., *45*, 15762–15778. (https://doi.org/10.1039/C6DT02184K)

[11] Smith, N.E., Bernskoetter, W.H., and Hazari, N. (2019). The Role of Proton Shuttles in the Reversible Activation of Hydrogen via Metal–Ligand Cooperation. J. Am. Chem. Soc., *141*, 17350–17360. (https://doi.org/10.1021/jacs.9b09062)

[12] Fogler, E., Garg, J.A., Hu, P., Leitus, G., Shimon, L.J.W., and Milstein, D. (2014). System with Potential Dual Modes of Metal–Ligand Cooperation: Highly Catalytically Active Pyridine-Based PNNH–Ru Pincer Complexes. Chem Eur J, *20*, 15727–15731. (https://doi.org/10.1002/chem.201405295)

[13] Shimbayashi, T., and Fujita, K. (2020). Recent Advances in Homogeneous Catalysis via Metal–Ligand Cooperation Involving Aromatization and Dearomatization. Catalysts, *10*, 635. (https://doi.org/10.3390/catal10060635)

[14] Khusnutdinova, J.R., and Milstein, D. (2015). Metal–Ligand Cooperation. Angew Chem Int Ed, *54*, 12236–12273. (https://doi.org/10.1002/anie.201503873)

[15] Milstein, D. (2015). Metal–ligand cooperation by aromatization–dearomatization as a tool in single bond activation. Phil. Trans. R. Soc. A., *373*, 20140189. (https://doi.org/10.1098/rsta.2014.0189)

[16] Ramspoth, T.-F., Kootstra, J., and Harutyunyan, S.R. (2024). Unlocking the potential of metal ligand cooperation for enantioselective transformations. Chem. Soc. Rev., *53*, 3216–3223. (https://doi.org/10.1039/D3CS00998J)

[17] Habraken, E.R.M., Jupp, A.R., Brands, M.B., Nieger, M., Ehlers, A.W., and Slootweg, J.C. (2019). Parallels between Metal-Ligand Cooperativity and Frustrated Lewis Pairs. Eur J Inorg Chem, *2019*, 2436–2442. (https://doi.org/10.1002/ejic.201900169)

[18] Hwang, L.C., and Wohland, T. (2007). Recent Advances in Fluorescence Cross-correlation Spectroscopy. Cell Biochem Biophys, *49*, 1–13. (https://doi.org/10.1007/s12013-007-0042-5)

[19] Ladokhin, A.S. (2000). Fluorescence Spectroscopy in Peptide and Protein Analysis. In Encyclopedia of Analytical Chemistry, R. A. Meyers, ed. (Wiley). (https://doi.org/10.1002/9780470027318.a1611)

[20] Mocz, G., and Ross, J.A. (2013). Fluorescence Techniques in Analysis of Protein–Ligand Interactions. In Protein-Ligand Interactions Methods in Molecular Biology., M. A. Williams and T. Daviter, eds. (Humana Press), pp. 169–210. (https://doi.org/10.1007/978-1-62703-398-5_7)

[21] Lindner, R., Van Den Bosch, B., Lutz, M., Reek, J.N.H., and Van Der Vlugt, J.I. (2011). Tunable Hemilabile Ligands for Adaptive Transition Metal Complexes. Organometallics, *30*, 499–510. (https://doi.org/10.1021/om100804k)

[22] De La Durantaye, L., McCormick, T., Liu, X.-Y., and Wang, S. (2006). Interaction of 2-(2′-pyridyl)benzimidazolyl derivative ligands with group 12 metal ions: coordination, structures and luminescence. Dalton Trans., 5675–5682. (https://doi.org/10.1039/B604047K)

[23] Somerville, R.J., and Campos, J. (2021). Cooperativity in Transition Metal Tetrylene Complexes. Eur J Inorg Chem, *2021*, 3488–3498. (https://doi.org/10.1002/ejic.202100460)

[24] Bassetti, M. (2006). Kinetic Evaluation of Ligand Hemilability in Transition Metal Complexes. Eur J Inorg Chem, *2006*, 4473–4482. (https://doi.org/10.1002/ejic.200600212)

[25] Nath, S., Yadav, E., Raghuvanshi, A., and Singh, A.K. (2023). Ru(II) Complexes with Protic- and Anionic-Naked-NHC Ligands for Cooperative Activation of Small Molecules**. Chem Eur J, *29*, e202301971. (https://doi.org/10.1002/chem.202301971)

[26] Dhanya, S., and Bhattacharyya, P.K. (1992). Fluorescence behaviour of 2,2′-bipyridine in aqueous solution. J. Photochem. Photobiol., *63*, 179–185. (https://doi.org/10.1016/1010-6030(92)85134-G)

[27] Zhu, L., Younes, A.H., Yuan, Z., and Clark, R.J. (2015). 5-Arylvinylene-2,2′-bipyridyls: Bright "push–pull" dyes as components in fluorescent indicators for zinc ions. J. Photochem. Photobiol., *311*, 1–15. (https://doi.org/10.1016/j.jphotochem.2015.05.008)

[28] Nath, S., and Singh, A.K. (2025). Substrate-assisted product release in hydrogenation of LOHCs facilitated by hemilabile pyridine in Ru(II)–NNC pincer complexes and enhanced activity of proton-responsive protic-NHC ligands. Catal. Sci. Technol., *15*, 2999–3008. (https://doi.org/10.1039/D5CY00209E)

[29] Wu, L., Liu, J., Li, P., Tang, B., and James, T.D. (2021). Two-photon small-molecule fluorescence-based agents for sensing, imaging, and therapy within biological systems. Chem. Soc. Rev., *50*, 702–734. (https://doi.org/10.1039/D0CS00861C)

[30] Sumalekshmy, S., and Fahrni, C.J. (2011). Metal-Ion-Responsive Fluorescent Probes for Two-Photon Excitation Microscopy. Chem. Mater., *23*, 483–500. (https://doi.org/10.1021/cm1021905)

[31] Dolomanov, O.V., Bourhis, L.J., Gildea, R.J., Howard, J.A.K., and Puschmann, H. (2009). *OLEX2* : a complete structure solution, refinement and analysis program. J Appl Crystallogr, *42*, 339–341. (https://doi.org/10.1107/S0021889808042726)

[32] Sheldrick, G.M. (2015). *SHELXT* – Integrated space-group and crystal-structure determination. Acta Crystallogr A Found Adv, *71*, 3–8. (https://doi.org/10.1107/S2053273314026370)

[33] Sheldrick, G.M. (2008). A short history of *SHELX*. Acta Crystallogr A Found Crystallogr, *64*, 112–122. (https://doi.org/10.1107/S0108767307043930)



CHAPTER 6

Summary and Future Scope



6.1 Summary

This thesis primarily explores the design of ligands and the development of the resulting Ru(II) pincer complexes that incorporate NHCs, aiming to assess their effectiveness in various applications. Even minor structural adjustments can alter the electronic characteristics, steric configurations, and potential for ligand-centered cooperation in catalytic systems. This study specifically delves into the structural variations of a ligand known as CPAP, an asymmetrical pincer ligand series synthesized by our group, providing an opportunity to study comparative reactivity and conduct mechanistic analyses based on different substituents.

Chapter 1 introduces transition metal catalysis driven by rational ligand design as a strategy for clean energy and sustainable synthesis. This study emphasizes how tunable pincer and NHC frameworks, especially protic NHCs (pNHCs) with *N*-H functionality, enhance the catalytic activity, selectivity, and stability through electronic and cooperative effects. It also defines the thesis objective: designing Ru-pincer complexes with systematic ligand variations to establish structure-activity relationships for robust, energy-relevant catalysis.

Chapter 2 provides an in-depth analysis of electrochemical water oxidation using Ru(II)-bis(pincer) complexes, highlighting the synthesis and significance of protic NHC ligands and their corresponding Ru(II) complexes. It discusses the comparative catalytic performance of complexes bearing protic or classical NHC ligands based on β-N substitution on the CPAP ligand framework. Additionally, a detailed discussion of electrochemical water oxidation is included, showcasing the electrochemical properties of all four saturated complexes. This discussion emphasizes the mechanistic investigation, along with pH dependence studies and stability experiments, to gain a deeper understanding of the behavior of the catalyst in this catalytic application.

Chapter 3 examines Ru(II)-protic-NHC complexes with various azole ring systems in the CPAP ligand for *N*-methylation of anilines using

methanol as a green C1 source. Unsymmetrical CNN pincer complexes containing benzimidazolylidene (**[Ru-A]-[Ru-b]**), triazolylidene (**[Ru-C]-[Ru-d]**), and imidazolylidene (**Ru5**, **Ru6**) were synthesized and tested. The benzimidazolylidene complex **[Ru-A]** exhibited the highest activity and selective mono-*N*-methylation. Microwave irradiation enhanced the efficiency, reducing the reaction time from 12 h to 35 min at 40 °C while maintaining the yield. The method exhibited broad substrate tolerance and enabled gram-scale synthesis. Mechanistic studies utilizing NMR, mass, and GC-MS analyses support a borrowing-hydrogen mechanism. The protic-NHC Ru(II) framework, combined with microwave irradiation, provides an efficient route for the selective *N*-methylation of anilines.

Chapter 4 explores the complexes formed through substitution on the γ-N of the ligand framework. The details of the synthesis and catalytic assessment of Ru(II)-protic-NHC complexes featuring β-NH backbones with either γ-NH (**Ru7**) or γ-NMe (**Ru8**) substituents are mentioned. These, along with previously documented Ru(II)-protic-NHC and classical NHC counterparts (**[Ru-A]-[Ru-d**]), serve as a basis for examining the impact of β- and γ-substituents on formic acid dehydrogenation (FADH). The complexes demonstrated catalytic activity under base-assisted, solvent-free conditions and in ionic liquid, 1-butyl-3-methylimidazolium acetate (BMIMOAc), as a solvent without requiring an external base. **[Ru-A]** showed the highest performance in ionic liquid, reaching a turnover frequency (TOF) of 4,300 h^{-1}. Mechanistic investigations indicate that catalysis follows a protic-NHC route under base-assisted conditions, whereas anionic-NHC intermediates are predominant in ionic-liquid-mediated FADH. The H_2/CO_2 mixture was employed for alkene hydrogenation, and CO_2 capture experiments verified the selective use of the gas. The β-NH group boosts catalytic activity compared to its *N*-methylated counterpart, whereas the γ-NH feature has negative effects compared to the γ-*N*-alkyl and γ-*N*-aryl derivatives.

Chapter 5 describes a new Ru(II)-protic-NHC complex made from a previously known precursor **[Ru-A]**, which shows dual fluorescence emission. To understand the origin of each emission band, a comparison was made with a set of related fluorescent ligands. The fluorescence behavior of both the free ligands and their complexes is affected by the flexible (hemilabile) substituents and the type of nitrogen linker in the ligand framework. Even small changes in donor flexibility or coordination strength influence light-emission properties, highlighting the important role of hemilability in excited-state behavior. Overall, the results demonstrate that careful ligand design and metal-ligand interactions can be utilized to fine-tune the emission properties of the complexes.

Overall, this thesis demonstrates how rational modifications to the CPAP pincer ligand framework, featuring tunable β-N, azole, and γ-N substitutions, enable the development of versatile Ru(II) complexes for sustainable catalysis. The work highlights the superior catalytic efficiency of protic NHCs over classical NHC counterparts, driven by β-N substitution effects that enhance activity, selectivity, and stability in water oxidation, *N*-methylation of anilines using methanol, and formic acid dehydrogenation (FADH) with **[Ru-A]** achieving higher efficiency. Different azole ring systems and γ-N substituents (NH vs. NMe) exert distinct influences on performance, revealing cooperative electronic and hemilabile effects. Notably, γ-NH had a detrimental catalytic effect. Fluorescence properties were used as a probe for the hemilability, as an additional effect of the γ-N substituents on the complexes. These structure-activity relationships validate the pNHC-based design as a powerful strategy for various chemical transformations.

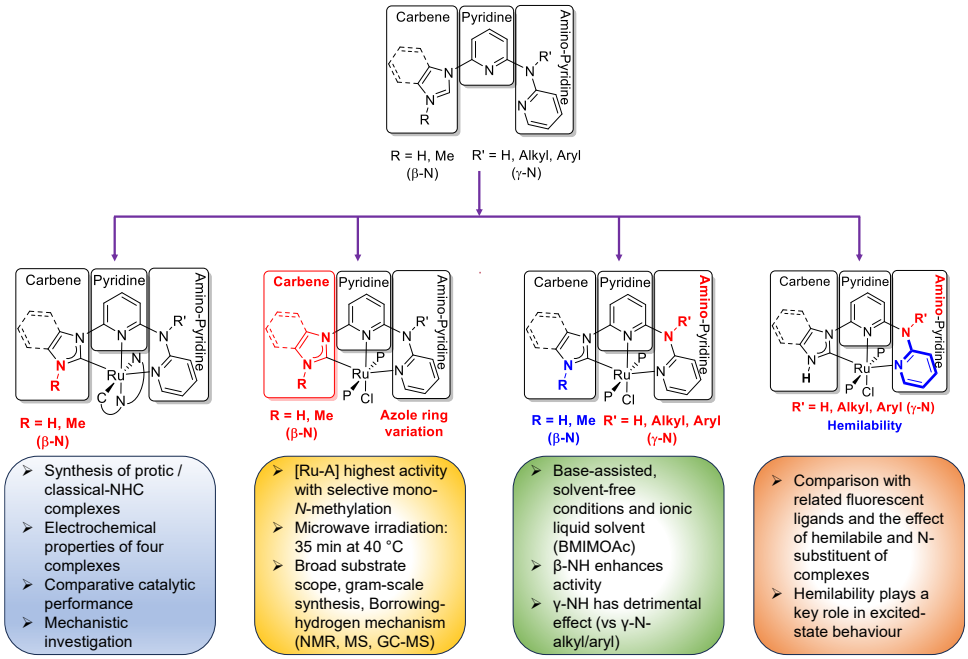

6.2 Future scope

Future investigations can build upon the existing CPAP platform by examining its ability to coordinate versatility with a wider range of first-row transition metals such as Fe, Co, and Mn. Utilizing these earth-abundant and cost-effective metals can significantly enhance the sustainability and scalability of catalytic systems. Systematic tuning of the β-/γ-N donors and carbene electronic parameters could further refine the electronic and steric environments of the ligand, resulting in significant enhancements in catalytic metrics, such as lower overpotentials, higher turnover numbers, and enhanced durability under operational conditions. These studies could be expanded to examine the ligand's adaptability in diverse catalytic transformations, including hydrogenation, dehydrogenation, and CO_2 reduction reactions, thereby establishing CPAP as a versatile scaffold for next-generation green catalysis applications.

Another promising avenue for future research involves the development of chiral CPAP-based catalysts designed to achieve enantioselective transformations. By incorporating asymmetric features into the CPAP

framework, the system can promote the selective synthesis of chiral molecules, which are valuable in the pharmaceutical and fine chemical industries. Conducting detailed mechanistic studies through kinetic studies, isotope labeling, and identification of active intermediates using spectroscopic and computational methods would offer a deeper insight into the reaction pathways and dynamics of metal-ligand cooperation. Such a mechanistic understanding would not only optimize catalyst design but also guide the rational development of CPAP analogs for specific catalytic applications.